



Ministério da
**Ciência, Tecnologia
e Inovação**



sid.inpe.br/mtc-m19/2013/02.20.19.07-TDI

IDENTIFICATION AND CHARACTERIZATION OF INTERPLANETARY MAGNETIC CLOUDS

Arian Ojeda González

Doctorate Thesis at Post Graduation Course in Space Geophysics, advised by Drs. Odim Mendes Jr., and Margarete Oliveira Domingues, approved in February 27, 2013.

URL of the original document:

<<http://urlib.net/8JMKD3MGP7W/3DJMQKS>>

INPE
São José dos Campos
2013

PUBLISHED BY:

Instituto Nacional de Pesquisas Espaciais - INPE

Gabinete do Diretor (GB)

Serviço de Informação e Documentação (SID)

Caixa Postal 515 - CEP 12.245-970

São José dos Campos - SP - Brasil

Tel.:(012) 3208-6923/6921

Fax: (012) 3208-6919

E-mail: pubtc@sid.inpe.br

BOARD OF PUBLISHING AND PRESERVATION OF INPE INTELLECTUAL PRODUCTION (RE/DIR-204):**Chairperson:**

Marciana Leite Ribeiro - Serviço de Informação e Documentação (SID)

Members:

Dr. Antonio Fernando Bertachini de Almeida Prado - Coordenação Engenharia e Tecnologia Espacial (ETE)

Dr^a Inez Staciarini Batista - Coordenação Ciências Espaciais e Atmosféricas (CEA)

Dr. Gerald Jean Francis Banon - Coordenação Observação da Terra (OBT)

Dr. Germano de Souza Kienbaum - Centro de Tecnologias Especiais (CTE)

Dr. Manoel Alonso Gan - Centro de Previsão de Tempo e Estudos Climáticos (CPT)

Dr^a Maria do Carmo de Andrade Nono - Conselho de Pós-Graduação

Dr. Plínio Carlos Alvalá - Centro de Ciência do Sistema Terrestre (CST)

DIGITAL LIBRARY:

Dr. Gerald Jean Francis Banon - Coordenação de Observação da Terra (OBT)

DOCUMENT REVIEW:

Marciana Leite Ribeiro - Serviço de Informação e Documentação (SID)

Yolanda Ribeiro da Silva Souza - Serviço de Informação e Documentação (SID)

ELECTRONIC EDITING:

Maria Tereza Smith de Brito - Serviço de Informação e Documentação (SID)

Luciana Manacero - Serviço de Informação e Documentação (SID)



Ministério da
**Ciência, Tecnologia
e Inovação**



sid.inpe.br/mtc-m19/2013/02.20.19.07-TDI

IDENTIFICATION AND CHARACTERIZATION OF INTERPLANETARY MAGNETIC CLOUDS

Arian Ojeda González

Doctorate Thesis at Post Graduation Course in Space Geophysics, advised by Drs. Odim Mendes Jr., and Margarete Oliveira Domingues, approved in February 27, 2013.

URL of the original document:

<<http://urlib.net/8JMKD3MGP7W/3DJMQKS>>

INPE
São José dos Campos
2013

Cataloging in Publication Data

- Ojeda G., A.
Oj2i Identification and characterization of interplanetary magnetic clouds / Arian Ojeda González. – São José dos Campos : INPE, 2013.
xxxviii + 292 p. ; (sid.inpe.br/mtc-m19/2013/02.20.19.07-TDI)
- Thesis (Doctorate in Space Geophysics) – Instituto Nacional de Pesquisas Espaciais, São José dos Campos, 2013.
Advised : Drs. Odim Mendes Jr., e Margarete Oliveira Domingues.
1. ICMEs. 2. magnetic cloud. 3. entropy. 4. space plasmas.
5. IMF. 6. space electrodynamics. I.Título.
- CDU 537.84:523.98
-

Copyright © 2013 do MCT/INPE. Nenhuma parte desta publicação pode ser reproduzida, armazenada em um sistema de recuperação, ou transmitida sob qualquer forma ou por qualquer meio, eletrônico, mecânico, fotográfico, reprográfico, de microfilmagem ou outros, sem a permissão escrita do INPE, com exceção de qualquer material fornecido especificamente com o propósito de ser entrado e executado num sistema computacional, para o uso exclusivo do leitor da obra.

Copyright © 2013 by MCT/INPE. No part of this publication may be reproduced, stored in a retrieval system, or transmitted in any form or by any means, electronic, mechanical, photocopying, recording, microfilming, or otherwise, without written permission from INPE, with the exception of any material supplied specifically for the purpose of being entered and executed on a computer system, for exclusive use of the reader of the work.

Aprovado (a) pela Banca Examinadora
em cumprimento ao requisito exigido para
obtenção do Título de **Doutor(a)** em
Geofísica Espacial

Dr. Alisson Dal Lago



Presidente / INPE / São José dos Campos - SP

Dra. Margarete Oliveira Domingues



Orientador(a) / INPE / SJCampos - SP

Dr. Odim Mendes Júnior



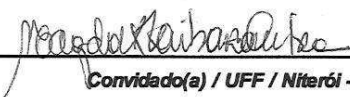
Orientador(a) / INPE / SJCampos - SP

Dr. Clezio Marcos De Nardin



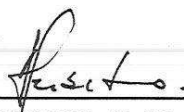
Membro da Banca / INPE / SJCampos - SP

Dra. Magda Kimico Kaibara



Convidado(a) / UFF / Niterói - RJ

Dr. Antonio de Padua Brito Serbeto



Convidado(a) / UFF / Niterói - RJ

Este trabalho foi aprovado por:

maioria simples

unanimidade

Aluno (a): **Arian Ojeda González**

São José dos Campos, 27 de Fevereiro de 2013

*“Liberty is the right of every man to be honest, to think and to speak
without hypocrisy. José Martí”.*

*To my wife Yuseen and my children Darian Ariel and
Daniel David. And my family.*

ACKNOWLEDGEMENTS

I am very grateful to my advisors Dr. Odim Mendes (Space Physics) and Dr. Margarete Oliveira Domingues (Applied Mathematics) for their valuable advice, patience and friendship along the adventures of a doctorate thesis.

I would like to thank INPE, GES and CEA for their support in this PhD project. Also to CAPES Grants number-00.889.834/0001-08 (2008-2010) and CNPq Grants number-141549/2010-6 (2010-2012) the PhD scholarship.

Acknowledgments to Eugene Kononov, author of the Visual Recurrence Analysis software. Also, I would like to thank ACE science team members for the datasets used in this work. I thank CAP team by the complementary courses. I can't forget IGA-Cuba by the help with the paperwork to travel to Brazil and the support offered by the colleagues of that institution. I am grateful with all INPE teachers during PhD courses; and with Eng. V. E. Menconni (FAPESP Grants number-2008/09736-1) for their helpful computational assistance. I would like to thank the postgraduate coordinators (CEA-INPE, 2008-2013): Dr. Alexandre Pimenta, Dr. Alisson dal Lago and, Dr. Polinaya Muralikrishna. I wish to thank my co-authors in conferences/congress/scholl/meetings proceedings and articles in scientific journals: Dra. Magda Kaibara, Dr. Alexander Calzadilla, Dr. Pablo Muñoz, Dr. Reinaldo R. Rosa, Dra. Virginia Klausner, Dr. Walter D. González, Dr. Clezio M. De Nardini, Dr. Andrés R. R. Papa, Dr. Christian Möstl and Dr. Charles J. Farrugia, and MSc. Marize Corrêa

To all people at the Space Geophysics Division (DGE) at INPE and in general to all Brazilian people that made me feel this country as my home. To Dra. Lourdes Palacio Suárez, Lic. Martha Zamora, Dra. Aracy Mendes, Dr. Francisco Carlos de Menezes Junior (Xico) and Dra. Alicia L. Clúa de Gonzalez who made it possible for me to come to Brazil. To all my friends at INPE, specially to Dr. Marcio Muela. To the small Cuban community at INPE: Regla Duthit, Siomel Savio, Neisy Forhan, Madeleine Sánchez, Eduardo S. Pereira and Germán Fariñas. To São José Wild Eagles Baseball team which shared unforgettable moments.

I would like to thank the all teachers who have cultivated my knowledge during 30 years. As said Isaac Newton "If I can see further than anyone else, it is only because

I am standing on the shoulders of giants". Special acknowledgments to Brazilian people by your hospitality. I would like to thank my family in Cuba.

ABSTRACT

A subset of Interplanetary Coronal Mass Ejections (ICMEs) has simple flux rope-like magnetic fields, named magnetic clouds (MCs). MCs present the characteristics of magnetic field strength higher than the average in the solar wind (SW), their magnetic field direction rotates smoothly through a large angle, and low-temperature protons. Plasmas and magnetic field typically accumulate in the sheath region ahead of MCs driving interplanetary shocks. The MCs have a significant importance due to effects on the geomagnetic activity. Depending on their characteristics, MCs can produce intense electrodynamic couplings with the Earth's magnetosphere. The aim of this work is to create a methodology to identify and subsequently characterize the dynamics of MCs from interplanetary magnetic field (IMF) signals received by satellites. Often, plasma data of SW are not available for this identification. A set of physical-mathematical techniques was analyzed and selected to study MC events. The spatio-temporal entropy, persistence exponents, discrete wavelet transform, and minimum variance analysis are the techniques applied. Datasets from ACE spacecraft localized at L1 Lagrangian point about 1.5 million km from Earth are used. MAG and SWEFAM are only used among a total of ten instruments onboard ACE. The SWEFAM measures the solar wind plasma and the MAG measures interplanetary magnetic field. Magnetic field vectors are given in the GSE and GSM coordinate systems with different time resolution available. This work deals with the 16 s time resolution most of the time. A total of 41 MCs identified by other authors were used, which allows dealing with the plasma sheath region, the MC and a pos-MC region. The physical basis for using these techniques were due to the existing characteristics related to the MC occurrences. As results, the time series analysis of the magnetic field inside the MCs regions shows that their fields are autocorrelated and structured. With few fluctuations and long memory in time series. From the above techniques, a set of indices were derived and related to the interplanetary entropy (IE), the persistence behavior and the wavelet coefficient identified features. The indices have been calculated continuously from 11.11 h (2500 records) windows using a proper SW time step. The use of these indices builds a useful tool to allow practical identification of MC candidates in the SW. We use the local Minimum Variance Analysis (MVA) to determine the direction of rotation of the magnetic field inside the MCs and the orientation of the MC axis, and identified their boundaries. The methodology was demonstrated to be useful with test cases. The tool was able to find MCs not previously identified. A case of double flux rope magnetic cloud presenting magnetic reconnection was studied from them. The reconstruction of two-dimensional maps of the magnetic configuration was also studied by using the Grad-Shafranov equation. In this case, we detect current sheet in this region, where two MCs are interacting, and the magnetic reconnection is observed. The wavelet coefficients technique becomes a tool for finding reconnection signatures or X-type

neutral point in interaction regions between flux-ropes. A second case of double flux rope magnetic cloud was studied, where X-type neutral point in the interaction region was not observed, because the magnetic fields were parallel among them (inside the interaction region). The major contribution of this work is the implementation of a methodology for the identification and characterization of MCs, adding new resources to the earlier tools. In a general sense, the proposed methodology can constitute an easy and automatic computational procedure for preliminary survey on MC occurrences for scientific goals, or even a convenient MC warning for the space weather purposes.

IDENTIFICAÇÃO E CARACTERIZAÇÃO DE NUVENS MAGNÉTICAS INTERPLANETÁRIAS

RESUMO

Nas Ejeções de Massa Coronal Interplanetária (ICMEs), há um subconjunto específico, onde o plasma possui um campo magnético bem estruturado em forma de corda de fluxo chamado de nuvem magnética (MC). As características principais são: o aumento da intensidade do campo magnético em relação ao valor médio no vento solar circundante, a rotação suave do vetor campo magnético, com duração na ordem de um dia e, a baixa densidade de prótons. Em consequência do rápido movimento das MCs em relação ao vento solar circundante, o plasma e as linhas de campo magnético se acumulam na frente da nuvem numa região chamada de bainha magnética. As MCs são importantes devido ao efeito sobre a atividade geomagnética. Dependendo das características, o plasma no interior da nuvem tem um acoplamento eletrodinâmico com a magnetosfera da Terra. O objetivo desta tese foi desenvolver uma metodologia para identificar e, posteriormente, caracterizar a dinâmica das MCs no meio interplanetário a partir de sinais recebidos pelos satélites. Nem sempre é possível usar os dados de plasma no vento solar (SW) devido à indisponibilidade para fazer esta identificação. Neste trabalho as ferramentas usadas foram: entropia espaço temporal, expoentes de persistência, transformada wavelet discreta e o método de mínima variância. Para isso, utilizou-se os dados do satélite ACE, localizado no ponto de Lagrange L1 à 1.5 milhões de km da Terra. Dos dez instrumentos a bordo do ACE, foram utilizados dois deles, o SWEPAM e o MAG que medem dados de plasma e campo magnético, respectivamente. Utilizou-se os sistemas de coordenadas GSE e GSM, com resolução temporal de 16 s, porém alguns resultados foram gerados com dados em outras resoluções temporais. As ferramentas físico-matemáticas citados foram testados, em 41 MCs identificadas anteriormente por outros autores, na região da bainha de plasma, da nuvem, e na região após nuvem visando validar a metodologia. A base física para a utilização das técnicas foi a existência de características relacionado com as ocorrências de MC, pois verificamos que as MCs tem um campo magnético ordenado, autocorrelacionado, com poucas flutuações e com aumento da memória na serie temporal. Das ferramentas utilizadas foi desenvolvido um grupo de índices relacionadas com a entropia (IE), o comportamento e as características de persistência, e os coeficientes wavelet. Os índices são calculados continuamente em janelas de 11.11 h em vários intervalos de vento solar. Eles auxiliam numa rápida identificação dos candidatos à MCs no vento solar. Foi utilizado a técnica de Análise de Mínima Variância (MVA) para determinar a direção de rotação do campo magnético dentro das MCs e a orientação do eixo das mesmas. Assim, as fronteiras da região da MC ficaram bem delimitadas. Nos casos utilizados para teste a metodologia mostrou-se útil. Comprovou-se a eficiência das ferramentas utilizadas, pois foi possível identificar novas MCs. Também foi estudado dois casos onde duas MCs interagem. Para isso, foi necessário gerar mapas

bidimensionais para visualizar as linhas de campo magnético, isto foi feito com uma técnica de reconstrução utilizando a equação diferencial de Grad-Shafranov (GS). No primeiro caso, onde duas MCs interagem, observa-se reconexão magnética, além de encontrar lâminas de correntes nessa região. A técnica dos coeficientes wavelet auxiliou na identificação do ponto X de reconexão. No segundo caso estudado, o ponto X de reconexão não é observado. Esses resultados concordam com a física do problema, das possíveis combinações de tipos de cordas de fluxos interagindo só vão se reconectar aqueles onde os campos magnéticos entre eles tenham sentidos opostos. A contribuição desta tese é a criação de uma nova metodologia para identificação e caracterização das MCs, utilizando novas ferramentas, até então não experimentadas, com as outras já existentes. A metodologia pode ser ajustada, em um curto prazo de tempo, como um produto eficiente para estudar variabilidade do Clima Espacial.

LIST OF FIGURES

	<u>Pág.</u>
2.1 Equilibrium in MHD fluid	11
2.2 Force-free field in an infinite cylinder. SOURCE: Lundquist (1950).	17
2.3 The sketch is reproduced from Burlaga (1991) to represent magnetic field lines inside of a magnetic cloud.	18
2.4 Magnetic vector potential and magnetic induction vector	21
2.5 Configurations of vectors in ideal MHD	24
2.6 Idealized sketch showing the expected magnetic field signatures during passage of a large-scale cylindrical magnetic flux tube over a s/c.	28
2.7 Sketch showing the different magnetic configuration of MCs and their magnetic helicity	30
2.8 Solar cycle dependence of the magnetic field structure of filaments at the Sun and that of the corresponding MCs in the interplanetary medium	33
3.1 The picture show all ACE instruments.	41
4.1 Recurrence plot using a data files included with VRA software. (left panel) In the RP organized patterns of color characteristics are shown for a periodic signal; sine wave with $STE = 0\%$. (right panel) In the RP an uniform distribution of color characteristics is shown for a random signal, white noise with $STE = 80\%$	47
4.2 (a): For a fractional Gaussian noises and fractional Brownian motions, β power spectrum has the range $-3 < \beta < 3$. The dependence with the Hurst exponent is not a linear function for all values. The straight-line correlation is with the relation $\beta = 2H_u - 1$. (b) is similar to (a), the dependence of the Hausdorff exponent versus β is shown.	
SOURCE: Malamud and Turcotte (1999) (Figures 17 and 25).	54
4.3 The variance ellipsoid. Eigenvectors, $\{\hat{x}_1, \hat{x}_2, \text{ and } \hat{x}_3\}$, are shown relative to the system (X, Y, Z) (e.g., GSE) in which the magnetic data are given. The normal direction is estimated to be along \hat{x}_3 .	
SOURCE: Sonnerup and Scheible (1998).	65
5.1 Time series plot of Lorenz data file included in VRA.	77

5.2	(a) $X(t)$ vs t is plotted, where $X(t)$ is a synthetic series created using a random number generator producing values in the range 0 to 1. To show the graph, a simple moving average is applied. The time series of random number has a recurrence plot similar to shown in Figure 4.1 (right panel) and STE value of this time series is $\sim 80\%$. (b) The STE values versus $\text{length}(X(t))$ of time series constructed. These values decrease in time series with a length greater than ~ 4500 points. The software should be used from zero to red vertical line.	78
5.3	Scheme to explain as the techniques are used.	83
5.4	Scheme used to identify MCs.	87
5.5	Values of spatio-temporal entropy (STE) as a function of the time for time series of IMF B_x (dotted line), B_y (dashed line) and B_z (continuous thin line) components in the SW. The thick curve represents the interplanetary entropy index (IE) calculated over the analyzed period. The shock, the start and end of the MC are represented by three vertical lines as is shown in Table A.1.	89
5.6	Values of STE as a function of the time for times series of IMF B_x (dotted line), B_y (dashed line) and B_z (continuous thin line) components in the SW. The thick curve represents the IE calculated over the analyzed period. The vertical lines represent the ICME reported by Dal Lago et al. (2006) from 21, 01 : 34 <i>UT</i> to 22, 06 : 15 <i>UT</i>	91
5.7	It is plotted the IE as a function of the time, February 14 – 23, 1999, but the three vertical lines correspond with the third event in Table A.1. The format is the same as in Figure 5.5.	92
5.8	The unipolar MC was observed by ACE on 19-22 March, 2001 and identify by Huttunen et al. (2005).	95
5.9	Persistence exponents as a function of the time for times series of IMF, January 03 – 13, 1998	97
5.10	Persistence exponents as a function of the time for times series of IMF, October 20-26, 1999	98
5.11	Persistence exponents as a function of the time for times series of IMF, February 14 – 24, 1999	100
5.12	Wavelet index or WI versus time for times series of IMF components . . .	101

5.13	(Both panels) Reconstruction results of ACE August 12, 2000, magnetic cloud. Plot of data $P_t(x, 0)$ versus $A(x, 0)$ along the x axis for the analysis interval, and the fitted $P_t(A)$ function. The vertical line denoted by A_b marks the point on A axis where $A = A_b$. (a) Source: Hu et al. (2003). (b) We used a program supplied by Christian Möstl during his PhD thesis to reproduce this result.	103
5.14	(Both panels) Reconstruction results of ACE August 12, 2000, magnetic cloud. The recovered cross-section of the two magnetic clouds. a) Source: Hu et al. (2003). (b) We used a program supplied by Christian Möstl during his PhD thesis to reproduce this result.	105
6.1	The STE values for 41 MCs from 1998 to 2003 that were presented in Table A.1. At the top, the STE values for the three IMF components (“o” $\equiv B_x$, “+” $\equiv B_y$, “x” $\equiv B_z$) versus cases as shown in Table A.1. At bottom, the same as to above but for the sheath regions. In the two panels without previous transformation in the time series.	108
6.2	A histogram of STE derived from Figure 6.1 for B_z corresponding to MCs regions (in black) and plasma sheaths regions (in grey) respectively.	109
6.3	Format is the same as in Figure 6.1, but the trend was removed through the first-order differences at the time series.	110
6.4	A histogram of STE derived from Figure 6.3 for B_z corresponding to MCs regions (in black) and plasma sheaths regions (in grey) respectively.	111
6.5	(top panel) STE values versus length of B_z time series using 41 MCs, where the “o” and “+” symbols corresponds to original and transformed (remove the Gaussian noise and trend through a rotation) time series respectively. To the right of the vertical line, larger clouds are shown, and by the software limitation the STE values are zero. (bottom panel) The histogram helps to identify overlapping points of MCs in the top panel.	112
6.6	In both panels, the format is the same as in Figure 6.5, but STE values 41 plasma sheaths are plotted. (bottom panel) The histogram helps to identify overlapping points of sheaths in the top panel.	113

6.7	We selected MCs sample with less of 5500 points, taking the intervals between the positions 500 until 4500 in IMF B_z . (top panel) The “o” and “x” symbols correspond to non-transform and transformed (reduced to 4001 points) time series respectively. (bottom panel) A histogram of STE derived from top panel corresponding to transformed (in grey) and non-transform (in black) of B_z time series.	114
6.8	The force-free model solution (axial, tangential and radial components and total magnetic field) as solved in Burlaga (1988) were plotted. Following Burlaga (1988), we show the boundaries with two vertical lines at the points where $B_A = 0$, i.e. where $\alpha \cdot R = 2.4$ and $B/B_0 = 0.5$, also $\alpha = 1$	116
6.9	RPs of the solution for a cylindrically symmetric force-free field with constant alpha are shown. (a) Axial component. : $B_A = B_0 J_0(\alpha R)$, $STE = 27\%$. (b) Tangential component : $B_T = B_0 H J_1(\alpha R)$, $STE = 0\%$.	117
6.10	At top: Plot of STE versus θ to B_x , B_y and B_z components and a parabola fitted to the data. At bottom: The corresponding histogram in which a Gaussian distribution is fitted.	119
6.11	The values of persistence exponents $\langle\beta\rangle$, $\langle\alpha\rangle$, $\langle H_u\rangle$ and $\langle H_a\rangle$ versus number of events (see Table A.1) to the sheath, MC and after MC regions were plotted respectively.	121
6.12	Histograms of Figure 6.11.	123
6.13	The filling rectangular regions are the set of validations of the persistence for each regions.	125
6.14	At top, IMF B_z (in GSM system) vs time from the ACE spacecraft with 16s time resolution, at February 11, 23 : 23 UT-February 13, 12 : 00 UT, 2000. At bottom, the square of the first decomposition level of wavelet coefficient $d1^2$ vs time for the sheath region (left of the first vertical dashed line), the MC (middle between the vertical dashed lines), and the quiet solar wind (right of the second vertical dashed line). The lower values of D_{d1} are noticed inside of MC region.	127

6.15	At top, IMF B_z (in GSM system) vs time from the ACE spacecraft with 16s time resolution, at July 11, 11 : 22 <i>UT</i> -July 14, 05 : 00 <i>UT</i> , 2000. At bottom, the square of the first decomposition level of wavelet coefficient $d1^2$ vs time for the sheath region (left of the first vertical dashed line), the MC (middle between the vertical dashed lines), and the quiet solar wind (right of the second vertical dashed line). The high amplitude of $d1^2$ inside the third region (After MC) is because arrived other event. The lower values of D_{d1} is noticed inside of MC region.	128
6.16	The $\langle D_{d1} \rangle$ values versus number of events were plotted, where (“□”), (“⊗”) and (“△”) symbols corresponds to the sheath, MC and after MC regions respectively. The y axis is plot with a logarithmic scale, because is best to visualization.	129
6.17	A histogram is constructed from a frequency table of $\langle D_{d1} \rangle$ values, the abscissa axis was normalized by 0.01. The $\langle D_{d1} \rangle$ values for the sheath, MC and after MC, the three select regions, plotted as the gray, black and white.	130
6.18	(top panel) At top, IMF B_x (in GSM system) vs time from the ACE spacecraft with 16 s time resolution, at date June 23, 12 : 00 <i>UT</i> -June 26, 16 : 00 <i>UT</i> , 1998; at bottom, the square of the first decomposition level of wavelet coefficient $d1^2$ vs time. Also, the other two components must be analyzed, as is shown in the middle and bottom panels.	133
6.19	It is plotted the IE as a function of the time, October 08 – 17, 2000, but the three vertical lines correspond with the event enumerated as 24 at Table A.1. The format is the same as in Figure 5.5.	134
6.20	Persistence exponents as a function of the time for times series of IMF, October 08 – 18, 2000	136
6.21	We shows D_{d1} values as a function of the time for times series of IMF B_x , B_y and B_z components in the solar wind. D_{d1} values for B_x , B_y , and B_z are plotted with red dotted line, green dashed line, and blue continuum line respectively. The thick curve represents the Wavelet index (WI) calculated over the analyzed period.	137

6.22	The bipolar MC was observed by ACE on October 07 – 09, 2000 and identify in this work. The Figure is composed by six panels from (a) to (f): magnetic field strength, polar (B_{lat}) and azimuthal (B_{long}) angles of the magnetic field vector in GSE coordinate system; proton plasma beta; rotation of the magnetic field vector in the plane of maximum variance and rotation of the magnetic field vector in the plane of minimum variance.	138
6.23	It is plotted the IE as a function of the time for April 01 – 11, 2010. The shock and the MC boundaries are shown with three vertical lines, those dates were identified in this work. The format is the same as in Figure 5.5. The thick curve represents the IE calculated over the analyzed period. The MC is identified.	140
6.24	Persistence exponents as a function of the time for times series of IMF, October 01 – 11, 2010	141
6.25	We shows D_{d1} values as a function of the time for times series of IMF B_x , B_y and B_z components in the SW. D_{d1} values for B_x , B_y , and B_z are plotted with red dotted line, green dashed line, and blue continuum line respectively. The thick curve represents the wavelet index (WI) calculated over the analyzed period.	142
6.26	The solar wind windows has been observed by ACE from April 01 to 10, 2010, in GSE coordinates system and with 1 h time resolution.	143
6.27	(to panel) The magnetic field data ($B_x \equiv$ Red, $B_y \equiv$ Green, $B_z \equiv$ Blue) with time resolution of 16 s in GSM coordinates system are shown. (bottom panel) Are shown values of Spatio-Temporal Entropy on 15 – 24 August, 1998 as a function of the time for times series of IMF components (STE in: $B_x \equiv$ red dotted line, $B_y \equiv$ green dashed line and $B_z \equiv$ blue continuous thin line) in the solar wind. The thick curve represents the IE calculated over the analyzed period. The shock of the ICMEs, the start and end of the MC2 are represented by three vertical lines as is shown in Table A.5. We identify the first MC (MC1), the start and end of it are represented by two vertical lines according to the identification that was done.	146
6.28	Are shown values of average wavelet coefficients on 15 – 25 August, 1998 as a function of the time for times series of IMF components (D_{d1} in: $B_x \equiv$ Red, $B_y \equiv$ Green and $B_z \equiv$ Blue) in the solar wind. The thick curve represents the WI calculated overall interval.	147

6.29	Study of the persistence exponents in solar wind windows from August 15 – 25, 1998	148
6.30	The plot, obtained from OMNI data set in CDAWeb (http://cdaweb.gsfc.nasa.gov/istp_public/), are based on 5-min averaged ACE data in August 19-22, 1998 in GSE. The shock of the ICMEs, the start and end of the MC2 are represented by three vertical lines as is shown in Table A.5. We identify the first MC (MC1), the start and end of it are represented by two vertical lines according to the identification that was done.	149
6.31	In the panels are shown the magnetic hodograms for two magnetic clouds: (top panels) the first MC or MC1 was observed from August 19 – 20 10 : 00 – 04 : 00, 1998 while (bottom panels) the second MC or MC2 was observed from August 20 – 21 09 : 00 – 18 : 00, 1998. The magnetic field rotation confined to one plane, the plane of maximum ($B_x^*B_y^*$) and minimum ($B_y^*B_z^*$) variance are used to find the boundaries of the two clouds.	150
6.32	In the panels (a) and (b) are plotted the results to MC1, Aug. 19-20 10:00-04:00, 1998 while in the panels (c) and (d) are plotted the results to MC2, Aug. 20-21 09:00-18:00, 1998.	154
6.33	Time series of ACE MAG and SWEPAM experiments from August 19 – 21, 1998. Plot of data $P_t(x, 0)$ versus $A(x, 0)$ along the x axis for the reconstruction interval and the fitted $P_t(A)$ function (black curve).	156
6.34	The recovered cross-section of the two magnetic clouds.	158
6.35	Current sheets of size of $\theta = 60^\circ$ detected by the single-spacecraft method applied over the time series of \vec{B} (black line), using four typical size (scale) of the current sheets. The position of the currents sheets are marked by red dots. A current sheets is observed in the contact region between the two MCs.	160
6.36	Study of solar wind windows from March 17 – 27, 2001	163
6.37	Study of the persistence exponents in solar wind windows from March 17 – 27, 2001	164
6.38	March, 19-22 2001	165
6.39	Magnetic hodograms for two magnetic clouds: March 19-20 21:00-13:00, 2001 and March 20-21 18:00-23:00, 2001.	168

6.40	In the panels (a) and (b) are plotted the results to MC1, March 19 – 20 21 : 00 – 13 : 00, 2001 while in the panels (c) and (d) are plotted the results to MC2, March 20 – 21 18 : 00 – 23 : 00, 2001.	169
6.41	The recovered cross-section of the two magnetic clouds.	171
6.42	Scheme to explain as the techniques were used. To identify and charac- terize a cloud, methodology is divided in three parts.	173
A.1	The effect of the flux rope type to the geoeffectivity	205
A.2	The Helios 1 and Voyager 1/2 were separated by 18° in solar longitude and by 1.6 AU in solar distance.	207
A.3	Log-log plot showing the radial sizes, s , of MCs observed by Helios 1/2, Voyager 1/2, Pioneer 10 between 0.3 and 4.2 AU versus solar distance, R	208
A.4	Log-log plot showing the average proton density ($\langle N_p \rangle$) inside MCs ob- served by Helios 1/2 between 0.3 and 1 AU during (1974 – 1981) versus solar distance, R	209
C.1	Map of exact analytical solution (or benchmark solution). Field lines are separated by equal flux.	229
C.2	Plot of $(B_{\tilde{x}}, B_{\tilde{y}}, B_{\tilde{z}}$ and $A(\tilde{x}, \tilde{y}))$ versus \tilde{x} at $\tilde{y} = 0$	230
C.3	Map of exact analytical solution, (a) $A(x, y)$; (b) B_x ; (c) B_y ; (d) B_z ; (e) p ; f) P_t ;(g) J_z in xy plane.	231
C.4	Reconstruction of Benchmark case with invariant (z) axis rotates around $\theta = 5.7^\circ$. (a) B_x, B_y, B_z at $y = 0$ as function of x ; (b) A at $y = 0$ as function of x ; (c) p at $y = 0$ as function of x ; (d) P_t as function of A at $y = 0$, the curve fitting is $Pt(A) = 0.398e^{-2A}$	233
C.5	Map of numerical solution, (a) $A(x, y)$; (b) B_x ; (c) B_y ; (d) B_z ; (e) p ; f) P_t ;(g) J_z in xy plane.	234
C.6	Contours of constant error, $(A_{calc} - A_{exact})/\langle A \rangle$, where $\langle A \rangle$ is the aver- age of the magnitude of A over the map. Error contours are separated by 1%. (a) Analytical solution map of $A(x, y)$; (b) numerical solution map of $A(x, y)$; (c) contours of constant error; (d) zoom of contours of constant error, idem to shown in Figure 1 of Hau and Sonnerup (1999).	235
C.7	(a) Map of exact analytical solution, $B_x(x, y)$ in xy plane. The other panels show numerical solution maps of B_x , where are used the following methods: (b) HS method; (c) first method; (d) second method; (e) third method.	237

C.8	In each pair of panels from top to bottom are shown: (a) the exact solution map and (b) contours of constant error, $(A_{calc} - A_{exact})/\langle A \rangle$, using the HS99 method; (c) and (d) the numerical solution map using the first method and contours of constant error; (e) and (f) are similar to (c) and (d) but for second method; (g) and (h) are similar to (c) and (d) but for third method.	239
C.9	Illustration of behavior of $P_t(A)$ for an incorrect z axis orientation.	240
D.1	Time series of AMPTE/IRM measurements during magnetopause crossing, October 19, 1984, in the interval 05 : 17 : 41 – 05 : 22 : 03 UT. The vertical dashed lines number 1 and 2 correspond at the dates 05 : 19 : 35 and 05 : 19 : 48 respectively. (a) B_x, B_y, B_z in nT (GSE); (b) Electron velocity and proton velocity; (c) number proton density, number electron density, electron temperature and proton temperature.	243
D.2	Analysis results for AMPTE/IRM event, October 19, 1984, in the interval 05 : 17 : 41 – 05 : 19 : 35 UT. The eigenvalues and eigenvectors of the magnetic hodogram pair from MVA, in the two top panels, are shown in the first rows of Table D.1. In the two bottom panels, the colors represent the components, i.e., <i>red</i> $\equiv x$, <i>black</i> $\equiv y$, <i>blue</i> $\equiv z$. The crosses are to identify points that were eliminated by Hau and Sonnerup (1999) to calculate the correlation coefficient (cc_{all}) and the slope ($slope_{all}$) of the linear fit. (a) Maximum Variance; (b) Minimum Variance; (c) HT correlation with $cc_{all} = 0.974$ and $slope_{all} = 0.998$; (d) Walén correlation. with $cc_{all} = -0.433$, $slope_{all} = -0.080$	245
D.3	Analysis results for AMPTE/IRM event, October 19, 1984, in the interval 05 : 17 : 41 – 05 : 19 : 48 UT for optimal angle, $\theta = -40^\circ$, of invariant (z) axis. Normalizations in the four panels are as follows. For distance x : $x_0 = 482$ km. For vector potential A : $A_0 = 39100$ Tm. For pressures p and P_t : $p_0 = 5.25 \cdot 10^{-9}$ Pa. For field components: $B_0 = 81.2$ nT. (a) B_X, B_Y, B_Z projection in GS system (xyz) vs x ; (b) A at $y = 0$ as a function of x ; (c) Transverse pressure P_t as a function of x ; (d) Plasma pressure p as a function of x	251
D.4	a) $P_t(x, 0)$ as function of $A(x, 0)$ where $P_t(A) = 0.51 + 0.10e^{-\frac{5}{2}A} - 0.43e^{-A}$. b) $P_t(x, 0)$ as function of $A(x, 0)$ with linear tail where $P_t(A) = 0.29 + 0.08e^{-\frac{5}{2}A} - 0.25e^{-A}$ and $P_t(A) = -0.03A + 0.12$	252

D.5 Analysis results for AMPTE/IRM event, October 19, 1984, in the interval 05 : 17 : 41 – 05 : 19 : 48 UT for optimal angle, $\theta = -40^\circ$, of invariant (z) axis. Format is the same as in Figure D.3, but an interpolation ($\tilde{N} = 128$) of the data is performed by use of a cubic spline to generate spatial increments Δx suitable for the integration. (a) B_X, B_Y, B_Z projection in GS system (xyz) vs x ; (b) A at $y = 0$ as a function of x ; (c) Transverse pressure P_t as a function of x ; (d) Plasma pressure p as a function of x . . 253

LIST OF TABLES

	<u>Pág.</u>
2.1	Summary of seven previous studies that identified MCs before 2003. In column one: 1- Bothmer and Rust (1997), 2- Bothmer and Schwenn (1998), 3- Mulligan et al. (1998), 4- Lynch et al. (2003), 5- Wu et al. (2003), 6- Huttunen et al. (2005), 7- Nieves-Chinchilla et al. (2005). 9
2.2	Distribution of NS and SN MC polarities in function of solar cycle epochs 32
3.1	The ten instruments on board of ACE. In red the instruments used in this thesis. 41
3.2	Summary of instrument characteristics. 43
4.1	Pseudo-period (seconds) regarding the Daubechies orthogonal wavelets. In this work $\Delta t = 16$ s, $j = 1$ and db2 then pseudo-period is 48.0 seconds. The information here could be useful for studying fluctuations with different frequencies. 58
4.2	Summary of techniques that are using in this work. 74
5.1	STE values related to trends for three time series with data file included in VRA 4.7. 76
5.2	STE values related to the first-order differences in time series. 77
5.3	We calculate the persistence in the IMF components by four different method: β exponent of power spectrum, α exponent of DFA, Hurst of R/S analysis and Hausdorff H_a exponent of semivariogram respectively. The interval from January 06, 13 : 19 to January 07, 02 : 59 1998 was classified as sheath. The intervals January 07, 03 : 00 to January 08, 09 : 00 and from January 08, 09 : 01 to January 09, 15 : 00 were classified as MC and solar wind after the MC respectively. Dates are shown in Table A.1, event No. 1. 80
5.4	Comparison results of MVA method with paper of Huttunen et al. (2005). 94
6.1	Mean D_{d1} of wavelet coefficients. 127
6.2	Table in form of correlation matrix between the six studied tools that shown in Figures 6.19, 6.20 and 6.21 respectively. 137
6.3	Magnetic cloud from 07 – 08 October 2000. 139

6.4	Table in form of correlation matrix between the six studied tools that shown in Figures 6.23, 6.24 and 6.25 respectively.	142
6.5	Magnetic cloud from 05 – 06 April 2010.	144
6.6	Summary of results to MVA method (first part, rows 1-12) and Grad Shafranov reconstruction techniques (second part, rows 14-18) for two MCs (August 19-21, 1998)	152
6.7	Summary of the interaction between two magnetic cloud with different flux rope type.	155
6.8	Summary of the five previous studies about clouds that identifies one or two magnetic clouds in the interval from 19 to 21 March.	161
6.9	Summary of results to MVA method (first part, rows 1-12) and Grad Shafranov reconstruction techniques (second part, rows 14-18) for two MCs (March 19-21, 2001)	167
D.1	The eigenvalues of the magnetic variance matrix are $\lambda_1, \lambda_2, \lambda_3$, in order of declining size and the corresponding normalized eigenvectors, $\hat{x}_1 = \hat{B}_L$, $\hat{x}_2 = \hat{B}_M$, $\hat{x}_3 = \hat{B}_N$	246
D.2	Applying the formula D.1 in the two intervals gives the components of the V_{HT} in GSE coordinates.	247
D.3	The results from the GS coordinate system are shown here, using the trial angle, and the optimal angle of -40° chosen by Hau and Sonnerup (1999).	249
E.1	Coefficients of central finite difference formulas on uniform grid.	257
A.1	Solar wind data studied (from Huttunen et al. (2005)).	259
A.2	Graphics of events shown in Table A.1.	259
A.3	MC events measured by WIND (not examined). Letter “Q” denotes whether the event was an MC (l) or cloud candidate (cl).	266
A.4	MC events not preceded by shock waves. Letter “Q” denotes whether the event was an MC (l) or cloud candidate (cl).	267
A.5	Four MCs events identified by Huttunen et al. (2005). In this work, we studied these events. The columns from the left to the right give: year, month, shock time (UT), MC start time (UT), MC end time (UT), inferred flux-rope type, direction of the MC axis (ϕ_C, θ_C).	267

A.6	The date of solar wind intervals studied in this work. The intervals are presented in the order that it appear in the paper. The columns from the left to the right give: year, month, solar wind star time interval, solar wind stop time interval, coordinates system, total of windows of 11.11 hours in the intervals.	268
-----	--	-----

LIST OF ABBREVIATIONS

ACE	–	Advanced Composition Explorer
AU	–	Astronomical Union
CME	–	Coronal Mass Ejection
DFA	–	Detrended Fluctuation Analysis
DPU	–	Data Processing and Control Unit
Dst	–	Disturbance Storm Time Index
DWT	–	Discrete Wavelet Transform
IE	–	Interplanetary Entropy Index
ENT	–	Entropy
FFT	–	Fast Fourier Transform
GEO	–	Geographic Coordinate System
GS	–	Grad Shafranov
GSE	–	Geocentric Solar Ecliptic Coordinate System
GSM	–	Geocentric Solar Magnetospheric Coordinate System
HT	–	DeHoffmann Teller
ICMEs	–	Interplanetary Coronal Mass Ejections
IGRF	–	International Geomagnetic Reference Field
IMF	–	Interplanetary Magnetic Field
IMP-8	–	Interplanetary Monitoring Platform-8
ISE-3	–	International Sun-Earth Explorer-3
L1	–	Lagrange Point Number 1
L2	–	Lagrange Point Number 2
L3	–	Lagrange Point Number 3
L4	–	Lagrange Point Number 4
L5	–	Lagrange Point Number 5
LH	–	Left handed
MAG	–	Magnetic Field Experiment
MC	–	Magnetic cloud
MCs	–	Magnetic clouds
MHD	–	Magnetohydrodynamics
MJD	–	Modified Julian Date
MVA	–	Minimum Variance Analysis
NS	–	Noth to the South
NOAA	–	National Oceanic and Atmospheric Administration
PSD	–	Power-Spectral Density
PVO	–	Pioneer Venus Orbiter Mission
RD	–	Rotational Discontinuity
RH	–	Right-handed

RP	–	Recurrence Plot
RPDE	–	Recurrence Period Density Entropy
RPs	–	Recurrence Plots
RQA	–	Recurrence Quantification Analysis
RTSW	–	Real-Time Solar Wind Data
SN	–	South to the North
STE	–	Spatio Temporal Entropy
SW	–	Solar Wind
SWEPAM	–	Solar Wind Electron, Proton and Alpha Monitor
TDT	–	Terrestrial Dynamical Time
TD	–	Tangential discontinuity
UT	–	Universal Time
UTC	–	Coordinated Universal Time
VRA	–	Visual Recurrence Analysis
WIND	–	Comprehensive Solar Wind Laboratory for Long-Term Solar Wind Measurements
WI	–	Wavelet Index

LIST OF SYMBOLS

β	– plasma beta
β_p	– proton plasma beta
μ_0	– magnetic permeability of the free space
F	– magnetic field strength
p	– plasma pressure or thermal pressure
B_0	– magnetic induction
B	– total magnetic field at solar wind
J	– current density
$\alpha(r)$	– function of position using on the force-free magnetic field model
α	– constant at the force-free magnetic field model
ρ	– mass density
v	– solar wind speed
g	– acceleration due to gravity
t	– time
L	– length scale
V_A	– Alfvén speed
\vec{E}	– electric field vector
σ_0	– electrical conductivity
F_m	– force from the magnetic field
V	– volume that contains \vec{B}
dV	– differential volume element that contains \vec{B}
H	– magnetic helicity
A	– magnetic vector potential
N	– 1 Newton
m	– 1 meter
ρ_0	– order of magnitude at mass density
v_0	– order of magnitude at velocity
L_0	– order of magnitude at length scale
B_0	– order of magnitude at magnetic induction
p_0	– order of magnitude at plasma pressure
B_C	– an estimate of magnetic field at cloud’s axis
(r, ϑ, z)	– cylindrical coordinates
(J_r, J_ϑ, J_z)	– current density components at cylindrical coordinates
(B_r, B_ϑ, B_z)	– IMF components at cylindrical coordinates
(x, y, z)	– Cartesian coordinates system
(μ, ν, φ)	– oblate spheroidal coordinates system
(η, ξ, φ)	– Another set of oblate spheroidal coordinates system

(r_d, ϑ_d, z_d)	– toroidally-distorted cylindrical coordinates system
Φ_t	– twist
L_{FR}	– length of the flux tube
J_0	– zeroth-order Bessel function
J_1	– first-order Bessel function
B_A	– axial magnetic field component at the force-free model solution
B_T	– tangential magnetic field component at the force-free model solution
B_R	– radial magnetic field component at the force-free model solution
ψ_{sp}	– scalar potential
b	– major axis at oblate spheroidal
c	– minor axis at oblate spheroidal
a	– it is defined from b and c $a = \sqrt{b^2 - c^2}$
R_0	– radius from the center to the middle of the ring of the torus
a_0	– radius of the cross section of ring of the torus
B_{r_d}	– magnetic field component, along r_d , at the force-free model solution, in toroidally-distorted cylindrical coordinates system
B_{ϑ_d}	– magnetic field component, along r_{ϑ} , at the force-free model solution, in toroidally-distorted cylindrical coordinates system
B_{z_d}	– magnetic field component, along z_d , at the force-free model solution in toroidally-distorted cylindrical coordinates system
$F(r_d)$	– function of r_d , parameters computing at the force-free model solution in toroidally-distorted cylindrical coordinates system
A_{00}, A_{01}	– free parameters computing the MC model with oblate spheroidal coordinates
A_x	– component-x of the magnetic vector potential
A_y	– component-y of the magnetic vector potential
$A(x, y)$	– projection of the magnetic vector potential onto xy plane
B_x	– component-x of the IMF
B_y	– component-y of the IMF
B_z	– component-z of the IMF
\vec{B}_z	– magnetic field vector parallel to z - axis
\vec{B}_{\perp}	– magnetic field vector onto xy plane
\vec{J}_z	– current density vector parallel to z - axis
\vec{J}_{\perp}	– current density vector onto xy plane
$\tilde{\mathcal{J}}$	– Jacobian matrix
B_x^*	– component of maximum variance
B_y^*	– component of intermediate variance
B_z^*	– component of minimum variance
x^*	– axis of maximum variance
y^*	– axis of intermediate variance
z^*	– axis of minimum variance

θ_p	– magnetic field’s polar angle
ϕ_p	– magnetic field’s azimuthal angle
θ_c	– magnetic field’s polar angle at direction in the ecliptic of the cloud’s axis
ϕ_c	– magnetic field’s azimuthal angle at direction in the ecliptic of the cloud’s axis
θ_{min}	– magnetic field’s polar angle at direction in the ecliptic of the minimum variance’s axis
ϕ_{min}	– magnetic field’s azimuthal angle at direction in the ecliptic of the minimum variance’s axis
E_M	– rotation matrix
E_M^{-1}	– inverse rotation matrix
E_{M1}	– rotation matrix 1
E_{M2}	– rotation matrix 2
ζ	– rotation angle about one axis
(X_{se}, Y_{se}, Z_{se})	– vector in GSE coordinates system
(X_{sm}, Y_{sm}, Z_{sm})	– vector in GSM coordinates system
X	– axis is directed towards the Sun
Y	– axis lies in the ecliptic plane in the direction opposite to the Earth’s velocity around the Sun (east)
$Z = X \times Y$	– this axis is essentially along the ecliptic north pole
ψ_{se-sm}	– it is the angle between the GSE Z axis and projection of the magnetic dipole axis on the GSE YZ plane (i.e. the GSM Z axis) measured positive for rotation towards the GSE Y axis
Q_e	– unit vector at dipole axis direction in the GSE coordinate system
(x_e, y_e, z_e)	– coordinates of Q_e
Q_g	– unit vector at dipole axis direction in the GEO coordinate system
ϕ_g	– geocentric latitude of the dipole North geomagnetic pole
λ_g	– geocentric longitude of the dipole North geomagnetic pole
g_1^0, g_1^1, h_1^1	– coefficients of the International Geomagnetic Reference Field (IGRF)
ε	– obliquity of the ecliptic
λ_\odot	– the Sun’s ecliptic longitude
M	– the Sun’s mean anomaly
\wedge	– mean longitude at Sun’s mean anomaly
ENT	– Shannon information entropy
$p(k)$	– probability
L_{min}	– the minimum length of diagonal lines in RP
H_{norm}	– the normalized entropy at RPDE method
$H(u)$	– the entropy of the spatio-temporal signal $u(t, j)$
D	– the fractal dimension
H_a	– the Hausdorff exponent
β	– slope of the best-fit straight line to PSD function, $\log(S(f))$ vs $\log(f)$

γ_k	–	semivariogram
H_u	–	Hurst exponent
α	–	detrended fluctuation analysis (DFA) exponent
L^2	–	functional space of the integrable square functions
V^j	–	complementary spaces of scale functions
W^j	–	complementary spaces of wavelet functions
Φ_k^j	–	scale function at scale j and position k
Ψ_k^j	–	wavelet function at scale j and position k
h	–	low-pass filter
g	–	high-pass filter
c_k^j	–	scale coefficients at scale j and position k
d_k^j	–	wavelet coefficients at scale j and position k
T_a	–	pseudo-period
F_c	–	center frequency of a wavelet in Hz
$d1$	–	wavelet coefficients at the first decomposition level
σ^2	–	variance
\wedge_L	–	Lagrange function
$\omega(y)$	–	statistic weight
$\langle \alpha \rangle$	–	mean value of α (persistence index)
$\langle \beta \rangle$	–	mean value of β (persistence index)
$\langle H_u \rangle$	–	mean value of H_u (persistence index)
$\langle H_a \rangle$	–	mean value of H_a (persistence index)
D_{d1}	–	mean value of $d1^2$
$\langle D_{d1} \rangle$	–	mean value of D_{d1} (wavelet index-WI)
R_f	–	fitting residues on GS reconstruction

CONTENTS

	<u>Pág.</u>
1 INTRODUCTION	1
2 A REVIEW ON THE THEORETICAL AND OBSERVATIONAL ASPECTS RELATED TO INTERPLANETARY MAGNETIC CLOUDS	7
2.1 Magnetic clouds	7
2.2 Magnetic cloud models	10
2.2.1 Linear force-free field model	10
2.2.2 Grad-Shafranov model	20
2.3 Observations	27
2.3.1 Magnetic polarity and orientation of the flux-rope	27
2.3.2 Solar cycle variation versus flux-rope type	31
3 INSTRUMENTATION AND DATASET	35
3.1 Lagrangian points and ACE spacecraft	35
3.2 Coordinate systems: GSE and GSM	36
3.3 The ACE Magnetic Field Instrument (MAG)	40
3.4 IMF Dataset	42
4 PHYSICAL-MATHEMATICAL TECHNIQUES	47
4.1 The entropy concepts in Recurrence Plot	47
4.2 Persistence analysis in time series	51
4.3 Wavelet Transform	56
4.4 Minimum variance analysis (MVA)	60
4.5 Grad-Shafranov reconstruction of magnetic flux ropes	64
4.6 Detection of current sheets	71
4.7 Reconstruction tool	72
4.8 Summary of techniques	73
5 METHODOLOGY	75
5.1 Characterization	75
5.1.1 Basic tests on STE analysis aiming to MC analysis	75

5.1.2	Calculation of persistence in the regions of an ICME	78
5.1.3	Wavelet coefficients for solar wind analysis	81
5.2	Identification	83
5.2.1	Methodology for analysis using an entropy index	84
5.2.2	Methodological applications	88
5.2.3	Validation of MVA method to identify the boundary of a MC	93
5.2.4	Persistence index to identify the region of a MC	96
5.2.5	DWT index to identify the sheath of a MC and solar wind fluctuations	99
5.3	Example: MC flux-rope reconstruction	102
6	RESULTS AND DISCUSSION	107
6.1	Part I: Results related to MC Identification	107
6.1.1	STE analysis	107
6.2	Part II: Results related to the MC characterization	120
6.2.1	Persistence analysis on the IMF variation	120
6.2.2	Daubechies wavelet analysis on the IMF behavior	126
6.3	Example of methodology applications	134
6.4	Part III: MC event analyses	144
6.4.1	Identification of a magnetic clouds with double rotations observed by the ACE spacecraft	144
6.4.2	A controversial event which has double magnetic field rotation	161
6.5	Summary of the validation of the methodology	172
7	CONCLUSION	175
	REFERENCES	181
	APPENDIX A - GEOEFFECTIVENESS AND EXPANSION OF MAGNETIC CLOUDS	205
	APPENDIX B - TOOL OF PERSISTENCE ANALYSIS AND SOURCE CODE IMPLEMENTED	211
B.1	Rescaled-Range (R/S) Analysis	211
B.2	Autocorrelations and Semivariograms	215
B.3	Power spectrum, implementation	218

APPENDIX C - GRAD SHAFRANOV EQUATION USING KINETIC THEORY. ANALYTICAL SOLUTION.	
221	
C.1 The Vlasov equation	224
C.2 BENCHMARK CASE. RESULTS FOR GRAD-SHAFRANOV EQUATION	228
C.3 Improved numerical resolution	233
C.4 Orientation of Magnetic flux ropes	238
APPENDIX D - REVIEW OF THE GRAD-SHAFRANOV EQUATION USEFUL IN THE RECONSTRUCTION OF TWO-DIMENSIONAL COHERENT STRUCTURES IN THE MAGNETOPAUSE.	
243	
APPENDIX E - FINITE DIFFERENCES SCHEME	255
ANNEX A - LISTS OF MCs STUDIED	259
ANNEX B - HANDBOOK FOR GRAD-SHAFRANOV RECONSTRUCTION OF MAGNETIC FLUX ROPES	
269	
ANNEX C - PUBLISHED ABSTRACT SUMMARY IN CONFERENCES/CONGRESS/SCHOOL/MEETINGS PROCEEDINGS	
281	
ANNEX D - ARTICLES IN SCIENTIFIC JOURNALS	289

1 INTRODUCTION

A subset of Interplanetary Coronal Mass Ejections (ICMEs) has simple flux rope-like magnetic fields, named magnetic clouds (MCs) (BURLAGA et al., 1981; KLEIN; BURLAGA, 1982; GOSLING, 1990). When the MC is moving faster than the surrounding solar wind (SW), the plasma and magnetic field typically accumulate in its front, forming a disturbed region so-called sheath region. The rapid decrease in the total SW pressure with solar distance is the main driver of the magnetic flux-rope radial expansion (DÉMOULIN; DASSO, 2009). However, if a MC is moving slower than the surrounding solar wind (KLEIN; BURLAGA, 1982; ZHANG; BURLAGA, 1988; BURLAGA, 1988), the sheath region is difficult to be detected and the MC could go unnoticed by the spacecraft.

The shock wave produced by the ICMEs is spatially greater than the MC, so a spacecraft can detect the shock wave only sometimes (SCHWENN, 2006). Near 1 AU MCs have enormous radial sizes (0.28 AU) with an average duration of 27 hours, an average peak of the magnetic field strength of 18 nT and an average SW speed of 420 km/s (KLEIN; BURLAGA, 1982). As it has been noted by many authors (e.g. Zwickl et al. (1983), Richardson and Cane (1995)), sometimes individual signatures may not be detected in all ICMEs, because they are not present or even there are data gaps.

The above results was obtained fundamentally in the 1980s, working with observational data from Helios, IMP and Voyager spacecraft respectively. Beginning in 1990s other spacecrafts are launched with better instrumentations and analysis of time series techniques began to be used. Thus, temporal evolution of SW structures and its interaction with the Earth's atmosphere have to be studied, using nonlinear dynamics tools which are applied to time series analysis of several physical parameters (e.g. Vassiliadis et al. (1991), Shan et al. (1991a), Shan et al. (1991b), Balasis et al. (2011)). These mathematical tools are useful for the estimation of some statistical coefficients, which are appropriated for characterize solar activity from the point of view of turbulence, intermittence (e.g. Chian et al. (2006), Chian and Muñoz (2011)) and instabilities in the interplanetary magnetic field (IMF), solar wind density and velocity (e.g. Roberts et al. (1987), Miura (1984), Remya and Unnikrishnan (2010)).

An example of the aforementioned tools is the spatio temporal entropy¹ (STE)

¹name given by Eugene Kononov's Visual Recurrence Analysis (VRA) software, not to be

and time correlation. It was used by Ojeda et al. (2005) to study solar wind events classified as MCs. Those authors studied 20 MCs, 17 plasmoids (events not identified as MC), and 20 time series of equivalent time duration representing quiet SW. We take data of B_z and SW V_x components starting 48 hour before for study each MC. Under MC conditions, a feature was noticed: the IMF B_z has the tendency to present lower STE values than the B_z in other cases, such as in plasmoids and during quiet solar wind. Thus, in this work a more detailed study of the STE in MCs is carried out, allowing propose a physical interpretation and the basis for a MC identification tool.

The test for independence and searching for correlations in a time series can be carried out by use of an analytical tool from nonlinear dynamics, the estimation of the Hurst exponent (HURST et al., 1965). It was first used by Mandelbrot and Wallis (1969) to study a series of monthly sunspot of 200 years. It had a Hurst exponent significantly larger than 0.5. On others papers such as Ruzmaikin et al. (1994), they showed that the solar activity have long-term persistence when explore time series of ^{14}C (Carbone-14). Calzadilla and Lazo (2001), Wei et al. (2004) studied time series of D_{st} geomagnetic index which showed chaotic properties in association with self-affine fractals. The D_{st} index can be viewed as a self-affine fractal dynamic process, as result of SW-magnetosphere interactions. In fact, the behavior of the D_{st} index, with a Hurst exponent $H_u \approx 0.5$ (power-law exponent $\beta \approx 2$) at high frequency, is similar to that of Brownian motion. Therefore, perhaps the dynamical invariants of some physical parameters of the solar wind, specifically the MCs, may have spectral characteristics similar to Brownian motion.

Price and Newman (2001) analyzed the behavior of solar wind dataset (IMF and solar wind speed) with 1 *min* resolution from September 1978 to July 1979 using the ISEE-3 spacecraft. They showed the time series, the power spectrum and the R/S analysis for the IMF B_z component for the month of March 1979. The B_z time series was self-similar for all time scales, highly coherent for time scales less than one day, and only slightly coherent for time scales greater than one day. Also, they found self-similarity and coherence properties when calculated β -power spectrum values to vBz , AE index and the horizontal (H) component of the Earth's magnetic field. So, in this paper, a detailed study of persistence in magnetic clouds was done.

The wavelet transform is other modern tool with many application in time series

confused with spatio-temporal entropy image (STEI) (MA; ZHANG, 2001)

analysis. The wavelet coefficients have been shown to be an useful tool for study non-stationary time series corresponding to the horizontal component of the magnetic field of ground stations (e.g. Mendes et al. (2005), Domingues et al. (2005)). The wavelet analysis has the following propriety: the larger amplitudes of the wavelet coefficients are associated with locally abrupt signal changes or “details” of higher frequency (SIMOES, 2011). In the work of Mendes et al. (2005) and the following work of Mendes da Costa et al. (2011), a method for the detection of the transition region and the exactly location of this discontinuities due to geomagnetic storms was implemented. In these cases, the highest amplitudes of the wavelet coefficients indicate the singularities on the geomagnetic signal in association with the disturbed periods. Nevertheless, when the magnetosphere is under quiet conditions for the geomagnetic signal, the wavelet coefficients show very small amplitudes. In this work, we applied this methodology with Daubechies orthogonal wavelet function of order 2 to study magnetic field fluctuations inside of MCs.

With data measured from a spacecraft, it is possible to study the topology magnetic field lines of a magnetic cloud and its axis orientation in the interplanetary medium. In specific conditions as magnetic field vector rotates in almost parallel planes, then we could use the minimum variance analysis (MVA) method (BOTHMER; SCHWENN, 1998) to determine the direction of the axis in the MC, as well as boundaries of it. Later, it was proven by Burlaga (1988) that the minimum variance analysis depended on the minimum distance between the trajectory of spacecraft and the cloud axis, especially, for large distances. Local MVA analysis have been widely used and still continue to be used (LUI et al., 2008; LUCAS, 2009; LUCAS et al., 2011), to identify the direction of the rotation inside of MCs, as well as to identify magnetic cloud boundary layer (SONNERUP; SCHEIBLE, 1998). Thus, the MVA method has been used in this work to identify the boundary of some MCs.

An isolated spacecraft measurement is only a dataset of records obtained in a line that cross a 3D magnetic structure of plasmas such as magnetic flux-ropes and MCs in the solar wind. Sonnerup and Guo (1996), Hau and Sonnerup (1999) developed a method for recovering two-dimensional structures in the magnetopause, from the Grad-Shafranov (GS) equation, in an ideal MHD formulation to examine magnetic flux-ropes near the magnetopause. The method is called Grad-Shafranov or GS reconstruction. Later, it was developed to study magnetic flux ropes in the solar wind, and in the magnetotail from a simple spacecraft (HU; SONNERUP, 2001; HU;

SONNERUP, 2003; TEH; HAU, 2004; TEH; HAU, 2007; DU et al., 2007; LUI et al., 2008) and it was extended to treat measurements from multiple satellites (SONNERUP et al., 2004; HASEGAWA et al., 2005; HASEGAWA et al., 2006; HASEGAWA et al., 2007; TEH, 2007; MÖSTL, 2009; LUI, 2011).

Hu and Sonnerup (2001), Hu and Sonnerup (2002) were the first in applied this method to magnetic flux ropes and MCs in the interplanetary medium. However here in this work, their two-dimensional (2-D) cross sections are recovered in a rectangular domain. We use the aforementioned method to study magnetic reconnection between multiple flux-ropes events at 1 AU. Magnetic reconnection is an important physical mechanism at least interacting with the trigger and acceleration of the erupting coronal magnetic structures in a good number of CME events (QIU et al., 2007). The relation between current sheets, intermittent turbulence and magnetic reconnection in the leading edge of an ICME was investigated by Chian and Muñoz (2011), Muñoz (2011). A significant change in magnetic field rotation from one side to the other of the structure is a characteristic feature of current sheets studied. They improve a method used by Li (2008) to search current sheets using single-spacecraft magnetic field data. This method to search for current sheets is used in this work.

The motivation of this thesis is to contribute for better understanding of the physics of magnetic clouds and create a methodology to identify and characterize this events in the SW. The importance is to provide in the future as application, diagnostics useful for Space Weather. As a futher result, we expect to provided an application which useful product to Space Weather Programme, mainly the INPE's program.

The general objective is to construct a methodology which will improve models to identify and characterize MCs.

The specific objectives are:

- 1) The dynamic of the MCs will be characterized from the spacecraft signal.
- 2) Analysis tools which will identify automatically cloud candidates from interplanetary magnetic field data.
- 3) MCs with double-rotation magnetic field configuration will be studied.

The main contributions of this work are:

- 1) Studies of a spatial structure that is one of the most geoeffective interplanetary events.
- 2) The establishment of a methodology to identify MC candidates using only the magnetic field dataset. By first time, with nonlinear dynamics tools will be possible identify flux-ropes associated with MCs.
- 3) The identification of complex multiple flux-rope associated with MCs and the transversal reconstruction of the structure to study magnetic reconnection between it.
- 4) The detection of current sheets between two MCs in reconnection.
- 5) Proposition of an interplanetary entropy (IE) index that allows a preliminary localization of events appointed as MC candidate.
- 6) Contributions with methodological bases for an easy and automatic computational procedure for preliminary survey on MC occurrences for scientific goals, or even a convenient MC warning for the space weather purposes.
- 7) New MC events are studied, and new informations are offered to the Space Physics Community.

This thesis is organized as follows: in Chapter 2, we presented a review on the theoretical and observational aspects of the MCs, which are still under discussion; Chapter 3, the instrumentation and dataset used in this work are presented; In Chapter 4, we introduce basic concepts of the physical and mathematical tools used in this work. In Chapter 5, we explain how to use the previous tools to identify and characterize flux-rope associated with MCs. In Chapter 6, the results and discussion of the thesis are presented; In Chapter 7 the conclusions are presented. Finally, for a better understanding of the work, a number of appendices and annexes are incorporated. Our philosophy for the realization of this thesis was to explain in detail all the physical-mathematical formalism up to the final results. So this thesis could be a useful study material for future works.

2 A REVIEW ON THE THEORETICAL AND OBSERVATIONAL ASPECTS RELATED TO INTERPLANETARY MAGNETIC CLOUDS

In this chapter, we present a review on the theoretical and observational aspects of the interplanetary magnetic clouds (MCs). It is an area under intensive discussion. We will talk about the most important models in the literature to study the magnetic clouds. Also we will present a review about the works that studied MCs through spacecraft observations.

2.1 Magnetic clouds

Coronal Mass Ejection (CMEs) are massive expulsions of magnetized plasma from the solar atmosphere (DASSO et al., 2005). As a consequence of this ejection, CMEs can form confined magnetic structures with both extremes of the magnetic field lines connected to the solar surface, extending far away from the Sun into the solar wind. Solar Ejecta (also known as Interplanetary Coronal Mass Ejections, ICMEs) are the interplanetary manifestation of CMEs events (DASSO et al., 2005). The important subset of ICMEs known as interplanetary magnetic clouds (MCs), a term introduced by Burlaga et al. (1981), is characterized fundamentally by enhanced magnetic field strengths with respect to ambient values (BURLAGA et al., 1981; KLEIN; BURLAGA, 1982; BURLAGA, 1991). A MC ejected from the Sun is simulated as a part of a toroid. Its evolution and propagation through interplanetary space can be studied using three-dimensional magnetohydrodynamic self-consistent numerical simulations (VANDAS et al., 2002).

The pioneer studies on plasma clouds emitted by the Sun were developed about 1950s (MORRISON, 1954; COCCONI et al., 1958; PIDDINGTON, 1958). However the definition and the term of “magnetic cloud” were presented by the first time in the work of Burlaga et al. (1981). Nowadays the specific signatures which have to be necessarily fulfilled are the following: (1) Smooth rotation in \vec{B} with low variance; (2) low proton temperature and (3) low plasma β , which is the ratio of the plasma pressure, $p = nk_B T$, to the magnetic pressure, $p_{mag} = B^2/2\mu_0$ where n is number density, K_B Boltzmann constant, T temperature, B magnetic field and μ_0 magnetic permeability of the free space.

Initial studies to analyze the three-dimensional configuration of the magnetic field of these phenomena has been developed by Burlaga et al. (1981). The minimum vari-

ance analysis (MVA) was used as a method to identify and describe planar magnetic field configuration associated with thin current sheets in the SW (BURLAGA; KLEIN, 1980) and planetary magnetospheres (LEPPING; BEHANNON, 1980). Burlaga et al. (1981) used MVA to analyze the magnetic field configuration in a MC observed with 4 spacecraft: Voyager 1 and 2, IMP 8, and Helios 2. They concluded that MC could be represented as a magnetic cylinder whose axis lies close in the equatorial plane, marking an angle of nearly 90° with respect to the radial direction.

Considering a cylindrical geometry for MCs, the MVA (SONNERUP; CAHILL, 1967) resulted an useful tool to calculate the direction of the cloud axis. Klein and Burlaga (1982) identified 45 events in the period from 1967 to 1978, where the latitude and longitude of the clouds axis were calculated. The results of Burlaga et al. (1981) also were consistent with other configurations. Ivanov and Harshiladze (1984) created a mathematical formulation using a cloud configuration as an oblate ellipsoidal.

Goldstein (1983) considered a force-free configuration in the search for a stable topology of the MCs. Marubashi (1986) studied IMF data from the Pioneer Venus orbiter (PVO) between December 1978 to May 1984 in search of interplanetary magnetic flux ropes near the Venus orbit. As a result, twenty-six well defined flux ropes were found which have characteristics similar to those of flux ropes observed near Earth. In one case, where the Sun, Venus and Earth were closely aligned, an almost identical structure was observed by the PVO and the Earth-orbiting spacecraft with a time delay of about 36 hours. This observation provides evidence that the structure of interplanetary magnetic flux ropes are maintained during propagation at least from 0.72 AU (Astronomical Unit (AU): the average distance from the Earth to the Sun. One AU = 93 million miles or 149.6 million km) to 1 AU. A simple solution for a cylindrically symmetric force-free field with constant alpha was studied by Lundquist (1950), and mentioned also in Lundquist (1951). Burlaga (1988) studied the aforementioned solution with constant alpha to describe the types of signatures observed in the SW at 1 AU.

To find plasma beta values significantly lower than 1 during the identification of a MC, magnetic field and plasma observations at spacecraft are required. Many times the temperature and density data on spacecraft have many gaps during periods in which the plasma instruments could be saturated as a result of intense particle fluxes (for example, Bastille Day in the ACE spacecraft). If this condition occurs, it makes impossible to calculate the plasma beta, but it is still possible to detect

Table 2.1 - Summary of seven previous studies that identified MCs before 2003. In column one: 1- Bothmer and Rust (1997), 2- Bothmer and Schwenn (1998), 3- Mulligan et al. (1998), 4- Lynch et al. (2003), 5- Wu et al. (2003), 6- Huttunen et al. (2005), 7- Nieves-Chinchilla et al. (2005).

Paper	Period	T_t (years)	Spacf	MC
1	1965-1993	28	OMNI	67
2	12/1974-07/1981	6.7	Helios 1/2	45
3	1979-1988	10	Pioneer	61
4	02/1998-07/2001	3.5	ACE	56
5	1995-2002	8	WIND	71
6	1997-2003	7	WIND/ACE	73 (and 7 cloud candidate)
7	2000-2003	4	WIND/ACE	35

SOURCE: Adapted from Huttunen et al. (2005) and updated by us.

the MC using magnetometers data (e.g. Huttunen et al. (2005), Nieves-Chinchilla et al. (2005)). Here is the contribution we intend to do with this work, showing an approach that could help to identify MCs, and it is proposed as basis for an auxiliary analysis tool.

The main contributions related to the identification of MCs are summarized in Table 2.1. It was adapted from Huttunen et al. (2005) and updated by us. We show in each column of this table, the paper, the period of the investigation, the examination period (T_t), the spacecrafts used (Spacf), and the quantities number of MCs identified. Bothmer and Rust (1997), Bothmer and Schwenn (1998), Huttunen et al. (2005) identified MCs based on the MVA method; Mulligan et al. (1998) identified and classified MCs using the visual inspection of the data; Lynch et al. (2003) and Wu et al. (2003, /WIND list) used the least-square fitting routine by Lepping et al. (1990); while Nieves-Chinchilla et al. (2005) studied all the MCs observed during the time interval 2000–2003 using the elliptical cross-section model (HIDALGO, 2003; HIDALGO, 2005), where a distortion and expansion of the cross-section of the cloud is included from first principles.

From 1997 – 2003 in solar cycle 23, SW data were investigated by Huttunen et al. (2005) using the MVA method (SONNERUP; CAHILL, 1967; BOTHMER; SCHWENN, 1998) to determine if they have flux-rope structures. They identified 73 MCs (and 7 MC candidates) observed by the ACE and WIND spacecraft. In principle the axis of a MC can have any orientation with respect to the ecliptic plane (BOTHMER;

(SCHWENN, 1994; BOTHMER; SCHWENN, 1998), identified by the azimuthal direction in the ecliptic, called ϕ_C , and the inclination relative to the ecliptic, called θ_C . With the MVA, the angles above can be calculated (BOTHMER; SCHWENN, 1998).

2.2 Magnetic cloud models

As was summarized by Dasso et al. (2005), an interplanetary flux tubes or flux ropes (in particular MCs) can be modeled locally using helical cylindrical geometry as first approximation (FARRUGIA et al., 1995) or using different approaches:

- 1) a linear force-free field (e.g. Burlaga et al. (1981), Burlaga (1988), Lepping et al. (1990)),
- 2) a force-free uniformly twisted field (e.g. Farrugia et al. (1999)) and
- 3) some non-force-free models. In particular *four* non-force-free models have been applied to interplanetary flux tubes: (i) a *non-axially symmetric* model (HU; SONNERUP, 2001), and three *axially symmetric* models: (ii) with a radial exponential dependency for the azimuthal and poloidal components of the magnetic field (MULLIGAN; RUSSEL, 2001), (iii) with a constant current density (HIDALGO et al., 2002), and (iv) with an azimuthal current density depending linearly on the distance to the axis of the tube (CID et al., 2002).

All those models are physically different and it is not yet clear which of them gives the best representation of interplanetary flux tubes (DASSO et al., 2005). Also for a rapid review of some of above models see Dasso et al. (2005).

In this section, we review the concepts of linear force-free field model and the non-axially symmetric model, it are used for the development of this thesis.

2.2.1 Linear force-free field model

Before beginning the study of MCs, it is important demonstrate the linear force-free condition (LUNDQUIST, 1950; GOLDSTEIN, 1983; IVANOV; HARSHILADZE, 1984; BURLAGA, 1988). Because it is the most typical and simple model that is used to study magnetic cloud and it will be used to explain some results of this work. We consider a region of space where the external magnetic field \vec{B} is in a fixed direction perpendicular to the plane, where a plasma volume exist in the form of

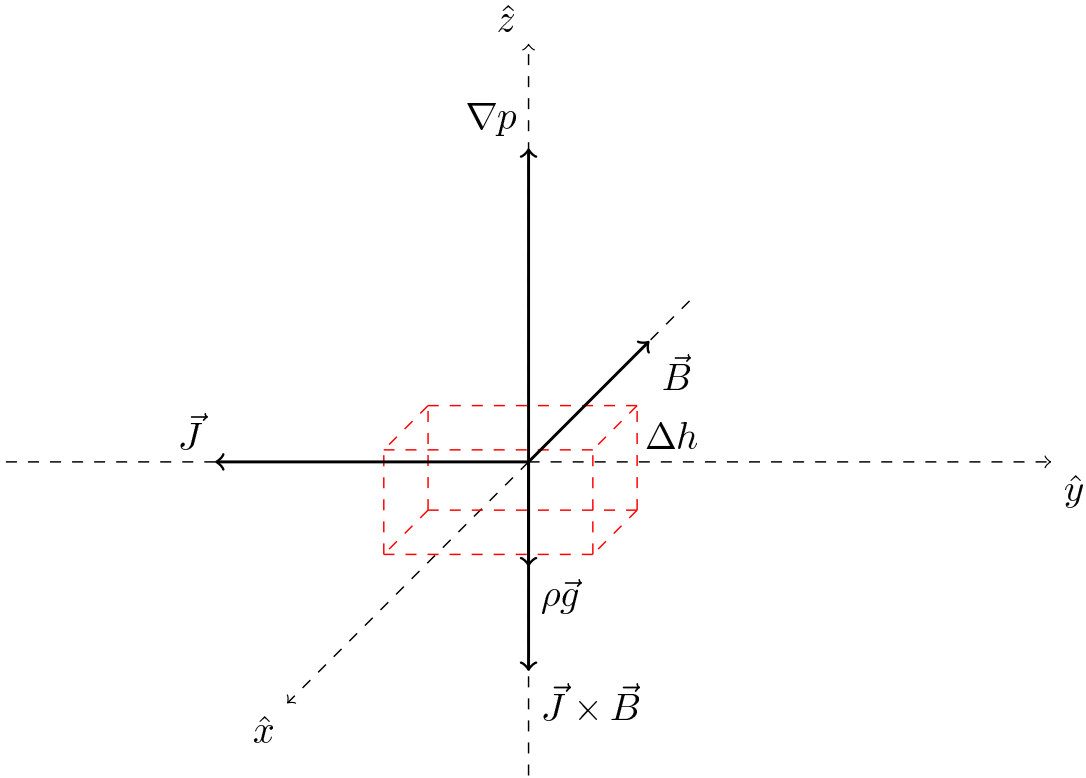


Figure 2.1 - This volume is at equilibrium in a MHD flow of an electrically conducting fluid under a gravitational field, a magnetic field and a pressure gradient.

fluid influenced by a hydrostatic pressure gradient. The particles are moving inside of plasma and form an electric current \vec{J} , on the plane perpendicular to magnetic field. A plasma in the interplanetary medium is influenced by the gravities of the other celestial bodies then we need to add a gravity force over plasma. All the above mentioned are summarized in Figure 2.1. The resultant of force per unit area [N/m^2] is:

$$\rho \frac{d\vec{v}}{dt} = -\nabla p + \vec{J} \times \vec{B} + \rho \vec{g}. \quad (2.1)$$

Plasma has typical parameters:

- a) Velocity v_0 (m/s).
- b) Density ρ_0 (kg/m^3).
- c) Pressure p_0 (N/m).
- d) Magnetic induction B_0 (nT).

e) Length scale L_0 (m).

To make considerations in MHD theory is common to write the equations in terms of orders of magnitudes and Equation 2.1 is:

$$\begin{aligned} \left[\frac{\rho_0 v_0^2}{L_0} \right] &= \left[\frac{p_0}{L_0} \right] + \left[\frac{B_0^2}{\mu_0 L_0} \right] + [\rho_0 g] \\ \left[\frac{N}{m^2} \right] &= \left[\frac{N}{m^2} \right] + \left[\frac{N}{m^2} \right] + \left[\frac{N}{m^2} \right] \end{aligned}$$

a) The second and third term of Equation 2.1 are directly compared. We can consider that inside of interplanetary magnetic cloud the gravitational term is smaller than the magnetic term, $\rho_0 g \ll B_0^2/(\mu_0 L_0)$. Then, the gravitational term can be neglected.

$$\rho \frac{d\vec{v}}{dt} = -\nabla p + \vec{J} \times \vec{B} \quad (2.2)$$

b) The two right-hand terms in the above equation are of same orders of magnitudes and we can compare the magnetic term with the left-hand term of the equation:

$$\left[\frac{\rho_0 v_0^2}{L_0} \right] \equiv \left[\frac{B_0^2}{\mu_0 L_0} \right] \quad (2.3)$$

c) In a stationary plasma the particle velocities are smaller than Alfvén velocity (v_A):

$$v_0^2 \ll \frac{B_0^2}{\mu_0 \rho_0} \equiv v_A^2, \quad (2.4)$$

dividing by L_0/ρ_0 :

$$\frac{\rho_0 v_0^2}{L_0} \ll \frac{B_0^2}{\mu_0 L_0} \equiv v_A^2.$$

Then, we obtain the magnetostatic equilibrium:

$$\nabla p = \vec{J} \times \vec{B}. \quad (2.5)$$

The term force-free means that the Lorentz force ($\vec{J} \times \vec{B}$) is zero. Also, the term is used when one refers to the magnetohydrostatic equilibrium, when external forces are neglected in the cloud (IVANOV; HARSHILADZE, 1984). If the gravitational force is neglected, for balance must be taken that the magnetic force is equal to the plasma

pressure gradient (see Equation 2.5). Comparing the size of the gas pressure, p , to the magnetic pressure, $B^2/(2\mu_0)$, it is introduced a parameter, called the plasma beta, $\beta = p/(B^2/(2\mu_0))$. If $\beta \gg 1$, then the magnetic field is dominated by the gas pressure and the Lorentz force is neglected. On the other hand, if $\beta \ll 1$, then the magnetic field dominates and p may be neglected. The plasma beta is low inside of a MC.

We write some of Maxwell's equations to start the study of force-free system:

$$\left\{ \begin{array}{ll} \nabla \times \vec{E} = -\frac{\partial \vec{B}}{\partial t} & \text{Faraday's law} \\ \nabla \times \vec{B} = \mu_0 \vec{J} & \text{Ampere's law} \\ \vec{J} = \sigma_0(\vec{E} + \vec{v} \times \vec{B}) & \text{Ohm's law} \end{array} \right. \quad (2.6)$$

The magnetohydrostatic equilibrium equation is reduced to $(\nabla \times \vec{B}) \times \vec{B} = \mu_0(\vec{J} \times \vec{B}) = 0$, and the magnetic field is said to be *force-free*. The solution is that the current is parallel to the magnetic field.

$$\nabla \times \vec{B} = \alpha \vec{B}, \quad (2.7)$$

$$\nabla \times (\nabla \times \vec{B}) = \alpha(\nabla \times \vec{B}) = \alpha^2 \vec{B}$$

or

$$\nabla^2 \vec{B} = -\alpha^2 \vec{B}$$

Since $\nabla \cdot \vec{B} = 0$ and α may be a scalar function of position, $(\nabla \times \vec{B}) \times \vec{B} = \alpha(\vec{B} \times \vec{B}) = 0$. There is an infinite number of configurations for different choices of α .

Besides, one can write the vector identities:

$$\begin{aligned} \nabla \times (\nabla \times \vec{D}) &= \nabla(\nabla \cdot \vec{D}) - (\nabla \cdot \nabla)\vec{D} \\ \nabla \cdot (\phi \vec{D}) &= \phi \nabla \cdot \vec{D} + (\vec{D} \cdot \nabla)\phi, \quad (\phi \text{ is a scalar function}) \\ \nabla \cdot (\nabla \times \vec{D}) &= 0 \end{aligned}$$

If $\vec{D} \equiv \vec{B}$, $\phi \equiv \alpha$ and $\nabla \cdot \vec{B} = 0$ (there are no magnetic monopole) then using the

previous identities we arrive to the expression

$$\begin{aligned}\nabla \cdot (\alpha \vec{B}) &= \alpha \nabla \cdot \vec{B} + (\vec{B} \cdot \nabla) \alpha \\ &= (\vec{B} \cdot \nabla) \alpha,\end{aligned}$$

from Equation 2.7:

$$\begin{aligned}\nabla \cdot (\alpha \vec{B}) &= \nabla \cdot (\nabla \times \vec{B}) = 0 \\ \therefore (\vec{B} \cdot \nabla) \alpha &= 0.\end{aligned}$$

Assuming that the magnetic field (force-free) falls due to finite conductivity of the fluid. We applied the curl operator onto Ohm's law that is shown in the Equation 2.6,

$$\begin{aligned}\nabla \times \vec{J} &= \sigma_0 \nabla \times \vec{E} + \sigma_0 \nabla \times (\vec{v} \times \vec{B}), \\ \nabla \times \vec{E} &= \frac{1}{\sigma_0} \nabla \times \vec{J} - \nabla \times (\vec{v} \times \vec{B}).\end{aligned}$$

If the magnetic field is force-free, $F_m = q(\vec{v} \times \vec{B}) = 0$, then the particles travel along magnetic field lines ($\vec{v} \parallel \vec{B}$). We join the Faraday and Ampere laws with the previous equation:

$$\frac{\partial \vec{B}}{\partial t} = -\frac{1}{\sigma_0} (\nabla \times \vec{J}) = -\frac{1}{\mu_0 \sigma_0} (\nabla \times (\nabla \times \vec{B})), \quad (2.8)$$

and from Equation 2.7

$$\frac{\partial \vec{B}}{\partial t} = -\frac{1}{\mu_0 \sigma_0} (\nabla \times (\alpha \vec{B})). \quad (2.9)$$

Using the mathematical identity: $\nabla \times (\alpha \vec{B}) = \alpha (\nabla \times \vec{B}) + (\nabla \alpha) \times \vec{B}$, the final expression is

$$\frac{\partial \vec{B}}{\partial t} = -\frac{1}{\mu_0 \sigma_0} [\alpha^2 \vec{B} + (\nabla \alpha) \times \vec{B}]. \quad (2.10)$$

The second term in the right-hand side of the above equation may twist the shape of the fluid, because, $\nabla \alpha \times \vec{B}$, will produce a force on the field line \vec{B} , causing twist. The topological magnitude to measuring the twist of magnetic field lines is the magnetic helicity H (DASSO et al., 2005):

$$H = \int_V \vec{A} \cdot \vec{B} dV \text{ with } \vec{B} = \nabla \times \vec{A}. \quad (2.11)$$

In this formalism the magnetic field helicity is invariant.

If we consider a force-free field and α as a constant. The Equation (2.10) becomes:

$$\frac{\partial \vec{B}}{\partial t} = - \left(\frac{\alpha^2}{\mu_0 \sigma_0} \right) \vec{B} \quad (2.12)$$

and the solution is:

$$\vec{B} = \vec{B}_C e^{-\frac{\alpha^2}{\mu_0 \sigma_0} t}. \quad (2.13)$$

Goldstein (1983) proposed a magnetic force-free configuration with cylindrical symmetry to study the MCs, but not shown a particular solution of Equation 2.7 to describe the observations.

Writing \vec{J} and \vec{B} in cylindrical coordinates ($\vec{J} = (J_r, J_\vartheta, J_z)$ and $\vec{B} = (B_r, B_\vartheta, B_z)$):

$$\vec{J} \times \vec{B} = (J_\vartheta B_z - J_z B_\vartheta) \hat{r} + (J_z B_r - J_r B_z) \hat{\vartheta} + (J_r B_\vartheta - J_\vartheta B_r) \hat{z}$$

and

$$\nabla p = \frac{\partial p}{\partial r} \hat{r} + \frac{1}{r} \frac{\partial p}{\partial \vartheta} \hat{\vartheta} + \frac{\partial p}{\partial z} \hat{z}.$$

Consider a cylindrically symmetric flux tube with magnetic field components $B_r(r) = 0$ and gas pressure, $p = p(r)$, then $\frac{\partial p}{\partial z} = \frac{\partial p}{\partial \vartheta} = 0$:

$$\frac{dp(r)}{dr} = J_\vartheta(r) B_z(r) - J_z(r) B_\vartheta(r) \quad (2.14)$$

Using equation from Ampere's law and calculating $\nabla \times \vec{B}$ in cylindrical coordinates, one can show that:

$$\vec{J} = \left(0, -\frac{1}{\mu_0} \frac{\partial B_z}{\partial r}, \frac{1}{\mu_0 r} \frac{\partial(r B_\vartheta)}{\partial r} \right), \quad (2.15)$$

Then, the Equation 2.7, for a cylindrical symmetry with infinite length and $\alpha = \alpha(r)$ is transformed in a differential system:

$$\alpha(r) B_\vartheta = -\frac{\partial B_z}{\partial r} \quad (2.16)$$

$$\alpha(r) B_z = \frac{1}{r} \frac{\partial(r B_\vartheta)}{\partial r}. \quad (2.17)$$

Alternatively, B_ϑ and B_z may be prescribed. If the field is force-free only one of B_ϑ

and B_z can be chosen:

$$B_\vartheta = \frac{r}{1+r^2}, B_z = \frac{1}{1+r^2} \quad (2.18)$$

and the two differential equations are transformed in a linear system dependent of $\alpha = \alpha(r)$.

$$\alpha \frac{r}{1+r^2} = \frac{2r}{(1+r^2)^2}$$

this implies $\alpha(r) = 2/(1+r^2)$.

Equation 2.18 gives a field with uniform twist, where the twist is defined as:

$$\Phi_t = \frac{L_{FR} B_\vartheta}{r B_z}, \text{ where } L_{FR} \text{ is the length of the flux tube} \quad (2.19)$$

Considering $\alpha = \text{constant}$, the above two differential Equations 2.16 and 2.17 can be written as

$$B_\vartheta(r) = -\frac{1}{\alpha} \frac{dB_z(r)}{dr} \quad (2.20)$$

$$\frac{1}{r} \frac{d}{dr} \left(r \frac{dB_z(r)}{dr} \right) + \alpha^2 B_z(r) = 0. \quad (2.21)$$

Solving 2.20 and 2.21 gives (LUNDQUIST, 1950)

$$B_\vartheta(r) = J_1(\alpha r) \text{ and } B_z(r) = J_0(\alpha r), \quad (2.22)$$

where J_0 and J_1 are the Bessel function of the first kind of order 0 and 1 (see field lines configuration in Figure 2.2)

Lepping et al. (1990) developed a scheme for fitting the interplanetary magnetic field data obtained within an observed cloud to a model that has proven to be successful for describing cloud field structure, at least to first order. The model, based on Lundquist (1950) constant- α force-free field solution, was introduced by Burlaga (1988) and employed by him in fitting many cases with trial and error solution with generally good results.

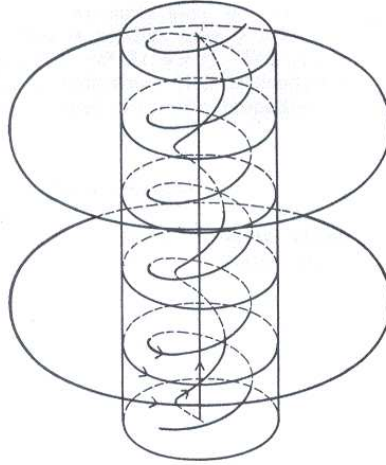


Figure 2.2 - Force-free field in an infinite cylinder. SOURCE: Lundquist (1950).

We rewritten the Equation 2.22 as Lepping et al. (1990):

$$\begin{aligned}
 \text{Axial component : } B_A &= B_C J_0(\alpha r), \\
 \text{Tangential component : } B_T &= B_C H J_1(\alpha r), \\
 \text{Radial component : } B_R &= 0,
 \end{aligned}
 \tag{2.23}$$

where $H = \pm 1$, the sign providing the handedness of the field helicity, and where B_C is an estimate of field at the axis of the cloud and r is the radial distance from the axis.

Figure 2.3a shows the field lines within a computer-simulated MC. The field is a straight line along the axis of the cloud and changes to helical lines as we move away from the axis, finally becoming circle at the boundary. We first see a heavy solid straight line on the axis, then dashed spiral curves of moderated density and moderate pitch angle, and low-density dotted curves of large pitch near the boundary. Also, the spacecraft trajectory is shown in the figure, if it is denoted by the unit vector S then Lepping et al. (1990) call's the Z axis, and the cross product $Z \times S$ is the Y axis. Finally, as usual $Y \times Z = X$. It is assumed that clouds are large loops (flux ropes) with their roots connected to the Sun. It is obvious that cylindrical geometry when applied for such bodies cannot describe effects of curvature on magnetic field profiles. For this purpose considering MCs as parts of toroids is more appropriate (ROMASHETS; VANDAS, 2003).

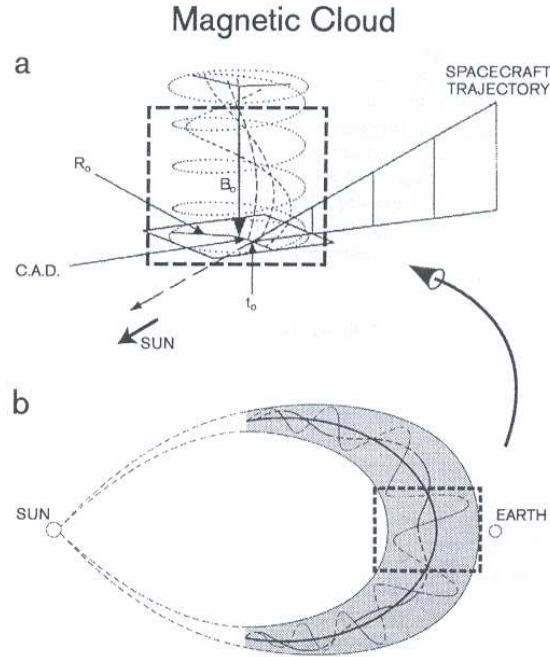


Figure 2.3 - The sketch is reproduced from Burlaga (1991) to represent magnetic field lines inside of a magnetic cloud. (a) Idealized cylindrically symmetric force free flux rope, representing the magnetic cloud as observed by a spacecraft traveling through it. (b) Shows a sketch of the cloud's envisioned global geometry (1 AU scale in this case). SOURCE: Lepping et al. (1997).

There have been attempts to treat interplanetary magnetic flux-ropes by toroidal force-free structures: Ivanov et al. (1989), Romashets and Vandas (2003) used the constant-alpha field distribution within a toroid found by Miller and Turner (1981). Ivanov et al. (1989) proposed two solution with different geometry respectively:

- a) The most common definition of oblate spheroidal coordinates (μ, ν, φ) is

$$x = a \cosh \mu \cos \nu \cos \varphi$$

$$y = a \cosh \mu \cos \nu \sin \varphi$$

$$z = a \sinh \mu \sin \nu$$

where μ is a nonnegative real number and the angle ν lies between $\pm 90^\circ$. The azimuthal angle φ can fall anywhere on a full circle, between $\pm 180^\circ$ for which $a = \sqrt{b^2 - c^2}$ is defined from b (major axis, along x) and c (minor axis, along z) (IVANOV; HARSHILADZE, 1984; LIPKIE, 2001). Another set

of oblate spheroidal coordinates (η, ξ, φ) are sometimes used where $\eta = \sinh \mu$ and $\xi = \sin \nu$ (LIPKIE, 2001). The curves of constant η are oblate spheroids and the curves of constant ξ are the hyperboloids of revolution. The coordinate η is restricted by $0 \leq \eta < \infty$ and ξ is restricted by $-1 \leq \xi < 1$. The relationship to Cartesian coordinates is

$$\begin{aligned} x &= a\sqrt{(1+\eta^2)(1-\xi^2)} \cos \varphi \\ y &= a\sqrt{(1+\eta^2)(1-\xi^2)} \sin \varphi \\ z &= a\eta\xi. \end{aligned}$$

The solution of the Equation 2.7 is (IVANOV; HARSHILADZE, 1984; IVANOV et al., 1989):

$$\vec{B} = \hat{z} \times \nabla \psi_{sp} + [\nabla \times (\hat{r} \times \nabla \psi_{sp})]/\alpha, \quad (2.24)$$

$$\psi_{sp} = A_{00} \frac{\sin(c_0\eta)}{c_0\eta} - A_{01} \frac{\xi(c_0\eta \cos(c_0\eta) - \sin(c_0\eta))}{c_0^2\eta^2} \quad (2.25)$$

where $c_0 = \alpha\sqrt{b^2 - c^2}$ and ψ_{sp} is the scalar potential ($\vec{B} = \nabla \times \nabla \psi_{sp}$) and A_{00}, A_{01}, α are sets of free parameters to computing the model.

- b) In the toroidally-distorted cylindrical coordinates, (r_d, ϑ_d, z_d) are related to cylindrical coordinates (r, ϑ, z) by (MILLER; TURNER, 1981)

$$r = R_0 + r_d \cos \vartheta_d, \quad z = r_d \sin \vartheta_d, \quad \vartheta = -z_d/R_0. \quad (2.26)$$

The solution of Equation 2.7 is

$$\begin{aligned} B_{r_d} &= B_0[a_0F(r_d) - J_0(\alpha r_d)] \sin \vartheta_d/(\alpha R_0), \\ B_{\vartheta_d} &= B_0[J_1(\alpha r_d) - \left(J_0(\alpha r_d) - a_0 \frac{dF(r_d)}{dr_d} \right) \cos \vartheta_d/(\alpha R_0)] \\ B_{z_d} &= B_0[J_0(\alpha r_d) - a_0F(r_d) \cos \vartheta_d] \end{aligned}$$

where

$$F(r_d) = \frac{r_d}{2a_0} J_0(\alpha r_d) + \frac{1}{2} \frac{J_0(\alpha a_0)}{J_1(\alpha a_0)} J_1(\alpha r_d),$$

a_0 and R_0 are radii of a compact toroid with the final ration; $a_0/R_0 \leq 1$.

The computer aided calculation of theoretical values of magnetic field was made for

different sets of free parameters B_0 , a_0 , α and R_0 . Ivanov et al. (1989) suggested that the extra parameter provided by that model gives somewhat better fits than the cylindrically symmetric model. Marubashi (1997) applied the Lundquist solution locally along a toroid. The solution by Miller and Turner (1981) is valid only for large aspect ratio tori. But in different parts of observed magnetic clouds this ratio can be small, which means small and large radii can be comparable (e.g., see the MHD simulations by Vandas et al. (2002)). An analytical solution of force-free magnetic fields inside a toroid with an arbitrary aspect ratio was founded by Romashets and Vandas (2003); if it is assumed that a magnetic cloud is a large loop with roots at the Sun, then its part can be locally treated as a part of a toroid.

Due to the frequent occurrence of CMEs, multiple magnetic clouds (multi-MCs), in which one MC catches up another, should be a relatively common phenomenon. A simple flux rope model can be used to get the primary magnetic field features of multi-MCs (WANG et al., 2002). Results indicate that the magnetic field configuration of multi-MCs mainly depends on the magnetic field characteristics of each member of multi-MCs (HU et al., 2003). In this thesis we study some multi-MCs event but using tools of non-linear dynamic, the MVA method and a non-axially symmetric (of the flux-rope) model known as Grad-Shafranov reconstruction (HAU; SONNERUP, 1999; HU et al., 2003; HU et al., 2004).

2.2.2 Grad-Shafranov model

Nowadays some important studies on space plasmas are based on the investigation of two fundamental questions: (1) what means exactly an electromagnetic confinement? (2) How is the evolution of plasmas within a such confinement? Those kinds of studies involve basically nonlinear elliptic partial differential equations with free boundary conditions and can be performed using the Grad-Shafranov (GS) equation (GRAD; RUBIN, 1958) in regions with toroidal symmetry. However, Sonnerup and Guo (1996), HAU and Sonnerup (1999) developed a method for recovering two-dimensional structures in the magnetopause, from the GS equation, in an ideal MHD formulation. The method is called Grad-Shafranov or GS reconstruction. Using the spacecraft measurements as initial values, this approach can treat the problem as a Cauchy problem - although it is ill-posed - and it can be solved numerically. This kind of study has been initiated at INPE by the authors of this work.

In this Subsection, we develop in detail the physical-mathematical methodology

from an ideal MHD formulation to reach the Grad-Shafranov equation. We use the mathematical representation shown by Sonnerup and Guo (1996), Hau and Sonnerup (1999).

We start from a Two-dimensional Cartesian Coordinate System where z -axis is invariant ($\partial/\partial z = 0$ for any physical quantity). Let \vec{A} the magnetic vector potential:

$$\vec{A} = A_x \hat{x} + A_y \hat{y} + A(x, y) \hat{z}, \quad (2.27)$$

where $A(x, y) = |A_x \hat{x} + A_y \hat{y}|$. We have by definition, $\nabla \times \vec{A} = \vec{B}$ then $\vec{B} \perp \vec{A}$ (see Figure 2.4).

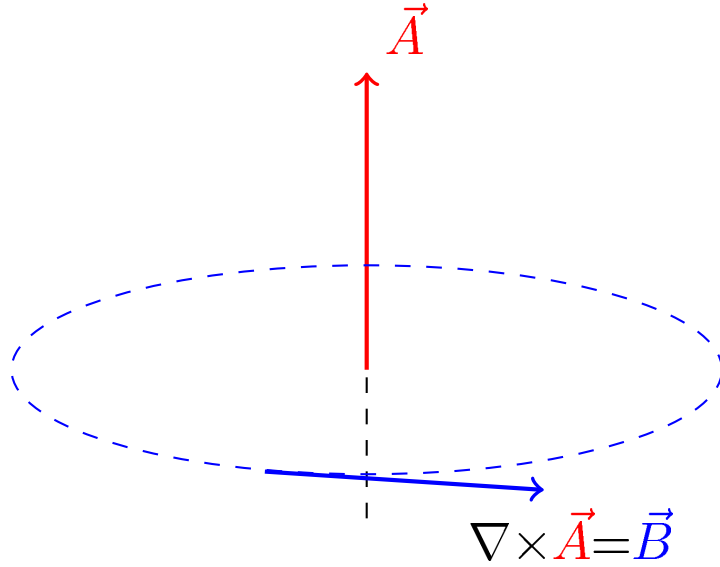


Figure 2.4 - We show the spatial configuration between the vectors \vec{A} and \vec{B} .

Hereafter, vectors in xy plane are denoted by \perp :

$$\vec{B} = B_x \hat{x} + B_y \hat{y} + B_z \hat{z} = \vec{B}_\perp + B_z \hat{z} \quad (2.28)$$

$$\begin{aligned} \vec{B} = \nabla \times \vec{A} &= \left(\frac{\partial A(x, y)}{\partial y} - \frac{\partial A_y}{\partial z} \right) \hat{x} - \left(\frac{\partial A(x, y)}{\partial x} - \frac{\partial A_x}{\partial z} \right) \hat{y} + \left(\frac{\partial A_y}{\partial x} - \frac{\partial A_x}{\partial y} \right) \hat{z} \\ \vec{B} &= \frac{\partial A(x, y)}{\partial y} \hat{x} - \frac{\partial A(x, y)}{\partial x} \hat{y} + \left(\frac{\partial A_y}{\partial x} - \frac{\partial A_x}{\partial y} \right) \hat{z}, \end{aligned} \quad (2.29)$$

remembering that $\partial/\partial z = 0$,

$$\begin{aligned}\nabla A(x, y) &= \frac{\partial A}{\partial x} \hat{x} + \frac{\partial A}{\partial y} \hat{y} \\ \hat{z} &= 0\hat{x} + 0\hat{y} + 1\hat{z},\end{aligned}$$

then,

$$\nabla A \times \hat{z} = \frac{\partial A}{\partial y} \hat{x} - \frac{\partial A}{\partial x} \hat{y} + 0\hat{z}, \quad (2.30)$$

substituting in 2.29

$$\begin{aligned}\vec{B} &= \nabla A \times \hat{z} + B_z \hat{z} \\ B_z &= \left(\frac{\partial A_y}{\partial x} - \frac{\partial A_x}{\partial y} \right) \\ \vec{B} &= \vec{B}_\perp + B_z \hat{z} \\ \vec{B}_\perp &= \nabla A \times \hat{z}.\end{aligned}$$

$A(x, y)$ is constant over a given magnetic field line, and $\nabla A(x, y)$ is always perpendicular to \vec{B} . That means, $\nabla A \cdot \vec{B} = 0$:

$$\begin{aligned}\nabla A \cdot \vec{B} &= \left(\frac{\partial A}{\partial x} \hat{x} + \frac{\partial A}{\partial y} \hat{y} + 0\hat{z} \right) \cdot \left(\frac{\partial A}{\partial y} \hat{x} - \frac{\partial A}{\partial x} \hat{y} + \left(\frac{\partial A_y}{\partial x} - \frac{\partial A_x}{\partial y} \right) \hat{z} \right) \\ &= \frac{\partial A}{\partial x} \frac{\partial A}{\partial y} - \frac{\partial A}{\partial y} \frac{\partial A}{\partial x} = 0.\end{aligned}$$

In the MHD theory, in two-dimensional and stationary structures, the Lorentz force has to be balanced by a pressure force, it is known as magnetostatic equilibrium:

$$\nabla p = \vec{J} \times \vec{B}, \quad \vec{J} \rightarrow \text{current density}, \quad p \rightarrow \text{plasma pressure}. \quad (2.31)$$

The Equation 2.31 has several theoretical considerations and it is related to the force-free model. We did a discussion of this equation in Subsection 2.2.1.

We continue to work with Equation 2.31:

$$\begin{aligned}\nabla p &= \vec{J} \times \vec{B} \\ \frac{\partial p}{\partial x} \hat{x} + \frac{\partial p}{\partial y} \hat{y} + 0 \hat{z} &= \left(\vec{J}_\perp + J_z \hat{z} \right) \times \left(\vec{B}_\perp + B_z \hat{z} \right) \\ \frac{\partial p}{\partial x} \hat{x} + \frac{\partial p}{\partial y} \hat{y} &= J_z \left(\hat{z} \times \vec{B}_\perp \right) + \left(\vec{J}_\perp \times \hat{z} \right) B_z + J_z B_z \left(\hat{z} \times \hat{z} \right) + \vec{J}_\perp \times \vec{B}_\perp,\end{aligned}$$

In right-hand side, first and second terms are into xy (or \perp) plane, the third term is zero and the fourth term is a vector parallel to z -axis. The vector identity is true if there is not component in the z -axis, therefore $\vec{J}_\perp \times \vec{B}_\perp \equiv 0$, this is $\vec{J}_\perp \parallel \vec{B}_\perp$. Finally,

$$\vec{J} \times \vec{B} = J_z \left(\hat{z} \times \vec{B}_\perp \right) + \left(\vec{J}_\perp \times \hat{z} \right) B_z. \quad (2.32)$$

The expressions for J_z and \vec{J}_\perp are searched using Ampere's law.

$$\nabla \times \vec{B} = \mu_0 \vec{J} = \mu_0 \left(\vec{J}_\perp + J_z \hat{z} \right) \quad (2.33)$$

also,

$$\begin{aligned}\nabla \times \vec{B} &= \nabla \times \left(\nabla \times \vec{A} \right) \\ &= \nabla \times \left(\frac{\partial A}{\partial y} \hat{x} - \frac{\partial A}{\partial x} \hat{y} + B_z \hat{z} \right) \\ &= \left(\frac{\partial B_z}{\partial y} - 0 \right) \hat{x} - \left(\frac{\partial B_z}{\partial x} - 0 \right) \hat{y} - \left(\frac{\partial^2 A}{\partial x^2} + \frac{\partial^2 A}{\partial y^2} \right) \hat{z} \\ &= \frac{\partial B_z}{\partial y} \hat{x} - \frac{\partial B_z}{\partial x} \hat{y} - \nabla^2 A \hat{z},\end{aligned} \quad (2.34)$$

and

$$\nabla B_z \times \hat{z} = \frac{\partial B_z}{\partial y} \hat{x} - \frac{\partial B_z}{\partial x} \hat{y},$$

considering Equation 2.33

$$\begin{aligned}\nabla \times \vec{B} &= \nabla B_z \times \hat{z} - \nabla^2 A \hat{z} \\ \vec{J}_\perp + J_z \hat{z} &= \frac{1}{\mu_0} \nabla B_z \times \hat{z} - \frac{\nabla^2 A}{\mu_0} \hat{z},\end{aligned}$$

where

$$\vec{J}_\perp = \frac{1}{\mu_0} \nabla B_z \times \hat{z}, \quad (2.35)$$

and

$$\vec{J}_z = \frac{\nabla^2 A}{\mu_0} \hat{z}. \quad (2.36)$$

If the vectors \vec{J}_\perp and \vec{B}_\perp are parallel, as indicated in the preceding paragraphs, then the vector ∇B_z is perpendicular to \vec{J}_\perp and \vec{B}_z respectively (see Figure 2.5). We recall that ∇A is in the xy plane, $\nabla A \perp \hat{z}$.

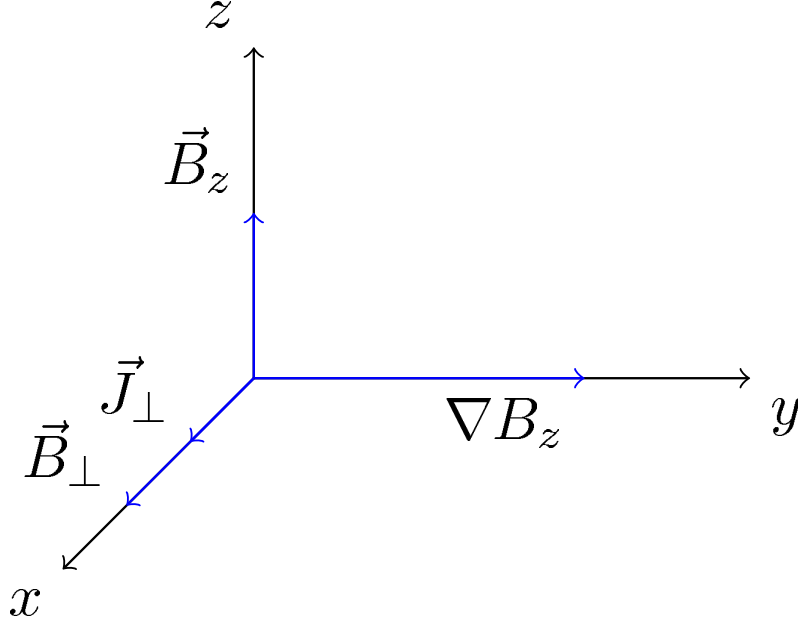


Figure 2.5 - We show the configuration of vectors \vec{J}_\perp , \vec{B}_\perp , ∇B_z and \vec{B}_z in ideal MHD fluid to obtain de GS equation. The vector ∇B_z is perpendicular to \vec{J}_\perp and \vec{B}_z respectively.

With the following vector identity $\vec{C} \times (\vec{D} \times \vec{E}) = \vec{D}(\vec{E} \cdot \vec{C}) - \vec{E}(\vec{D} \cdot \vec{C})$ and using the equation $\vec{E}_\perp = \nabla D \times \hat{z}$, we have that:

$$\begin{aligned} \hat{z} \times \vec{B}_\perp &= \hat{z} \times (\nabla A \times \hat{z}) \\ &= \nabla A (\hat{z} \cdot \hat{z}) - \hat{z} (\nabla A \cdot \hat{z}) \\ &= \nabla A, \end{aligned} \quad (2.37)$$

because $\nabla A \perp \hat{z}$, then $\hat{z} \times \vec{B}_\perp$ is a vector in xy -plane.

We use the Equation 2.35 and the vector identity $(\vec{D} \times \vec{E}) \times \vec{C} = \vec{E}(\vec{D} \cdot \vec{C}) - \vec{D}(\vec{E} \cdot \vec{C})$

to obtain the following result:

$$\begin{aligned}
\vec{J}_\perp \times \hat{z}B_z &= \frac{1}{\mu_0}(\nabla B_z \times \hat{z}) \times \hat{z}B_z \\
&= \frac{B_z}{\mu_0} [\hat{z}(\nabla B_z \cdot \hat{z}) - \nabla B_z(\hat{z} \cdot \hat{z})] \\
&= -\frac{B_z}{\mu_0} \nabla B_z,
\end{aligned} \tag{2.38}$$

Where it is considered that $\nabla B_z \perp \hat{z}$. The Equation 2.38 represent a vector in the xy -plane. We make the substitution of the Equations 2.36, 2.37 and 2.38 into 2.32:

$$\vec{J} \times \vec{B} = \nabla p = -\frac{1}{\mu_0} \{[\nabla^2 A] \nabla A + B_z \nabla B_z\}. \tag{2.39}$$

As the vectors ∇A and ∇B_z are in xy -plane then the above equation represent a vector in the same plane. Since p and ∇B_z are constant along a field line and should be only functions of A , it is $\nabla p = (dp/dA)\nabla A$ and $\nabla B_z = (dB_z/dA)\nabla A$. Substituting in 2.39,

$$\frac{dp}{dA} \nabla A = -\frac{1}{\mu_0} \{[\nabla^2 A] \nabla A + B_z \frac{dB_z}{dA} \nabla A\} \text{ multiplied by } \cdot \frac{1}{\nabla A},$$

and solve for $\nabla^2 A$ in the above equation

$$\begin{aligned}
\frac{\nabla^2 A}{\mu_0} &= -\frac{dp}{dA} - \frac{1}{2\mu_0} \frac{dB_z^2}{dA} \\
\nabla^2 A &= -\mu_0 \frac{d}{dA} \left(p + \frac{B_z^2}{2\mu_0} \right),
\end{aligned} \tag{2.40}$$

The Equation 2.40 is known as Grad-Shafranov equation. We present a summary of the theoretical concepts to obtain de Grad-Shafranov equation:

- 1) 2D-system with \hat{z} -axis invariant, $\partial/\partial z = 0$ for any parameter.
- 2) ∇A is always \perp to \vec{B} .
- 3) Two-dimensional structure of a stationary plasma described by the balance of pressure force and magnetic forces, respectively.
- 4) A stationary plasma means that the velocity of the particles is less than the Alfvén velocity, $v^2 \ll v_A^2$.

- 5) The plasma gravity term is smaller than the magnetic and the plasma beta is small $\beta \ll 1$ (in \perp -plane).
- 6) We have a magnetostatic equilibrium, $\nabla p = \vec{J} \times \vec{B}$.
- 7) $\vec{J}_\perp \parallel \vec{B}_\perp$. This causes the system to be force-free out of the xy -plane but the system is not completely force-free, there is a force in the xy -plane to ensure the equilibrium, see Equation 2.32.
- 8) $\nabla B_z \perp (\vec{J}_\perp$ and $\vec{B}_z)$.
- 9) ∇A is in the xy -plane or \perp plane, $\nabla A \perp \hat{z}$.
- 10) p and ∇B_z are constants along a magnetic field line.

Grad-Shafranov equation of force-free model

We may also obtain the Grad-Shafranov equation from the special case of a force-free system. If the system is force-free then $p = 0$ in the GS equation and it is obtained $\nabla^2 A = -d(B_z^2)/(2dA)$. At above result also is arrived from the force-free condition. We started working with the equation of force-free model to obtain the GS equation.

$$\nabla \times \vec{B} = \alpha \vec{B}, \quad (2.41)$$

Recalling the Equations 2.34 and 2.29:

$$\begin{aligned} \nabla \times \vec{B} &= \frac{\partial B_z}{\partial y} \hat{x} - \frac{\partial B_z}{\partial x} \hat{y} - \nabla^2 A \hat{z} \\ \vec{B} &= \frac{\partial A}{\partial y} \hat{x} - \frac{\partial A}{\partial x} \hat{y} + \left(\frac{\partial A_y}{\partial x} - \frac{\partial A_x}{\partial y} \right) \hat{z} \end{aligned}$$

Replacing the previous two equations in 2.41, we have a vector equation:

$$\left[\frac{\partial B_z}{\partial y}, -\frac{\partial B_z}{\partial x}, -\nabla^2 A \right] = \left[\alpha \frac{\partial A}{\partial y}, -\alpha \frac{\partial A}{\partial x}, \alpha B_z \right]$$

that can be transformed in a system of three equations. We can write two equations of the above system to eliminate α :

$$\begin{cases} \partial B_z / \partial y - \alpha \partial A / \partial y = 0 & / \partial A / \partial x \\ -\partial B_z / \partial x + \alpha \partial A / \partial x = 0 & / \partial A / \partial y \end{cases}$$

We arrived at the expression that defines the Jacobian (\mathfrak{J}).

$$\frac{\partial A}{\partial x} \frac{\partial B_z}{\partial y} - \frac{\partial A}{\partial y} \frac{\partial B_z}{\partial x} = \mathfrak{J} \left(\begin{array}{c} A, B_z \\ x, y \end{array} \right) = 0$$

When the Jacobian is zero, the most general solution is $B_z = B_z(A)$, then:

$$\begin{aligned} \frac{\partial B_z}{\partial x} &= \frac{dB_z}{dA} \frac{\partial A}{\partial x}, \\ \alpha &= \frac{dB_z}{dA}, \\ -\nabla A^2 &= \alpha B_z. \end{aligned}$$

So the Grad-Shafranov equation for a force-free system is:

$$\nabla^2 A = -B_z \frac{dB_z}{dA} = -\mu_0 \frac{d}{dA} \left(\frac{B_z^2(A)}{2\mu_0} \right) \quad (2.42)$$

2.3 Observations

The MCs are observed in a clear way when the spacecraft crosses the magnetic field structure close by its center (SCHWENN, 2006). *In-situ* measurements are limited to the spacecraft trajectory crossing the incoming ICME. Therefore, one needs to rely on modeling evaluation in order to derive the global magnetic structure from available local measurements (DÉMOULIN; DASSO, 2009). When the flux rope is moving faster than the surrounding solar wind (SW), plasmas and magnetic field accumulate typically in front it, that create a plasma sheath region.

2.3.1 Magnetic polarity and orientation of the flux-rope

Satellite measurements made in the interplanetary medium have revealed the frequent occurrence of transient large-scale solar wind streams (radial sizes of 0.25 AU at 1 AU) that exhibit the internal field structure of helical magnetic flux ropes (e.g. Klein and Burlaga (1982), Lepping et al. (1990), Bothmer and Schwenn (1998)). These low plasma- β flows are called MCs. The ratio of ICMEs being helical is important to investigate questions about the Sun's helicity (see Equation 2.11) budget and its possible variation over the solar cycle. Helicity quantifies several aspects of a given magnetic structure, such as the twist, the kink, the number of knots between magnetic field lines, the linking between magnetic flux tubes, etc. Magnetic

helicity is observed in the SW on all scales (KUMAR; RUST, 1996), from more than 1 AU to less than the gyro-radius of a thermal proton (e.g. Dasso et al. (2005)). In a dynamically turbulent medium, such as the solar wind, magnetic helicity tends to be transported to larger scales. When a MC is ejected from the solar corona, it carries an important amount of H . Thus, estimations of the content of H in MCs can help us to understand the physical processes involved in the expulsion of twisted magnetic flux tubes from the Sun and their dynamical evolution in the SW (e.g. Dasso et al. (2005)). There is observational evidence showing that the helicity sign in MCs matches with their source regions (e.g. Bothmer and Schwenn (1994), Rust (1994), Marubashi (1997)).

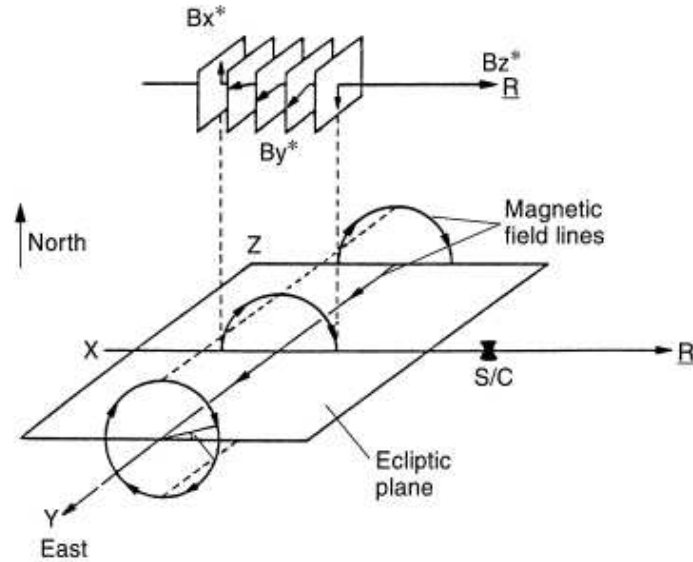






Figure 2.6 - Idealized sketch showing the expected magnetic field signatures during passage of a large-scale cylindrical magnetic flux tube over a s/c. B_x^* , B_y^* and B_z^* are the components of maximum, intermediate and minimum variance of the magnetic field vector. The south to north $[-B_x^*(S)$ to $+B_x^*(N)]$ turning of the magnetic field vector is associated with passage of the circular field lines at the cloud's outer boundaries. At the center of the flux tube (at the axis) the magnetic field is directed along the $+B_y^*$ (east)-direction. A semicircular rotation appears when B_y^* is plotted versus B_x^* (*top diagram*). According to Figure 2.7(a), MCs can be classified into SEN clouds with left-handed magnetic helicity H . SOURCE: Bothmer and Schwenn (1998) adapted from Goldstein (1983).





The four possible flux-rope configurations, as predicted in function of the helic-

ity H from Equation 6.1, have been confirmed to occur in the SW (BOTHMER; SCHWENN, 1994; BOTHMER; SCHWENN, 1998). In Figure 2.6 the calculation is usually done with data in the solar ecliptic coordinate system (SEC). Where x axis is the Earth-Sun line (in the Earth frame), y axis is in the ecliptic plane and at right (in the East direction) angles perpendicular to the Earth-Sun line, z axis normal to the ecliptic, towards the ecliptic north pole. Accordingly θ_d and ϕ_d are the magnetic field's polar ($\theta_d = (90^\circ \equiv N; -90^\circ \equiv S)$) and azimuthal ($\phi_d = (0^\circ \equiv \text{sunward direction}; 90^\circ \equiv E; 270^\circ \equiv W)$) angles. The idealized sketch in Figure 2.6 depicts the magnetic field signatures expected for a cylindrical magnetic flux tube which moves radially away from the Sun, i.e., in the x -direction, and centrally passes a spacecraft in the ecliptic. We also used other Cartesian coordinates system x^*, y^*, z^* from the minimum variance method (MVA) (SONNERUP; CAHILL, 1967; SONNERUP; SCHEIBLE, 1998) (*see Chapter 4, for more details*).

In Figure 2.6 the maximum change in the magnetic field direction would occur normal to the ecliptic in the B_x^* -component due to the south (S) to north (N) turning of the magnetic field vector (BOTHMER; SCHWENN, 1998). The component of minimum variance, B_z^* , corresponds to the radial component B_x , because B_x is zero in the whole MC (*see Equation 6.1, the radial component is zero*). At the center of the flux tube, i.e., at the cloud's axis, the magnetic field is directed in the $+y$ direction, eastern (E)-direction. This is also the direction of intermediate variance, because B_y^* is zero at the cloud's outer boundaries (on the surface of the cylinder). A flux rope category (SEN-type) is often used to classify the above MC where the magnetic field vector rotates from the south (S) at the leading edge to the north (N) at the trailing edge, being eastward (E) at the axis (BOTHMER; SCHWENN, 1994; BOTHMER; SCHWENN, 1998; MULLIGAN et al., 1998). When viewed by an observer looking towards the Sun (positive axis direction) the clockwise rotation is defined as left-handed magnetic helicity H . The actual variance directions x^*, y^*, z^* usually differ from the solar ecliptic coordinate system in x, y, z and the flux-tube axis may have any orientation relative to the ecliptic plane and to the radial direction. The MVA can help to found the x^*, y^*, z^* directions. The hodogram (SONNERUP; CAHILL, 1967) is the plot of the component of intermediate variance B_y^* versus the component of maximum variance B_x^* . If we do the hodogram of the case shown in Figure 2.6, the magnetic field vector rotate smoothly forming a semicircle in the plane of maximum variance (KLEIN; BURLAGA, 1982). We find a rotation of the magnetic field vector from negative to positive B_x^* -values and $+B_y^*$ values.

Magnetic Cloud Type				
	SEN	SWN	NES	NWS
Leading Field	South (-Bz)	South (-Bz)	North (+Bz)	North (+Bz)
Axial Field	East (+By)	West (-By)	East (+By)	West (-By)
Trailing Field	North (+Bz)	North (+Bz)	South (-Bz)	South (-Bz)
Helicity	LH	RH	RH	LH

(a) Bipolar MCs. Four orientations of ecliptically oriented flux rope model and its magnetic signatures. Note N=north, S=south, E=east, W=west

Magnetic Cloud Type				
	WNE	ESW	ENW	WSE
Leading Field	West (-By)	East (+By)	East (+By)	West (-By)
Axial Field	North (+Bz)	South (-Bz)	North (+Bz)	South (-Bz)
Trailing Field	East (+By)	West (-By)	West (-By)	East (+By)
Helicity	RH	RH	LH	LH

(b) Unipolar MCs. Four flux rope model orientations highly inclined with respect to the ecliptic plane. Note N=north, S=south, E=east, W=west

Figure 2.7 - Sketch showing the different magnetic configuration of MCs and their magnetic helicity (left-handed (LH), right-handed (RH)) based on the magnetic flux-tube concept and the field rotation that a spacecraft would observe during the cloud's passage. SOURCE: Mulligan et al. (1998)

The axis of a MC (ϕ_C, θ_C) can have any orientation over ecliptic plane and depending on the observed directions of the magnetic field at the front boundary, at the axis and at the end boundary eight flux rope categories are often used to classify MCs (BOTHMER; SCHWENN, 1994; BOTHMER; SCHWENN, 1998; MULLIGAN et al., 1998; HUTTUNEN et al., 2005). For example, the flux tube in Figure 2.6 possess one of the four magnetic configuration (SEN, SWN, NES and NWS) given by the orientation of the magnetic field lines at the cloud's outer boundaries and on its axes

(see Figure 2.7(a)). SEN, SWN, NES and NWS denote the field variations in GSE coordinates that an observer would measure when passing through the center of a horizontally directed MC with respect to the ecliptic. In the Figure 2.7(b) note that the middle letter denotes the direction of the flux ropes axial field, so that vertical to the ecliptic oriented MCs would lead to directional changes as ESW, ENW, WSE and WNE (MULLIGAN et al., 1998; BOTHMER, 2003; HUTTUNEN et al., 2005). Summarizing, following the terminology by Mulligan et al. (1998) to classify MCs, eight flux rope categories are often used:

- Bipolar MCs (low inclination and flux rope-type: SWN, SEN, NES, NWS), $\theta_C \leq 45^\circ$ (see Figure 2.7(a)) and
- Unipolar MCs (high inclination, and flux rope-type: WNE, ESW, ENW, WSE), $\theta_C > 45^\circ$ (see Figure 2.7(b)).

2.3.2 Solar cycle variation versus flux-rope type

The studies of MCs during different activity phases for solar activity phases 21 – 23 revealed systematic variations in the preferred flux rope types (BOTHMER; RUST, 1997; BOTHMER; SCHWENN, 1998; MULLIGAN et al., 1998; HUTTUNEN et al., 2005; ECHER et al., 2005). The bipolar MCs in the rising phase of:

- Odd solar cycles: the magnetic field in MCs rotates predominantly from the south to the north (SN).
- Even solar cycles: the magnetic field in MCs rotates predominantly from the north to the south (NS).

and during the years of high solar activity, both SN and NS type MCs are observed. Additionally, Mulligan et al. (1998) found for the years 1979-1988 that **unipolar** MCs were most frequently observed in the *declining phase* of solar activity cycle. At solar minimum and in the *rising phase* most MCs were **bipolar**.

Huttunen et al. (2005) found in the rising phase nearly all bipolar MCs that are lying near the ecliptic plane were associated with the SN rotation. At solar maximum (peaked in April 2000) and in the declining phase (2001 – 2003) the number of bipolar MCs with the opposite sense of rotation was increased. Also they suggest

Table 2.2 - Distribution of NS and SN MC polarities in function of solar cycle epochs.

Solar cycle epoch	NS (%)	SN(%)
Solar minimum 1973 – 1978	40	60
Solar minimum 1983 – 1988	80	20
Solar minimum 1993 – 1998	19	81
Solar miximum 1966 – 1971	60	40
Solar miximum 1977 – 1982	38	63
Solar miximum 1987 – 1992	75	25
Solar miximum 1998 – 2001	29	71

SOURCE: Echer et al. (2005)

that at solar maximum the grouping of bipolar regions and in the declining phase the presence of magnetic regions from both new and old solar cycles, result in the mixture of NS and SN type MCs. The MC polarity percentage per solar cycle phase was shown by Echer et al. (2005), see Table 2.2.

The MC polarity varies in response to changes in the magnetic structures of their source region while the inclination of the coronal streamer belt controls the clouds axial symmetry (MULLIGAN et al., 1998). Figure 2.8 shows a sketch of the solar magnetic field and MC polarity for alternate solar cycle. The magnetic field structure is predominantly left-handed twisted in the northern hemisphere and right-handed twisted in the southern hemisphere as viewed by an observer looking towards the Sun (RUST; KUMAR, 1994; MARTIN et al., 1994; BOTHMER, 2003). The orientation of the forward MC field is the same as the global dipole solar magnetic field. Figure 2.8 also shows that left-handed twisted MCs originate from filament sites with the depicted magnetic polarities in the northern hemisphere and right-handed twisted MCs originate from filament sites with the depicted polarity in the southern hemisphere. A simplification of Figure 2.8 is that it does not take into account the phases during the solar cycle when magnetic regions of both the old and new cycle are present (BOTHMER, 2003). During these overlapping time periods, disappearing filaments (eruptive prominences) could lead to the origin of SN or NS fields in MCs.

The plasma cloud is cooled as it moves away from the surface of the sun and therefore expands. The magnetic clouds are considered geoeffective events. The expansion and geoeffectiveness of MCs is summary in the Appendix A.

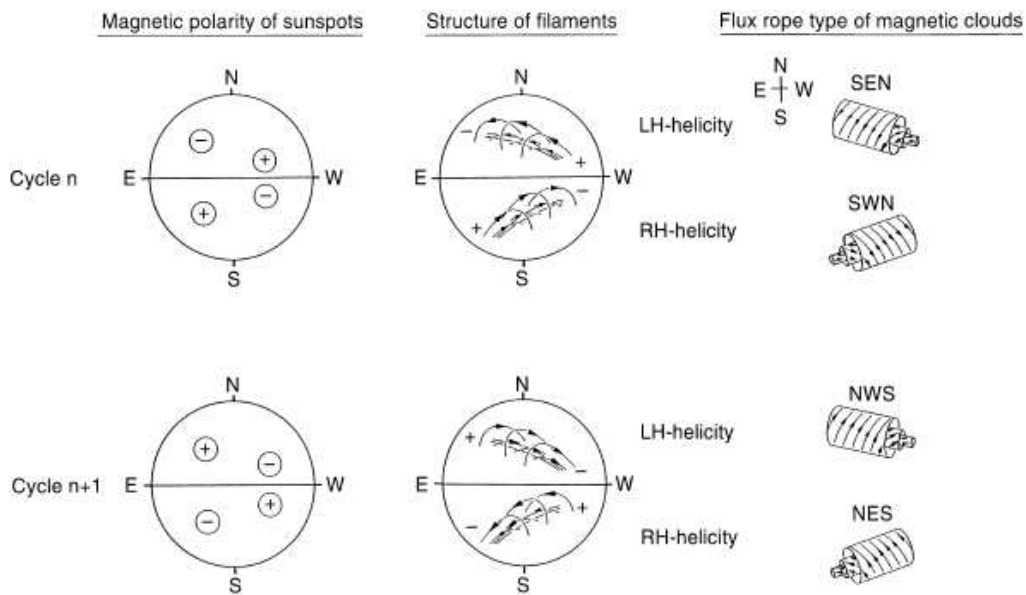


Figure 2.8 - Solar cycle dependence of the magnetic field structure of filaments at the Sun and that of the corresponding MCs in the interplanetary medium. The *left panel* shown the polarity of sunspots during two subsequent cycles. The solar cycle, n , is assumed to be odd number. The *middle panel* shows the expected preferential magnetic structure of filaments in the two solar hemispheres and the *right panel* shows the expected structures of MCs. During odd (n) cycles SN MCs are dominant whereas NS dominate during even ($n + 1$) cycles (BOTHMER; RUST, 1997). Note that for simplicity the MCs are oriented horizontally with respect to the ecliptic plane and that the cycles do not indicate any overlaps. SOURCE: Bothmer and Schwenn (1998).

3 INSTRUMENTATION AND DATASET

The IMF dataset used in this work are measurements from ACE spacecraft. The ACE spacecraft is in orbit around $L1$ from 1997 (SMITH *et al.*, 1998). Where the $L1$ Lagrangian point is a place of Earth-Sun gravitational equilibrium about 1.5 million km from Earth and 148.5 million km from the Sun. Onboard of ACE a total of ten instruments, was launched toward $L1$ (MCCOMAS *et al.*, 1998). The data ([http : //www.srl.caltech.edu/ACE/ASC/level2/index.html](http://www.srl.caltech.edu/ACE/ASC/level2/index.html)) contains time averages of the magnetic field over time periods 1 s, 16 s, 4 min, hourly, daily and 27 days (1 Bartels rotation). Magnetic field vectors are given there in the RTN (Radial Tangential Normal)¹, GSE, and GSM coordinate systems.

In order to provide a better understanding to the content addressed in this thesis, the chapter is divided into four sections. In first section is explains the importance of the Lagrangian points for space research. Second section show a mathematical development to understand how is do the coordinates transformation from GSM to GSE. The above coordinates systems are used in this work. In third section, the instrumentation onboard ACE is described, specifically the instrument more used in this thesis, the Magnetic Field Experiment (MAG). In last section, the data and the analyzed periods are presented.

3.1 Lagrangian points and ACE spacecraft

The gravitational laws require according to a formula founded by Johannes Kepler in 1619 that planets nearer the Sun move faster. Thus, any vehicle around the Sun in an orbit smaller than Earth, it will not maintain a fixed position relative to it. However, there is a solution. If the vehicle is positioned on the axis Sun-Earth, Earth's gravity pulls in the opposite direction and cancels some of the attraction of the Sun (DEPRIT; Deprit-Bartholome, 1967). With less force of gravity towards the Sun, the vehicle needs less speed to maintain its orbit. In 1772, the Italian-French mathematician Joseph Louis Lagrange was working on the famous three-body problem (CELLETTI; GIORGILLI, 1990). He discovered the existence of equilibrium positions where the fields of gravity between two massive objects like the Sun and Earth are balanced. A point where this happens is the $L1$ Lagrangian point.

¹ \mathbf{R} = Sun to Spacecraft unit vector, $\mathbf{T} = (\mathbf{\Omega} \times \mathbf{R}) / |(\mathbf{\Omega} \times \mathbf{R})|$, where $\mathbf{\Omega}$ is Sun's spin axis (in J2000 Geocentric inertial reference frame using the Julian Epoch of January 1, 2000) and \mathbf{N} completes the right-handed triad.

From the NASA home page is known that in 1978 was launched towards $L1$ point the “International Sun-Earth Explorer-3” (ISEE-3) spacecraft to do investigation in the interplanetary medium. Equipped with a rocket and a lot of fuel, the ISEE-3 was subsequently sent to the Earth Magnetotail and then has been sent to intercept the Giacobini-Zinner comet. Also, in November 1994 a new spacecraft, the “WIND”, was launched towards $L1$ point. It was originally scheduled to be placed in an orbit near $L1$ point in 1996, but after, the mission was sent to an orbit with form of “flower petal” around the Earth. Other spacecrafts, SOHO and ACE was launched towards $L1$ in 1995 and 1997 respectively (information on NASA home page).

A space vehicle in $L1$ point must have its own rocket, as the position is unstable, have a drift velocity that need correcting. In fact, the preferred position is currently at some distance from the side of $L1$, where the vehicle is situated on the Sun-Earth line. Therefore corrections are made regularly (MCCOMAS et al., 1998). Furthermore, the most economical way to arrive to $L1$ is using the Moon gravity as an impulsive force. The above is common in interplanetary travel of spacecrafts. In these maneuvers are required onboard propulsion, as in final approach to $L1$.

$L1$ position is very important in the study of solar wind parameters and the Sun itself. A spacecraft in the $L1$ point is outside of magnetosphere and the structures of the solar wind (e.g., ICME) associated with solar events are seen with some anticipation 30 min – 1h. Datasets of a spacecraft in this position is used in this work.

3.2 Coordinate systems: GSE and GSM

We work during the development of this thesis with GSE and GSM coordinates system respectively. Then, it is important to understand the relationship between these two coordinate system.

To transform GSE to Geocentric Solar Magnetic (GSM) system the method proposed by Hapgood (1992) and enhanced by Fränz and Harper (2002) are used. The GSE system is defined such that the X axis is directed towards the Sun while the Y axis lies in the ecliptic plane in the direction opposite to the Earth’s velocity around the Sun; the Z axis completes the right-hand system ($\hat{Z} = \hat{X} \times \hat{Y}$) which places it essentially along the ecliptic North pole. The origin is located at the center of the Earth. The GSE system is not inertial, making a full rotation about the Z axis in

one year.

The GSM system differs from GSE by a rotation about the X axis such that the terrestrial magnetic dipole lies in the ZX plane. That is, GSM Z axis is the projection of the magnetic dipole onto the GSE YZ plane (MENDES, 1992). In addition to the annual rotation, this coordinate system exhibits a diurnal wobble. Since the magnetic dipole is usually taken from a geomagnetic model, there can be disagreements between investigators regard to which one they use.

The transformations described in the following paragraph are presented as matrices, which are either a simple rotation matrix (a rotation of angle ζ about one of the principal axes) or are the products of simple rotation matrices (HAPGOOD, 1992). These simple matrices have only two degrees of freedom and so only two parameters are needed to specify the nine terms in the matrix. These two terms can be the rotation angle and the name of the rotation axis: X , Y or Z .

$$E_M = \langle \zeta, \text{axis} \rangle$$

and specify a product matrix as

$$T = E_{M1}E_{M2} = \langle \zeta_1, \text{axis}_1 \rangle * \langle \zeta_2, \text{axis}_2 \rangle.$$

Inversion is straightforward:

$$\begin{aligned} E_M^{-1} &= \langle -\zeta, \text{axis} \rangle \\ T^{-1} &= E_{M2}^{-1}E_{M1}^{-1} = \langle -\zeta_2, \text{axis}_2 \rangle * \langle -\zeta_1, \text{axis}_1 \rangle \end{aligned}$$

Thus, for a rotation angle ζ about the Z axis we obtain the matrix shown below:

$$\langle \zeta, Z \rangle = \begin{bmatrix} \cos \zeta & \sin \zeta & 0 \\ -\sin \zeta & \cos \zeta & 0 \\ 0 & 0 & 1 \end{bmatrix}$$

For two vectors (X_{se}, Y_{se}, Z_{se}) , (X_{sm}, Y_{sm}, Z_{sm}) in GSE and GSM coordinates respectively, the matrix of coordinates transform is $T3 = -\langle \psi_{se-sm}, X \rangle$ (HAPGOOD,

1992), then:

$$\begin{aligned} X_{sm} &= X_{se} \\ Y_{sm} &= Y_{se} \cos \psi_{se-sm} - Z_{se} \sin \psi_{se-sm} \\ Z_{sm} &= Y_{se} \sin \psi_{se-sm} + Z_{se} \cos \psi_{se-sm} \end{aligned}$$

Where ψ_{se-sm} lies between $+90^\circ$ and -90° and is the angle between the GSE Z axis and projection of the magnetic dipole axis on the GSE YZ plane (i.e. the GSM Z axis) measured positive for rotation towards the GSE Y axis. It can be calculated by:

$$\psi_{se-sm} = \arctan \frac{y_e}{z_e}.$$

the values of y_e and z_e are obtained (HAPGOOD, 1992) from an unit vector:

$$Q_e = \begin{bmatrix} x_e \\ y_e \\ z_e \end{bmatrix}$$

describing the dipole axis direction in the GSE coordinate system. This direction is usually defined in the GEO coordinate system as (HAPGOOD, 1992):

$$Q_g = \begin{bmatrix} \cos \phi_g \cos \lambda_g \\ \cos \phi_g \sin \lambda_g \\ \sin \phi_g \end{bmatrix}$$

where ϕ_g and λ_g are the geocentric latitude and longitude of the dipole North geomagnetic pole. These may be derived from the first order coefficients of the International Geomagnetic Reference Field (IGRF) (FRASER-SMITH, 1987), eventually adjusted to the time of interest. Longitude is given by:

$$\lambda_g = \arctan \frac{h_1^1}{g_1^1}$$

where, in practice, λ must lie in the fourth quadrant. The latitude is given by:

$$\phi_g = 90^\circ - \arctan \frac{g_1^1 \cos \lambda_g + h_1^1 \sin \lambda_g}{g_1^0}$$

Hapgood (1992) used the matrix arithmetic to obtain Q_e :

$$Q_e = T_2 T_1^{-1} Q_g \quad (3.1)$$

with,

$$T_1 = \langle \theta, Z \rangle = \begin{bmatrix} \cos \theta & \sin \theta & 0 \\ -\sin \theta & \cos \theta & 0 \\ 0 & 0 & 1 \end{bmatrix}$$

This matrix corresponds to a rotation in the plane of the Earth's geographic equator from the First Point of Aries to the Greenwich meridian. The rotation angle θ is the Greenwich mean sidereal time:

$$\theta = 100.461 + 36000.770T_0 + 15.04107UT$$

T_0 is the time Julian centuries (36525 days) from 12 : 00 UT on 1 January 2000 (known as epoch 2000) to the previous midnight:

$$T_0 = \frac{MJD - 51544.5}{36525.0},$$

time is there specified by modified Julian date (MJD), which is the time measured in days from 00 : 00 UT on 17 November 1858 (Julian date 2400000.5). Hapgood (1992) used only the integer part of MJD, i.e. the value at 00 : 00 UT on the day of interest. For some applications it is also necessary to give the time within the day as Universal Time in hours (UT). It is also necessary to consider the explanation of Hapgood (1992), i.e. Universal Time is different from coordinated Universal Time (UTC) which is the time scale usually used for data recording. UTC is atomic time adjusted by an integral number of seconds to keep it within 0.6 s of UT. Where the difference between UT and UTC may be neglected. The apparent position of the Sun is calculated using yet another time scale: terrestrial dynamical time or TDT. For example, the difference between UT and TDT is 57 s in 1991, may also be neglected.

T_2 is calculated as (HAPGOOD, 1992):

$$T_2 = \langle \lambda_{\odot}, Z \rangle * \langle \varepsilon, X \rangle = \begin{bmatrix} \cos \lambda_{\odot} & \sin \lambda_{\odot} \cos \varepsilon & \sin \lambda_{\odot} \sin \varepsilon \\ -\sin \lambda_{\odot} & \cos \lambda_{\odot} \cos \varepsilon & \cos \lambda_{\odot} \sin \varepsilon \\ 0 & -\sin \varepsilon & \cos \varepsilon \end{bmatrix}$$

These two matrices correspond to:

- a) rotation from the Earth's equator to the plane of the ecliptic;
- b) rotation in the plane of the ecliptic from the First Point of Aries to the Earth-Sun direction.

Where ε is the obliquity of the ecliptic

$$\varepsilon = 23.439 - 0.013T_0,$$

and λ_{\odot} is the Sun's ecliptic longitude:

$$\lambda_{\odot} = \wedge + (1.915 - 0.0048T_0) \sin M + 0.020 \sin 2M$$

M is the Sun's mean anomaly and \wedge its mean longitude:

$$M = 357.528 + 35999.050T_0 + 0.04107UT$$

$$\wedge = 280.460 + 36000.772T_0 + 0.04107UT$$

The final expression to calculate x_e , y_e and z_e is obtained substituting into the Equation 3.1. (Hapgood (1992) do not show these calculations but we arrived at the expressions:

$$Q_e = \begin{bmatrix} x_e \\ y_e \\ z_e \end{bmatrix} = \begin{bmatrix} \cos \theta \cos \lambda \cos \lambda_{\odot} \cos \phi - \cos \varepsilon \cos \phi \sin \theta \sin \lambda_{\odot} \\ \cos \theta \sin \lambda \cos \lambda_{\odot} \cos \phi \cos \varepsilon - \cos \lambda \cos \phi \sin \theta \sin \lambda_{\odot} \\ \cos \varepsilon \sin \phi \end{bmatrix} \quad (3.2)$$

3.3 The ACE Magnetic Field Instrument (MAG)

The spacecraft ACE² was launched on a McDonnell-Douglas Delta *II* 7920 launch vehicle on August 25, 1997 from the Kennedy Space Center in Florida. From its location ACE has a prime view of the solar wind, IMF and higher energy particles accelerated by the Sun, as well as particles accelerated in the Heliosphere and the galactic regions beyond. The ten experiments onboard of ACE are shown in Figure 3.1. We show a description of these instruments in Table 3.1.

²ACE spacecraft 2011 home page: http://www.srl.caltech.edu/ACE/ace_mission.html.

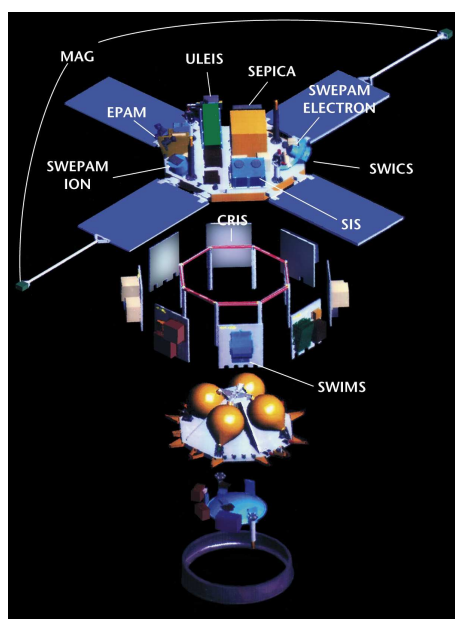


Figure 3.1 - The picture show all ACE instruments.

SOURCE: ACE spacecraft 2011 home page.

Table 3.1 - The ten instruments on board of ACE. In red the instruments used in this thesis.

Instrument	Description
CRIS	Cosmic Ray Isotope Spectrometer
SIS	Solar Isotope Spectrometer
ULEIS	Ultra Low Energy Isotope Spectrometer
SEPICA	Solar Energetic Particle Ionic Charge Analyzer
SWIMS	Solar Wind Ions Mass Spectrometer
SWICS	Solar Wind Ion Composition Spectrometer
EPAM	Electron, Proton and Alpha Monitor
SWEPAM	The Solar Wind Electron, Proton and Alpha Monitor
RTSW	Real-Time Solar Wind Data
MAG	Magnetic Field Experiment

SOURCE: <http://www.ssg.sr.unh.edu/mag/ace/otherinstruments.htm>.

The ACE Magnetic Field Experiment (MAG) (SMITH et al., 1998) establishes the time-varying, large-scale structure of the interplanetary magnetic field (IMF) near the L1 point as derived from continuous measurement of the local field at the spacecraft. It is the principal instrument used in this thesis. The ACE MAG instrument is the reconditioned flight spare of the WIND/MFI experiment (LEPPING et al., 1995).

The only changes made to the unit were to accommodate the ACE data bus (the MFI I/O board was replaced) and to change the sampling rate of the instrument so that it better met the telemetry allocation for ACE (down from 44 vector s^{-1} for WIND to 24 vector s^{-1} for ACE). The WIND/MFI and ACE/MAG instruments are based on the magnetometers previously developed for the *Voyager*, *ISPM*, *GIOTTO*, *Mars Observer*, and *Mars Global Surveyor* missions which represent state-of-the-art instruments with unparalleled performance.

Table 3.2 summarizes the principal characteristics of this instrument. The basic configuration consists of twin, wide-range (0.001 to 65,536 nT) triaxial fluxgate magnetometers mounted on two deployable, titanium booms, a 12 – bit resolution A/D converter system and a microprocessor controlled data processing and control unit (DPU). Both magnetometer sensors are deployed 4.19 meters from the center of the spacecraft along the $\pm Y$ axes of the spacecraft.

A triaxial magnetometer is thus created when three single axis sensors are arranged in an orthogonal configuration and three sets of signal processing electronics are used to produce three output voltages proportional to the orthogonal components of the ambient magnetic field. This enables the study of the physics of the fine-scale structure of shock waves directional discontinuities boundary structures including those of CMEs, magnetic clouds, current sheets, and CIRs. And other transient phenomena associated with the acceleration and modulation of energetic charged particle populations, as well as the dissipation range of IMF fluctuations. And other various wave modes and non-coherent fluctuations occurring regularly in the SW.

3.4 IMF Dataset

In this work we use data from the IMF GSM-components with time resolution of 16 s. We work with 41 of 80 events (73 MCs and 7 cloud candidate) identified by Huttunen et al. (2005). These events in chronological order are shown in Table A.1. The columns from the left to the right give: a numeration of the events, year, shock

Table 3.2 - Summary of instrument characteristics.

Instrument Characteristics	Description
Instrument type	Twin, triaxial fluxgate magnetometers (boom mounted)
Dynamic ranges (8)	± 4 nT (Range 0); ± 16 nT (Range 1); ± 64 nT (Range 2); ± 256 nT (Range 3); ± 1024 nT (Range 4); ± 4096 nT (Range 5); $\pm 16,384$ nT (Range 6); $\pm 65,536$ nT (Range 7)
Digital Resolution (12-bit)	± 0.001 nT (Range 0); ± 0.004 nT (Range 1); ± 0.016 nT (Range 2); ± 0.0625 nT (Range 3); ± 0.25 nT (Range 4); ± 1.0 nT (Range 5); ± 4.0 nT (Range 6); ± 16.0 nT (Range 7)
Bandwidth	12 Hz
Sensor noise level	< 0.006 nT RMS, 0 – 10 Hz
Sampling rate	24 vector samples/s in snapshot memory and 3, 4 or 6 vector samples/s continuous data stream
Signal processing	FFT Processor, 32 logarithmically spaced channels, 0 to 12 Hz. Full spectral matrices generated every 80 seconds for four time series ($B_x, B_y, B_z, B $)
FFT windows/filters	Full despinn of spin plane components, 10% cosine taper, Hanning window, first difference filter
FFT dynamic range	72 dB, μ -Law log-compressed, 13-bit normalized to 7-bit with sign
Sensitivity threshold	$\sim 0.5 \times 10^{-3}$ nT/Hz in Range 0
Snapshot memory capacity	256 Kbits
Trigger modes (3)	Overall magnitude ratio, directional max.-min. peak-to-peak change, Spectral increase across frequency band (RMS)
Telemetry modes	Three, selectable by command
Mass	Sensors (2): 450 g total Electronics (redundant): 2100 g. total
Power consumption	2.4 watts, electronics - regulated 28 Volts $\pm 2\%$ 1.0 watts, heaters- unregulated 28 Volts

SOURCE: Smith et al. (1998).

time (UT), MC start time (UT), MC end time (UT), and the end time (UT) of the third region respectively.

It is convenient to inform here that a total of 17 events are not treated in this work, listed in Table A.3. The reason is that the ACE data before about the end of 1997 were not qualified for research uses. Huttunen et al. (2005) used for this initial period the measurements recorded by the satellite WIND. The Magnetic Field Instrument (MFI) onboard WIND is composed of dual triaxial fluxgate magnetometers. Due to result comparisons, we avoid mixing in the analyses data from different satellites. Other problem is that the WIND data available in averages present 3 s, 1 min, and 1 h time resolution, a worse data resolution than the one used by us from ACE.

The events of MCs not associated with shock waves are not applied to define an analysis methodology. They are presented in Table A.4. The purpose with this selection in this exploratory study is to deal with the cases presenting the three periods (clear Pre-MC, MC and Pos-MC). So, with the well defined MC cases, the assumption is to unravel objectively the magnetically quiescent interval related to the MC period. If there are significant differences of the tools features among the periods, then these tools can be used to identify MCs in more clear bases. Other solar wind disturbances then MCs are not studied here.

Table A.5 presents 4 MCs that we have used during validation of some techniques as useful tools to identify MC regions. The above MCs was identified by Huttunen et al. (2005). We have selected ten days from SW data around the MCs. Also, other two cases were selected and a total of 6 SW intervals have been studied. Table A.6 presents the dates of above intervals. The intervals are presented in the order that it appear in this thesis (Chapters 5 and 6).

The Solar Wind Electron, Proton, and Alpha Monitor (SWEPAM) (MCCOMAS et al., 1998) measures the SW plasma electron and ion fluxes (rates of particle flow) as functions of direction and energy (MCCOMAS et al., 1998). The data contain time averages of SW parameters over time periods 64 s (ion data only), 128 s (electron data only), hourly (all data), daily (all data) and 27 days (all data). The above instruments provided the measurements used in this work. Thus, magnetic field and plasma data, with 5 min or 1 h of time resolution, are used.

The IMF and solar wind plasma data used in this work correspond to events from two

main lists of interplanetary phenomena. One is the MC identification by [Huttunen et al. \(2005\)](#), where there are a event number, year, shock time (UT), MC start time (UT) and MC end time (UT) respectively. The other is the [Cane and Richardson \(2003\)](#)'s summarization of the occurrence of ICMEs recorded in the SW that reached the Earth during 1996 – 2002, corresponding to the increasing and maximum phases of solar cycle 23. They give a detailed list of such events based on in situ observations.

In summary, we only work with data measurements using two instruments onboard of ACE, MAG and SWEPAM, but different time resolutions will be used.

4 PHYSICAL-MATHEMATICAL TECHNIQUES

In order to fulfill theoretical requirements related to this work, an objective review on all physical-mathematical techniques is presented. The techniques are: spatio-temporal entropy, persistence exponents, discrete wavelet transform, minimum variance analysis, Grad-Shafranov reconstruction, and detection of current sheets. A table compiling the main characteristics of the techniques is presented (see Section 4.8).

4.1 The entropy concepts in Recurrence Plot

A summary of the ideas expressed in the Eugene Kononov's Visual Recurrence Analysis (VRA) software (VRA v4.7 <http://nonlinear.110mb.com/vra/>) about recurrence plots (RPs) is presented. In order to present the ideas, some figures are used to guide the description. Figure 4.1 (left panel) shows a recurrence plot (RP) for a simple sine wave, using the data file just included in VRA software. In it organized patterns of color characteristics are shown for the periodical signal. In order to allow a comparative view, a RP of white noise is shown in Figure 4.1 (right panel), with the data file also included. With a different result, an uniform distribution of color characteristics is noticed for the random signal.

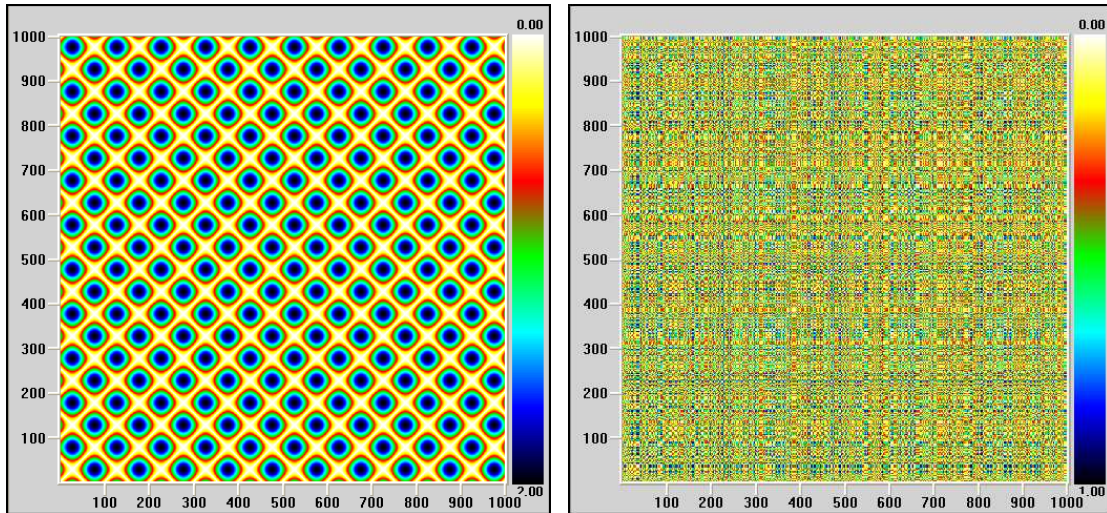


Figure 4.1 - Recurrence plot using a data files included with VRA software. (left panel) In the RP organized patterns of color characteristics are shown for a periodic signal; sine wave with $STE = 0\%$. (right panel) In the RP an uniform distribution of color characteristics is shown for a random signal, white noise with $STE = 80\%$.

In the RPs a one-dimensional time series from a data file is expanded into a higher-dimensional space, in which the dynamic of the underlying generator takes place. This is done by a technique called “delayed coordinate embedding”, which recreates a phase space portrait of the dynamical system under study from a single (scalar) time series. To expand a one-dimensional signal into an M -dimensional phase space, one substitutes each observation in the original signal $X(t)$ with vector $(y(i) = \{x(i), x(i - d), x(i - 2d), \dots, x(i - (m - 1)d)\})$, where i is the time index, m is the embedding dimension, d is the time delay. As a result, we have a series of vectors $Y = y(1), y(2), y(3), \dots, y(N - (m - 1)d)$, where N is the length of the original series ¹.

With such reconstruction it is possible to reproduce the original system states at each time where we have an observation of that system output. Each unknown state $Z(t)$ at time t is approximated by a vector of delayed coordinates $Y(t) = x(t), x(t - d), x(t - 2d), \dots, x(t - (m - 1)d$. After the Euclidean distances between all vectors are calculated, they are mapped to colors from the pre-defined color map and are displayed as colored pixels in their corresponding places (see Figure 4.1 (left panel), for example). The RP is a graphical representation of a correlation integral. The important distinction (and an advantage) is that the RP, unlike the correlation integrals, preserve the temporal dependence in the time series, in addition to the spatial dependence.

In RPs, if the underlying signal is truly random and it has not structure, the distribution of colors is uniform and does not have any identifiable patterns (see Figure 4.1 (right panel), for example). There is some determinism in the signal generator, which can be detected by some distinctive color distribution. For example, hot colors (yellow, red, and orange) can be associated with small distances between the vectors, while others colors (blue, black) may be used to show large distances. In this printed work colors are noticed as a grey pattern (from white to black). Therefore one can visualize and study the motion of the system trajectories and infer some characteristics of the dynamical system that generated the time series. Also, the length of diagonal line segments of the same color on the RP brings an idea about the signal predictability. But, RP is mostly a qualitative tool. For random signals, the uniform (even) distribution of colors over the entire RP is expected. So for the purpose of comparison in Figure 4.1 (left panel) the RP of a strictly periodic signal is plotted

¹see http://www.visualization-2002.org/VRA_Main_Description_.html

and in Figure 4.1 (right panel) the RP from a white noise is shown.

The RP is a visual tool for the investigation of temporal recurrence in phase space (TAKENS, 1981). With the purpose of reaching a quantitative tool in this work, a brief review about some methods to calculate the entropy in the RP and the phase space is presented here.

The calculation of the spatio-temporal entropy, called in short way as STE was used to measure the image “structuredness” in a bidimensional representation, *i.e.*, both in “space” and time domains. Its implementation in VRA software is to quantify the order found in RPs. In physical terms, this quantity compares the distribution of distances between all pairs of vectors in the reconstructed state space with that of distances between different orbits evolving in time. The result is normalized and presented as a percentage of “maximum” entropy (randomness). When the entropy has a value of 100% it means the absence of any structure whatsoever (uniform distribution of colors, pure randomness, seen in Figure 4.1 (right panel)). On the other hand, 0% of entropy implies “perfect” structure (distinct color patterns, perfect “structuredness” and predictability, seen in Figure 4.1 (left panel)).

Recurrence is the most important feature of chaotic systems (ECKMANN et al., 1987). The popularity of RPs lies in the fact that their structures are visually appealing, and that they allow the investigation of high dimensional dynamics by means of a simple two-dimensional plot (FACCHINI et al., 2009). For a better understanding and quantification of the recurrences, Webber and Zbilut (1994) have proposed a set of quantification measures, which are mainly based on the statistical distribution of the line structures in the RP. Recurrence quantification analysis (RQA) is a nonlinear technique used to quantify the information supplied by a RP (WEBBER; ZBILUT, 1994; ZBILUT; WEBBER, 1992). Recurrence variables are calculated from the upper triangular area of the recurrence plot, excluding the central diagonal, because the plot is symmetrical about the main diagonal. The RQA can be used as a tool for the exploration of bifurcation phenomena and dynamics changes also in nonstationary and short time series. The entropy (ENT) is one of the recurrence variables of the RQA method. It is the Shannon information entropy for the distribution probability of the diagonal lines. That is:

$$ENT = - \sum_{k=L_{min}, p(k) \neq 0}^{L_{max}} p(k) \log_2(p(k)), \quad (4.1)$$

where L_{min} is the minimum length of diagonal lines in RP and

$$p(k) = \frac{\text{number of diagonal lines of length } k \text{ in RP}}{\text{number of diagonal lines in RP}}. \quad (4.2)$$

The ENT can be calculated using the VRA software; but it should not be confused with the STE.

Little et al. (2007) developed a Recurrence Period Density Entropy (RPDE) method, first it requires the embedding of a time series in phase space, which, according to Taken's embedding theorems, can be carried out by forming time-delayed vectors for each value x_n in the time series. Then, around each point in the embedded phase space, a recurrence neighbourhood of radius ϵ is created. All recurrences into this neighbourhood are tracked, and the time interval T' between recurrences is recorded in a histogram. This histogram is normalized to create an estimate of the recurrence period density function $p(T')$. The normalized entropy of this density is the RPDE value H_{norm} (LITTLE et al., 2007).

$$H_{norm} = -(\ln T'_{max})^{-1} \sum_{t=1}^{T'_{max}} p(t) \ln p(t). \quad (4.3)$$

The RPDE value is a scalar in the range zero to one. For purely periodic signals, $H_{norm} = 0$ (STE=0%) whereas for purely uniform white noise, $H_{norm} = 1$ (STE=100%). However, estimates obtained with this technique (RPDE) are different from those obtained with the STE.

Dasan et al. (2002) report an analysis, using the tools of nonlinear dynamics and chaos theory, of the fluctuations in the stress determined from simulations of shear flow of Stokesian suspensions. They also computed the STE using VRA for the stress. The calculated values of the STE for the shear and normal stresses were nearly zero, showing perfect structure in the data. They observed definite structure in the phase-space plot of the stress components (DASAN et al., 2002). They cited the works of Peacock (1983), Carr and Schwartz (1998). Peacock (1983) presented a two-dimensional analogue of Kolmogorov-Smirnov test, useful for analysing the

distribution of data in two dimensions, as is the RP. Carr and Schwartz (1998) investigated the fluctuation phenomena in plasmas that often needs the analysis of spatio-temporal signals. It was shown how such signals can be analyzed using the biorthogonal decomposition, which splits them into orthogonal spatial and temporal modes. Several parameters allow one to quantify the weight distribution in the biorthogonal decomposition. The total energy of spatio-temporal signal is found to be equal to the sum of the eigenvalues, α_m :

$$E(u) = \sum_{m=1}^N \alpha_m^2. \quad (4.4)$$

They can define the relative energy of the m^{th} structure as

$$E_m(u) = \frac{\alpha_m^2}{E(u)}, \quad (4.5)$$

and the entropy of the spatio-temporal signal $u(t, j)$ is defined as

$$H(u) = -\frac{1}{\log N} \sum_{m=1}^N E_m(u) \log E_m(u). \quad (4.6)$$

It describes how the energy is distributed across the N_s significant structures. Signal whose energy is concentrated in a single structure such that $N_s = 1$ will have very low entropy $H(u) = 0$, or $H(u) = 1$, if the energy is distributed equally among the N_s significant structures. Further, the results will be presented in this work shows the usefulness of STE implemented by Eugene Kononov's software to study MCs.

4.2 Persistence analysis in time series

In this work the persistence analysis has been used to study IMF time series. The purpose throughout this section is to review the physical- mathematical concepts of these tools.

The main attributes of a time series include the statistical distribution of values in the signal and the autocorrelations (interpreted as the memory or persistence) between values. Positive values of autocorrelation function, $r_k = C_k/C_0$, indicate persistence while negative value indicate antipersistence. For example, if each value in a time series is chosen randomly, Gaussian white noise, all values are independent

of other values, there are no correlations and the persistence is zero. The running sum of a Gaussian white noise results in a Brownian motion. It is an example of a time series that exhibits long-range persistence, each value in the time series has a correlation with all other values. The persistence of values with respect to each other can be strong, weak, or nonexistent. A strong correlation implies a “memory” of previous values in the time series. To study the long-range persistence in time series semivariograms, rescaled-range, detrended fluctuation analysis, Fourier spectral analysis, and wavelet variance analysis could be used respectively (e.g. Malamud and Turcotte (1999)).

A statistically self-similar fractal is by definition isotropic. A formal definition of a self-similar fractal in two-dimensional xy -space is that $f(rx, ry)$ is statistically similar to $f(x, y)$, where r is a scaling factor. This result is quantified by the fractal relation $N_i \sim r_i^{-D}$ where the number of objects, N_i , and the characteristic linear dimension, r_i , are related by a power law, and the constant exponent, D , is the fractal dimension (TURCOTTE, 1997).

A statistically self-affine fractal is generally not isotropic, the x and y coordinates can scale differently. A definition of a self-affine fractal (Mandelbrot, 1983; VOSS, 1985a) in a two-dimensional xy -space is that $f(rx, r^{H_a}y)$ is statistically similar to $f(x, y)$ where the Hausdorff exponent $H_a = 2 - D$ is a constant (e.g. Malamud and Turcotte (1999)). For the special case where $H_a = 1$, the self-affine fractal is also self-similar. The classic example of a self-affine time series is a Brownian motion.

The power spectrum of a time series is the Fourier transform of the autocorrelation function. The power spectrum (PRIESTLEY, 1981), a measure of long-range persistence and antipersistence, is used frequently in the analysis of geophysical time series (e.g. Pelletier and Turcotte (1999)). A plot of power-spectral density (PSD) function $S(f)$ vs f (frequency) is known as a periodogram. For a time series that is self-affine, the power spectral density is defined (e.g. Voss (1985b)) to have a power-law dependence on frequency $S(f) \sim f^{-\beta}$. The value of β , the slope of the best-fit straight line to $\log(S(f))$ vs $\log(f)$, is a measure of the strength of persistence or antipersistence in a time series. Using a derivation from Voss (1986), we can obtain a relationship between the power β , the Hausdorff exponent H_a , and the fractal dimension D :

$$\beta = 2H_a + 1 = 5 - 2D$$

For a self-affine fractal ($0 \leq H_a \leq 1$, $1 \leq D \leq 2$), we have $1 \leq \beta \leq 3$. For a Brownian motion with $H_a = 1/2$, $D = 3/2$ we have $\beta = 2$. Although H_a , the Hausdorff exponent, is only applicable for self-affine time series from $0 \leq H_a \leq 1$, the spectral-power exponent, β , is a measure of the strength of persistence which is valid for all β , not just $1 \leq \beta \leq 3$. For self-affine time series a white noise has $\beta = 0$, an antipersistent time series has $\beta < 0$ and persistent time series has $\beta > 0$.

An alternative measure of a self-affine time series is that the semivariogram, γ_k , scale with k , the lag, such that $\gamma_k \sim k^{2H_a}$ (MANDELBROT; NESS, 1968) i.e.,

$$\gamma_k = \frac{1}{2(N-k)} \sum_{n=1}^{N-k} (y_{n+k} - y_n)^2.$$

For the uncorrelated Gaussian white noise ($\beta = 0$), the semivariogram is about $\gamma_k = 1$, the same as the variance, $V_a = 1$. For $\beta = 1, 2$, and 3 , excellent correlations are obtained with $\gamma_k \sim k^{2H_a}$, see page 40 of Malamud and Turcotte (1999).

Following Malamud and Turcotte (1999) is possible read that other alternative method to measure the persistence in time series was developed by Hurst (1951), Hurst et al. (1965). They studied the Nile River flow as a time series and introduced empirically the concept of rescaled-range (R/S) method used to calculate the scaling exponent (Hurst exponent), H_u , to give quantitative measure of the persistence of a signal. Hurst (1951), Hurst et al. (1965) found empirically that many data sets in nature satisfy the power-law relation:

$$\left[\frac{R(\tau)}{S(\tau)} \right]_{av} = \left(\frac{\tau}{2} \right)^{H_u} \quad (4.7)$$

where the successive subintervals τ varies over all N values in the time series, y_n . The running sum, y_m , of the time series, y_n , relative to its mean is:

$$y_m = \sum_{n=1}^m (y_n - \bar{y}_N). \quad (4.8)$$

The range is defined by $R_N = (y_m)_{max} - (y_m)_{min}$ with $S_N = \sigma_N$ where \bar{y}_N and σ_N are the mean and standard deviation of all N values in the time series, y_n . The R/S analysis is a statistical method to analyse long records of natural phenomena (VANOUPINES, 1995).

Following [Tapiero and Vallois \(1996\)](#) a white noise ($\beta = 0$) is a random process that has adjacent values which are uncorrelated, it is appropriate to conclude that $H_u = 0.5$ implies a time series that is uncorrelated. It follows that $0.5 < H_u \leq 1.0$ implies persistence and that $0 \leq H_u < 0.5$ implies antipersistence. This would imply that ([TAPIERO; VALLOIS, 1996; MALAMUD; TURCOTTE, 1999](#)):

$$\beta = 2H_u - 1 = 2H_a + 1 \quad (4.9)$$

The Equation 4.9 only has a small validation region, see Figure 4.2 (a) and (b) from [Malamud and Turcotte \(1999\)](#). This result should be considered when an exponent is derived from another.

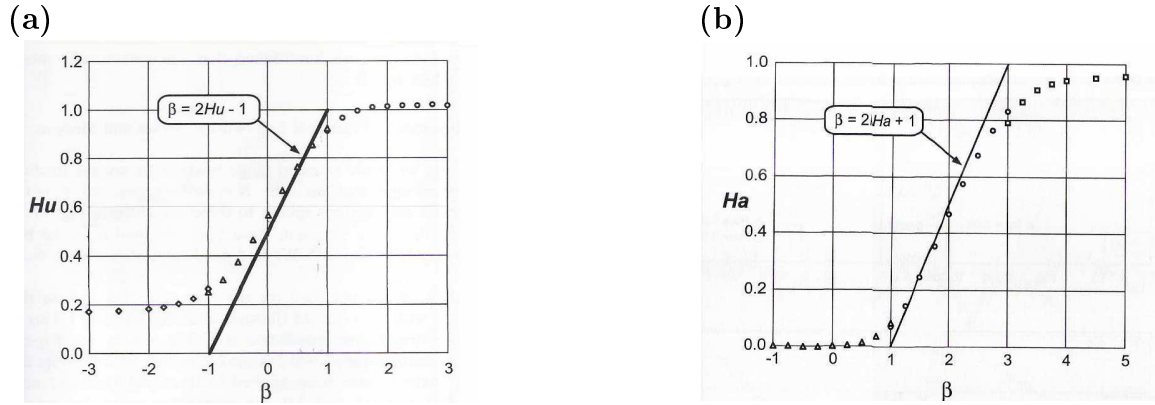


Figure 4.2 - (a): For a fractional Gaussian noises and fractional Brownian motions, β power spectrum has the range $-3 < \beta < 3$. The dependence with the Hurst exponent is not a linear function for all values. The straight-line correlation is with the relation $\beta = 2H_u - 1$. (b) is similar to (a), the dependence of the Hausdorff exponent versus β is shown.

SOURCE: [Malamud and Turcotte \(1999\)](#) (Figures 17 and 25).

The detrended fluctuation analysis (DFA) was introduced by [Peng et al. \(1994\)](#). Also this tool could be used to study persistence on IMF time series.

The fluctuation function $F(L)$ is construct over the whole signal at a range of different window size L where $F(L) \sim L^\alpha$. The obtained exponent, α , is similar to the Hurst exponent, but it also may be applied to signal whose underlying statistics (such as mean and variance) or dynamics are non-stationary. It is related to measure

based upon spectral techniques such as autocorrelation and Fourier transform. DFA measures scaling exponents from non-stationary time series for determining the statistical self-affinity of an underlying dynamical non-linear process (e.g. Veronese et al. (2011)). It is useful for characterizing temporal patterns that appear to be due to long-range memory stochastic processes. A detailed description of this method, step by step, see Peng et al. (1994), Baroni et al. (2010), Veronese et al. (2011), Little et al. (2006).

Based on the Wiener-Khinchin theorem (KAY; MARPLE, 1981), it is possible to show that the two exponents β (from PSD) and α (from DFA) are related by:

$$\beta = 2\alpha - 1. \quad (4.10)$$

For fractional Brownian motion we have $1 \leq \beta \leq 3$, and then $1 \leq \alpha \leq 2$. The exponent of the fluctuations can be classified according to a dynamic range values (KANTEHARDT et al., 2002; BASHAN et al., 2008; ZHENG et al., 2008):

- $\alpha < \frac{1}{2}$: anti-correlated, antipersistence signal.
- $\alpha \cong \frac{1}{2}$: uncorrelated, white noise, no memory.
- $\alpha > \frac{1}{2}$: long-range persistence.
- $\alpha \cong 1$: 1/f-noise or pink noise.
- $\alpha > 1$: non-stationary, random walk like, unbounded.
- $\alpha \cong \frac{3}{2}$: Brownian noise.

There are different orders of DFA. In general, DFA_n uses polynomial fits of order n (BULDYREV et al., 1995). DFA1 (used in this work) only removes constant trends in the time series. The Hurst R/S analysis also removes constants trends in the original signal and it is equivalent to DFA1. Effect of trends on DFA were studied in Hu et al. (2001) and the relation to the power spectrum method is presented in Heneghan and McDarby (2000). Veronese et al. (2011) showed that DFA method is especially useful for short records of stochastic and non-linear processes.

4.3 Wavelet Transform

The mathematical property chosen in this work is the statistical mean of the wavelet coefficients obtained by applying the Discrete Wavelet Transform (Daubechies scale filters order 2, db2). The analysis is done using the components of the IMF as recorded by the instruments of the Magnetic Field Experiment (MAG) onboard of the ACE S/C at the L1 point. Therefore, our interest is to study the wavelet coefficients behavior for diagnose of disturbance level in interval of the SW data containing the MC occurrences.

The Wavelet theory was proposed by Morlet and his collaborators in the 1980s (MORLET, 1983; GROSSMANN; MORLET, 1984; GOUPILLAUD et al., 1984). The Wavelet Transform is a modern tool with many applications: time series analysis (autocorrelation, persistence, series with gaps, etc); clean signal; image filtering and compression; numerical solution of differential equations; useful in all areas of science (JAFFARD et al., 1987; MENEVEAU, 1991; FARGE, 1992; FRICK et al., 1998; VAN DEN BERG, 2004; DOMINGUES et al., 2005; VAN YEN et al., 2010; CASTILHO et al., 2012; DOMINGUES; KAIBARA, 2012). This transform can be used in the analysis of non-stationary signals to obtain information on the frequency or scale variations of those signals and to detect their structures localization in time and/or in space. The last properties are not possible to be recognized with Fourier transform, where the presence of involved frequencies is detected.

The Discrete Wavelet Transform (DWT) is a linear multilevel efficient transform that is very popular in data compression (HUBBARD, 1997). Mathematically, this transform is built based on a multiscale tool called Multiresolution analysis $\{V^j, \Phi\} \in L^2$ proposed by S. Mallat (see details in Mallat (1989)), where Φ is a scale function, $V^j = span\{\Phi_k^j\}_{k=0, \dots, 2^{j_0-j}-1}$, and L^2 is the functional space of the integrable square functions. The DWT uses discrete values of scale (j) and position (k), where j_0 is the number of the decomposed levels.

The great contribution of wavelet theory is the characterization of complementary spaces between two embedded spaces $V^{j+1} \subset V^j$, through direct sums $V^j = V^{j+1} \oplus W^{j+1}$, where $W^j = span\{\Psi_k^j\}_{k=0, \dots, 2^{j_0-j}-1}$ with Ψ the wavelet function.

Mallat also developed an efficient and very simple way to compute this multilevel transform based on filter banks. With this tool, one can compute the so called

discrete scale coefficient c_k^j and wavelet coefficient d_k^j associate with discrete values of scale j and position k . Roughly speaking, the basic ingredients to compute one level step of this transform are the low filter (h) related to the analyzing scale function and its relation with the high-pass filter (g) related to the analyzing wavelet function. These filters are used to compute the scale coefficients and the wavelet coefficients as follows:

$$c_k^j = \sqrt{2} \sum_m h(m - 2k) c_m^{j+1} \quad (4.11)$$

and

$$d_k^j = \sqrt{2} \sum_m g(m - 2k) c_m^{j+1}. \quad (4.12)$$

The multilevel transform is done repeating recursively this procedure: convolute the scale coefficients with the filter and performing the downsampling procedure, *i.e.*, removing one data point between two. Therefore in each scale decomposition levels the number of data is reduced by two. Follows a scheme for the DWT and its inverse (IDWT),

$$\{c^{j+1}\} \begin{matrix} \xrightarrow{DWT} \\ \xleftarrow{IDWT} \end{matrix} \{c^j, d^j, d^{j-1} \dots, d^{j-j_0}\}$$

The initial data is consider the first level scale coefficient c^{j+1} .

The wavelet coefficients have the property that their amplitude are related to the local regularity of the analyzed data (DAUBECHIES, 1992; MALLAT, 1989). That means, where the data has a smooth behavior, the wavelet coefficients are smaller, and vice-versa. This is the basic idea of data compression and the application we are doing here. The wavelet coefficient amplitudes are also related to the analysing wavelet order and the scale level.

There is not a perfect wavelet choice for a certain data analysis. However, one can follow certain criteria to provide a good choice (see, for instance, Domingues et al. (2005)).

On this work, we choose the Daubechies scaling function of order 2, with the choice that the wavelet function reproduces locally a linear polynomial. On one hand, high order analyzing Daubechies functions are not adding a better local reproduction of the MC disturbance data. And on the other hand, the analyzing function of order 1 does not reproduce well these disturbances locally.

We also observe that just one decomposition level is enough for the energy analysis methodology that we propose here, it corresponds to a pseudo-period of 48 seconds. The pseudo-period is $T_a = (a\Delta)/F_c$ where $a = 2^j$ is a scale, $\Delta = 16$ s is the sampling period, $F_c = 0.6667$ is the center frequency of a wavelet in Hz (ABRY, 1997)². In Table 4.1, as a test, some decomposition levels and the Daubechies scaling function of order 1 to 4 are shown where $F_c = [0.9961, 0.6667, 0.8000, 0.7143]$. Pseudo-periods (seconds) regarding to the Daubechies orthogonal wavelets are presented. It also shows that the information here could be useful for studying fluctuations with different frequencies, not done in this work.

Table 4.1 - Pseudo-period (seconds) regarding the Daubechies orthogonal wavelets. In this work $\Delta t = 16$ s, $j = 1$ and db2 then pseudo-period is 48.0 seconds. The information here could be useful for studying fluctuations with different frequencies.

Level	Order			
j	1	2	3	4
1	32.1	48.0	40.0	44.8
2	64.3	96.0	80.0	89.6
3	128.5	192.0	160.0	179.2
4	257.0	384.0	320.0	358.4
5	514.0	768.0	640.0	716.8

The non zero values of the low filter h for Daubechies order 2 analysing wavelet are

$$[h_0, h_1, h_2, h_3] = [0.4829629131445, 0.8365163037378, \\ 0.2241438680420, -0.1294095225512]$$

and $[g_0, g_1, g_2, g_3] = [h_0, -h_1, h_2, -h_3]$ is the high-pass band filter (see page 195 in Daubechies (1992)).

The orthogonal property is very important here, because with it, we can guarantee a preserving energy property in the wavelet transform similarly to the Parseval theorem for Fourier analysis (DAUBECHIES, 1992). Therefore the total energy of the signal is equal to the superposition of the individual contributions of energy of their wavelet coefficient in each decomposition level (HOLSCHNEIDER, 1991).

²computed with scal2frq.m, <http://www.mathworks.com/help/wavelet/ref/scal2frq.html>

Example:

Let $f \in L^2$ and $j_0 = \text{Log}_2 8 = 3$ (quantity of decomposition levels), shows the decomposition using Multiresolution analysis.

The first decomposition level of f is: $V^0 = V^1 \oplus W^1$, where $V^1 = \{\Phi_0^1, \Phi_1^1, \Phi_2^1, \Phi_3^1\}$ and $W^1 = \{\Psi_0^1, \Psi_1^1, \Psi_2^1, \Psi_3^1\}$ then

$$\begin{aligned} f = & \langle f, \Phi_0^1 \rangle \Phi_0^1 + \langle f, \Phi_1^1 \rangle \Phi_1^1 + \langle f, \Phi_2^1 \rangle \Phi_2^1 + \langle f, \Phi_3^1 \rangle \Phi_3^1 + \\ & \langle f, \Psi_0^1 \rangle \Psi_0^1 + \langle f, \Psi_1^1 \rangle \Psi_1^1 + \langle f, \Psi_2^1 \rangle \Psi_2^1 + \langle f, \Psi_3^1 \rangle \Psi_3^1 \end{aligned} \quad (4.13)$$

The inner products $\langle f, \Phi_k^j \rangle = c_k^j$ are called scaling coefficients, and inner products $\langle f, \Psi_k^j \rangle = d_k^j$ are called wavelet coefficients, when is performed the decomposition by levels. Thus, the above equation could be written as

$$\begin{aligned} f = & c_0^1 \Phi_0^1 + c_1^1 \Phi_1^1 + c_2^1 \Phi_2^1 + c_3^1 \Phi_3^1 + \\ & d_0^1 \Psi_0^1 + d_1^1 \Psi_1^1 + d_2^1 \Psi_2^1 + d_3^1 \Psi_3^1 \end{aligned} \quad (4.14)$$

As described before, the wavelet coefficients at the first level used here are called as $d^1 \equiv d1$, i.e., for this case $d1 = (d_0^1, d_1^1, d_2^1, d_3^1)$.

The second decomposition level is: $V^0 = V^2 \oplus W^2 \oplus W^1$, where $V^2 = \{\Phi_0^2, \Phi_1^2\}$ and $W^2 = \{\Psi_0^2, \Psi_1^2\}$ then

$$\begin{aligned} f = & \langle f, \Phi_0^2 \rangle \Phi_0^2 + \langle f, \Phi_1^2 \rangle \Phi_1^2 + \langle f, \Psi_0^2 \rangle \Psi_0^2 + \langle f, \Psi_1^2 \rangle \Psi_1^2 + \\ & \langle f, \Psi_0^1 \rangle \Psi_0^1 + \langle f, \Psi_1^1 \rangle \Psi_1^1 + \langle f, \Psi_2^1 \rangle \Psi_2^1 + \langle f, \Psi_3^1 \rangle \Psi_3^1, \end{aligned} \quad (4.15)$$

$$\begin{aligned} f = & c_0^2 \Phi_0^2 + c_1^2 \Phi_1^2 + d_0^2 \Psi_0^2 + d_1^2 \Psi_1^2 + \\ & d_0^1 \Psi_0^1 + d_1^1 \Psi_1^1 + d_2^1 \Psi_2^1 + d_3^1 \Psi_3^1. \end{aligned} \quad (4.16)$$

And the wavelet coefficients at the second decomposition level are $d_2 = (d_0^2, d_1^2)$.

In the last decomposition level the space V^0 is more refined: $V^0 = V^3 \oplus W^3 \oplus W^2 \oplus W^1$

with $V^3 = \{\Phi_0^3\}$ and $W^3 = \{\Psi_0^3\}$:

$$f = c_0^3 \Phi_0^3 + d_0^3 \Psi_0^3 + d_0^2 \Psi_0^2 + d_1^2 \Psi_1^2 + d_0^1 \Psi_0^1 + d_1^1 \Psi_1^1 + d_2^1 \Psi_2^1 + d_3^1 \Psi_3^1. \quad (4.17)$$

The wavelet coefficient at the third decomposition level is $d_3 = (d_0^3)$.

4.4 Minimum variance analysis (MVA)

In this work, we used the local Minimum Variance Analysis (MVA) to determine the direction of rotation of the magnetic field inside the MCs and the orientation of the MC axis.

The minimum variance analysis technique (SONNERUP; CAHILL, 1967; SONNERUP; SCHEIBLE, 1998), applied to magnetic field vector measured during a spacecraft traveling in transverse orbit to transition layer, is based on an idealized onedimensional ($\partial/\partial x = \partial/\partial y = 0$) model of the layer so that only one of the three terms remains in the Cartesian expression for the divergence of \vec{B} :

$$\nabla \cdot \vec{B} = \partial \vec{B}_z / \partial z = 0. \quad (4.18)$$

In other words, \vec{B}_z is independent of z . Here (x, y, z) is a local Cartesian coordinate system unknown a priori with its z axis pointing along the sought-after vector, \hat{n} , normal to the layer. It follows from Faraday's law, $\nabla \times \vec{E} = -\partial \vec{B} / \partial t$, that the field component \vec{B}_z must also be time independent, $\partial \vec{B}_z / \partial t = 0$, in such an idealized structure so that a spacecraft traversing it would observe a strictly constant value of \vec{B}_z .

During the travel of a MC, the magnetic field vector \vec{B} is measured N times, at time t . The average of \vec{B} in the Cartesian coordinates system is:

$$\langle \vec{B} \rangle = \frac{1}{N} \sum_{i=1}^N \vec{B}^i = (\langle B_x \rangle, \langle B_y \rangle, \langle B_z \rangle) \quad (4.19)$$

with: $\vec{B}^i = (B_x^i, B_y^i, B_z^i)$.

As the estimative of $\hat{n} = (n_x, n_y, n_z)$, normal direction, the method identifies that

direction in space along which the field-component set $\{\vec{B}^{(i)} \cdot \vec{n}\}$ ($i = 1, 2, 3, \dots, N$) has minimum variance. In other words, \hat{n} is determined by minimization of variance, σ^2 :

$$\sigma^2 = \frac{1}{N} \sum_{i=1}^N (\vec{B}^i \cdot \hat{n} - \langle \vec{B} \rangle \cdot \hat{n})^2 \quad (4.20)$$

and where the minimization is subject to the normalization constraint $|\hat{n}|^2 = 1$. In mathematical optimization, the method of Lagrange multipliers (named after Joseph Louis Lagrange) provides a strategy for finding the local maximal and minimal of a function subject to equality constraints. Thus, using a Lagrange multiplier, λ , to implement this constraint, the Lagrange function (\wedge_L) is written as:

$$\wedge_L(n_x, n_y, n_z, \lambda) = \sigma^2(n_x, n_y, n_z, B_x, B_y, B_z) - \lambda(|n_x \hat{i} + n_y \hat{j} + n_z \hat{k}|^2 - 1)$$

and one then seeks the solution of the set of three homogeneous linear equation (SONNERUP; SCHEIBLE, 1998):

$$\begin{aligned} \frac{\partial}{\partial n_x} (\sigma^2 - \lambda(|\hat{n}|^2 - 1)) &= 0, \\ \frac{\partial}{\partial n_y} (\sigma^2 - \lambda(|\hat{n}|^2 - 1)) &= 0, \\ \frac{\partial}{\partial n_z} (\sigma^2 - \lambda(|\hat{n}|^2 - 1)) &= 0, \end{aligned}$$

or

$$\frac{\partial \sigma^2}{\partial n_x} = 2\lambda n_x; \quad \frac{\partial \sigma^2}{\partial n_y} = 2\lambda n_y; \quad \frac{\partial \sigma^2}{\partial n_z} = 2\lambda n_z \quad (4.21)$$

The Equation 4.20 is rewritten:

$$\sigma^2 = \frac{1}{N} \sum_{i=1}^N \left(n_x B_x^{(i)} + n_y B_y^{(i)} + n_z B_z^{(i)} - (n_x \langle B_x \rangle + n_y \langle B_y \rangle + n_z \langle B_z \rangle) \right)^2.$$

The derivative of the function σ^2 at the points n_x, n_y and n_z is given by:

$$\frac{\partial \sigma^2}{\partial n_x} = \frac{2}{N} \sum_{i=1}^N [n_x B_x^{(i)} + n_y B_y^{(i)} + n_z B_z^{(i)} - (n_x \langle B_x \rangle + n_y \langle B_y \rangle + n_z \langle B_z \rangle) (B_x^{(i)} - \langle B_x \rangle)]$$

$$\frac{\partial \sigma^2}{\partial n_y} = \frac{2}{N} \sum_{i=1}^N [n_x B_x^{(i)} + n_y B_y^{(i)} + n_z B_z^{(i)} - (n_x \langle B_x \rangle + n_y \langle B_y \rangle + n_z \langle B_z \rangle)(B_y^{(i)} - \langle B_y \rangle)]$$

$$\frac{\partial \sigma^2}{\partial n_z} = \frac{2}{N} \sum_{i=1}^N [n_x B_x^{(i)} + n_y B_y^{(i)} + n_z B_z^{(i)} - (n_x \langle B_x \rangle + n_y \langle B_y \rangle + n_z \langle B_z \rangle)(B_z^{(i)} - \langle B_z \rangle)]$$

largest where $\frac{1}{N} \sum_{i=1}^N \langle B_{x,y,z} \rangle = \langle B_{x,y,z} \rangle$ and using Equation 4.19:

$$\frac{\partial \sigma^2}{\partial n_x} = 2[(\langle B_x B_x \rangle - \langle B_x \rangle \langle B_x \rangle) n_x + (\langle B_x B_y \rangle - \langle B_x \rangle \langle B_y \rangle) n_y + (\langle B_x B_z \rangle - \langle B_x \rangle \langle B_z \rangle) n_z]$$

$$\frac{\partial \sigma^2}{\partial n_y} = 2[(\langle B_y B_x \rangle - \langle B_y \rangle \langle B_x \rangle) n_x + (\langle B_y B_y \rangle - \langle B_y \rangle \langle B_y \rangle) n_y + (\langle B_y B_z \rangle - \langle B_y \rangle \langle B_z \rangle) n_z]$$

$$\frac{\partial \sigma^2}{\partial n_z} = 2[(\langle B_z B_x \rangle - \langle B_z \rangle \langle B_x \rangle) n_x + (\langle B_z B_y \rangle - \langle B_z \rangle \langle B_y \rangle) n_y + (\langle B_z B_z \rangle - \langle B_z \rangle \langle B_z \rangle) n_z].$$

The above equations are substituted in 4.21, the resulting set of three equations can be written in matrix form as

$$\sum_{\beta=1}^3 M_{\alpha,\beta}^B n_\beta = \lambda n_\alpha \quad (4.22)$$

where the subscripts $\alpha, \beta = 1, 2, 3$ denote Cartesian components along the x, y, z system and

$$M_{\alpha,\beta}^B = (\langle B_\alpha B_\beta \rangle - \langle B_\alpha \rangle \langle B_\beta \rangle) \quad (4.23)$$

is the magnetic variance matrix. It is seen from Equation 4.22 that allowed λ values are the eigenvalues $\lambda_1, \lambda_2, \lambda_3$ (given here in order of decreasing magnitude) of $M_{\alpha,\beta}^B$. Since $M_{\alpha,\beta}^B$ is symmetric, the eigenvalues are all real and the corresponding eigenvectors, $\hat{x}_1, \hat{x}_2, \hat{x}_3$, are orthogonal.

In summary, the minimum variance analysis consists of constructing the matrix $M_{\alpha,\beta}^B$ defined by Equation 4.23 in terms of the measured field data and the Cartesian coordinate system in which the measured data are represented, and then finding the three eigenvalues λ_i , and corresponding eigenvectors \hat{x}_i , of the matrix (SONNERUP; SCHEIBLE, 1998). The eigenvector \hat{x}_3 corresponding to the smallest eigenvalue, λ_3 , is used as the estimator for the vector normal to the current sheet and λ_3 itself represents the variance of the magnetic field component along the estimated normal. The eigenvectors \hat{x}_1 and \hat{x}_2 , corresponding to maximum and intermediate variance,

are then tangential to the transition layer and the set $\{\hat{x}_1, \hat{x}_2, \hat{x}_3\}$ arranged as a right-handed orthonormal triad provides suitable basis vectors for the local coordinates (x, y, z) discussed in connection with Equation 4.18. More generally, for any measured set of vectors $\{\vec{B}^m\}$, not necessarily obtained from a spacecraft traversal of a transition layer or wave front, the eigenvector set of the variance matrix $M_{\alpha,\beta}^B$ derived from the data provides a convenient natural coordinate system in which to display and analyse the data.

The variance directions are well determined if the error criteria given by Lepping and Behannon (1980), Siscoe and Suey (1972) are satisfied (BOTHMER; SCHWENN, 1998):

$$\frac{\lambda_2}{\lambda_3} \geq 2; \quad \angle(\vec{B}_1, \vec{B}_N) \geq 30^\circ \quad (4.24)$$

The approximate error of the minimum variance direction is $\sim 10^\circ$ (BURLAGA; BEHANNON, 1982). The calculated variance directions in solar ecliptic coordinates (SEC) are (BOTHMER; SCHWENN, 1998):

$$\vartheta_k = \arctan \frac{y_k}{x_k}, \quad \Theta_k = \arctan \frac{\sqrt{x_k^2 + y_k^2}}{z_k} \text{ with: } |\hat{e}| = 1; \quad \hat{e}_k = (x_k, y_k, z_k); \quad k = 1, 2, 3.$$

Consequently, the measured components of \vec{B} in the minimum variance system are:

$$B_k^{i*} = \hat{e}_k \cdot \vec{B}^i, \quad (4.25)$$

with the following components: $B_1^* = B_x^* = B_L$ at maximum variance, $B_2^* = B_y^* = B_M$ at intermediate variance and $B_3^* = B_z^* = B_N$ at minimum variance (BOTHMER; SCHWENN, 1998). In above sentence, three notation to represent components on MVA system are used. Those notations are found in the literature, i.e. to magnetopause is used (B_L, B_M, B_N) while to MCs (B_x^*, B_y^*, B_z^*) . However, MVA model when is used during Grad-Shafranov reconstruction applied to clouds also use the notations (B_L, B_M, B_N) , it is because the model was created to study flux rope inside magnetopause.

The variance, σ^2 , of the magnetic field component along an arbitrarily chosen di-

rection, defined by the unit vector \hat{k} , say, can be written in terms of the variance matrix as (SONNERUP; SCHEIBLE, 1998):

$$\sigma^2 = \sum_{\alpha,\beta} k_\alpha M_{\alpha,\beta}^B k_\beta. \quad (4.26)$$

This result follows from Equation 4.20 with \hat{n} replaced by \hat{k} , where $k_i = \hat{k} \cdot \vec{x}_i$, $i = 1, 2, 3$. If the expression 4.26 is transformed to the eigenvector basis:

$$\sigma^2 = \lambda_1 k_1^2 + \lambda_2 k_2^2 + \lambda_3 k_3^2 \quad (4.27)$$

Then, Equation 4.27 can define a “variance space” in which the coordinates along the eigenvectors \vec{x}_1 , \vec{x}_2 , and \vec{x}_3 are $\sigma_i = \sqrt{\lambda_i} k_i$, $i = 1, 2, 3$, and in which the variance, $\sigma^2 = \sigma_1^2 + \sigma_2^2 + \sigma_3^2$, is the distance from the origin, with the normalization condition, $|\hat{k}|^2 = k_1^2 + k_2^2 + k_3^2 = 1$:

$$\frac{\sigma_1^2}{\lambda_1} + \frac{\sigma_2^2}{\lambda_2} + \frac{\sigma_3^2}{\lambda_3} = 1 \quad (4.28)$$

This expression defines the variance ellipsoid with principal-axes are $\sqrt{\lambda_1}$, $\sqrt{\lambda_2}$, and $\sqrt{\lambda_3}$ as shown in Figure 4.3.

4.5 Grad-Shafranov reconstruction of magnetic flux ropes

An alternative approach to modeling magnetic clouds came from a different direction, namely from modeling of magnetopause structures with an invariance direction (SONNERUP; GUO, 1996; HAU; SONNERUP, 1999). The Grad-Shafranov (GS) reconstruction is a data analysis tool for reconstruction of 2D equilibrium structures from the magnetic field and plasma data collected by an observing platform (SONNERUP; GUO, 1996; HAU; SONNERUP, 1999; TEH, 2007; LUI et al., 2008; MÖSTL, 2009; LUI, 2011). The spacecraft measurements are used as initial conditions and the problem can be treated as a Cauchy problem, though it is ill-posed, and can be integrated numerically. Hu and Sonnerup (2001), Hu and Sonnerup (2002) first applied this method to magnetic flux ropes and MCs in the interplanetary medium. In this section, we summarize main properties of Grad-Shafranov model. After, in Chapter 6 we used the model applied to magnetic flux ropes (HU; SONNERUP, 2001; HU;

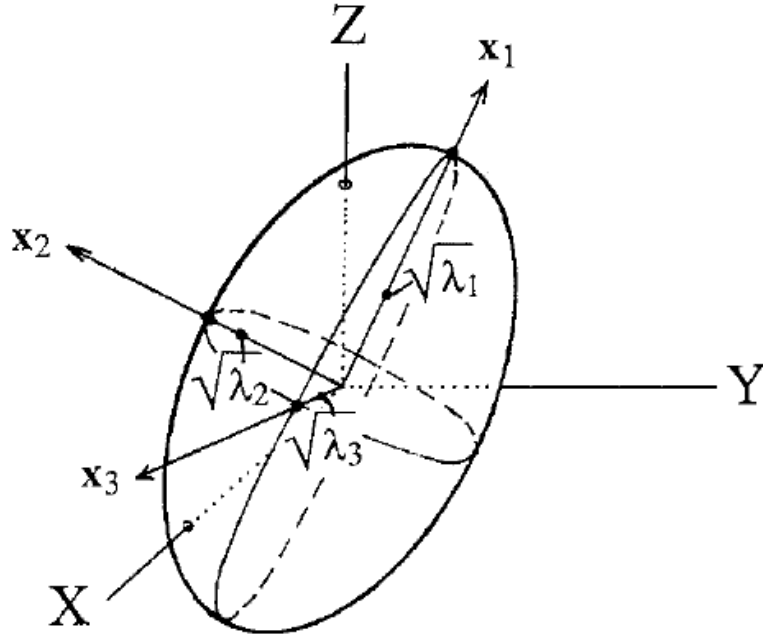


Figure 4.3 - The variance ellipsoid. Eigenvectors, $\{\hat{x}_1, \hat{x}_2, \text{ and } \hat{x}_3\}$, are shown relative to the system (X, Y, Z) (e.g., GSE) in which the magnetic data are given. The normal direction is estimated to be along \hat{x}_3 .

SOURCE: Sonnerup and Scheible (1998).

SONNERUP, 2002) to view the magnetic reconnection between two MCs.

Grad-Shafranov solver

The Grad-Shafranov Equation 2.40 can be rewritten as

$$\nabla^2 A(x, y) = -\mu_0 \frac{dP_t(x, y)}{dA(x, y)} \quad (4.29)$$

for which the transverse pressure is given by $P_t = p + B_z^2/2\mu_0$ (p is the plasma pressure), $\nabla^2 = \nabla_t^2 = \partial^2/\partial x^2 + \partial^2/\partial y^2$, and A is the magnetic vector potential. For 2D static MHD, both the pressure p and the axial field component B_z are functions of A that is constant along the field line as a result of $\vec{B} \cdot \nabla A = 0$, (e.g. Teh (2007)). We may write the second-order Taylor expansion (SONNERUP; GUO, 1996) at the y values away from the spacecraft trajectory with step $\pm\Delta y$ in the integration process.

The calculation starts at $y = 0$ (step 1):

$$A(x, \pm\Delta y) \cong A(x, 0) \pm \left(\frac{\partial A}{\partial y}\right)_{x,0} \Delta y + \frac{1}{2} \left(\frac{\partial^2 A}{\partial y^2}\right)_{x,0} (\Delta y)^2. \quad (4.30)$$

The function $A(x, \pm\Delta y)$ has been determined from the initial condition at points along the spacecraft trajectory with $y = 0$, i.e., $A(x, 0) = -\int_0^x B_y(x'', 0) dx''$, $(\partial A/\partial y)_{x,0} = B_x(x, 0)$. Also, a single-valued function $P_t(A)$ is used to fit the spacecraft data along $y = 0$, i.e., $[d(p + B_z^2/2\mu_0)/dA]_{x,0}$. The second derivative in Equation 4.30 can be evaluated from GS Equation 2.40 as (HAU; SONNERUP, 1999):

$$\left(\frac{\partial^2 A}{\partial y^2}\right)_{x,0} = -\left(\frac{\partial^2 A}{\partial x^2}\right)_{x,0} - \mu_0 \frac{dP_t(A(x, 0))}{dA}. \quad (4.31)$$

And using finite differences with central scheme, one grid point will be lost at each end of the data interval, resulting in the rhombus-shaped integration domain as was showed by Sonnerup and Guo (1996). Hau and Sonnerup (1999) extended the integration domain to a rectangular box, to do a second-order Taylor expansion for forward and backward differentiation respectively (see the development done by us in Appendix E).

$$\begin{aligned} \left(\frac{\partial^2 A}{\partial x^2}\right)_i &= \frac{2A_i - 5A_{i\pm 1} + 4A_{i\pm 2} - A_{i\pm 3}}{(\Delta x)^2} + O(\Delta x^2) \text{ (forward(+)) and backward(-)} \\ \left(\frac{\partial^2 A}{\partial x^2}\right)_i &= \frac{A_{i+1} - 2A_i + A_{i-1}}{(\Delta x)^2} + O(\Delta x^2) \text{ (central)}. \end{aligned}$$

The plot of $P_t(A)$ vs A can be fit by a third order polynomial with exponential tails; differentiate it to put of the right-hand side of the GS Equation 4.31. Thus, 4.31 is ready to put into 4.30 to calculate $A(x, \pm\Delta y)$ and start the new integration step.

But, a smoothing is done before for the solution of A at each integration step to reduce spurious results:

$$\begin{aligned} \bar{A}_1 &= \omega(y)A_1 + \frac{1}{2}(1 - \omega(y))(A_1 + A_2), \\ \bar{A}_i &= \omega(y)A_i + \frac{1}{2}(1 - \omega(y))(A_{i-1} + A_{i+1}) \text{ and} \\ \bar{A}_N &= \omega(y)A_N + \frac{1}{2}(1 - \omega(y))(A_N + A_N), \end{aligned} \quad (4.32)$$

where the subscript i denotes position along x . The weight $\omega(y)$ is a chosen function of y i.e.,

$$\omega(y) = \begin{cases} 1 & \text{for } y = 0, \\ 1 - \frac{1}{3} \left| \frac{y}{y_{max}} \right| & \text{for other,} \\ 2/3 & \text{for } y = |y_{max}|. \end{cases} \quad (4.33)$$

This approach suppresses growth at short wavelengths but does not eliminate the development of singularities associated with the longer wavelengths (HAU; SONNERUP, 1999).

The B_y values are found by $B_y(x, \pm\Delta y) = -(\partial A/\partial x)_{x, \pm\Delta y}$ using finite differences scheme (see Table E.1 (1st derivative), in Appendix E). The B_x values are obtained from the first order Taylor expansion to the next step of integration:

$$B_x(x, \pm\Delta y) \cong B_x(x, 0) \pm (\partial^2 A/\partial y^2)_{x,0} \Delta y,$$

where it is required again the Grad-Shafranov Equation 4.31.

In the step 2, $y = \pm\Delta y$,

$$A(x, \pm 2\Delta y) \cong A(x, \pm\Delta y) \pm \left(\frac{\partial A}{\partial y} \right)_{x, \pm\Delta y} \Delta y + \frac{1}{2} \left(\frac{\partial^2 A}{\partial y^2} \right)_{x, \pm\Delta y} (\Delta y)^2, \quad (4.34)$$

$$B_y(x, \pm 2\Delta y) \cong -(\partial A/\partial x)_{x \pm 2\Delta y}, \quad (4.35)$$

$$B_x(x, \pm 2\Delta y) \cong B_x(x, \pm\Delta y) \pm (\partial^2 A/\partial y^2)_{x, \pm\Delta y} \Delta y. \quad (4.36)$$

And at the step n where $y = \pm(n-1)\Delta y$:

$$A(x, \pm n\Delta y) \cong A(x, \pm(n-1)\Delta y) \pm \left(\frac{\partial A}{\partial y} \right)_{x, \pm(n-1)\Delta y} \Delta y + \frac{1}{2} \left(\frac{\partial^2 A}{\partial y^2} \right)_{x, \pm(n-1)\Delta y} (\Delta y)^2 \quad (4.37)$$

$$B_y(x, \pm n\Delta y) \cong -(\partial A/\partial x)_{x \pm n\Delta y}, \quad (4.38)$$

$$B_x(x, \pm n\Delta y) \cong B_x(x, \pm(n-1)\Delta y) \pm (\partial^2 A/\partial y^2)_{x, \pm(n-1)\Delta y} \Delta y. \quad (4.39)$$

An important topic in the reconstruction scheme is of finding the optimal invariant axis \hat{z} of the 2D structures. The structures are treated as approximately

time-independent in a frame moving with the structures, the aforementioned is deHoffmann-Teller frame (KHRABROV; SONNERUP, 1998) with constant velocity V_{HT} . The previous difficult the model implementation, because are need to do a group of tests before perform the reconstruction.

The GS equation is solved as a spatial initial value problem. According with Lui (2011) a precise determination of the optimal axis is not strictly required for Grad-Shafranov reconstruction (GSR), else the more important is that the orientation allows a reasonable fit of the observed parameters. A significant deviation from the optimal orientation for the axis of the approximate 2D structure will reveal itself as non-singular values of $P_t(x, 0)$ as a function of $A(x, 0)$ (HU; SONNERUP, 2001; HU; SONNERUP, 2002).

Therefore, if an axis can be found such that the variation along that direction is minimum and reasonable fit of the observed parameters can be obtained, then the technique can in principle reconstruct the parameters on a plane perpendicular to the least variability direction (LUI, 2011). The usefulness of GSR is its ability to reconstruct an approximate shape and extract properties of the feature outside the satellite path where no observations are available. The procedures of the reconstruction technique, as applied to the magnetopause, have been described in detail by Hau and Sonnerup (1999). For magnetopause applications the vector normal to the magnetopause current layer is approximated by $\hat{n} = \hat{x}_3$ (minimum variance eigenvector). For magnetic flux rope (clouds) the determination of the invariant axis can be obtained from MVA on measured (HU; SONNERUP, 2002).

We check out the code with one test case given by Hau and Sonnerup (1999), in their Figures 4, 5 and 6 respectively. We show details that were not addressed in the aforementioned article. This is a contribution of this thesis, see Appendix D. Using kinetic theory can be obtained some analytical solutions of Grad-Shafranov equation, it is show in Appendix C. Also, we studied a benchmark case and improved numerical resolution, see Appendix C, Section C.2. Thus, we join in this manuscript, all theoretical aspects in relationship with the GSR. Because in the literatures it are scattered, e.g., it was very difficult to find how to obtain analytical solution of Grad-Shafranov equation, now in Appendix C is shown.

Physical considerations in the reconstruction of magnetic flux rope in the solar wind

The pioneer studies about this technique has been developed from 1996 to 2000 (SONNERUP; GUO, 1996; HAU; SONNERUP, 1999; HU; SONNERUP, 2000) and has been applied to recovering two-dimensional (2-D) coherent magnetohydrostatic structures from spacecraft data (AMPTE/IRM and UKS) inside of magnetopause. Another candidate for application of the reconstruction techniques was the magnetic flux rope. The first paper written with this purpose has been published by Hu and Sonnerup (2001). A second paper was published by the same authors one year later (HU; SONNERUP, 2002). The previous manuscripts are the core of the GSR of magnetic flux rope in the solar wind. To explain physical considerations in the reconstruction of magnetic flux rope in the solar wind, the earlies manuscripts are followed.

Details of the reconstruction techniques employed by Hu and Sonnerup (2001), Hu and Sonnerup (2002) are the same described in Hau and Sonnerup (1999). In this thesis, the above has been explained in Appendices C and D.

In summary, the numerical method is straightforward: an explicit numerical GS solver is applied to compute the value of the vector potential, A , in a rectangular domain. Taylor expansion and the GS Equation 4.31 are used to step away from the projected spacecraft trajectory, located at $y = 0$, where the spacecraft data provide initial values. A proper frame of reference, usually the deHoffmann-Teller (HT) frame, moving with constant frame velocity, V_{HT} (KHRABROV; SONNERUP, 1998), is obtained in advance. By use of $x = -(\vec{V}_{HT} \cdot \hat{x})t$, time can then be converted to distance along the x axis. The final output of the the technique is a contour plot of recovered transverse field lines in a rectangular domain surrounding the spacecraft trajectory, together with the distributions of axial field, axial current density, plasma pressure, etc.

Hu and Sonnerup (2001) used the Lundquist solution 6.1 to evaluate the performance of the numerical GS solver and to discuss how the function $P_t(A)$ behaves with the correct z axis. The magnetic vector potential for this geometry is $A = B_A/\alpha$, which satisfies the GS Equation 4.31, $\nabla_t^2 = -\alpha^2 A$, with $P_t(A) = \alpha^2 A^2/2\mu_0$. They compared numerical and exact solution to the model GS equation (on a 21×101 uniform grid), $\nabla_t^2 = -\alpha^2 A$ for $\alpha L_0 = 0.4$ (L_0 is the length normalization). Also, they showed that an axial symmetric flux rope centered at $(x_0, y_0) = (0.2L_0, 0.5L_0)$ is well recovered.

With the correct z axis, the plot of $P_t(A)$ is a single valued curve (a parabola): as the spacecraft moves toward the center of the flux rope, the data samples move along the curve in one direction and then move back the opposite way on the same curve after the spacecraft passes the point of closest approach. The invariant axis is therefore determined by searching for optimal single-branch behavior of $P_t(A)$. In detail, the invariant axis direction, \hat{z} , is initially set to be the intermediate variance direction, \hat{x}_2 , obtained from minimum-variance analysis of the measured magnetic field vectors (SONNERUP; SCHEIBLE, 1998). In a process of trial and error, it is then tilted away from \hat{x}_2 . In each trial, a single-valued function $P_t(A)$ is used to fit the spacecraft data along $y = 0$. The optimal invariant axis is that for which the fitting residual for $P_t(A)$ is minimized. The intermediate variance direction is used as the initial guess for \hat{x} because, for small “impact parameters”, y_0 , Lepping et al. (1990) found the axis of their cylindrically symmetric flux rope to be near the \hat{x}'_2 direction, obtained from application of MVA to magnetic vectors normalized to unit magnitude (HU; SONNERUP, 2001). The previous idea was extended by Hu and Sonnerup (2002) and it is shown in Appendix C, Section C.4.

The following are the steps of the numerical reconstruction technique:

- 1) Select a specific time interval of interest. The data needed are as follows: the GSE components of the magnetic field (B_X, B_Y, B_Z); the plasma bulk velocity (V_X, V_Y, V_Z); the plasma number density, $N_i = N_e = N$, and the isotropic temperatures T_i and T_e . From these quantities an isotropic plasma pressure, $p = Nk(T_i + T_e)$, is calculate.
- 2) Perform minimum variance analysis on the measured magnetic field vectors $\vec{B}^{(m)}$, ($m = 1, 2, \dots, M$) (SONNERUP; CAHILL, 1967; SONNERUP; SCHEIBLE, 1998). The normalized eigenvectors, $\hat{x}_1, \hat{x}_2, \hat{x}_3$, corresponding to the eigenvalues of the magnetic variance matrix, $\lambda_1, \lambda_2, \lambda_3$ (in descending order), form a right-handed, orthogonal coordinate system.
- 3) Determine the optimal HT frame velocity, \vec{V}_{HT} , from measured plasma flow velocities, $\vec{v}^{(m)}$ and magnetic fields $\vec{B}^{(m)}$, ($m = 1, 2, \dots, M$) (SONNERUP et al., 1987; KHRABROV; SONNERUP, 1998); by minimizing the residual electric field, $\vec{E}'^{(m)}$, in a frame moving with unknown velocity \vec{V} . A constant vector \vec{V}_{HT} will be used initially, but a time-varying frame velocity, $\vec{V}_{HT}(t) = \vec{V}_{HT0} + \vec{a}_{HT}t$, with constant acceleration vector, \vec{a}_{HT} , is also obtained. The quality of an HT frame

can be assessed by the correlation coefficient, cc , between the components of $-\vec{v}^{(m)} \times \vec{B}^{(m)}$ and the corresponding components of $\vec{V}_{HT} \times \vec{B}^{(m)}$ (KHRABROV; SONNERUP, 1998).

- 4) Determine the reconstruction frame, (x, y, z) . For flux rope applications, first determine the optimal z axis as discussed in Appendix C, Section C.4. The x axis is along the projection of \vec{V}_{HT} onto the plane perpendicular to \hat{z} ; that is, it is along the projected spacecraft trajectory relative to the flux rope. Because of the invariance of the structure in the \hat{z} direction, the spacecraft measurements are known along the x axis. The y axis completes the right-handed orthogonal triad.
- 5) Obtain the value $A(x,0)$ from Equation 2.29 by integration of the measured B_y values along the x axis ($y = 0$):

$$A(x, 0) = \int_0^x \frac{\partial A}{\partial x''} dx'' = \int_0^x -B_y(x'', 0) dx''. \quad (4.40)$$

The data are resampled to a uniform grid along the x axis prior to the integration in Equation 4.40. A scatter plot of the transverse pressure $P_t(x, 0) = [p(x, 0) + B_z^2(x, 0)/2\mu_0]$ versus $A(x, 0)$ is prepared.

- 6) Use a combination of polynomials and/or exponentials to construct a function $P_t(A)$ that is optimally fitted to the data pairs $P_t(x_i, 0)$ and $A(x_i, 0)$ generated in Step 5. Optimal fitting is achieved by minimizing $\sum_i [P_t(x_i, 0) - P_t(A(x_i, 0))]^2$, where the integer i denotes individual values. The resulting function $P_t(A)$ is then differentiated to obtain the right-hand side of the GS Equation 4.37.
- 7) Solve the GS equation, using the numerical GS solver, to reconstruct the transverse magnetic field map, i.e., the contour plot of $A(x, y)$ in a rectangular domain. The axial field distribution, B_z , can be obtained by evaluating a fitting function $B_z(A)$ of the measured $B_z(x, 0)$ versus $A(x, 0)$, over the whole domain.

The numerical GS solver employed in this thesis is the same as that given by (HAU; SONNERUP, 1999), as shown in the beginning of this section.

4.6 Detection of current sheets

With a time series of magnetic field dataset $B(t)$ measurement by a single spacecraft current sheets could be detected. Li (2008) developed a systematic method to search

current-sheet-like structures in the solar wind. Recently, the method was used with success to search for current sheets at the leading edge of an ICME event of 21 January 2005, based on the Cluster magnetic field data. Chian and Muñoz (2011), Muñoz (2011) reported the observational evidence of two magnetically reconnected current sheets in the vicinity of a front magnetic cloud boundary layer.

In the method, angles (θ) between the vectors $B(t)$ and $B(t + \tau)$ in a window of width 2τ are calculated. The probability density within the interval θ and $\theta + \Delta\theta$ can be computed directly from magnetic field measurements as

$$f(\theta, \tau)\Delta\theta = \frac{N^\tau(\theta < \theta' < \theta + \Delta\theta)}{N^\tau(\theta < \theta' < \pi)} \quad (4.41)$$

where $N^\tau(\theta < \theta' < \theta + \Delta\theta)$ is the number of measurement pairs where the angle large than θ . The integrated distribution function is defined as

$$F(\theta, \tau) = \int_{\theta}^{\pi} f(\theta')d\theta', \quad (4.42)$$

representing the frequency of having the measured angle large than θ . If the quantity $F(\theta, \tau)$ shall scale linearly with the time separation τ when θ is larger than some critical angle θ_0 then there are current sheets associated with the magnetic field time series, i. e.,

$$F(\theta, N\tau) \sim NF(\theta, \tau) \text{ when } \theta > \theta_0. \quad (4.43)$$

If the majority ($> 60\%$) of the angles between $B(t)$ and $B(t + \tau)$ in a window of size 2τ centered at time T are greater than θ , then a current sheet is located.

4.7 Reconstruction tool

We had access to a program package in MATLAB that are based on those used by Qiang Hu for his 2002 JGR paper (HU; SONNERUP, 2002) which were part of the PhD Thesis at Dartmouth University. These programs were upgraded in a graphical user interface (GUI) by Christian Möstl during his PhD thesis ³ (Space Research Institute, Graz, Austria, Finished in 2009). The program read merged plasma and magnetic field data from ACE satellite obtained from ftp://nssdcftp.gsfc.nasa.gov/spacecraft_data/ace/4_min_merged_mag_plasma/. The data are converts to a proper format which can be read by the reconstruction

³http://www.uni-graz.at/~moestlc/moestl_thesis.pdf

programs (see Annex B).

4.8 Summary of techniques

In Table 4.2 is a summary of techniques that were studied. In each column is show the name of the technique, the characteristics and how could be used to identify and characterize interplanetary magnetic clouds at 1 AU.

Table 4.2 - Summary of techniques that are using in this work.

Techniques	Characteristics	Purpose of use
Spatio-temporal entropy	This quantity compares the distribution of distances between all pairs of vectors in the reconstructed state space with that of distances between different orbits evolving in time. The result is normalized and presented as a percentage of “maximum” entropy.	To identify cloud candidates i.e., the magnetic structures highly organized.
Persistence exponents	Positive values of autocorrelation function indicate persistence while negative value indicate antipersistence. A strong correlation implies a “memory” of previous values in the time series.	MCs have simple flux rope-like magnetic fields and magnetic field values are autocorrelated (higher “memory”). The exponents could be used to identify MC candidates.
Discrete Wavelet Transform	One can compute the so called discrete scale coefficient c_k^j and wavelet coefficient d_k^j associate with discrete values of scale j and position k . The wavelet coefficients have the property that their amplitude are related to the local regularity of the analyzed data.	A <i>zoom in</i> made in the magnetic fluctuations could be used as an auxiliary tool to identifying boundaries (with human help) in the SW.
Minimum Variance Analysis	It consists of constructing the matrix $M_{\alpha,\beta}^B$ defined by Equation 4.23 in terms of the measured field data and the Cartesian coordinate system in which the measured data are represented, and then finding the three eigenvalues λ_i , and corresponding eigenvectors \vec{x}_i , of the matrix.	It is used to determine the direction of rotation of the magnetic field inside the MCs and the MC axis orientation.
Grad-Shafranov reconstruction	The spacecraft measurements are used as initial conditions and the problem can be treated as a Cauchy problem, though it is ill-posed, and can be integrated numerically.	It is a data analysis tool for reconstruction of 2D equilibrium structures from the magnetic field and plasma data collected by an observing platform.
Detection of current sheets	Angles (θ) between the vectors $B(t)$ and $B(t + \tau)$ in a window of width 2τ are calculated. If θ is larger than some critical angle θ_0 then there are current sheets associated with the magnetic field time series.	To find current sheets inside of double flux-rope magnetic cloud observed by ACE spacecraft.

5 METHODOLOGY

In the earlier text, theoretical aspects of the physical question and the techniques of analyses were described. First of all, as part of a new approach that is proposed, a characterization in order to understand better the phenomenon under analysis is required. Then as a second step, the complete set of techniques to analyze the MC events is used, mainly the identification of its occurrence. In this part, we are dealing with MCs identified by other authors to create a methodology of analysis, and demonstrate the usefulness of it as a significant tool for identification and characterization of MCs. This work reaches also the studies on magnetic reconnection and identification of related current sheets.

5.1 Characterization

The STE calculation is basis for MC identification. As consequence, some tests are conducted to verify the behavior of this technique in relationship with the features that exist in the interplanetary medium, and mainly in MCs. Some dataset conditions are examined. In a complementary way, the analyses of persistence in those kinds of data are relevant to classify regimes existing in the solar wind. Completing this initial set of techniques, the wavelet analysis by means of its mathematical features has a skill to characterize the magnetically quiescent and non quiescent regime of the IMF.

5.1.1 Basic tests on STE analysis aiming to MC analysis

From an intuitive point of view, a time series is said to be stationary if there is no systematic change in its mean value (no trend) and no systematic change in variance and if strictly periodic variations have been removed (CHARTFIELD, 2003). Trend estimation is a statistical technique that could be aid in the interpretation of data (CHARTFIELD, 2003). When a time series related to measurements of a process are treated, trend estimation can be used to make and justify statements about tendencies in the data. Given a set of data and the desire to produce some kind of function fitted through of those data the simplest function to fit is a straight line. Once it has been decided to fit a straight line, there are various ways to do that, but the most usual choice is a least-squares fit. If there is no global trend in time series the angle (“trend angle”) between the straight line and the positive x axis must be zero.

In Table 5.1 in the five columns are shown: time series data file included in VRA version 4.7; these time series are rotated about the origin with angles of 0 rad, -0.01 rad, 0.01 rad and 0.0175 rad respectively; and it calculated the STE of each temporal series. Figure 5.1 shows a time series plot of Lorenz data file included in VRA software. We gave trends to the series through angular rotations about the origin. The results were included in row 2 presented in Table 5.1. The effects of the trends in every series related with STE values are quantified. We follow the same idea, to cause a trend in time series for another cases, Sine and White Noise data file also included in VRA software. The results were included in rows 3 and 4 in Table 5.1. For periodic time series (sine data file) the value of STE is always zero independently from the increasing trend. For the other two cases, if time series trend increases then the entropy value decreases (see row 2 and 4 in Table 5.1). We are doing these test because we know that inside MCs increase the trend of IMF components; and we are interested in knowing how it could affect STE values.

Table 5.1 - STE values related to trends for three time series with data file included in VRA 4.7.

Series	$\theta = 0$ rad	$\theta = -0.01$ rad	$\theta = 0.01$ rad	$\theta = 0.0175$ rad
STE(Lorenz)	73%	30%	29%	0%
STE(Sine)	0%	0%	0%	0%
STE(White Noise)	80%	34%	34%	3%

To continue with the above idea is good know that: the time series of the first difference is often enough to convert series with a trend into a stationary time series. The first-order differences of time series values $x_1, x_2, x_3, \dots, x_N$ are given by a new series y_1, y_2, \dots, y_{N-1} , where $y_{N-1} = x_N - x_{N-1}$. The operation $y_t = x_t - x_{t-1} = \nabla x_t$ is called the first difference and ∇ is the difference operator (CHARTFIELD, 2003).

Our interest is to study variations in the STE values when a first-order differences are applied on stationary time series. In the previously studied time series (Lorenz, Sine and White Noise data file included in VRA), we constructed time series of the first-order differences. After that, we calculated STE values of each time series and the results were compared with the original series (no differences) shown in Table 5.2. The STE values are similar in both of them, *i.e.*, for transformed (first-order differences) and untransformed time series. Thus, when the time series has no trend,

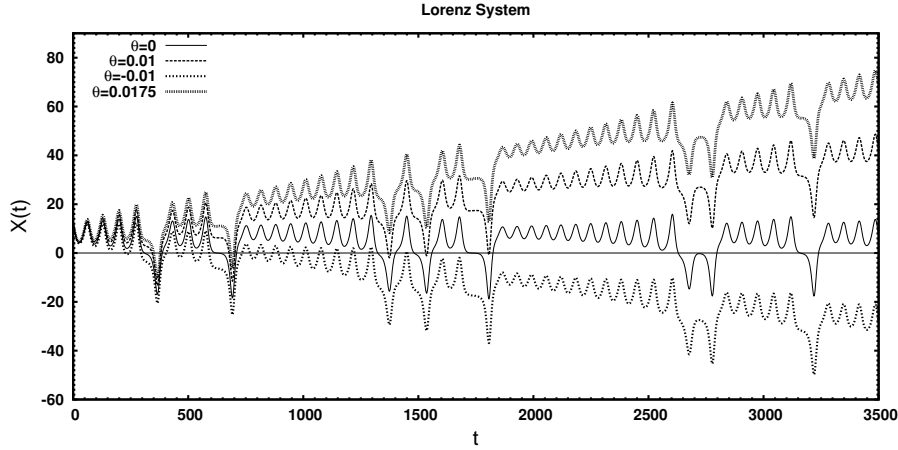


Figure 5.1 - Time series plot of Lorenz data file included in VRA (case with $\theta = 0$). Three time series rotated about origin ($\theta = -0.01$ rad , $\theta = 0.01$ rad , $\theta = 0.0175$ rad) were plotted. After that, we calculate the STE of each series.

the non-linear delicate structures are not destroyed.

Table 5.2 - STE values related to the first-order differences in time series.

Series	Untransformed	first-order differences
STE(Lorenz)	73%	75%
STE(Sine)	0%	0%
STE(White Noise)	80%	82%

The STE value is low and may tend to zero in any time series with trend. If there is a trend in the time series, you might want to consider removing it by differencing the original time series before calculating the STE. Keep in mind, however, that taking the first differences may destroy the delicate nonlinear structure in the time series (if there is any). Thus STE values are calculated on the untransformed series and then in the transformed series, where the first-order differences is applied. This is done on a trial basis after calculating STE values of the original series.

The calculation of the STE with the VRA software, version 4.7, can not be made in time series with sizes greater than ~ 4500 points because the STE has a rapid decrease to zero. It seems to be a limitation of the software by some reason not explained in its tutorial. When using the VRA software someone must take into

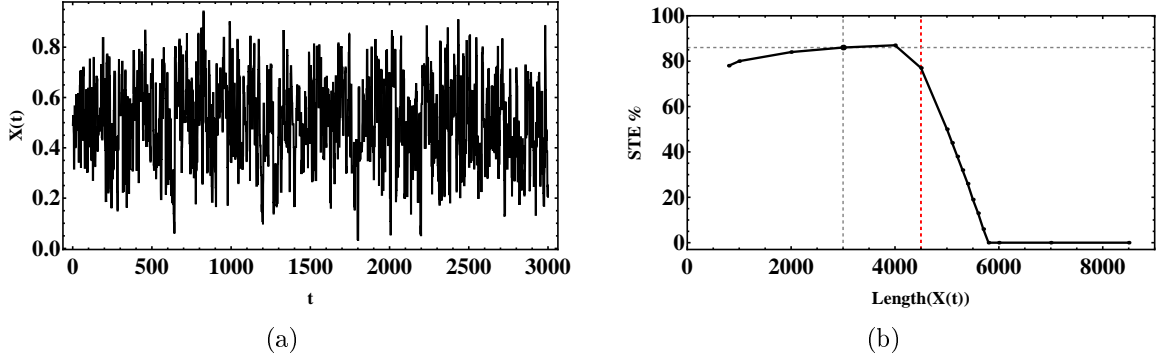


Figure 5.2 - (a) $X(t)$ vs t is plotted, where $X(t)$ is a synthetic series created using a random number generator producing values in the range 0 to 1. To show the graph, a simple moving average is applied. The time series of random number has a recurrence plot similar to shown in Figure 4.1 (right panel) and STE value of this time series is $\sim 80\%$. (b) The STE values versus $\text{length}(X(t))$ of time series constructed. These values decrease in time series with a length greater than ~ 4500 points. The software should be used from zero to red vertical line.

account this identified limitation in the extension (length) of the data under analysis. To exemplify the previous statement, synthetic time series were created using a random number generator (RNG) producing values in the range 0 to 1. In the Figure 5.2(a), an example with 3000 points was shown. In this time series a STE value of 86% was calculated. The Figure 5.2(b) show the plot of STE values versus $\text{length}(X(t))$ of 18 time series constructed as shown in 5.2(a).

As someone can notice now, the main features of the interplanetary magnetic dataset have been taken into account here with those set of test cases.

5.1.2 Calculation of persistence in the regions of an ICME

To calculate the persistence exponents were used the following computational programs:

- a) If we installed Octave in Ubuntu, a computer operating system based on the Debian distribution and distributed as free and open source software, then a *hurst(x)* function is created for example in */usr/share/octave/3.0.1/m/signal/*. This function to calculate the Hurst exponent (H_u), is used in this thesis. In Appendix B this function is shown.

Following the work of Malamud and Turcotte (1999) another implementation was done by us (see Appendix B). With the aforementioned implementation, the results to calculate the hurst exponent are different, but this problem is discussed by Mielniczuk and Wojdylo (2007). With the hurst function provided by GNU/Octave the results are more consistent, e.g. the values are greater inside MC. In future works, a comparative study is suggested to explain in detail the difference between these results.

- b) An alternative way to measure long-range correlation, which is valid for both stationary and nonstationary time series, is the semivariogram γ . Following the work of Malamud and Turcotte (1999), we done a program in GNU/Octave to calculate the Hausdorff exponent (see Appendix B). This program is used in this thesis.
- c) Power spectral analyses are first used to examine the long-range persistence (long memory) of values in the time domain. One way of defining long-range persistence is if the power spectral density, $S(f)$, is proportional to the frequency, f , raised to the power-beta. To calculate the β -exponent a program in Octave done by McSharry and Malamud (2005) is used (see Appendix B). We understand that in non-stationary time series the Fourier transform is not suitable, because the core functions of the transform is composed of sines and cosines.
- d) A fast Matlab implementation¹ of the DFA algorithm was performed by Little et al. (2006) and we use it in this document.

The behavior of the persistence in time series of the IMF components, measured by the ACE spacecraft with a time resolution of 16 s, is explored. We studied the persistence between time series corresponding to sheaths, MCs and a quiet SW after the MC with equivalent time duration to it. We calculate one exponent of persistence (e.g., α , β , H_u , H_a) over each of three windows. For example, we calculate the persistence for event number 1 in Table A.1 (Annex A), correspond to the solar wind temporal window January 06 – 09, 1998. The interval from January 06, 13 : 19 to January 07, 02 : 59 was classified as sheath. We calculate in the sheath the exponents of persistence to B_x component, the values were $\alpha = 1.27$, $\beta = 1.71$, $H_u = 0.86$, $H_a = 0.31$, respectively. The intervals from January 07, 03 : 00 to January 08,

¹<http://www.maxlittle.net/software/>

Table 5.3 - We calculate the persistence in the IMF components by four different method: β exponent of power spectrum, α exponent of DFA, Hurst of R/S analysis and Hausdorff H_a exponent of semivariogram respectively. The interval from January 06, 13 : 19 to January 07, 02 : 59 1998 was classified as sheath. The intervals January 07, 03 : 00 to January 08, 09 : 00 and from January 08, 09 : 01 to January 09, 15 : 00 were classified as MC and solar wind after the MC respectively. Dates are shown in Table A.1, event No. 1.

Event No. 1	α	β	H_u	H_a
B_x :				
<i>Sheath</i>	1.27	1.71	0.86	0.31
<i>Magnetic Cloud</i>	1.41	1.60	0.89	0.31
<i>After Magnetic Cloud</i>	1.31	1.70	0.87	0.31
B_y :				
<i>Sheath</i>	1.34	1.68	0.87	0.27
<i>Magnetic Cloud</i>	1.52	1.55	0.91	0.42
<i>After Magnetic Cloud</i>	1.37	1.65	0.88	0.31
B_z :				
<i>Sheath</i>	1.39	1.65	0.85	0.31
<i>Magnetic Cloud</i>	1.45	1.75	0.90	0.36
<i>After Magnetic Cloud</i>	1.23	1.64	0.86	0.23
Mean Values:				
	$\langle\alpha\rangle$	$\langle\beta\rangle$	$\langle H_u\rangle$	$\langle H_a\rangle$
<i>Sheath</i>	1.33 ± 0.06	1.68 ± 0.03	0.86 ± 0.01	0.30 ± 0.02
<i>Magnetic Cloud</i>	1.46 ± 0.06	1.64 ± 0.11	0.90 ± 0.01	0.37 ± 0.05
<i>After Magnetic Cloud</i>	1.30 ± 0.07	1.66 ± 0.04	0.87 ± 0.01	0.28 ± 0.05

09 : 00, and from January 08, 09 : 01 to January 09, 15 : 00 were classified as MC and solar wind after the MC respectively. We calculate the exponents of persistence to B_x component and shown in Table 5.3 rows 4 and 5 respectively. We extend these calculations for the others two components (B_y and B_z) and shown the results in the Table 5.3 rows 6-13.

MCs exhibit flux-rope characteristics: a large-scale winding of a closed magnetic structure that is nearly force-free. And it is possible to see anisotropy of magnetic field fluctuations in an average interplanetary MC at 1 AU (NAROCK; LEPPING, 2007). We do not expect to find the same behavior in all three components by the

existence of anisotropy. The anisotropic behavior, in our opinion, is caused by the geometry of flux-rope and the axis inclination angle. We have interest in a single value to characterize the persistence in the IMF, for this reason we calculated the mean value, using all three components. It is the only form that we found to quantify the persistence in all structure and to minimize the anisotropy in the calculation. This is, for example:

$$\langle \alpha_{sheath} \rangle = \frac{1}{3} \sum_{i=1}^3 \alpha_{sheath}^{(i)}. \quad (5.1)$$

The angle brackets $\langle \dots \rangle$ denote an average of the IMF components ($i = 1, 2, 3 = B_x, B_y, B_z$), also the standard deviation is calculated. We show this calculation in the Table 5.3, $\langle \alpha_{sheath} \rangle = 1.33 \pm 0.06$. In the last three rows of Table 5.3 the remaining calculations of mean and standard deviation values for all persistence exponents are shown. In Table 5.3, as we thought, the persistence values increases inside the MC. The above idea is not always true when using the spectral-power β -exponent. But two of the main problems in using a discrete Fourier transform are spectral variance and leakage (PRIESTLEY, 1981; PERCIVAL; WALDEN, 1993). This show a range of uncertainty in the values of β , as in our case. Other problem is the nonstationarity of the IMF components. The previous study was generalized for a group of 41 events shown in Table A.1; and will be discussed in Chapter 6, Section 6.1.

5.1.3 Wavelet coefficients for solar wind analysis

As used in this work, a methodology is presented to help the solar/heliospheric physics community efforts to deal with the MCs. The wavelet analysis has important advantages, adding resources to other classical mathematical tools, that could be used to study solar wind fluctuations. The wavelet coefficients allow finding fluctuations with pseudo-frequencies corresponding to the scales given by j , the chosen wavelet function, and the sampling period. The idea is to associate with a given wavelet a purely periodic signal of frequency F_c . The frequency maximizing the fast Fourier Transform (FFT) of the wavelet modulus is F_c . It allows the plotting of the wavelet with the associated approximation based on the center frequency. Thus, the center frequency based approximation captures the main wavelet oscillations. So the center frequency is a convenient and simple characterization of the leading dominant frequency of the wavelet (ABRY, 1997).

As we are interested in studying fluctuations with larger frequencies (in this case

on data from 16-second time resolution), the Daubechies function db2 with one decomposition level seems proper to be used. A zooming in analyzing the IMF fluctuations with a pseudo-period of 48 seconds could help to locate better the MC boundaries. A statistical study has to be performed. For this reason, three regions from 41 ICMEs will be studied, *i.e.* plasma sheath, magnetic cloud, and region after the MC.

In the characterization of a solar wind disturbance, we perform one decomposition level, and we compute the square of wavelet coefficients (d^1 or $d1$) (energy content on that level), as in Mendes da Costa et al. (2011), Mendes et al. (2005), and its mean value D_{d1} .

$$D_{d1} = \frac{\sum_{i=1}^{N/2} d1_i^2}{N/2}, \text{ where } N = \text{length}(\mathbf{y}). \quad (5.2)$$

Also an average value ($\langle D_{d1} \rangle$) of wavelet coefficient D_{d1} in the three magnetic field components are calculated.

$$\langle D_{d1} \rangle = \frac{1}{3} \sum_{i=1}^3 D_{d1}^{(i)}, \quad (5.3)$$

where the angle brackets $\langle \dots \rangle$ denote an average of the D_{d1} in IMF components ($i = 1, 2, 3 = B_x, B_y, B_z$).

As the dynamics features of the physical problem of our interest, *i.e.* the occurrence of the MC, are recorded in the IMF, we study time series of IMF B_x, B_y, B_z components measured by the ACE spacecraft. The treatment procedure is able to characterize regular/non regular behavior existing in experimental data to identify in an objective basis the transition between regions with these two primary behaviors. The solar wind time interval is separated in three new time intervals (windows) corresponding to the preceding sheath or pre-MC, the MC itself, and the SW after the MC or post-MC. The methodology is established.

The criteria to select the data window after the MC has not physic justification. Each post-MC region was selected with the same length of the cloud regions. The mains efforts is to study solar wind data interval containing the ICMEs, where a shock event and cloud region were reported. Someone can be aware that arbitrary selection of post-MC region could affect the results, because this region could be

disturbed by other process not related with the MC itself. However, the natural physics of the system should not avoid tests of the proposed methodology. Further analyses of complicated events can indeed help to understand the true processes occurring in the interplanetary medium. In an evident way, to show the behavior in the different regions is valuable, because only then will be possible to justify that wavelet coefficients may help to find boundaries. A “zoom in” treatment in the fluctuations from variables with random variations (i.e., IMF) could help to separate disturbance process, i.e., the cloud candidate originated from an ICME. The hypothesis is that wavelet coefficients help to identify boundaries in the SW data, specifically the shock wave and the leading edge of ICMEs.

5.2 Identification

Based on all earlier considerations, a methodology has been structured in order to allows identifying and characterizing MC events. Figure 5.3 presents the diagram of the analyses that are presented as follows.

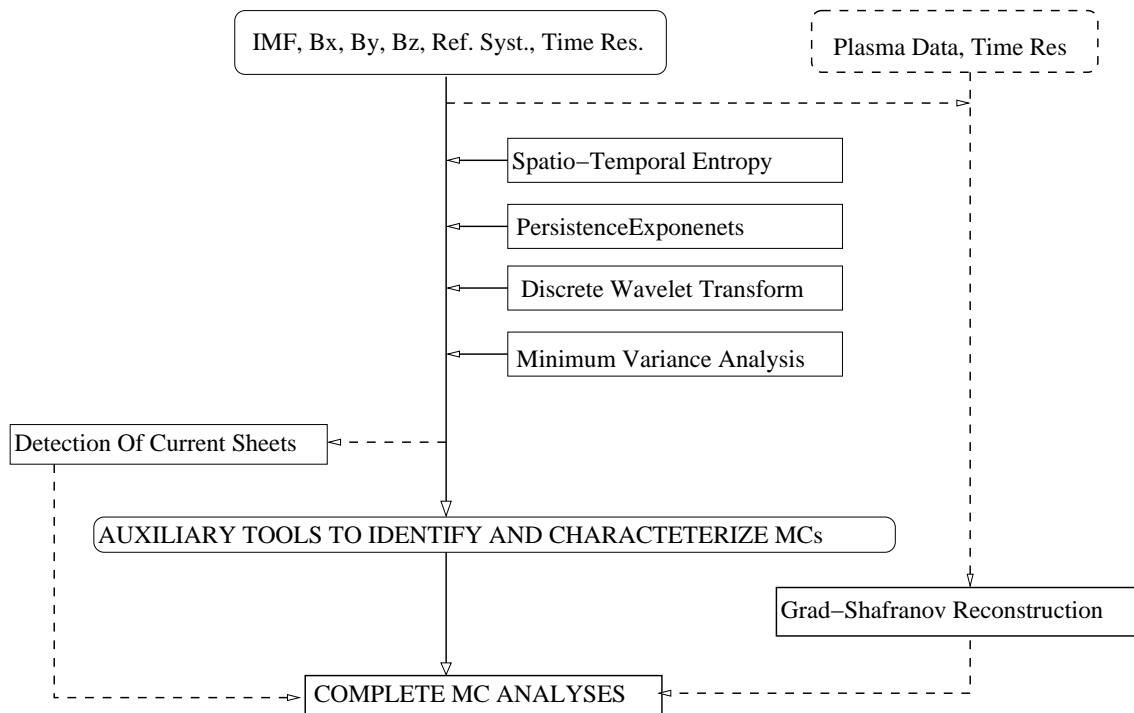


Figure 5.3 - Scheme to explain as the techniques are used.

As represented in the scheme, the IMF dataset is evaluated by STE technique com-

posing together other resources a mathematical tool for studies on MCs. Using STE, the flux rope related to MCs are identified by an easy and quick computational procedure at about 1 AU. The main advantage of the approach proposed is that it takes only the IMF data to identify the flux rope-like associated to the cloud. Nevertheless, this STE method does not solve the problem of identifying the boundaries of the clouds. The boundaries can be delimited with MVA technique, as shown by [Huttunen et al. \(2005, and references therein\)](#). Adding information with this intention, the persistence analysis and DWT analysis are also used. In order to test and validate this identification methodology, MCs identified by other authors are used here. The methodology uses mainly mathematical criteria from the nonlinear dynamics techniques to identify MCs in the solar wind. When available (condition not fulfilled in many cases), the solar plasmas data allows the reconstruction of MC flux-rope configuration aiming to obtain the most complete MC characterization.

5.2.1 Methodology for analysis using an entropy index

As was explain in Section 3.4, we decided to study in more details the STE variations taking into account some days before and after of a MC to a total of 10 days.

The bases for the procedure of identification of MC candidates using only the IMF data are presented. Although its simplicity, the approach shows an effective analysis with little computational efforts. This numerical tool can indeed help the specialist, that develops a visual inspection, by allowing a pre-selection of candidate cases.

Idea and calculations

The Recurrence Plot is a relatively recent technique for the qualitative assessment of time series ([ECKMANN et al., 1987](#)). With this technique, someone can detect hidden patterns and structural changes in data or evaluate similarities in patterns across the time series under analysis using graphical representation. The fundamental assumption underlying the idea is that an observable time series (a sequence of observations) is the manifestation of some dynamic process. It has been proved mathematically that one can recreate a topologically equivalent picture of the original multidimensional system behavior by using the time series of a single observable variable ([TAKENS, 1981](#)). The basic idea is that the effect of all the other (unobserved) variables is already reflected in the series of the observed output. Furthermore, the rules that govern the behavior of the original system can be recovered from its output.

Using recurrence plot analysis, the STE measures the level of organization/structuredness of process features in physical records. The calculation of STE is done by the Eugene Kononov's Visual Recurrence Analysis (VRA), version 4.7 (see, <http://nonlinear.110mb.com/vra>).

With the assumption that MCs generated by ICMEs evolve with a flux-rope-like configuration, an organization in the IMF exists due to the MC structure. Although many times the visual identification of MC configuration using the IMF components collected by satellites is not an easy task, the STE analysis intend to makes it easier.

Formulating a procedure, we analyze IMF data using an arbitrary time interval of 10 days, where we are sure to use a wide interval that contains at least the occurrence of one MC already identified. As a criterion for calculation using the data, we select a convenient data interval of 2500 records moving forward by 200 record steps until the end of the time series. For every data segment, the STE is calculated at each step. It allows analyzing the STE evolution along the series, with an adequate resolution defined by the chosen step. We select 2500 points because this interval represents an interval of 11.11 h, and the MCs have a smooth rotation of the magnetic field vector in the order of 1 day, where the field reaches a peak and decreases (BURLAGA, 1988). With a temporal window size of 11.11 h and a resolution of 16 s, it is possible to cover the entire range of trend in the most of MCs with dimensions larger than 24 h. The STE values are calculated every 0.89 h (time resolution adopted, with 200 records) and representing $\sim 8\%$ of the size of each temporal window. So, the variation of the values of STE between two contiguous windows (11.11 h) must also be in the order of $\sim \pm 8\%$. Further it allows a blind test to this technique by analyzing a large data series of solar wind data, obtaining plasma MC-candidates regions.

Higher STE values (close to 100%) indicate disorganization, i. e., no flux rope structure; while lower values (close to zero), an organization being reached, i. e., flux rope structure-like.

Based on the MC magnetic structure, not all the magnetic components are expected to have STE values close to zero simultaneously, and even if more than one component present values at the same time in MC. That is the reason to create a standardization interplanetary entropy index (called by us IE index) that joins the STE results of the three variable (B_x, B_y, B_z) , which are affected by the physical

process, in an easy interpretation diagnose. The index is the result of multiplying the STE values obtained from the calculation on each of the three variables, using a dataset taken at the same time t , normalized by 10^4 , presented as:

$$IE = \prod_i \frac{STE_i}{10^4} [\%], \text{ where } i=[x, y, z]. \quad (5.4)$$

The normalization is convenient to show the IE in the same scale of the STE from 0% to 100%.

Scheme for the identification of MC occurrence

The scheme used to identify the MC occurrence using IMF and to test the method using SW data is presented in Figure 5.4. Its description is as follows.

In the first part of the scheme, the IMF data (in any reference system) with the best time resolution are acquired. Then Data in an arbitrary time interval are taken, using an interval large enough to contain a significant portion of the an eventual MC. After that, records from the data taken within a convenient time length (called window) are selected in each displacement under a constant time step till the end of the data series. Following, the STE value is calculated in each window respectively for B_x , B_y , and B_z components, that allows obtaining a time evolution to STE. Finally, the IE values are obtained using the Equation 5.4. When in the IE time series has value equal zero, then there is a cloud-candidate region and it could be examined in order to identify the MC boundaries.

In the second part of the scheme, after the identification of the MC occurrence and its probable location, the evaluation of the MC boundaries can be done using the IMF data or, if available, using also the SW plasma data together, for more precise results. For the MC boundary analysis, MVA on IMF data can be applied. A more complete analysis is done using plasma beta calculation resultant from plasma data and IMF data together. At the end, both the identification and the characterization of MCs are done.

In order to be clear about the approach, some comments are made on the methodological primary features. We did not use the techniques of bi-directional streaming of solar wind supra-thermal electrons (BDE) along magnetic field lines to find the candidate MCs (BAME et al., 1981; GOSLING, 1990). On one hand, BDEs are also

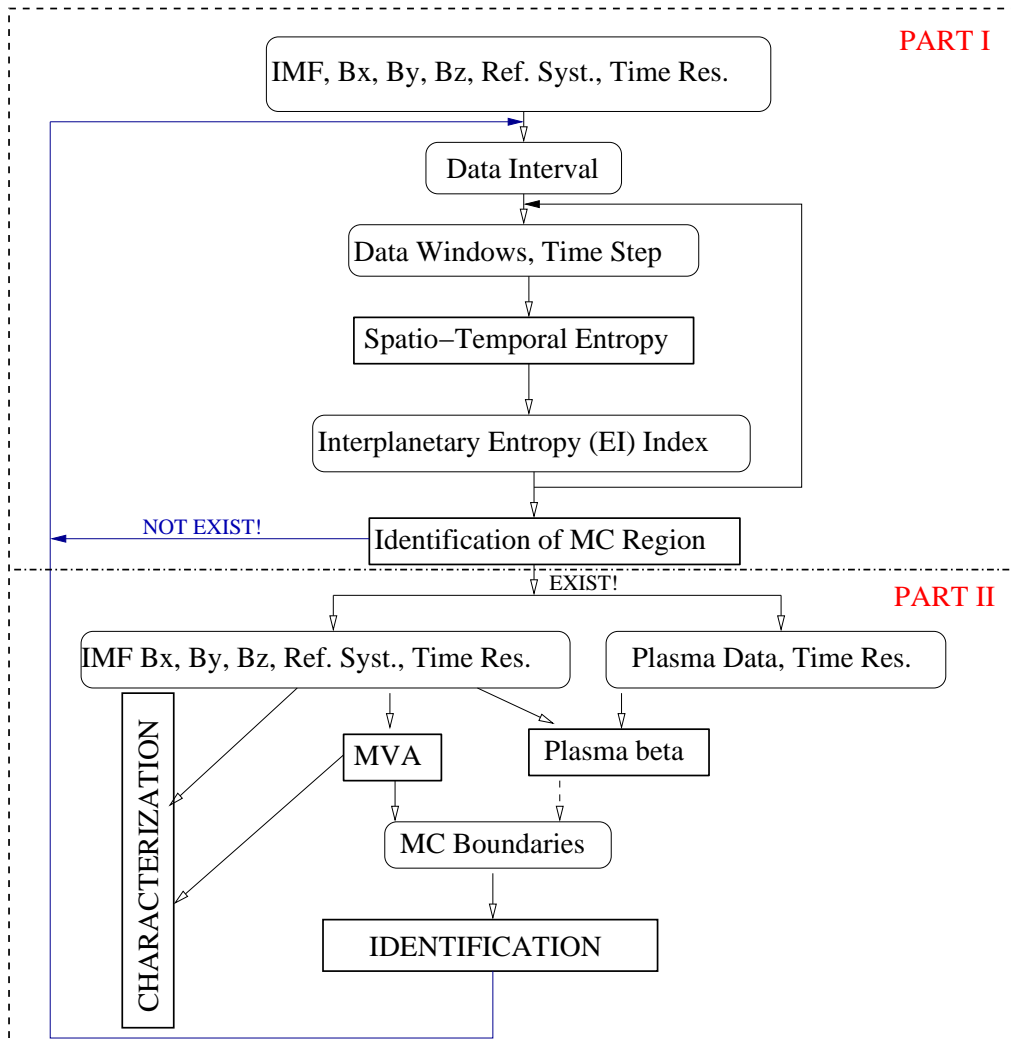


Figure 5.4 - Scheme used to identify MCs.

present in ICMEs without the MC structure, and, in addition, we should use plasma data for building it. On the other hand, the calculation of the IE does not use the plasma data. This is an advantage of the above technique, added by the fact that IMF data have few or short gaps and a better time resolution. Also, there is a major point. The skill of the strategy is to show a mathematical tool like the STE, that allows an easy computational technique, to identify simply and quickly the occurrence of a flux rope-like associated with the cloud at about 1 AU. Nevertheless, this STE method does not solve the problem of identifying the boundaries of the clouds. To delimit the boundaries, if this is the case, the methodology presented in the work of [Huttunen et al. \(2005\)](#), and references therein, is available to be used.

5.2.2 Methodological applications

In order to test the proposed identification methodology and demonstrate its usefulness, three well identified events by other authors are now used. Table A.5 presents 4 MCs picked up from the [Huttunen et al. \(2005\)](#)'s work. In Table A.6, the SW intervals used for the analysis of these events are shown. Also included, an ICME (from [Dal Lago et al. \(2006\)](#)) allows verifying the quality of the method. The chosen phenomenon tests the skill of the tool to recognize MC features from features of other similar structures.

MC occurrence identification

Based on the test case of MC at Jan. 06-08, 1998 (Table A.1, a SW dataset for 10 days from January 03-12, 1998 (Table A.6), is selected. The STE was calculated in a total of 256 time windows, each with 2500 records. In Figure 5.5, we show STE values versus date for the time series of IMF components for this interval. STE values for B_x , B_y , and B_z are plotted with dotted line, dashed line, and continuous thin line, respectively. Additionally, we have investigated if ACE detected some other events during those ten days.

[Cane and Richardson \(2003\)](#) summarized the occurrence of ICMEs recorded in the SW that reached the Earth during 1996 – 2002, corresponding to the increasing and maximum phases of solar cycle 23. In particular, they give a detailed list of such events based on in situ observations. They reported two ICME in this interval: from January 07, 01 : 00 to January 08, 22 : 00, the event is a MC; while from January 09, 07 : 00 to January 10, 08 : 00 1998, no event is classified as MC. Thus, in Figure

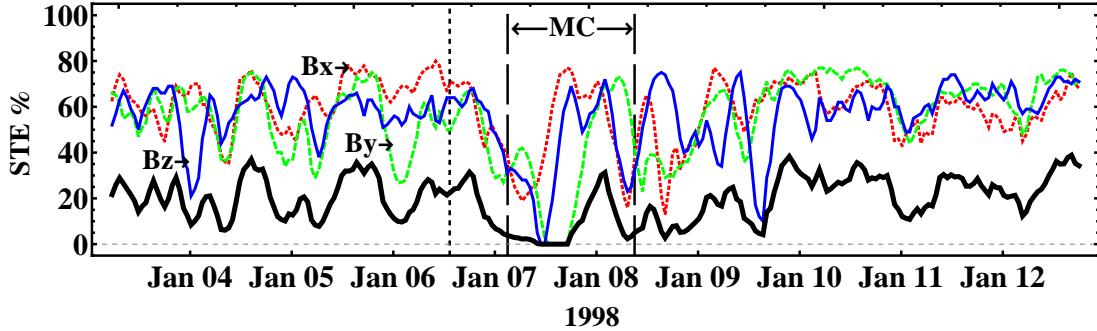


Figure 5.5 - Values of spatio-temporal entropy (STE) as a function of the time for time series of IMF B_x (dotted line), B_y (dashed line) and B_z (continuous thin line) components in the SW. The thick curve represents the interplanetary entropy index (IE) calculated over the analyzed period. The shock, the start and end of the MC are represented by three vertical lines as is shown in Table A.1.

5.5, we have one MC, one interplanetary disturbance not classified as MC, and a *quiet* SW period. Some features related to the ICME classified as MC in January 07 were reported by Cane and Richardson (2003): $V_{ICME} = 400 \text{ km/s}$, this is the mean SW speed in the ICME; $V_{max} = 410 \text{ km/s}$, the maximum SW speed in the post disturbance region; $B = 16 \text{ nT}$ the mean field strength; and $V_T = 480 \text{ km/s}$, the transit speed. The MC was also reported by Huttunen et al. (2005), but with different size.

In Figure 5.5, the shock, the start, and end of the MC are represented by three vertical lines, at the time informed in Table A.1. The B_y , B_z components have zero STE values only during the passage of the MC, approximately in the first half of it. The second minimum value of $STE = 10\%$ corresponds to B_z component in January, 09. At this date (January 09, 07 : 00 – January 10, 08 : 00), Cane and Richardson (2003) detected one ICME with $V_{ICME} = 450 \text{ km/s}$, $V_{max} = 500 \text{ km/s}$, $B = 6 \text{ nT}$. It is not classified as MC. This result seems to be very interesting, because, in this interval of ten days of SW data, only two magnetic components (B_y and B_z) have zero STE values, and it is within the MC. Huttunen et al. (2005) first performed a visual inspection of the data to find the cloud candidates. This is always the first step in any work aiming at studying MCs. Although exist automatic ways of identification, still the plasma data need to be used in the usual tools (LEPPING et al., 1995). Then, the calculation of STE could be a very useful mathematical tool to

help finding the MC candidates.

The thick curve in Figure 5.5 is the representation of the IE calculated along the analyzed period. We could think of a similarity with the Dst index, which is a geomagnetic index which monitors the world wide magnetic storm level. Therefore when the Dst index reaches negative values, it indicates that a magnetic storm is in progress. More negative the Dst index, more intense the magnetic storm. While the Dst can present positive and negative values, the IE value can only decrease to zero somewhere inside the MC. The MCs have simple flux rope-like magnetic fields, characterized by enhanced magnetic fields that rotate slowly through a large angle. Then, the time series of IMF components have a trend and a more ordered dynamic behavior, and a higher degree of correlation with its temporary neighbors (OJEDA et al., 2005; OJEDA et al., 2013). The aforementioned behavior is found only in the magnetic structures of the MCs, a necessary condition for the zero IE value.

A case chosen for a false positive result test

To test that the STE is not zero for other interplanetary disturbance than MC is required to validate the use of IE as a methodology. That is the reason for the name *false positive* used here. Although it is not a true proof, this empirical test corroborates with the results obtained for a large number of SW data till now. This case chosen to create an adversity situation of analysis by the physical similarity with the MC serves as an example for validation, or initial acceptance, of the method.

In Table A.6, a SW dataset for 6 days from October 20-25, 1999 is indicated. Because the interface between the interplanetary ejecta and the high-speed stream on October 22, 1999 is an excellent study case (Dal Lago et al., 2006). High-speed streams, originating in coronal holes, are observed often following ICME at 1 AU (KLEIN; BURLAGA, 1982). Dal Lago et al. (2006) studied the October 17 – 22, 1999 solar-interplanetary event, which was associated to a very intense magnetic storm ($Dst = -237$ nT).

In Figure 5.6, we show the values of STE as a function of the time for times series of IMF B_x , B_y and B_z components in the SW from 20 – 25 October, 1999. In this SW data intervals, 150 time windows (each with 2500 records) were obtained. STE values of each of the three IMF components are calculated. Using Equation 5.4, the IE is calculated and it is plotted with thick curve over the analyzed period in this

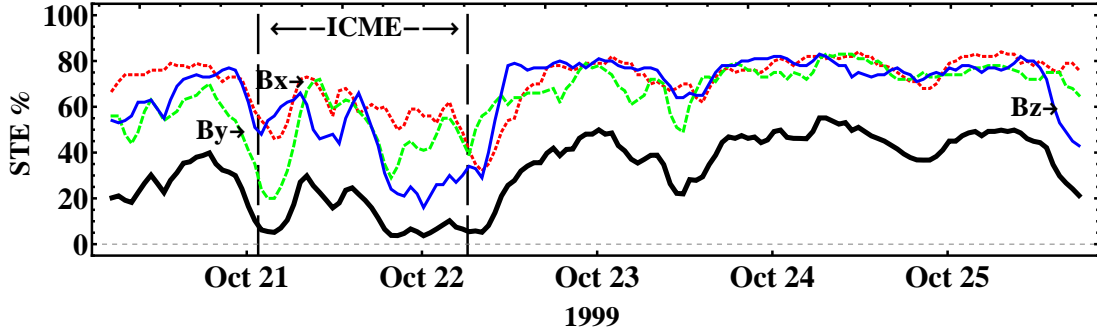


Figure 5.6 - Values of STE as a function of the time for times series of IMF B_x (dotted line), B_y (dashed line) and B_z (continuous thin line) components in the SW. The thick curve represents the IE calculated over the analyzed period. The vertical lines represent the ICME reported by Dal Lago et al. (2006) from 21, 01 : 34 UT to 22, 06 : 15 UT.

figure.

Dal Lago et al. (2006) presented an analysis of pressure balance between the ICME observed on October 21 – 22 and the high-speed streams following it. Close to the Earth, at $L1$, an interplanetary shock was detected by ACE magnetic field and plasma instruments on October 21, 01 : 34 1999, as shown in Figure 5.6 by the first vertical dotted line. The driver of this shock is an ICME, which can be distinguished from the normal SW by its intense magnetic field, of the order of 20 nT throughout the most part of October 21, and its low plasma beta (~ 0.1) (Dal Lago et al., 2006). The start of the ejecta was on October 21, 03 : 58. Toward the end of this ejecta, an increase of the magnetic field intensity was observed, starting on October 22, 02 : 30, reaching a peak value of 37 nT (Dal Lago et al., 2006). At 06 : 15 UT of 22 October (the second vertical dotted line in Figure 5.6), the magnetic field dropped abruptly around 10 nT. (Dal Lago et al., 2006) defined this point as the end of the ICME. They were not sure whether this ICME is an MC or not according to the criteria of Burlaga et al. (1981), because the direction of the magnetic field does not rotate smoothly. (CANE; RICHARDSON, 2003) also detected an ICME not classified as MC at the date from October 21, 08 : 00 to October 22, 07 : 00 1999 with $V_{ICME} = 500$ km/s, $V_{max} = 580$ km/s, $B = 20$ nT and $V_T = 480$ km/s.

As presented in the previous paragraph, it is clear that, during the period of October 20 – 25, 1999, no event was identified as MC. In the Figure 5.6, the values of STE

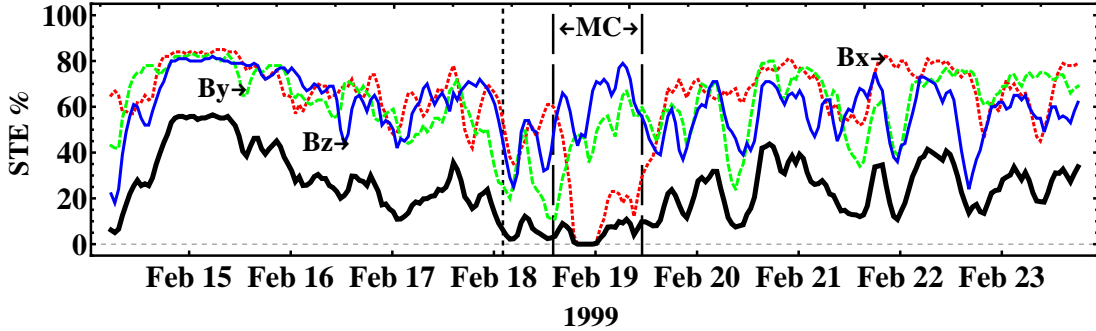


Figure 5.7 - It is plotted the IE as a function of the time, February 14 – 23, 1999, but the three vertical lines correspond with the third event in Table A.1. The format is the same as in Figure 5.5.

are always different of zero, so the IE also is different of zero. This result helps to validate the IE to detect MC, because IE methodology can differentiate when an ICME is not classified as MC, since the IE is zero only inside of MC. This skill is related to the correct diagnose of the intrinsic magnetic field configuration existing in a MC, representing a very higher organized plasma structure.

A blind test case

With the idea of trying the method, we done a random selection of one MC among the 80 MC events (73 MCs and 7 cloud candidates) identified in the work of [Huttunen et al. \(2005\)](#). It is the second case in the Table A.1, identified as the MC event of February 18 – 19, 1999. Table A.6 indicates the ten-day interval, February 14 – 23, 1999, of SW dataset collected to be analyzed. Considering a total of 256 time windows, the STE values are calculated. in Figure 5.7 the result was shown. The STE reaches value zero for the B_x component. So, there is a IE index presenting value zero in the examined period.

[Cane and Richardson \(2003\)](#) detected an ICME not classified as MC at the date from February 13, 19 : 00 to February 14, 15 : 00 1999 with $V_{ICME} = 440$ km/s, $V_{max} = 470$ km/s and $B = 9$ nT. Figure 5.7 shows the results of the calculation of STE at February 14, 15 : 00, 1999, where the IE has a small, but non-zero, value. During February 18 – 21, 1999, the ACE spacecraft detected an ICME, classified as MC with $V_{ICME} = 520$ km/s, $V_{max} = 700$ km/s, $B = 8$ nT and $V_T = 870$ km/s as the transit speed ([CANE; RICHARDSON, 2003](#)). Inside the MC, that is limited by

the vertical lines in the Figure 5.7, we can see that $STE = 0\%$ only for one IMF component (in this case, for B_x). It generates a IE index presenting a value zero that occurs only inside the MC region. So, the IE index identifies indeed the occurrence of one MC event in this data interval.

So far, many times we see MCs with zero STE values only in one of the IMF components. However, the IE has always detected the existence of MCs, located by the value zero. Thus, using the IE we find the MC occurrence, but not the boundaries (or the time extension) of the cloud. The consistent results from other aleatory cases are not showed in this work.

5.2.3 Validation of MVA method to identify the boundary of a MC

The proposed methodology in the above sections are not used to identify the boundaries of the clouds and to obtain geometry parameters of the flux rope structure respectively. We need to use the method presented in the paper of [Huttunen et al. \(2005\)](#) to validate an analysis methodology.

Huttunen and collaborators have also included seven cloud candidate events for which either the fitting with MVA was not successful (e.g. the eigenvalue ratio < 2 or the directional change less than 30°) or there were large values of beta throughout the event. In their study the criterion to define a MC were based on the smoothness of the rotation in the magnetic field direction confined to one plane. Additionally they required that a MC must have the average values of the plasma beta less than 0.5, the maximum value of the magnetic field at least 8 nT, and the duration at least 6 h. With the last two criteria, they aimed to remove the ambiguity of identifying the small and weak MCs. All selected events were investigated by analyzing 1 h magnetic field data with MVA, where MCs are identified from the smooth rotation of the magnetic field vector in the plane of the maximum variance ([KLEIN; BURLAGA, 1982](#)).

We done a computational implementation to analyze MC with the above methodology. The Figure 2 left panel (19 – 22 March 2001) in the paper of [Huttunen et al. \(2005\)](#) is selected with the KSnapshot program. The KSnapshot program in Linux (Ubuntu) is capable of capturing images of the whole desktop, a single window, a section of a window or a selected region. The images can then be saved in a variety of formats. After that, the g3data program in Linux (Ubuntu) is used for extracting

Table 5.4 - Comparison the results of MVA method with paper of [Huttunen et al. \(2005\)](#). The eigenvalues of the magnetic variance matrix are $\lambda_1, \lambda_2, \lambda_3$, in order of declining size and the corresponding normalized eigenvectors, $\hat{x}_1 = \hat{B}_x^*$, $\hat{x}_2 = \hat{B}_y^*$, $\hat{x}_3 = \hat{B}_z^*$. Our results, shown in the third column, are consistent with the second column. The rows from the top to the bottom: the eigenvectors (nT), eigenvalues, eigenvalue ratio (λ_2/λ_3), direction of the MC axis (ϕ_C, θ_C), direction of minimum variance axis (ϕ_{Min}, θ_{Min}), difference between the initial and the final magnetic field vectors (χ), inferred flux-rope type (see [Figure 2.7](#)), handedness of the cloud (LH=left-handed).

19-22 March, 2001		
Parameters	Huttunen et al. (2005)	Our implementation
\hat{x}_1, \hat{B}_x^*	-	(0.26, 0.91, 0.32)
\hat{x}_2, \hat{B}_y^*	-	(-0.37, 0.40, -0.84)
\hat{x}_3, \hat{B}_z^*	-	(-0.89, 0.1, 0.44)
$[\lambda_1, \lambda_2, \lambda_3]$	-	[110.52, 48.44, 0.93]
λ_2/λ_3	52	52.12
ϕ_C	133	132.62
θ_C	-57	-56.78
ϕ_{Min}	-	173.74
θ_{Min}	-	26.26
χ	156	155.61
Type	WSE	WSE
CH	LH	LH

data from graphs. The results are plotted with red color in the [Figure 5.8](#). Also in the [Figure 5.8](#) with blue color, our results are plotted. It is possible observe that the results agree. For more security, the quantitative results are compare in [Table 5.4](#). The description of the parameters in the caption of the table is shown . Thus, our implementation is ready for the studies of new MCs.

[Nieves-Chinchilla et al. \(2005\)](#) performed a systematic study of MCs in the time interval 2000 – 2003. They used the non force-free model of [Hidalgo](#) to identified magnetic clouds. The total of clouds identified in that study were presented in [Table 2.1](#). Also the MC of (19 – 22 March 2001) was studied, but [Nieves-Chinchilla et al. \(2005\)](#) report two MCs in this time interval (see [Table 1](#) in the work of [Nieves-Chinchilla et al. \(2005\)](#)). In [Chapter 6](#), we will use this contradictory result to validate our methodology.

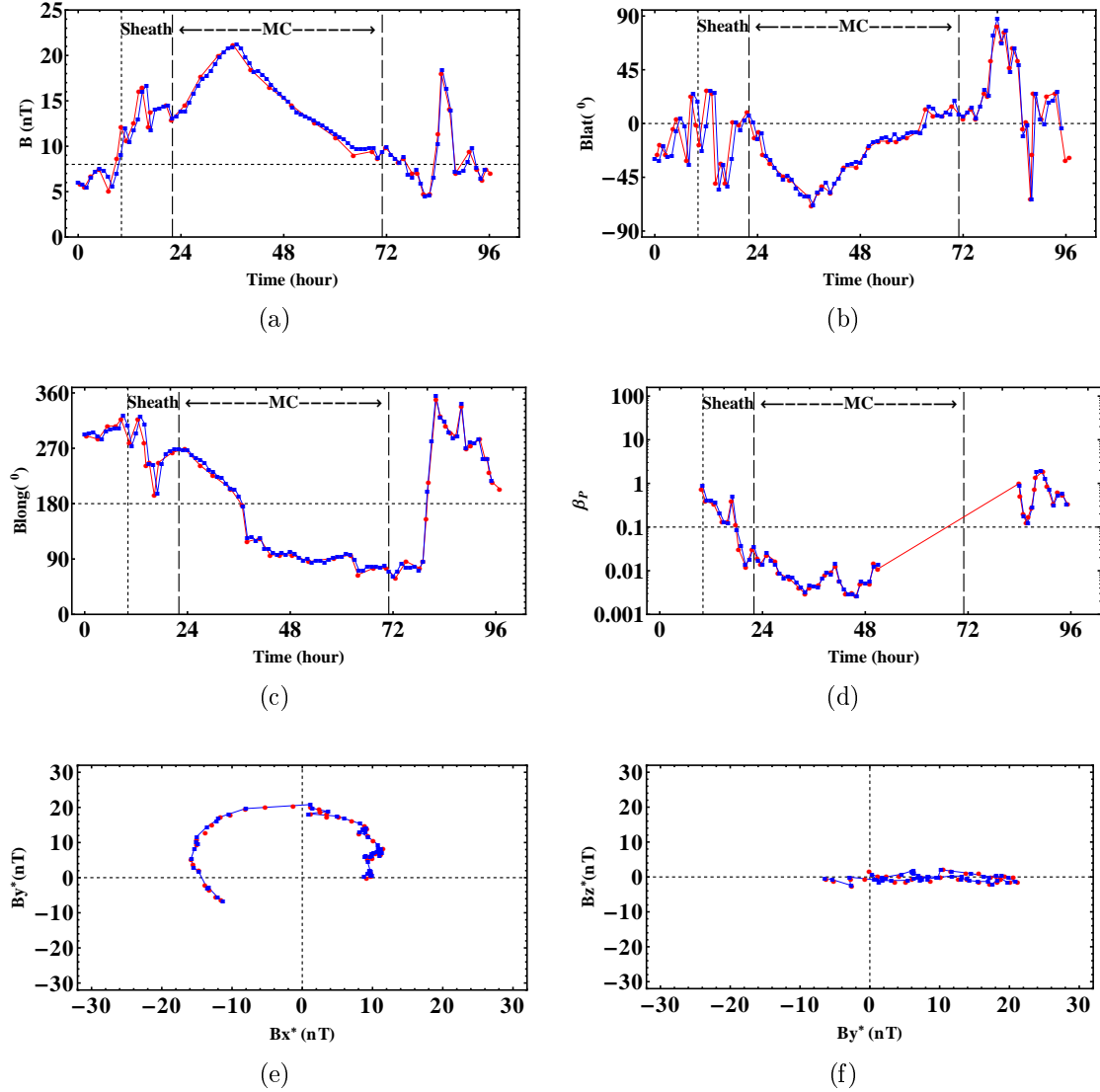


Figure 5.8 - The unipolar MC was observed by ACE on 19-22 March, 2001 and identify by [Huttunen et al. \(2005\)](#) (see event number 27 in Table A.1, Annex A). In all panels: red color shown the results of [Huttunen et al. \(2005\)](#), our implementation is shown with blue color. (a) magnetic field strength; (b) polar angles of the magnetic field vector in GSE coordinate system (B_{lat}); (c) azimuthal angles of the magnetic field vector in GSE coordinate system (B_{long}); (d) proton plasma beta; (e) the rotation of the magnetic field vector in the plane of maximum variance; (f) the rotation of the magnetic field vector in the plane of minimum variance.

5.2.4 Persistence index to identify the region of a MC

Following the same idea of IE, we calculated the four persistence exponents β , α , Hu , Ha in time windows of ten days. Figure 5.9 (All panels) are the same as Figure 5.5 but in each panel, different persistence exponents are shown. We found a threshold for each exponent that will be discussed in chapter 6, derived from Figure 6.13. In Figure 5.9 threshold values are represented with a horizontal dashed line. The horizontal thick curve in each panel, is an average value or persistence index similar to Equation 5.1, that is:

$$\langle \beta \rangle = \frac{1}{3} \sum_{i=1}^3 \beta^{(i)} \quad (5.5)$$

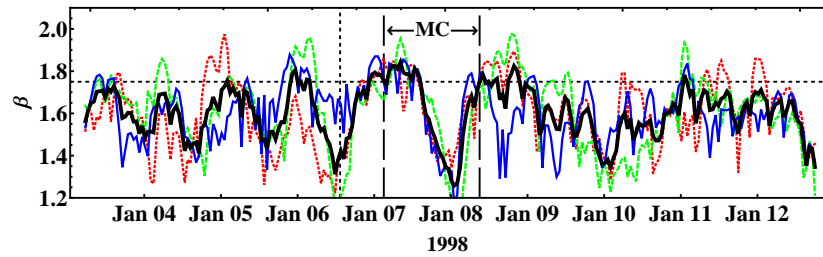
$$\langle \alpha \rangle = \frac{1}{3} \sum_{i=1}^3 \alpha^{(i)} \quad (5.6)$$

$$\langle Hu \rangle = \frac{1}{3} \sum_{i=1}^3 Hu^{(i)} \quad (5.7)$$

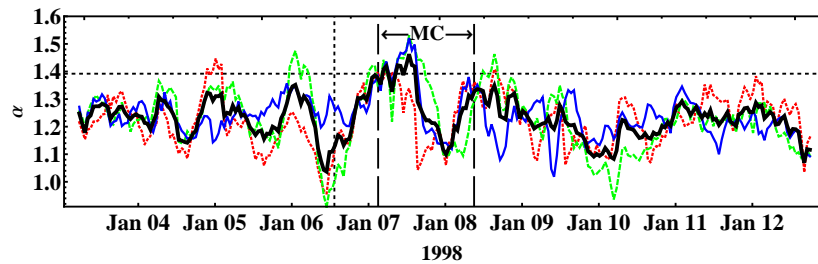
$$\langle Ha \rangle = \frac{1}{3} \sum_{i=1}^3 Ha^{(i)}. \quad (5.8)$$

The angle brackets $\langle \dots \rangle$ denote an average of IMF components, $i = 1, 2, 3 = B_x, B_y, B_z$. If each persistence index is over threshold in all panels at same time then exist a region that could be identified as a magnetic cloud candidate. The previous condition is only true inside of a MC that shown in Figure 5.9. The α -index threshold was exceeded only inside of MC, therefore was the best index. Also Hausdorff-index had a great increase in the MC region.

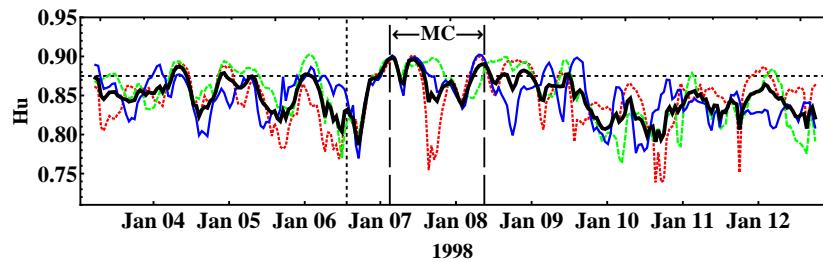
As was done to validate the IE methodology, is necessary to prove that in other interplanetary disturbances, persistence index does not satisfy the condition to identify MCs, e.g. all persistence index exceeds the threshold at same time only inside a MC. Thus, we use the same event studied by Dal Lago et al. (2006) and shown in Figure 5.6. It is the interaction between an ICME with a high-speed stream. The results are show in Figure 5.10, we saw an increase in the indices over the threshold on October 22. But alpha index fails. We conclude that not exist a MC in that SW interval. Then, this methodology is valid to identify flux rope associated with MCs. And it will be used for this purpose in the next chapter.



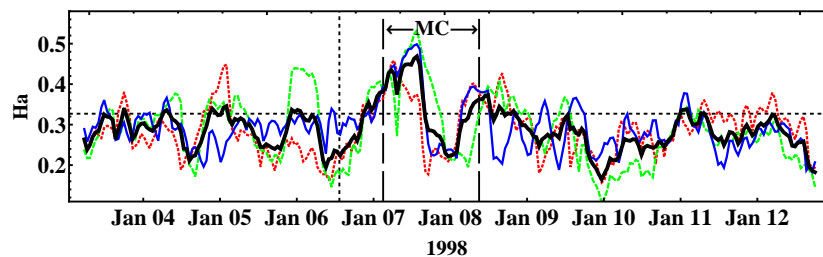
(a)



(b)

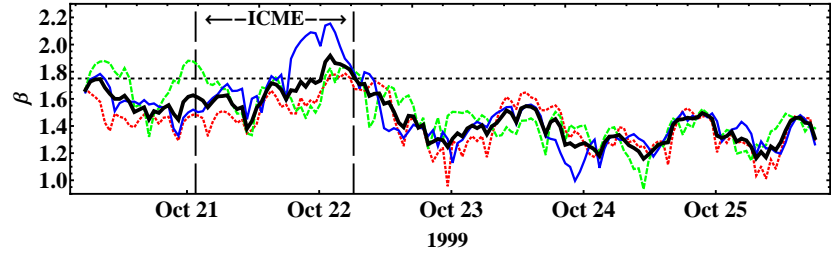


(c)

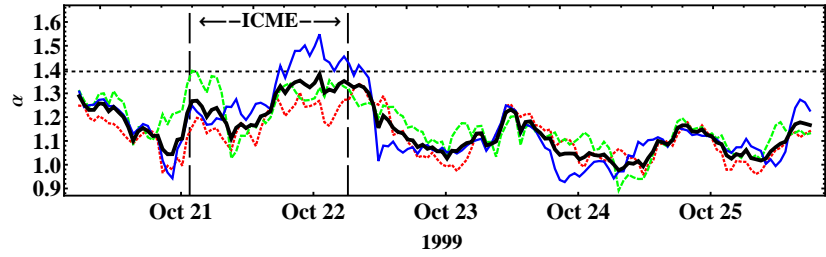


(d)

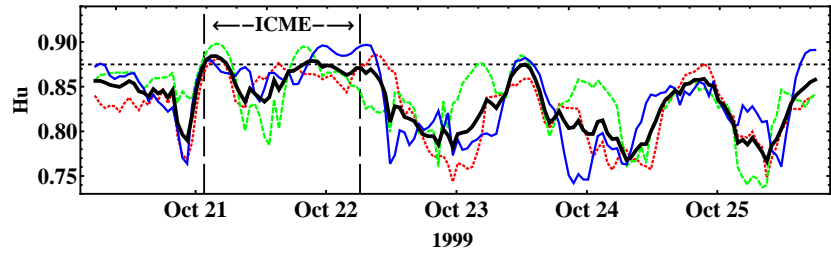
Figure 5.9 - Persistence exponents as a function of the time for times series of IMF B_x (red), B_y (green) and B_z (blue) components in the solar wind. In the four panels are shown: (a) β -index; (b) α -index; (c) Hurts-index; (d) Hausdorff-index. The thick curve represents the persistence indices calculated over the analyzed period. The shock, the start and end of the MC are represented by three vertical dotted lines.



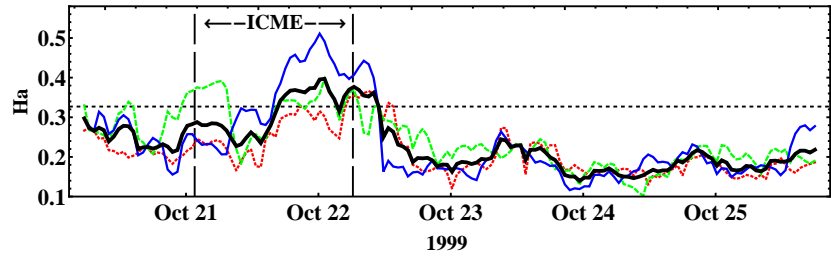
(a)



(b)



(c)



(d)

Figure 5.10 - Persistence exponents as a function of the time for times series of IMF B_x (red), B_y (green) and B_z (blue) components in the solar wind. In the four panels are shown: (a) β -index; (b) α -index; (c) Hurts-index; (d) Hausdorff-index. The thick curve represents the persistence indices calculated over the analyzed period. The shock, the start and end of the MC are represented by three vertical dotted lines.

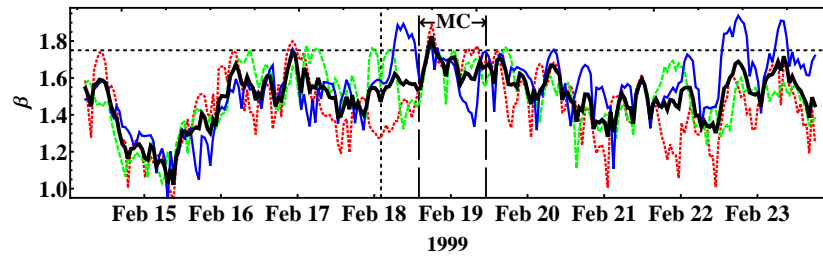
We tested the methodology on other SW interval from February 14 – 24, 1999. The results are shown in the Figure 5.11. Again only the four indices are over threshold inside of magnetic cloud. As we use four indices at same time this is not very efficient methodology for identifying the cloud region. It can be used as an auxiliary tool because is very easy to do an automatic and rapid computational implementation. However, the IE is most precise to identify the cloud regions, also the computational implementation is delayed because the entropy is calculated on RP.

5.2.5 DWT index to identify the sheath of a MC and solar wind fluctuations

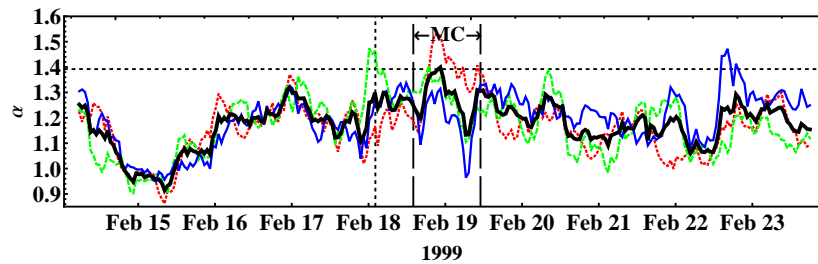
We calculated the wavelet coefficient $d1^2$ using the same idea presented along this section: in time intervals of 2500 records moving forward as 200 records over 10 days on IMF dataset. Thus, the Equation 5.2 is used to calculate an average wavelet coefficient D_{d1} on each window of 2500 records of dataset. The dataset are the components of IMF (B_x, B_y, B_z). In the Subsection 5.1.2 was explain the existence of anisotropy in the IMF, and the necessity to calculate an average value of the persistence exponent between the three IMF components. Using the Equation 5.3 an average value ($\langle D_{d1} \rangle$) of wavelet coefficient D_{d1} in the three components is calculated.

In Figure 5.12(a), we show D_{d1} values versus date for the time series of IMF B_x , B_y and B_z for this event (January 03-12, 1998). D_{d1} values for B_x , B_y , and B_z are plotted with red dotted line, green dashed line, and blue continuum line respectively. With black thin line the $\langle D_{d1} \rangle$ values are represented. We will call this average coefficient as a wavelet index or WI. In the Figure 5.12(a) shows the same solar wind windows shown in the Figures 5.5 and 5.9. We see a decrease of WI inside of the MC, if is compare with the boundaries of it. But, the WI is lowest in other places where not exist MC. However, the maximum WI value is detect in the center of the sheath of the cloud. Then, this tool is not useful to identify the magnetic cloud region, but could help to delimit the start of the cloud. Other applications could be found to investigate the solar wind fluctuation and the calculate correlation with geomagnetic indices. Also, we found an important application in the Chapter 6 using this methodology to identify a reconnection region between two MC.

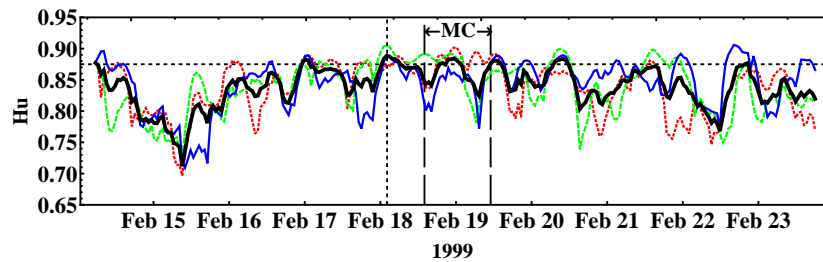
In the Figure 5.12(b) the WI was plotted. The WI allows viewing the shock and the existence of a sheath in this ICME although the flux-rope after the sheath is not classified as cloud magnetic. The index shows that the high-speed streams following



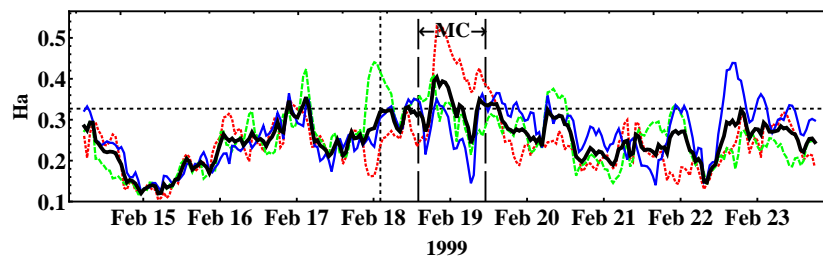
(a)



(b)

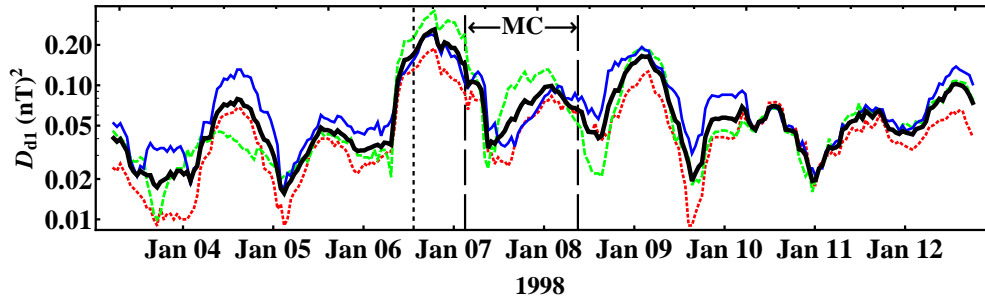


(c)

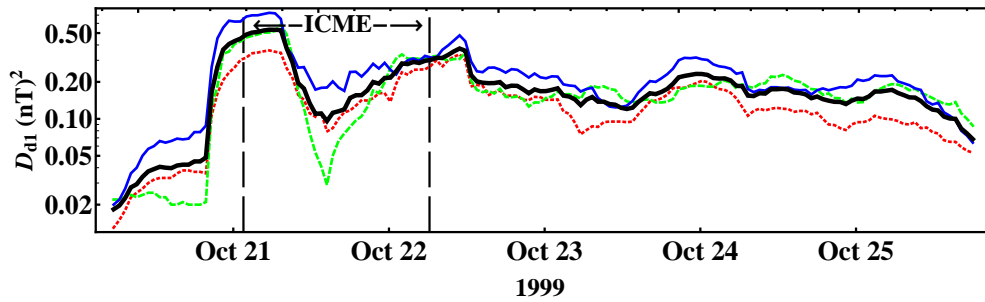


(d)

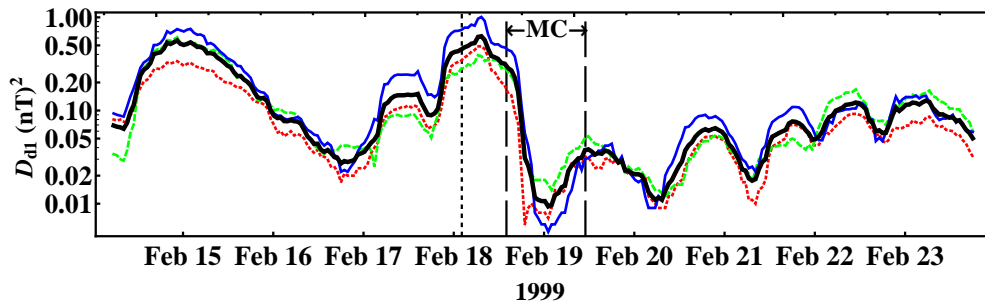
Figure 5.11 - Persistence exponents as a function of the time for times series of IMF B_x (red), B_y (green) and B_z (blue) components in the solar wind. In the four panels are shown: (a) β -index; (b) α -index; (c) Hurts-index; (d) Hausdorff-index. The thick curve represents the persistence indices calculated over the analyzed period. The shock, the start and end of the MC are represented by three vertical dotted lines.



(a)



(b)



(c)

Figure 5.12 - D_{d1} values as a function of the time for times series of IMF B_x , B_y and B_z components in the solar wind. D_{d1} values for B_x , B_y , and B_z are plotted with red dotted line, green dashed line, and blue continuum line respectively. The thick curve represents the Wavelet index (WI) calculated over the analyzed period. The shock, the start and end of the MC are represented by three vertical dotted lines.

this ICME has great fluctuations in an along time period. The IMF fluctuation are lower inside the MC than in the plasma sheaths but we do not require a wavelet analysis to infer that. However, WI is a tool to measure the size of these fluctuations, for comparison with other regions in the solar wind itself.

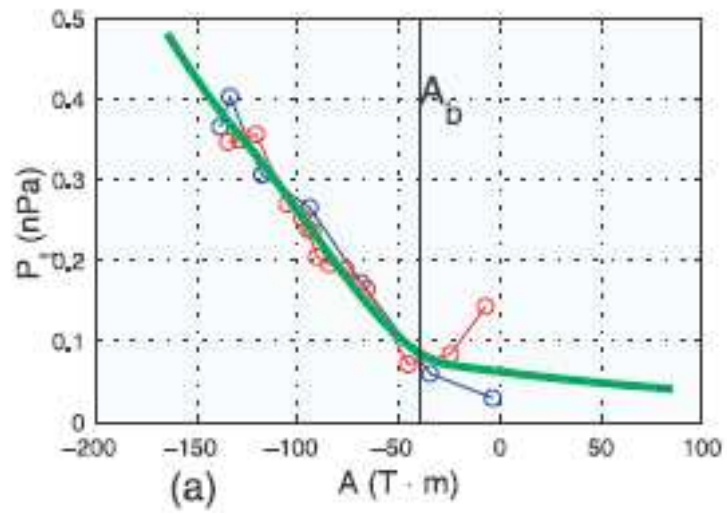
Figure 5.12(c) is similar to 5.12(a) and 5.12(b) but for the date February 14 – 24, 1999. We remember that two ICMEs were reported during this ten day of SW interval; the first from February 13, 19 : 00 to February 14, 15 : 00, the second at the date February 18 – 21. Anew, great values of the WI was found in the plasma sheath. In conclusion this methodology is not useful to identify magnetic cloud but is an auxiliary tool that could used to study the fluctuation in the plasma sheath.

5.3 Example: MC flux-rope reconstruction

A magnetic cloud of double flux rope configuration of apparent asymmetry was studied by Hu et al. (2003). They employed the Grad-Shafranov reconstruction techniques to derive the local magnetic structure from data of a single spacecraft. Their results showed two cylindrical flux ropes next to each other where a single X point was formed between them. The interval studied correspond to a MC observed by ACE in the solar wind at 1 AU on August 12, 0519 : 43 – 1933 : 05 UT 2000. Evidence of multiple flux rope magnetic clouds were reported by Osherovich et al. (1999), Haggerty et al. (2000), Skoug et al. (2000), Vandas et al. (1999). Other four magnetic flux rope events that are not necessarily CMEs or MC were observed by ACE and are examined by the GS reconstruction techniques in the work of Hu et al. (2004).

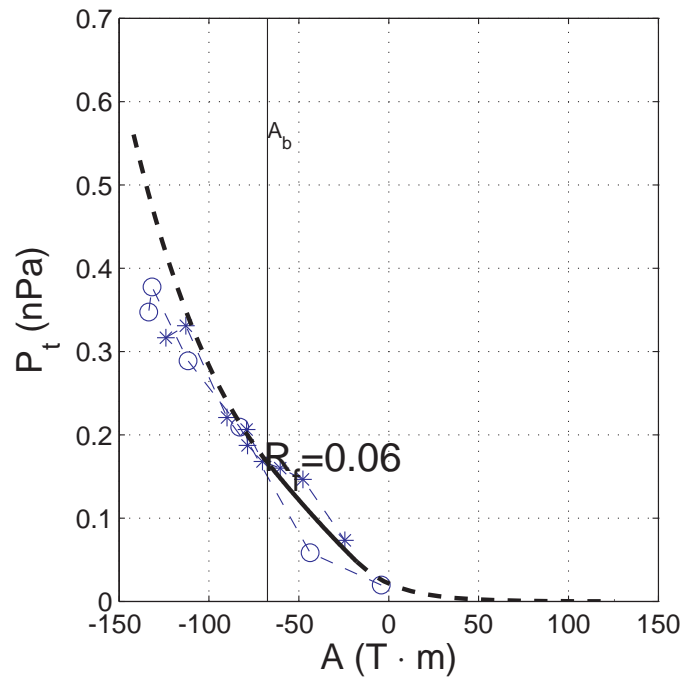
We used a program package in MATLAB (see Annex B). We studied the interval correspond to a MC observed by ACE in the solar wind at 1 AU on August 12, 0524 : 00 – 1904 : 00 UT 2000. It is the same event studied by Hu et al. (2003). In Figures 5.13 and 5.14, the results are compared.

The relationship between P_t and A in the Figure 5.13 shows scatter around the fitted polynomial curve (order 2) for $P_t(A)$ used in the reconstruction. The vertical line denoted by A_b marks the point on A axis where $A = A_b$ (HU et al., 2003). The intervals $A \in [A_l, A_m]$ (see pag 4, Hu and Sonnerup (2002)) are the A valid values in the reconstruction. The value A_b is determined form the P_t versus A plot shown in Figure 5.13 as the point on the A axis beyond which the requirements that $P_t(A)$



(a)

ACE 8/12/2000



(b)

Figure 5.13 - (Both panels) Reconstruction results of ACE August 12, 2000, magnetic cloud. Plot of data $P_t(x, 0)$ versus $A(x, 0)$ along the x axis for the analysis interval, and the fitted $P_t(A)$ function. The vertical line denoted by A_b marks the point on A axis where $A = A_b$. (a) Source: Hu et al. (2003). (b) We used a program supplied by Christian Möstl during his PhD thesis to reproduce this result.

be all functions of A alone are violated. In practice, A_b can be manually selected on the graph, doing trial and error.

In Figure 5.13 (b) is plotted data $P_t(x, 0)$ versus $A(x, 0)$ along the x axis for the reconstruction interval and the fitted $P_t(A)$ function (black curve). Circles are data along the spacecraft inbound path, while stars are along the outbound path. The fitting residues $R_f = 0.06$ is defined on Equation C.45 (Appendix C). The spacecraft crosses the X point. The reconstruction scheme is done with the invariant z axis, $z_s = [0.3430, 0.8966, -0.2799]$. The archive “ALLCASE.par” contains all information necessary for controlling the programs, i.e. control the GS-solver program:

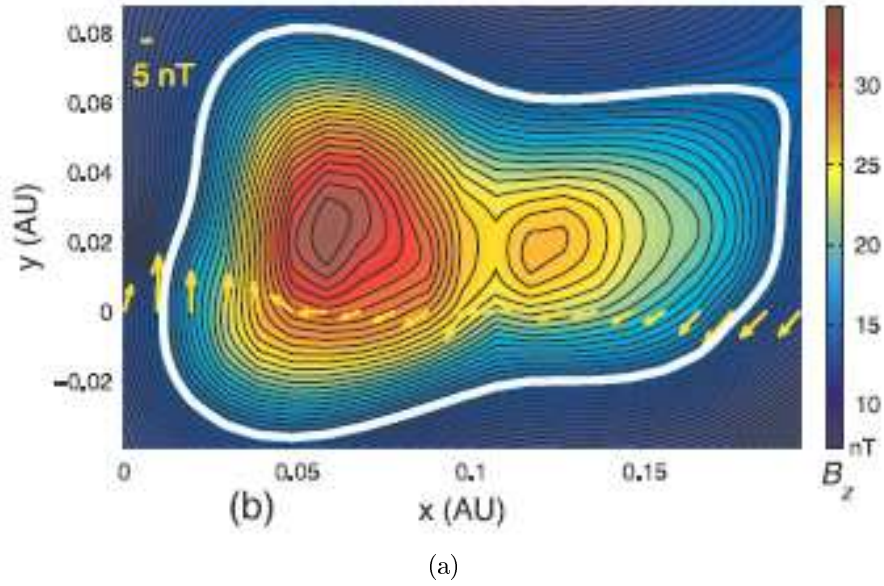
```

ACE_225_226_00
  1
  2
 15 110 20
  1 0.5 0.1

```

We do not explain the previous numbers, because with the program is provided help with a PDF (see Annex B). In Figure 5.13 both panels are similar.

In Figure 5.14 (a and b) is shown the recovered cross-section of the two magnetic clouds. The white thickened contour line is of value $A = A_b$ shown in Figure 5.13. The black contour lines show the transverse magnetic field lines (contours of $A(x, y)$), and the colors show the axial magnetic field, B_z , distribution (scales given by the color bar). White dot shows the magnetic-field maximum in the center of the magnetic cloud best organized. In Figure 5.14(b), the yellow arrows along $y = 0$ denote measured transverse magnetic field vectors, direction and magnitude measurements at ACE (scales given by the arrow in upper left corner of magnitude 10 nT) utilized as initial input into the numerical solver. In Figure 5.14(b) the green arrows are residual velocities in the deHoffmann-Teller frame at ACE (scales given by the arrow in upper left corner of magnitude 50 km/s). Therefore, a single-X point is formed between them. Thus, the program is ready to study other MCs.



ACE 8/12/2000

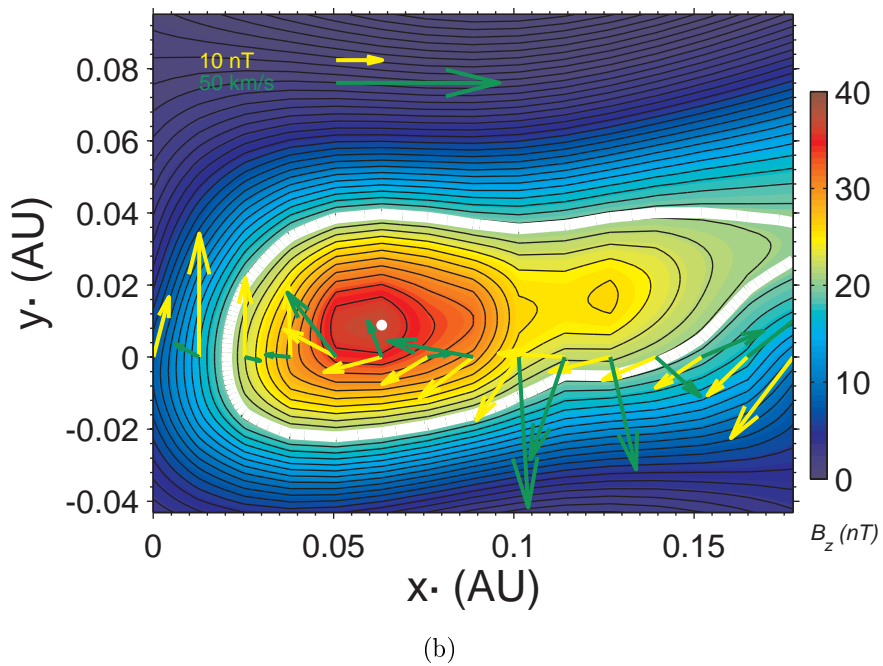


Figure 5.14 - (Both panels) Reconstruction results of ACE August 12, 2000, magnetic cloud. The recovered cross-section of the two magnetic clouds. a) Source: Hu et al. (2003). (b) We used a program supplied by Christian Möstl during his PhD thesis to reproduce this result.

6 RESULTS AND DISCUSSION

This chapter is composed by three main parts related to the work developed. The results and discussions are presented along the text in order to reach physical interpretations. In the first part, studies on the MC identifying procedure are done. The STE technique is the basis. In the second part, the complementary techniques to MC characterization are considered. In those parts, all the studies have been developed using only the IMF data according to the major purpose of this work. Following, the example cases demonstrate the use of this methodology. In the third part, MC events discovered in this work are studied dealing with IMF and interplanetary plasma data. They are indeed new results. At last, a scheme presents the MC analysis methodology based only on the IMF data developed in this work, as well as a complete methodology structured to examine interesting MC-candidate cases.

6.1 Part I: Results related to MC Identification

41 events present a well defined shock wave preceding the MC. For this reason, they constitute the better cases to define a methodology of analysis to identify MC candidates. The events are used to verify the behavior of the STE calculation in a consistent way. The list of events is in Table A.1. For these events, the plots of the time series of the IMF components (B_x , B_y and B_z) are presented in Table A.2.

6.1.1 STE analysis

The STE values for the 41 MC events are shown in Figure 6.1. At the top, the STE values calculated from the three IMF components B_x , B_y and B_z , plotted respectively as “o”, “+” and “x”, corresponding to MCs. At the bottom of the figure the same as above is shown, but for the sheath regions. The STE values of the 246 time series were plotted in chronological order as appeared in Table A.1, column 1. Some MCs do not have STE values close to zero in the three components simultaneously. Then, it is possible to find components with perfect structuredness (low STE) and absence of structure (high STE) in the same MC.

If STE values between the same components for the plasma sheath and the cloud regions are compared (for example, B_x -sheath ($STE = 56\%$) with B_x -cloud ($STE = 0\%$) in the event number 1) then in 5/41 (3/41) of the cases in the B_x (B_y, B_z) component(s) the STE value in the MC is larger than the one in the sheath respectively. These are few cases, and shows a clear tendency to decrease the STE

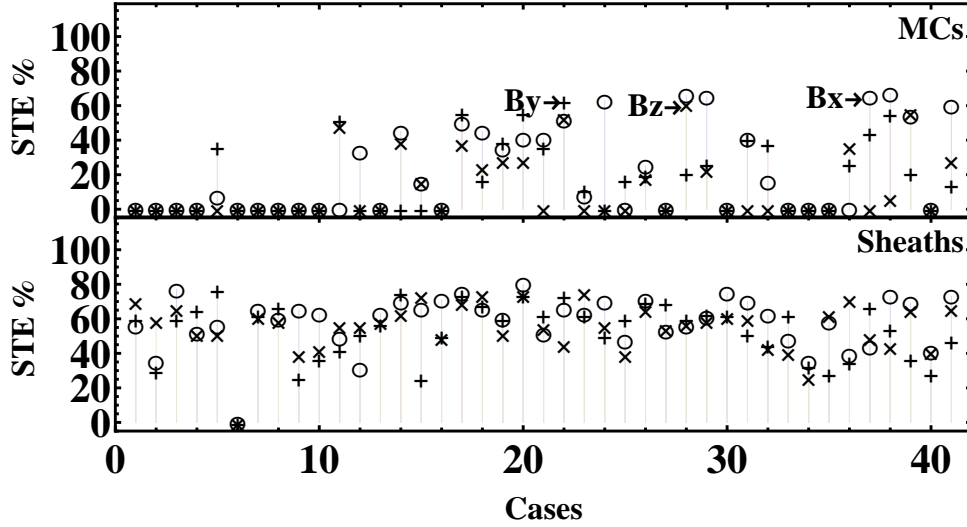


Figure 6.1 - The STE values for 41 MCs from 1998 to 2003 that were presented in Table A.1. At the top, the STE values for the three IMF components (“o” $\equiv B_x$, “+” $\equiv B_y$, “x” $\equiv B_z$) versus cases as shown in Table A.1. At bottom, the same as to above but for the sheath regions. In the two panels without previous transformation in the time series.

value within the cloud region in all IMF components. Someone can notice a clear tendency of the cloud events to present STE with lowest values, close to zero, as was noticed in Ojeda et al. (2005) and extended in this work, which is proposed as new feature added to the usual features (BURLAGA et al., 1981) established to the MCs.

Other interesting result is that STE was zero in 20/41, 21/41, 26/41 MCs to B_x , B_y , B_z components respectively. The three components has zero entropy ($STE = 0\%$) at the same time in 17/41 MCs and 1/41 sheath. The plasma sheath region with $STE = 0\%$ corresponds to event number 06 in Table A.1.

Figure 6.2 shows a histogram of STE derived from 6.1 for the B_z component corresponding to MCs (in black) and plasma sheaths (in grey) regions respectively. We have 37/41 or 90.2% of MCs with STE less than 40%. However, if we analyze the plasma sheath, then the result is exactly opposite, we found 37/41 or 90.2% of sheaths with STE larger than 40%. This shows the large difference between the two regions: the sheath is a turbulent region (CHIAN; MUÑOZ, 2011) where the plasma and magnetic field typically accumulate in ahead of the MC and cause fluctuations in the magnetic field. Thus, the time series could have more noise and therefore large STE values. On the other hand, the magnetic configuration of a MC is described

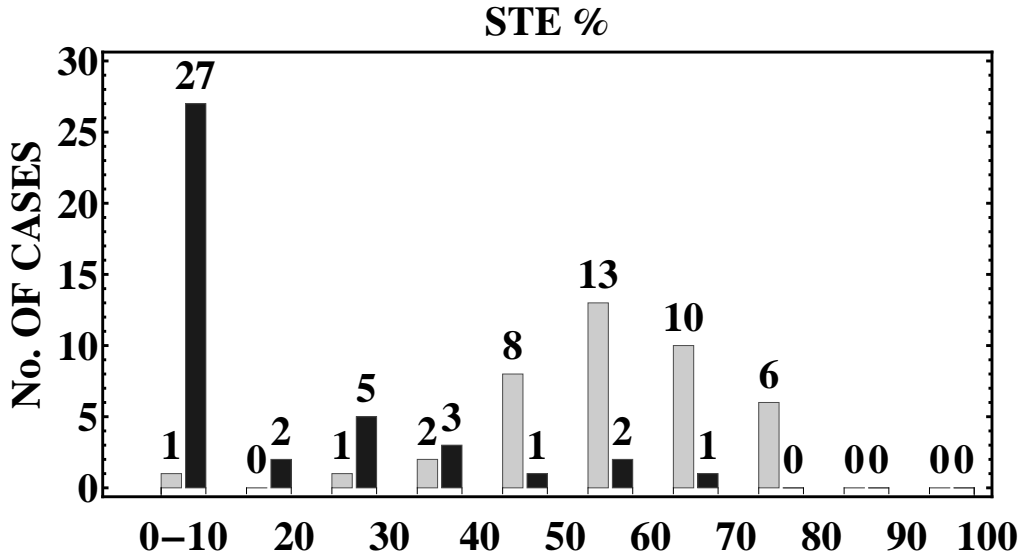


Figure 6.2 - A histogram of STE derived from Figure 6.1 for B_z corresponding to MCs regions (in black) and plasma sheaths regions (in grey) respectively.

by a flux-rope with cylindrical geometry where the magnetic field has slow rotation along one day, increasing the trend and decreasing the noise and therefore the STE values decrease. Low entropy structures were found in the SW (e.g. Neugebauer et al. (2004)), and physically we expected to find low entropy in the cloud. But the new result shows that large amount of MCs with $STE = 0\%$ has been found.

We did some tests with time series to explain the above results. First, if the Gaussian noise is removed from the signal and the STE is calculated, the STE value tend to decrease in less than 5% from its initial value. Second, when a trend is removed of the time series through a rotation (with the angle of slope line of best fit) the STE varies, but still the three components had $STE = 0\%$ at the same time in 17/41 MCs and 1/41 sheaths (see Figure 6.5, top panel). Third, by removing the trend through the first order difference in time series (see Figure 6.3). After that, there are still MCs with $STE = 0\%$.

In Figure 6.3 the study is the same as in Figure 6.1, but we have eliminated the trend through the first order difference in time series as mentioned in Section 5.1. In this case, most of calculating the STE values of all three components increased to $\sim 90\%$ in the plasma sheaths. Figure 6.4 shows a histogram of STE values in B_z component of MCs and sheaths derived from Figure 6.3. If we eliminate the trend in the time series, then the STE value increase. Leaving now 11 of a total of 27 MCs

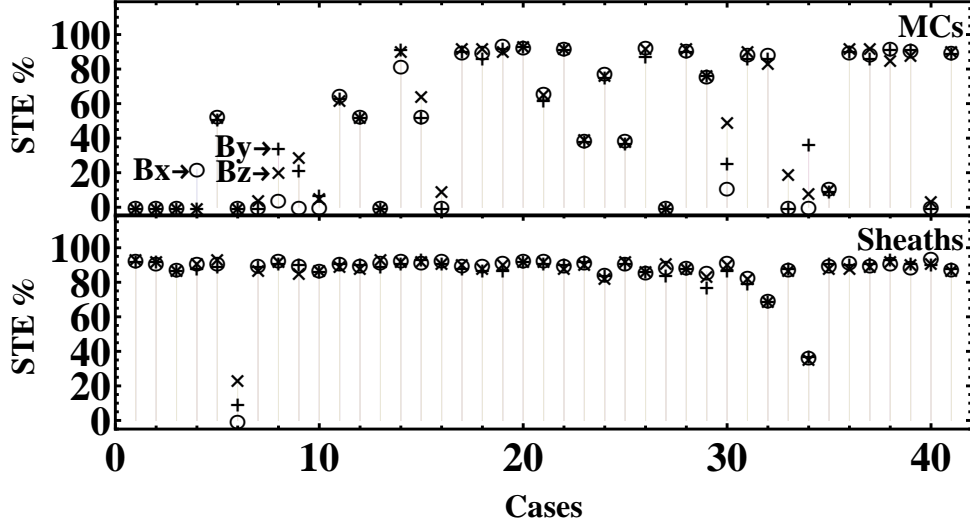


Figure 6.3 - Format is the same as in Figure 6.1, but the trend was removed through the first-order differences at the time series.

(see Figure 6.2) with STE values between 0% and 10%. Also the STE increases in the MC region, but there are still MCs with zero STE value.

Due to a software limitation, presented earlier (Figure 5.2), we investigated the effect of the length of the time series that have studied in Figure 6.1. Then, in Figure 6.5 (top panel), a plot of STE versus length of B_z time series for all MCs are shown. The “o” and “+” symbols correspond to the original and transformed (removing the Gaussian noise and “trend” through a rotation about the origin) time series respectively. A vertical line was drawn in the point with $length(B_z) = 5500$ points. To the right of the vertical line, due to a software limitation (this was discussed in the end of Section 5.1.1) the STE value is zero.

In Figure 6.5 (bottom panel) the histogram of the original or untransformed time series helps to identify overlapping points of MC that are shown in the top panel. Exist a total number of 17/41 MCs with zero STE values to the right of the vertical line. These are the events 1–4, 6–10, 13, 16, 27, 30, 33–35, 40 shown in Table A.1. This is a problem because the larger MCs are just the best structured. However, there still 9/41 MCs with zero STE values to the left of the vertical line, these are the events 5, 12, 21, 23–25, 31, 32, 37 shown in Table A.1. Event No. 38 has $STE = 6\%$ and complete the total of 27 events with STE between 0–10% shown in the histogram at Figure 6.2.

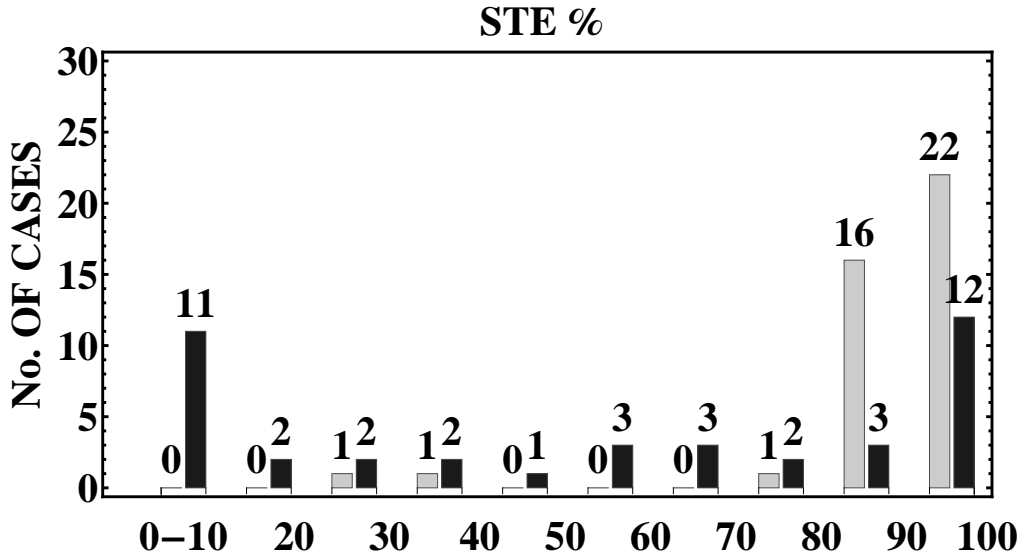


Figure 6.4 - A histogram of STE derived from Figure 6.3 for B_z corresponding to MCs regions (in black) and plasma sheaths regions (in grey) respectively.

In Figure 6.5 the STE values of the transformed time series (“+” symbol) increase and it are different from zero in the MC with less than 5500 points. The smooth increase of trend occur in time series of IMF in a MC and it is caused by the travel of an organized structure in form of flux-rope, crossing the spacecraft. The trend grows smoothly for the IMF in a MC with length less than 5500 and are the main causes of lower STE values. Since the STE results of this tool can be affected by the trend, this tool could be useful in computational applications to identify MC regions but not boundaries of them.

In Figure 6.6 the study is the same as in Figure 6.5, but for the plasma sheaths regions. The length of the sheaths have less points than the MCs, only one sheath had more than 5500 points, the event number 6 shown in Table A.1. Both histograms at the Figures 6.5 and 6.6 are only builded to help in the visualization of the distribution of lengths at the top panels of it. The main result is that the STE values in the sheaths, of the transformed time series (“+” symbol), are approximately the same as the original (“o” symbol) time series. We conclude that the trend in the plasma sheath is less important and STE have large values.

To study the true STE values of the MC with more than 5500 points and overcome the software limitation, we have two options: (1) select data with other temporal resolution (i.e., it to become poor the data information); or (2) select a MC sample

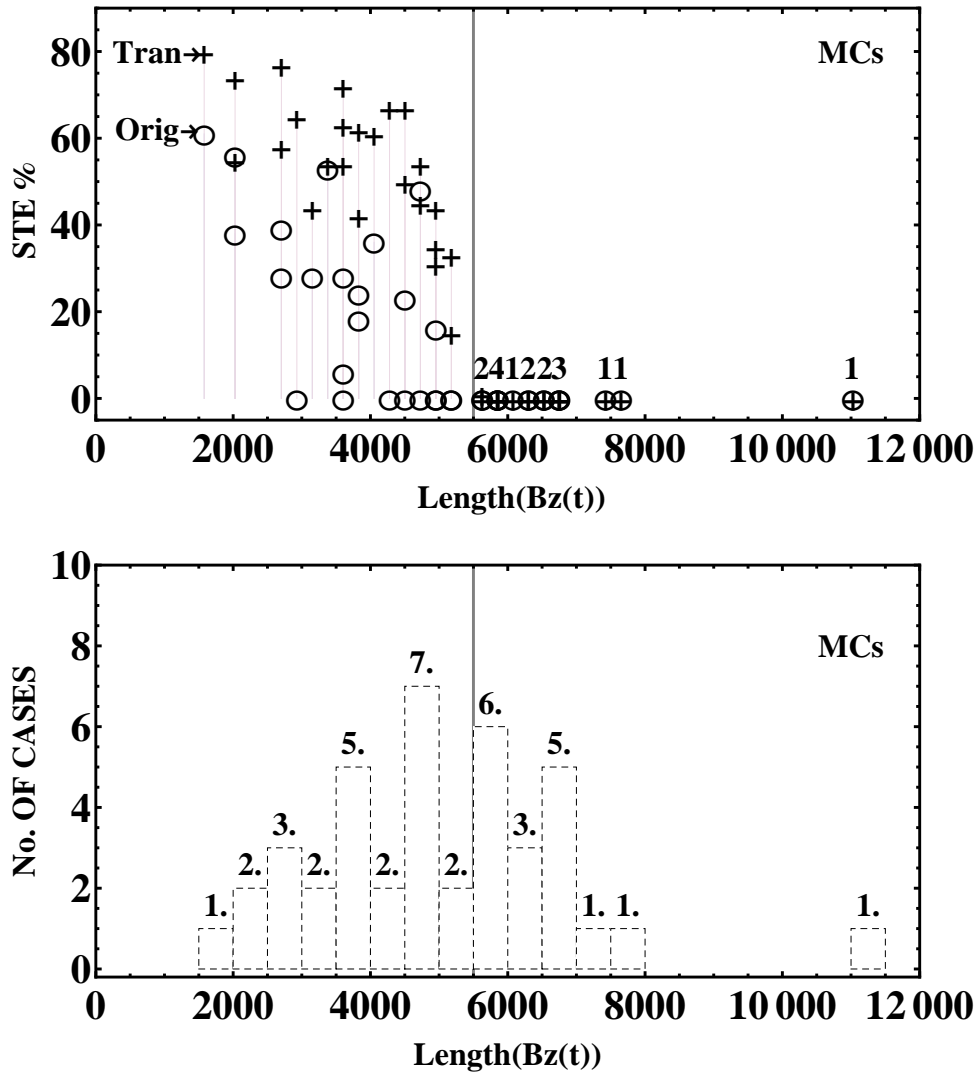


Figure 6.5 - (top panel) STE values versus length of B_z time series using 41 MCs, where the “o” and “+” symbols corresponds to original and transformed (remove the Gaussian noise and trend through a rotation) time series respectively. To the right of the vertical line, larger clouds are shown, and by the software limitation the STE values are zero. (bottom panel) The histogram helps to identify overlapping points of MCs in the top panel.

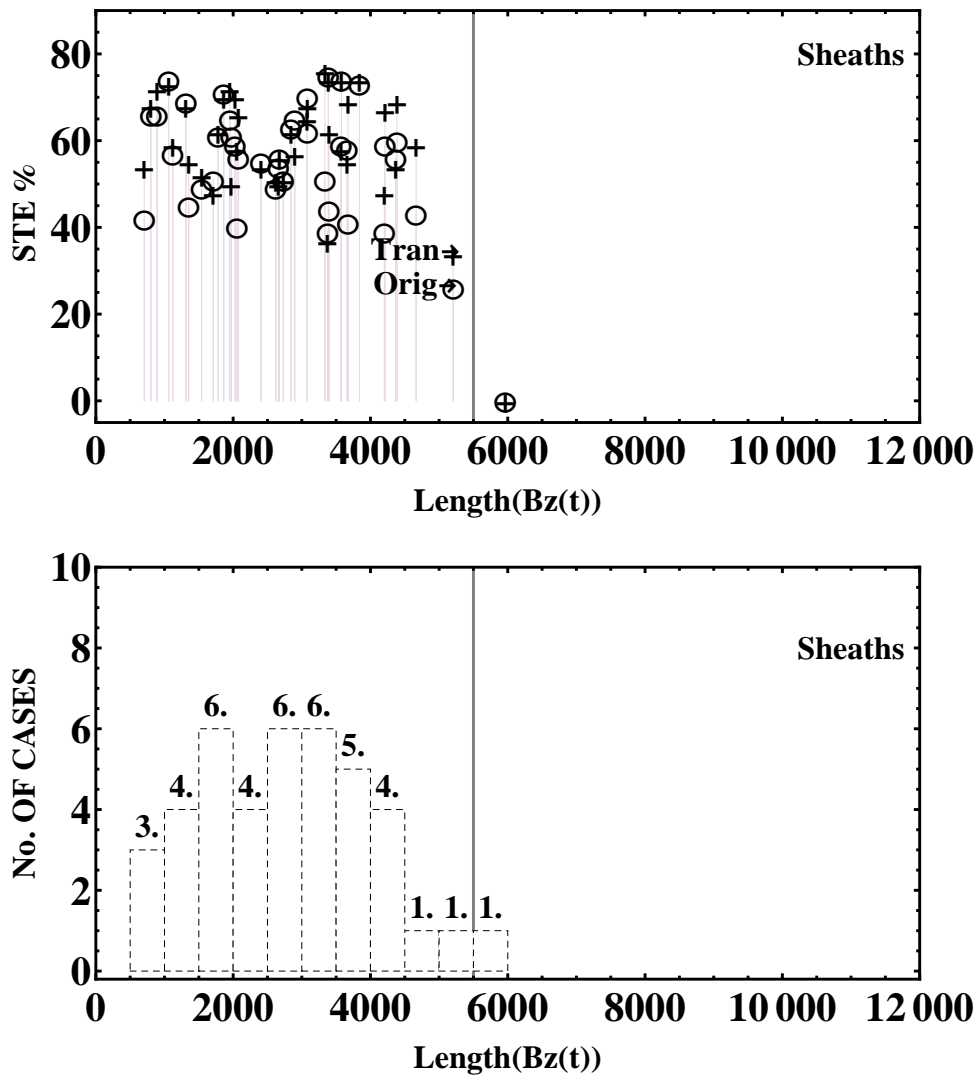


Figure 6.6 - In both panels, the format is the same as in Figure 6.5, but STE values 41 plasma sheaths are plotted. (bottom panel) The histogram helps to identify overlapping points of sheaths in the top panel.

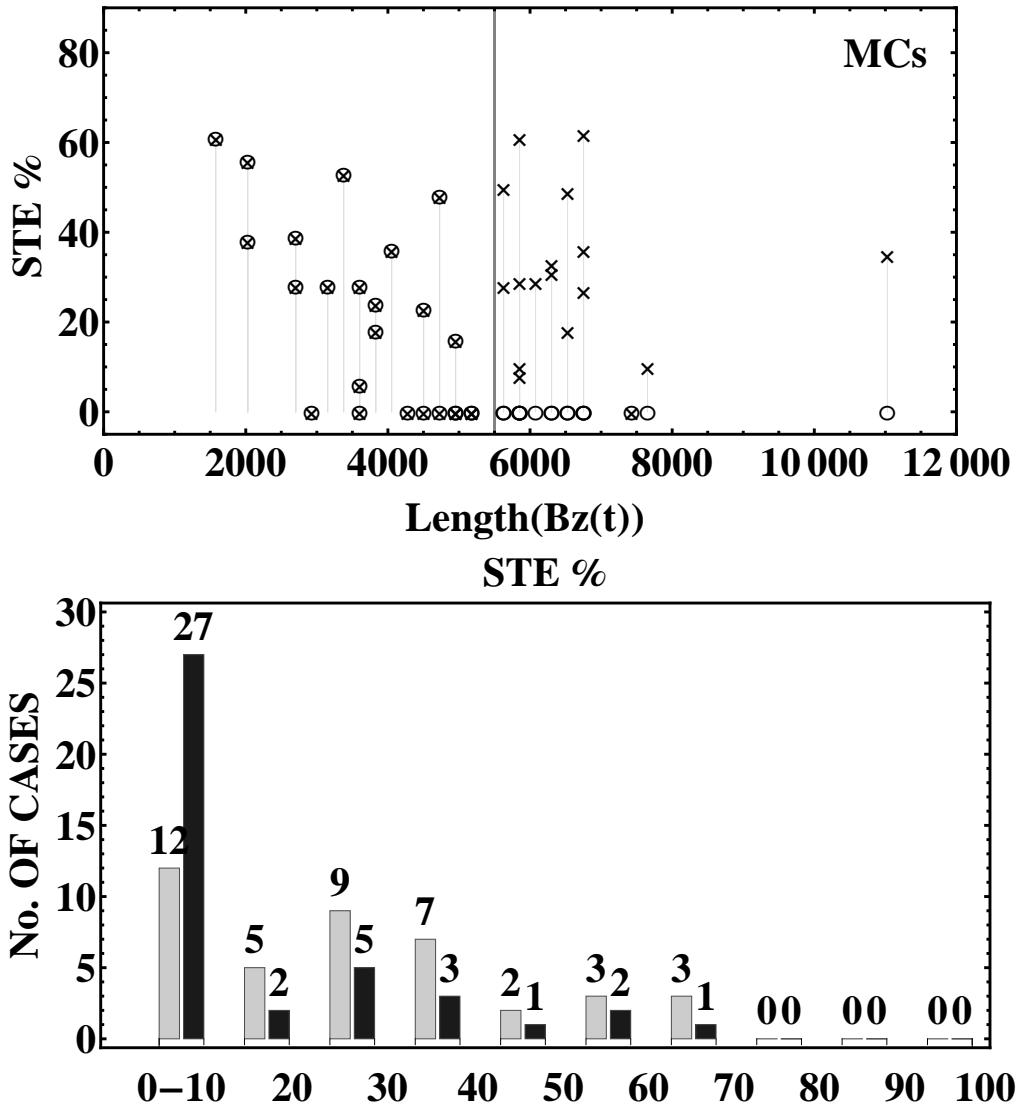


Figure 6.7 - We selected MCs sample with less of 5500 points, taking the intervals between the positions 500 until 4500 in IMF B_z . (top panel) The “o” and “x” symbols correspond to non-transform and transformed (reduced to 4001 points) time series respectively. (bottom panel) A histogram of STE derived from top panel corresponding to transformed (in grey) and non-transform (in black) of B_z time series.

with less than 5500 points. We performed option 2, taking the intervals from the positions 500 (to avoid effects caused by the identification of the boundaries) to 4500 in IMF B_z . Thus, the length of the time series is reconstructed with 4001 data points. These 17/41 cases are represented by “×” symbol are shown in Figure 6.7 (top panel); the “○” symbol represent non-transform MCs similar to 6.5. In the right hand of the vertical line, the MCs sample (“×” symbol and 4001 data points) are plotted in the position with same length of non-transform MCs (“○”). Only 1/17 case remains with zero STE and a total of 4/17 events remains with STE less than 11%. To make a better comparison, the histogram in the bottom panel at Figure 6.7 was built. We have 33/41 or 80.5% of MCs with STE less than 40%. Still a good percentage (80.5%) that enables us to keep the findings of low STE in MCs.

A physical interpretation can be established as following:

It was observed during the data processing that entropy values less than 40% could appear only in one or two of the IMF components. This has a physical explanation: magnetic field axis of a magnetic flux-rope in a MC could have different inclinations. Then, the trend of IMF components is larger in one plane or direction. It is advisable to work in a reference frame found by a MVA analysis. So far, we have been seeking the causes of the large amount of MCs with $STE = 0\%$. During a MC, the magnetic field strength is higher than the average, the magnetic field direction rotates smoothly through a large angle, then the periods with MCs present more trend in the magnetic behavior than the periods of sheaths or quiet SW. The trend is the principal cause of the lower STE values in MC. Also, the MCs are more structured than sheath and quiet SW.

To demonstrate quantitatively all results that have been shown up here, a simple solution for a cylindrically symmetric force-free field with constant alpha (LUNDQUIST, 1950; LUNDQUIST, 1951) was studied. Burlaga (1988) studied the above solution to describe the types of signatures observed in the SW at 1 AU when MCs travel through of a spacecraft. And the kinds of variations of the magnetic field direction of the MC in the spacecraft can be reproduced by this model. Burlaga (1988) concluded that the observed magnetic field profiles depend on the position and orientation of the MC axis. We written the force-free model solution as Burlaga (1988):

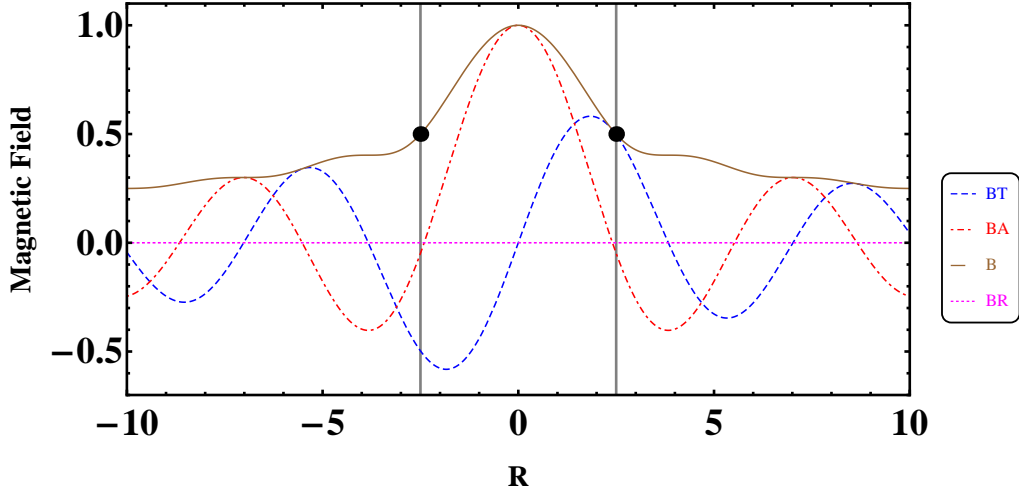


Figure 6.8 - The force-free model solution (axial, tangential and radial components and total magnetic field) as solved in Burlaga (1988) were plotted. Following Burlaga (1988), we show the boundaries with two vertical lines at the points where $B_A = 0$, i.e. where $\alpha \cdot R = 2.4$ and $B/B_0 = 0.5$, also $\alpha = 1$.

$$\begin{aligned}
 \text{Axial component : } B_A &= B_0 J_0(\alpha R), \\
 \text{Tangential component : } B_T &= B_0 H J_1(\alpha R), \\
 \text{Radial component : } B_R &= 0, \\
 \text{Total magnetic field : } B &= \sqrt{B_A^2 + B_T^2 + B_R^2}, \quad (6.1)
 \end{aligned}$$

where $H = \pm 1$, the sign providing the handedness of the field helicity, and where B_0 is an estimate of field at the axis of the cloud and R is the radial distance from the axis, J_0 and J_1 are the Bessel function of the first kind of order 0 and 1. In Figure 6.8 the above equations were plotted. The magnitude of the magnetic field at any instant is B , which decreases from a maximum B_{max} on the axis of the MC to $\sim 0.5B_{max}$ at the outer boundary. Following Burlaga (1988), we show the boundaries with two vertical line in Figure 6.8, as the points where $B_A = 0$, i.e. where $\alpha \cdot R = 2.4$ and $B/B_0 = 0.5$.

Time series with 2001 points inside the boundaries of the cloud shown in Figure 6.8 are constructed. On other hand, we obtained the recurrence plots of B_A , B_T and B respectively. After that, the STE values are calculated; with the STE of $B_A = 27\%$;

STE of $B_T = 0\%$; STE of $B = 25\%$.

Time series with 2001 points inside the boundaries of the cloud shown in Figure 6.8 are constructed. On other hand, we obtained the recurrence plots of B_A , B_T and B respectively. The recurrence plots of B_A , B_T are shown in Figures 6.9(a) and 6.9(b) respectively. After that, the STE values are calculated; with the STE of $B_A = 27\%$; STE of $B_T = 0\%$; STE of $B = 25\%$.

Those low STE values are the physical justification of our results. If the spacecraft crosses near the cloud axis then zero entropy values of some IMF components of the structure are consequences of a nearly cylindrically symmetric force-free field. These results reinforce our initial hypothesis that STE could be established as a feature or tool to help in analysis of IMF data for the MC identification, mainly when the only measurements obtained by satellites are the IMF.

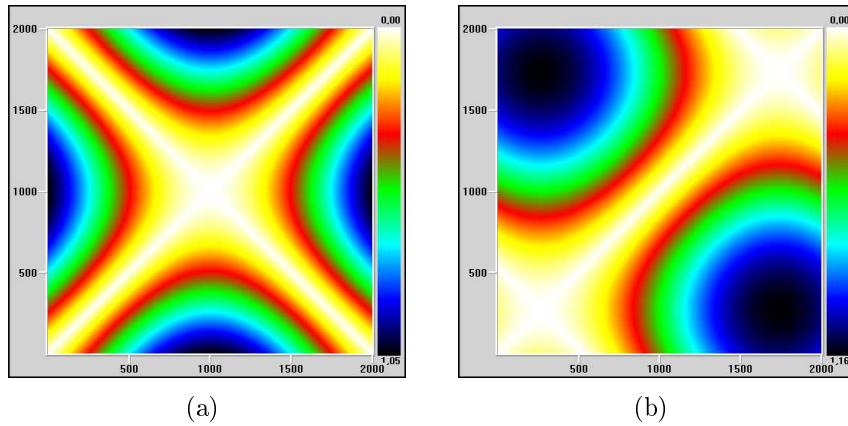


Figure 6.9 - RPs of the solution for a cylindrically symmetric force-free field with constant alpha are shown. (a) Axial component : $B_A = B_0 J_0(\alpha R)$, $STE = 27\%$. (b) Tangential component : $B_T = B_0 H J_1(\alpha R)$, $STE = 0\%$.

To understand better the STE behavior, we calculate the STE values versus trends presents in IMF data. The analysis has followed the same idea presented in Subsection 5.1.1. In Figure 5.1, we presented time series plot of Lorenz data file include in the VRA for four different trend angles. We mentioned earlier that MCs time series are not stationary, there is a trend. The linear least squares fitting technique is the simplest and most commonly applied form of linear regression and provides a solution to the problem of finding the best fitting straight line through a set of

points and to obtain the equation of the line. The angle θ that a line makes with the positive x axis is closely related to the slope m via the inverse tangent function $\theta = \tan^{-1}(m)$.

To illustrate the idea, a few events are considered for a quantitative result. We applied the previous methodology to all IMF time series shown in the Figures 5.5, 5.6, 5.7, 6.19, 6.27. Thus, we separate all pairs of points formed by the trend angle θ and STE for the data.

The top panel of Figure 6.10 shows the B_X component. At the top, the plot of STE versus θ or trend angle where a parabola is fitted to the data; at the bottom, the corresponding histogram where a Gaussian distribution is fitted. The other two panels (middle and bottom) are shown the same graphic, but to B_Y and B_Z components respectively. At B_X panel, on the plot of STE versus θ , the correlation coefficient (a Pearson's correlation coefficient between two time series, STE vs θ) is $C = -70.8\%$. If the variables tend to go up and down in opposition, with low values of one variable associated with large values of the other then the correlation coefficient will be negative (anti-correlation), as is shown in Figure 6.10. The anti-correlation between STE and θ gives the idea that the trend in the B_X series is responsible for the lowest STE values. But the above idea is not totally true; because we have points of $STE \neq 0\%$ with large trend, i.e. see the more separated points of the vertical line. One explication to these kinds of problems can be the existence of fluctuations in the signal. In the three figures, the histogram show the distribution of the trend angle. Sometimes, the trend in the records for a plasma sheath region is larger than the trend for a cloud, but the plasma sheath has rapid fluctuations that changes the sign of the signal and the STE is not zero.

Then the $STE = 0\%$ at magnetic clouds is related to the simultaneous occurrence of two factors: (1) the trend existing in the signal, (2) the analyzed variable has a more ordered dynamical behavior (*i.e.* few fluctuations) and higher degree of correlation between its time neighbors.

The correlation coefficient, for B_Y , from STE versus θ is $C = -67.6\%$ and for B_Z is $C = -65.7\%$. From the three panels, it is possible to see that B_Z component has largest trend compared to the others two cases. This is because B_Z is the only component that is not contained in ecliptic plane. The construction of the Figure 6.10 was done with 46 days of SW data. The MCs contained in these data are bipolar,

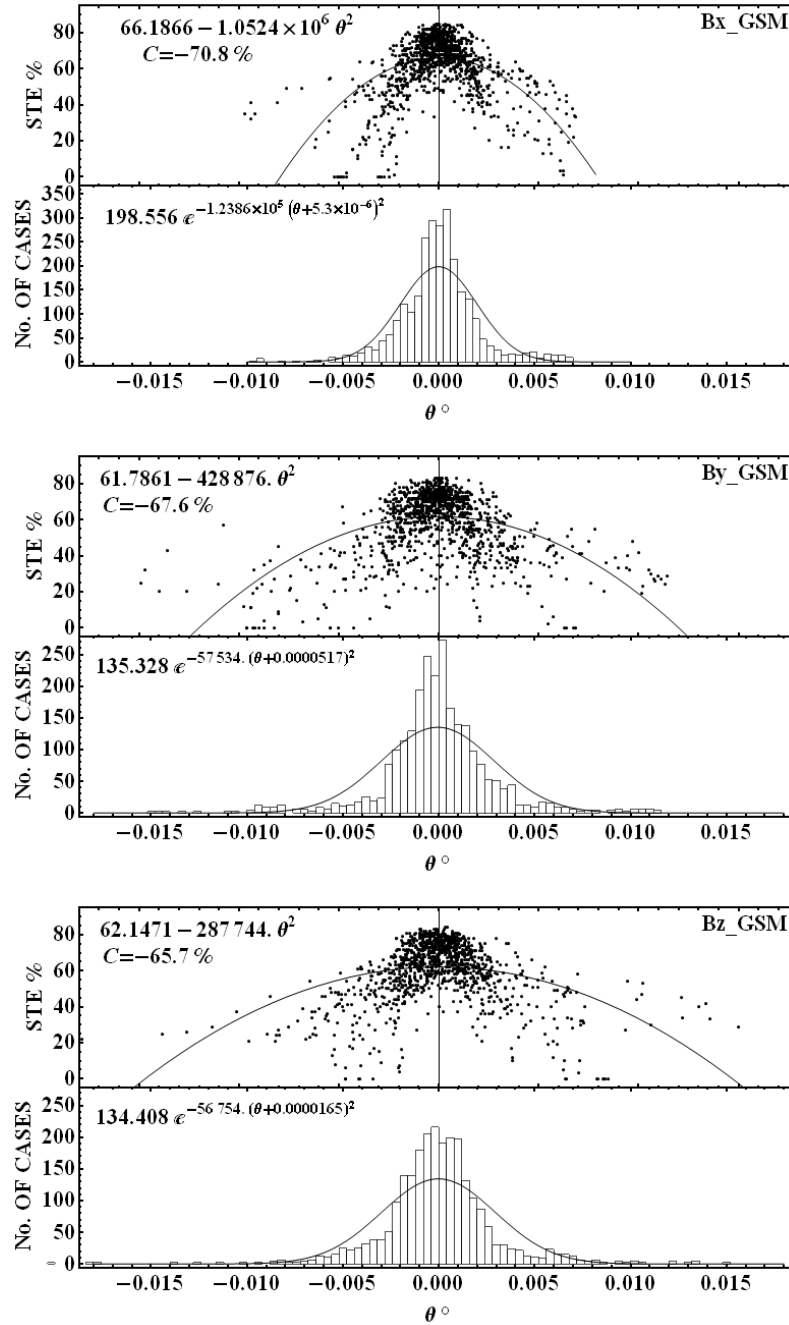


Figure 6.10 - At top: Plot of STE versus θ to B_x , B_y and B_z components and a parabola fitted to the data. At bottom: The corresponding histogram in which a Gaussian distribution is fitted.

i.e. the idealized sketch is a cylindrical magnetic flux tube which moves radially away from the Sun (see Figure 2.6). Thus in GSE coordinates system, B_Z , B_Y , B_X are approximately the components of maximum, intermediate and minimum variance or trend.

6.2 Part II: Results related to the MC characterization

Initially, the persistence analysis is done to establish a preliminary categorization of the periods in the SW related to the MC occurrences.

6.2.1 Persistence analysis on the IMF variation

The methodology that uses the persistence exponents (see section 5.1) for the group of 41 events is generalized. Using Equation 5.5 the $\langle\beta\rangle$ values are calculated. Its values for the 41 MC events are shown in Figure 6.11(a). The three time intervals corresponding to the sheath, the MC and after the MC with the same size of the precedent cloud. It were plotted as “□”, “⊗” and “△” symbols respectively. The error bar represents the standard deviation for each value. It shows the power spectral density (PSD) scaling exponent $\langle\beta\rangle$ as a self-affine fractal ($1 < \langle\beta\rangle < 2$) but there is not a pattern that allows the separation of MC from the other two cases; exist a total of 18/41 events where the clouds do not have the larger values. We provided comments in Subsection 5.1.2 about limitation of this tool, fundamentally to the nonstationarity of the time series .

For short time series, DFA can detect the correlation length more accurately than the PSD scaling exponent (β) (VERONESE et al., 2011). The alpha exponent is not affect by spectral variance and leakage and is possible to use in non-stationary time series. Figure 6.11(b) has the same format that 6.11(a), but is builded for $\langle\alpha\rangle$ exponent using the Equation 5.6. The results show $\langle\alpha\rangle$ values between 1.0 and 1.6, in other words, long-range persistence and some MCs with typical values of a Brownian noise ($\langle\alpha\rangle \cong 1.5$). If we compare the $\langle\alpha\rangle$ values between the same components for the sheath (“□”) and the MC (“⊗”) regions then in 38/41 cases the $\langle\alpha\rangle$ value in the cloud is larger than the one in sheath respectively. We have some exceptions, the events 5, 20 and 25 that shown in Table A.1. We did not stop to examine these cases in detail, it are few for the statistics of 41 cases. Nevertheless, it is recommended to study in the future, because we think that could be need to re-define the cloud boundaries or there are two clouds (as the two cases, that will be discussed in this

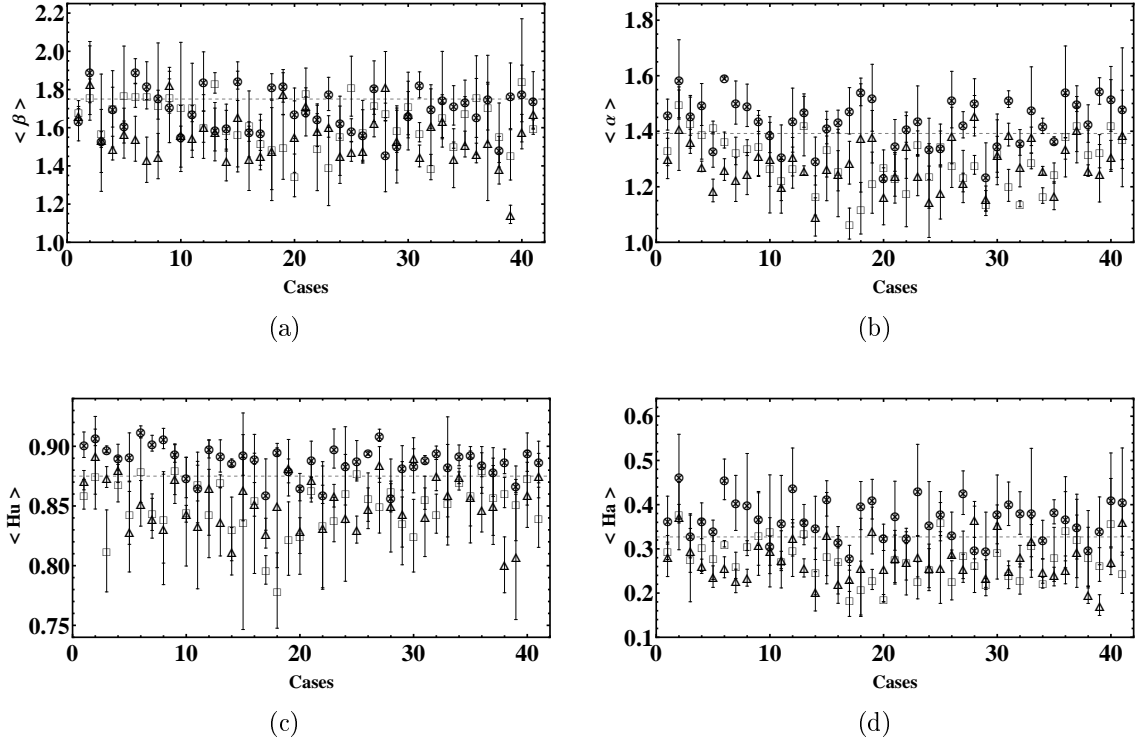


Figure 6.11 - In (a), the PSD scaling exponent $\langle \beta \rangle$ values versus number of events (see Table A.1) were plotted, where (“□”), (“⊗”) and (“△”) symbols corresponds to the sheath, MC and after MC regions respectively. The other panels (b), (c) and (d) are similar to (a) but for $\langle \alpha \rangle$, $\langle H_u \rangle$ and $\langle H_a \rangle$ exponents respectively. The results in the four panels show long-range persistence in IMF time series ($1 < \langle \beta \rangle < 2$, $1 < \langle \alpha \rangle < 1.6$, $0.75 < \langle H_u \rangle < 0.95$ and $0.1 < \langle H_a \rangle < 0.5$). A increase in the persistence exponents in the magnetic cloud regions are shown. The persistence in IMF time series of some magnetic clouds are such as a Brownian motion. The horizontal dashed line is a threshold derived from Figure 6.13

chapter).

Also, the Hurst exponent was presented in Section 5.1 as an useful methodology to study MCs. Using the Equation 5.7, the $\langle H_u \rangle$ exponents in the three regions are calculated. Figure 6.11(c) has the same format that 6.11(a) and 6.11(b), but for $\langle H_u \rangle$ exponent. Similar to 6.11(b), the $\langle H_u \rangle$ exponents have larger values in the MC. Nevertheless, 4/41 MC (events 11, 19, 28 and 30) does not have largest $\langle H_u \rangle$ exponents in the region of the MC. None of this cases coincide with the three events (5, 20 and 25) when the alpha exponent is used. This draws attention to have a certain degree of distrust in the identification of these clouds, but also suggest that all techniques must be used together to increase the confidence level in the results. Still in 34/41 events both exponents have largest values in the cloud region.

The last tools to use is the Hausdorff exponent (H_a). To calculate the mean Hausdorff exponents, the Equation 5.8 is used. In Figure 6.11(d), the $\langle H_a \rangle$ exponents have largest values in the MC regions, only 2/41 MC (events 10 and 28) does not have highest $\langle H_a \rangle$ exponents. Thus, this tool showed the best results.

In conclusion, the PSD scaling exponent is not a suitable tools to study persistence in IMF components in the SW. Nevertheless, the other three exponents are suitable to study persistence, and the exponents values has increased in the cloud region. It means that the three exponents report the largest persistence in 33 of total 41 cloud regions. In 80.5% of the cases studied these tools were able to separate the region of the cloud of neighboring regions.

To make a comparison between all events, it is necessary to build a histogram. In Figure 6.12(a), the histogram is builded from a frequency table of $\langle \beta \rangle$ values plotted in Figure 6.11(a). The $\langle \beta \rangle$ values for the sheath, MC and after MC (AFTERMC) regions where plotted as gray, black and white bar respectively. We see an uniformity in the distribution of all bar between $1.5 < \langle \beta \rangle < 1.8$. For $\langle \beta \rangle < 1.5$, we have 7/41 sheath, 2/41 MC and 15/41 AFTERMC events, while for $\langle \beta \rangle > 1.8$ we have 3/41 sheath, 9/41 MC and 3/41 AFTERMC events respectively. Although the calculation of $\langle \beta \rangle$ is not a completely reliable value but the largest values of $\langle \beta \rangle$ are in the MC regions.

Figure 6.12(b) has the same format that 6.12(a), but for $\langle \alpha \rangle$ exponent. For $\langle \alpha \rangle > 1.4$, we have 6/41 sheath, 29/41 MC and 3/41 AFTERMC events respectively. So, we

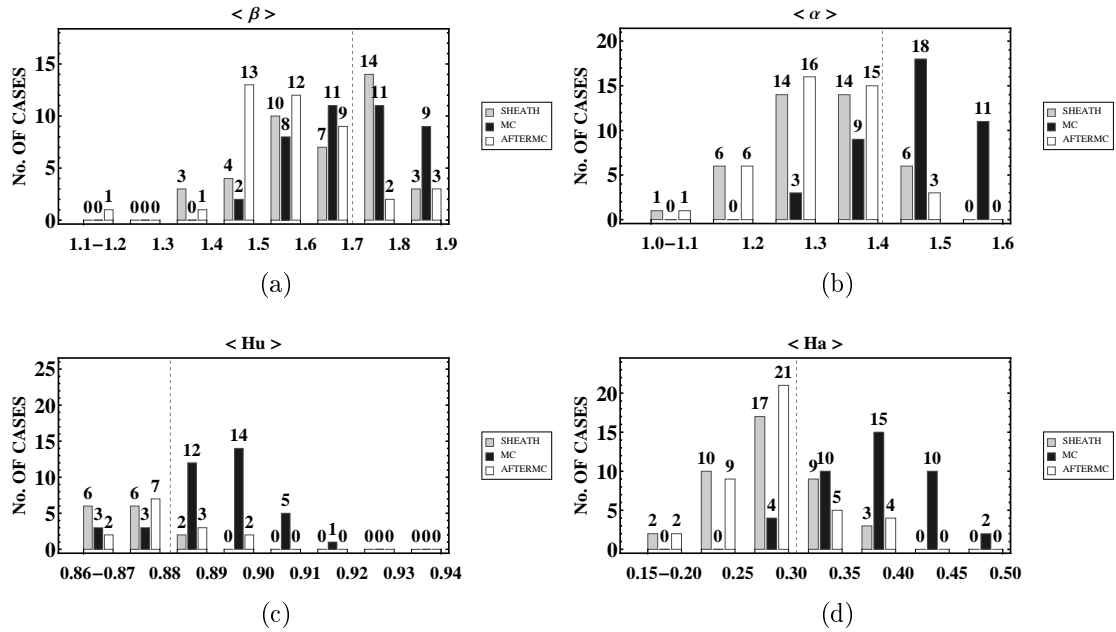


Figure 6.12 - In (a), a histogram is construct from a frequency table of $\langle \beta \rangle$ values plotted in Figure 6.11(a). We want to have a better view of the distribution of $\langle \beta \rangle$ values between the three regions. The other panels (b), (c) and (d) are similar to (a) but for $\langle \alpha \rangle$, $\langle H_u \rangle$ and $\langle H_a \rangle$ exponents respectively.

have many MCs with the largest alpha values. For $1.0 < \langle \alpha \rangle < 1.3$ the number of events by regions are 21/41 in the sheath, 3/41 in the MC and 23/41 in the AFTERMC. In MC events, the separation of the $\langle \alpha \rangle$ values to the right corner is an interesting result. In the Figure 6.12(c) and 6.12(d), approximately 30/41 MC events have the largest values of the persistence exponents. A persistent value increase in the MC is observed. One difficulty to study the persistence between time series is the dimension of it (VERONESE et al., 2011). As was shown in Figure 6.6, the dimension of the cloud is larger than the plasmas sheath. However, we can see a pattern in the persistence values between all MC events. We believe that these results are valid, because we know that MCs are organized structures of plasma and that creates a certain increase of memory in the time series.

We considered a better way to view these results. Thus, the average values for each exponent from 41 events and for each of the three regions are calculated respectively.

The equations for calculating the average values are:

$$\langle \beta \rangle_T = \frac{1}{N} \sum_{i=1}^N \langle \beta \rangle^{(i)} \quad (6.2)$$

$$\langle \alpha \rangle_T = \frac{1}{N} \sum_{i=1}^N \langle \alpha \rangle^{(i)} \quad (6.3)$$

$$\langle Hu \rangle_T = \frac{1}{N} \sum_{i=1}^N \langle Hu \rangle^{(i)} \quad (6.4)$$

$$\langle Ha \rangle_T = \frac{1}{N} \sum_{i=1}^N \langle Ha \rangle^{(i)}. \quad (6.5)$$

with $N = 41$.

The calculation of the standard deviation shows, how much variation or dispersion exists from the average. If we build a rectangular area using the mean and standard deviation then we have a validity region where join up all exponents. Following the above idea, the panels of Figure 6.13 were builded. In Figure 6.13(a) the black points are $(\langle \alpha \rangle_T, \langle \beta \rangle_T)$ in each one of three regions, from 41 events plotted in the Figures 6.11(a) and 6.11(b). For 2D graphic, filling is done in the x and y directions between the standard deviation of the mean, and the shade rectangular regions are the set of validations of the persistence for each regions. Thus, the graph allows a conjugate analysis of persistence. In Figure 6.13(a), we see in $\langle \beta \rangle_T$ axis that the MC is the region with the largest average value. But, shade rectangular regions are overlapping. It is not possible to separate the MC region. Still, the result is important because we can see that persistence is large in the MCs. On the other hand, if we see the $\langle \alpha \rangle_T$ axis 75% of the shade rectangular regions, are not overlapping. The MCs have $\langle \alpha \rangle$ values between 1.39 and 1.54. A vertical dashed line is drawn in the point 1.392. We propose, use this value as a threshold when the alpha exponent is calculated in a MC regions. Also, this values could be useful to create a identification methodology of MCs as shown in Section 5.2.4.

In Figure 6.13(b) has the same format that 6.13(a) but in the y axis $\langle H_a \rangle_T$ was plotted. Along $\langle H_a \rangle_T$ axis, the shaded rectangular region corresponding to the MC is less overlap with other regions than seen in the previous Figure 6.13(b). Only the MCs have $\langle H_a \rangle$ values between 0.32 and 0.42. A horizontal dashed line is drawn in

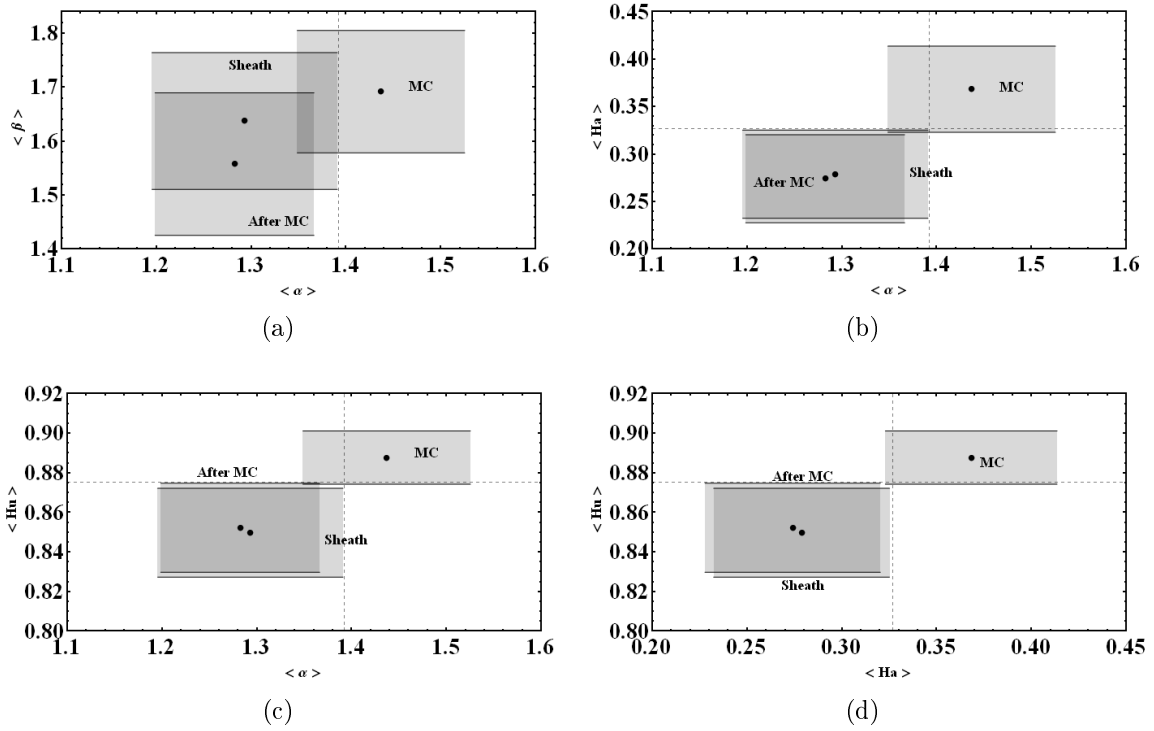


Figure 6.13 - In (a), the black points are $(\langle \alpha \rangle_T, \langle \beta \rangle_T)$ in each of three regions, of the 41 events plotted in the Figures 6.11(a) and 6.11(b). We calculate the standard deviation of the mean for each persistence exponent that was shown in the Equation 6.2. For 2D graphic, filling is done in the x and y directions between the standard deviation of the mean. The filling rectangular regions are the set of validations of the persistence for each regions, $(\langle \beta \rangle_T \pm \sigma)$ vs $(\langle \alpha \rangle_T \pm \sigma)$. The other panels (b), (c) and (d) are similar to (a) but for other exponents combinations i.e.: (b) $(\langle H_a \rangle_T \pm \sigma)$ vs $(\langle \alpha \rangle_T \pm \sigma)$; (c) $(\langle H_u \rangle_T \pm \sigma)$ vs $(\langle \alpha \rangle_T \pm \sigma)$; (d) $(\langle H_u \rangle_T \pm \sigma)$ vs $(\langle H_a \rangle_T \pm \sigma)$.

the point 0.327.

Figure 6.13(c) has the same format that 6.13(a) and 6.13(b) but in the y axis $\langle H_u \rangle_T$ was plotted. Also the MCs was separated of the other two regions. And the horizontal dashed line is drawn in the point 0.875. The regions with least overlap correspond to the Hurst and Hausdorff exponents respectively. In Figure 6.13(d) $(\langle H_u \rangle_T \pm \sigma)$ vs $(\langle H_a \rangle_T \pm \sigma)$ is plotted. It is the best graphic to separate the MC of the other two regions. The Hurst (R/S) and Hausdorff exponents respectively are good to identified the MC regions.

With these results, we conclude that the persistence values increases in the IMF

components inside of MCs. In this study the investigated period covers the rising phase of solar activity (1998 – 1999), solar maximum (2000) and the early declining phase (2001 – 2003) when defined by the yearly sunspot number. We have a variety of MCs in five year (1998 – 2003) and the rotation of the magnetic field direction can occur in any direction relative to the ecliptic. But there are some MCs where identification is not completely secure. For example, Lepping et al. (1990) show a table¹ with a quality factor (1 = Excellent, 2=Good, 3=Poor) when identify the MC intervals. This methodology can help to evaluate the quality of the identification. After identifying a MC, if their persistence exponents occupy non overlapping regions in Figure 6.13 (panels b, c and d) then the cloud was identified with good quality. Avoid using plasma data is important in this new methodology, because sometime it has large gaps.

6.2.2 Daubechies wavelet analysis on the IMF behavior

To illustrate, we present two case studies based on the analysis of Huttunen et al. (2005), where we applied this methodology to analyze MC periods (events 14 and 16, Table A.1). The study is extended to a total of 41 cases shown in the table, although the results are not presented individually here. In this section, a discussion is done to reach an interpretation.

February 11-13, 2000 ICME event

In Figure 6.14, at the top, we show the time series of IMF B_z component measured by the ACE spacecraft at the date February 11, 23 : 23 *UT*-February 13, 12 : 00 *UT*, 2000. The data was measured in GSM coordinate system with resolution time of 16 s. The three regions under study are separated by two vertical dashed lines. At bottom, we show the square of the first decomposition level of wavelet coefficients, $d1$, and results of D_{d1} . The mean of wavelet coefficient D_{d1} in time series at plasma sheath is $0.828 nT^2$. The result is that the lower D_{d1} ($0.156 nT^2$) corresponds to the MC.

In Table 6.1, the results of D_{d1} for the three components of \vec{B} are presented. Seen in the figure, the MC region in the three components always have the lowest D_{d1} value. While the higher D_{d1} values in all components correspond to the sheath region.

As a previously known feature, the larger amplitude of the wavelet coefficients $d1$

¹http://wind.nasa.gov/mfi/mag_cloud_pub1.html

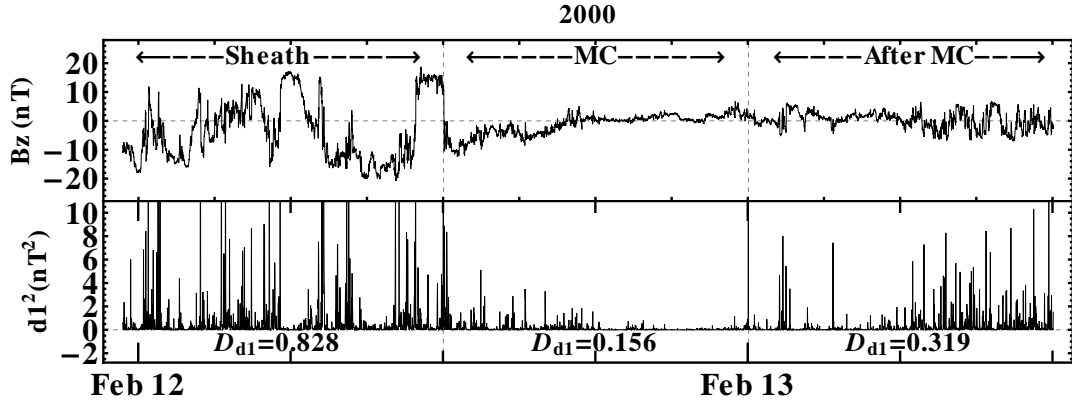


Figure 6.14 - At top, IMF B_z (in GSM system) vs time from the ACE spacecraft with 16s time resolution, at February 11, 23 : 23 UT-February 13, 12 : 00 UT, 2000. At bottom, the square of the first decomposition level of wavelet coefficient d_1^2 vs time for the sheath region (left of the first vertical dashed line), the MC (middle between the vertical dashed lines), and the quiet solar wind (right of the second vertical dashed line). The lower values of D_{d_1} are noticed inside of MC region.

are indeed associated with abrupt signal locally. From a visual inspection of data, detections may not be an easy task; but the wavelet transform aids to find those kinds of phenomena.

Table 6.1 - Mean D_{d_1} of wavelet coefficients.

Events	$D_{d_1} B_x$	$D_{d_1} B_y$	$D_{d_1} B_z$	$\langle D_{d_1} \rangle$
Feb 11-13, 2000:				
<i>Sheath</i>	0.524	0.814	0.828	0.722
<i>Magnetic Cloud</i>	0.093	0.124	0.156	0.124
<i>After Magnetic Cloud</i>	0.177	0.247	0.319	0.248
Jul 11-14, 2000:				
<i>Sheath</i>	0.279	0.270	0.625	0.391
<i>Magnetic Cloud</i>	0.016	0.032	0.042	0.030
<i>After Magnetic Cloud</i>	0.233	0.230	0.458	0.307

July 11-14, 2000 ICME event

In Figure 6.15, a similar study is done. At top, we show the time series of IMF B_z component measured by ACE spacecraft at the date July 11, 11 : 22 *UT*-July 14, 05 : 00 *UT*, 2000. The three regions under study are separated by two vertical dashed lines. At bottom, the square of first decomposition level of wavelet coefficient $d1^2$ vs time is plotted.

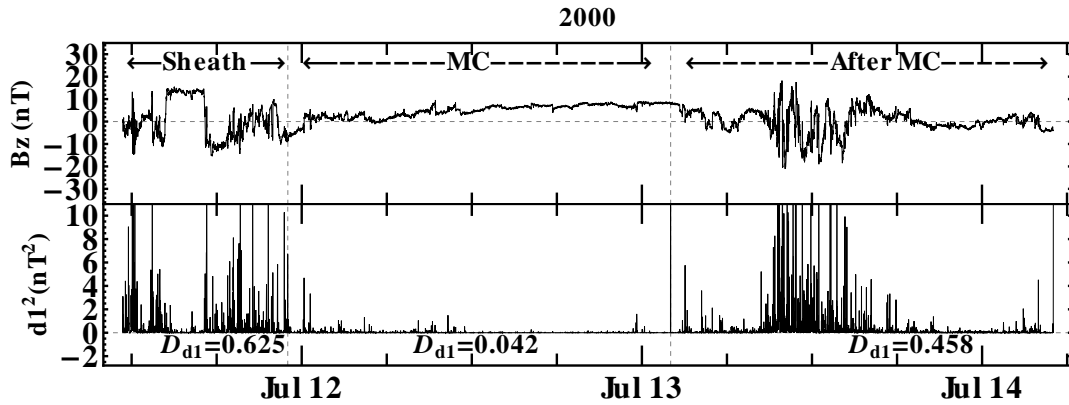


Figure 6.15 - At top, IMF B_z (in GSM system) vs time from the ACE spacecraft with 16s time resolution, at July 11, 11 : 22 *UT*-July 14, 05 : 00 *UT*, 2000. At bottom, the square of the first decomposition level of wavelet coefficient $d1^2$ vs time for the sheath region (left of the first vertical dashed line), the MC (middle between the vertical dashed lines), and the quiet solar wind (right of the second vertical dashed line). The high amplitude of $d1^2$ inside the third region (After MC) is because arrived other event. The lower values of D_{d1} is noticed inside of MC region.

The statistical mean of the wavelet coefficient D_{d1} in the sheath region is $0.625 nT^2$. Again the lower D_{d1} ($0.042 nT^2$) corresponds to the MC region; and the higher D_{d1} ($0.625 nT^2$) corresponds to the sheath region. The higher amplitude of $d1^2$ inside the third region (After MC) is due to the arrival of other event (event 17 in Table A.1).

Related to this case, the results of D_{d1} for the three components of \vec{B} are presented in Table 6.1. Also seen in the earlier figure, the MC region in the three components always have the lowest D_{d1} value. While the higher D_{d1} value in all components correspond to the sheath region.

It can be noticed the tendency of the MC events to have lower values of D_{d1} in comparison with the processes of the other regions. This feature is clear identified using this approach, that can be added to the usual features (BURLAGA et al., 1981) established earlier to the MCs. Also, we found higher D_{d1} values in the sheath. The higher amplitudes of the wavelet coefficients indicate singularity patterns which are identified in the sheath region (see top panel on Figures 6.14 and 6.15).

41 ICMEs events

Aiming to a conclusive analysis, the calculations of D_{d1} for the three IMF components are done for the other cases of Table A.1. The procedure is the same of the case studies.

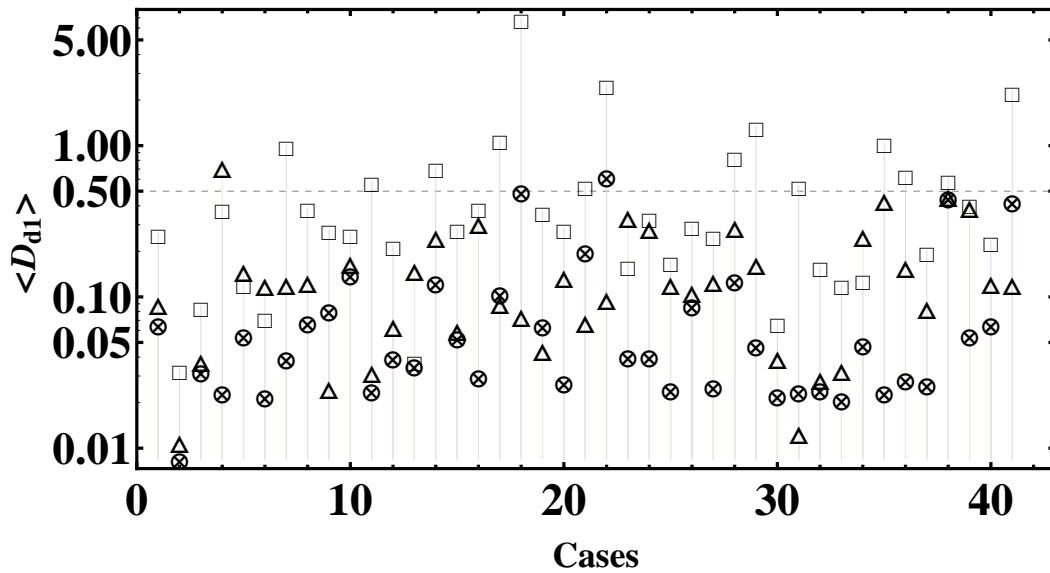


Figure 6.16 - The $\langle D_{d1} \rangle$ values versus number of events were plotted, where (“□”), (“⊗”) and (“△”) symbols corresponds to the sheath, MC and after MC regions respectively. The y axis is plot with a logarithmic scale, because is best to visualization.

In Figure 6.16, the $\langle D_{d1} \rangle$ values versus number of events were plotted, where (“□”), (“⊗”) and (“△”) symbols corresponds respectively to the sheath, MC and after MC regions. We can compare the $\langle D_{d1} \rangle$ values of the three regions for every events. The $\langle D_{d1} \rangle$ values are largest in the sheath region in $35/41 = 85.4\%$ events. This does not occur in the events numbered as 4, 5, 6, 13, 24, 34 in Table A.1, where the

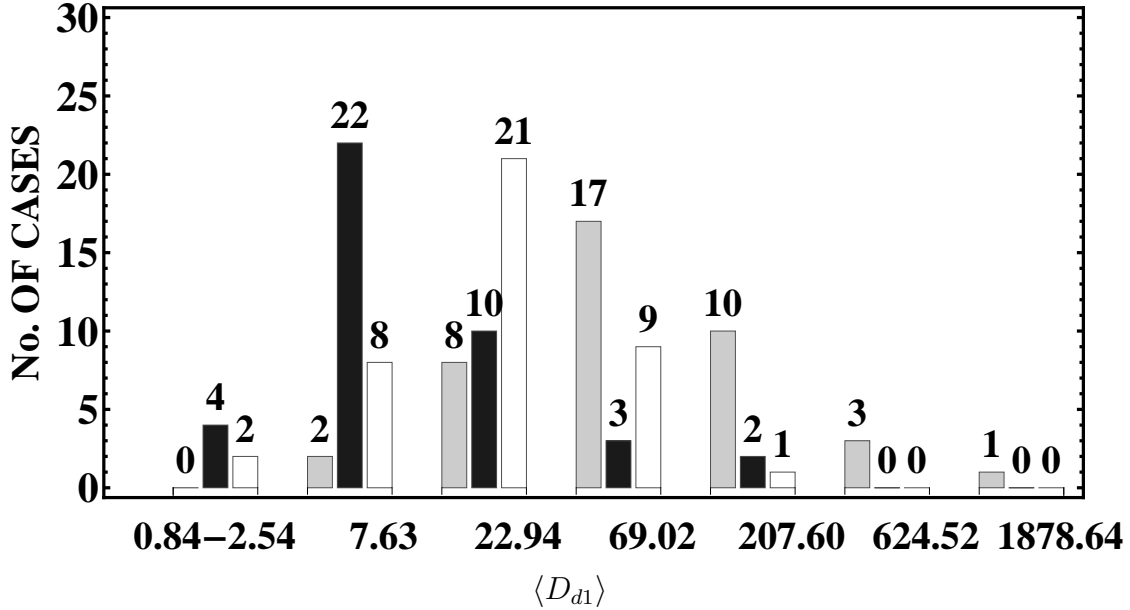


Figure 6.17 - A histogram is constructed from a frequency table of $\langle D_{d1} \rangle$ values, the abscissa axis was normalized by 0.01. The $\langle D_{d1} \rangle$ values for the sheath, MC and after MC, the three select regions, plotted as the gray, black and white.

largest values are found in the “After MC” regions. The explanation is that after MCs as shown in Figure 6.15, there may be an arrival of a shock or an ICMEs. However, the magnetic field fluctuation in the sheath is always larger than one in the cloud that follows. On the other hand, the magnetic field fluctuation in some MC regions (events numbered as 9, 19, 17, 20, 21, 31, 41) is larger than one in the solar wind that follows. The goal is to test the usefulness of this wavelet technique to study fluctuations in the SW data, with details like the few untypical MCs not yet investigated in order to explore any intrinsic physical process.

Figure 6.17 shows a histogram constructed from the occurrence frequencies of the $\langle D_{d1} \rangle$ values. The $\langle D_{d1} \rangle$ values for the sheath, MC and after MC regions are plotted respectively as gray, black and white bins. In this figure, 63.4% of the MCs are located in the first two sets of bars on the left, while there are 4.9% and 24.4% of the sheaths and after MC regions respectively. The wavelet coefficients are low in some sheath regions. That means that, if an ICME is not moving faster than the surrounding SW (KLEIN; BURLAGA, 1982; ZHANG; BURLAGA, 1988; BURLAGA, 1988), the sheath region does not present a very corrugated feature in the magnetic

field. In principle, the identification by visual inspection could be more difficult to be done under this conditions. Conversely, in the last four sets of bars we have 75.6% of the sheaths and only 12.2% of the MCs regions. The results showed in the two previous case studies are confirmed: the bigger amplitudes of the magnetic field fluctuations are in the sheath, and the lower ones are during the MC.

As in Table 6.1, the higher D_{d1} values are found in B_z component for every regions. By direct visual inspection, the most of the time, this detection is not possible. However, the wavelet transform allows finding this phenomenon easily. The B_z component is very important in the magnetic reconnection at Earth’s magnetopause. An open question could be recalled: how important are the fluctuations for the geoeffectiveness? We think that this is an important example of application of this technique in order to evaluate the solar wind fluctuation. Also, the wavelet coefficients can help to obtain a better visualization of the shock and to identify the initial border of the MC.

The wavelet coefficients recover the expected behaviors of the physical processes underlying in the magnetic records. This is understandable, because the MC has a geometric structure in form of flux-rope, unlike the sheath region and the “quiet” SW. The sheath is naturally a turbulent region, presenting many fluctuations in the IMF values with large D_{d1} values. A smoother magnetic field are the cause of the low values of D_{d1} in the MCs regions. The SW after the MC can present an extended quiet behavior, or an increasing of random characteristics, or even turbulences from an arrival event, *e.g.*, the events 16 and 20. The existence of MCs with large values of the wavelet coefficients was unexpected in this study. We have five MCs with this feature, and further they will deserve specific studies.

If this technique is applied to a large dataset IMF, the wavelet coefficients could be also large in other regions in which there are no ICMEs. On other hand, the wavelet coefficients are relatively lower in quiet SW regions. Although it does not allow identifying clouds automatically, it is an useful tool for experts. Because, this technique can be used as auxiliary tools to find cloud boundaries, when, for example, the minimum variance analysis (MVA) is used. In fact, we have used for this purpose. In our opinion, the presentation of this tool for the Space Physics Community is the most important result of this subsection. The technique could “open doors” for other applications. For example, we speculate that it might be useful to study Alfvén waves, because, with them, fluctuations in the SW with different pseudo-frequencies

can be investigated.

Application to identify the shock and leader edge of ICME

Now, this study considers the events of MCs not associated with shock waves, presented in Table A.4 (see event 3).

With illustration purpose, a case study is presented for the date June 24, 12 : 00 *UT*-June 25, 16 : 00 *UT*, 1998. The criteria to select the data interval after the MC are the same used previously. The duration time in regions at 41 sheath is less than one day, then a region with this equivalent duration from the initial time of the cloud is chosen. In Figure 6.18, the above interval at the date June 23, 12 : 00 *UT*-June 26, 16 : 00 *UT*, 1998 is shown. Each panel presents, from top to bottom, the B_x , B_y , and B_z component time series respectively. At the bottom of the respective panels, the square of the first decomposition level of wavelet coefficients, $d1$, versus time is plotted. The two vertical dashed lines correspond with the MC region delimitations identified by Huttunen et al. (2005). The wavelet coefficients permit doing a *zoom in* in the fluctuations of magnetic components. As large amplitudes inside the initial border of MC is observed, then we think that this boundary should be redefined. Thus, the leader edge at date June 24, 16 : 32 *UT* 1998 is redefined. The second vertical thick line corresponds with the above data.

Also, wavelet coefficients could be used to identify shock waves. However, the confirmation on the type of electrodynamic discontinuity implies the use of plasma data. So, a probable discontinuity at date June 24, 04 : 00 *UT* 1998 is identified. Thus, with help of SW plasma parameters, an interplanetary shock can be associated to this event. The first vertical thick line corresponds with its location.

In Figure 6.18 (all panels), the D_{d1} values in each regions are shown. We found higher D_{d1} values in the sheath while the lower values correspond to cloud region. The results related to this part are consistent with the earlier results.

In conclusion, this methodology has a practical application. Maybe other applications for Space Physics Community uses will be found, mainly taking into account fluctuations that occur in several frequency ranges.

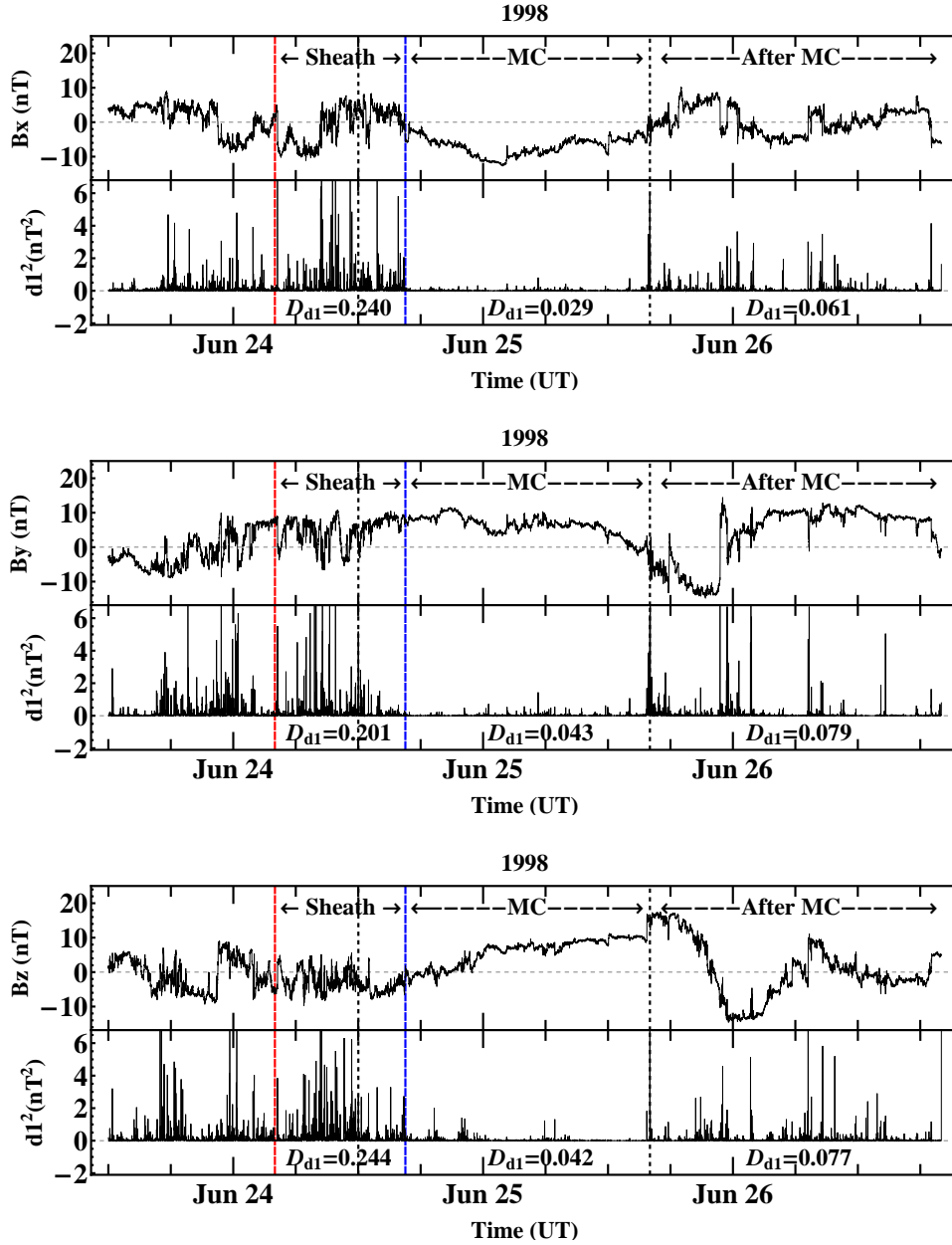


Figure 6.18 - (top panel) At top, IMF B_x (in GSM system) vs time from the ACE spacecraft with 16 s time resolution, at date June 23, 12 : 00 UT-June 26, 16 : 00 UT, 1998; at bottom, the square of the first decomposition level of wavelet coefficient dI^2 vs time. Also, the other two components must be analyzed, as is shown in the middle and bottom panels.

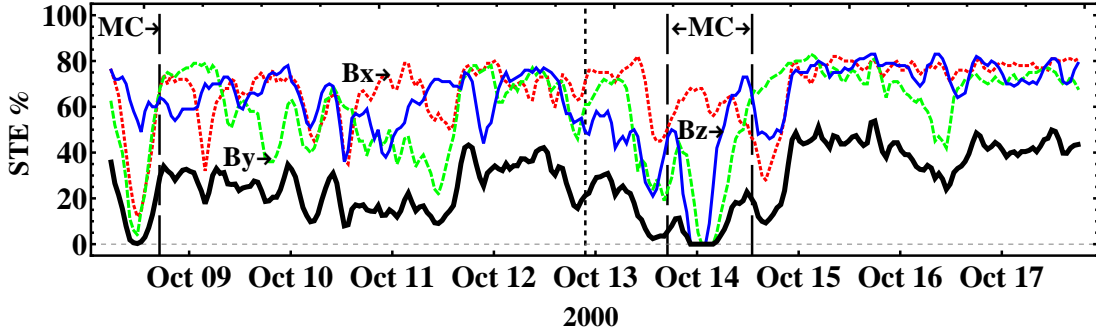


Figure 6.19 - It is plotted the IE as a function of the time, October 08 – 17, 2000, but the three vertical lines correspond with the event enumerated as 24 at Table A.1. The format is the same as in Figure 5.5.

6.3 Example of methodology applications

From the 41 MCs studied in previous section, the decreasing of STE inside the MC in relation to the sheath region can be noticed. The IE index helps to identify MC candidates. Adding resources to this identification, the persistence exponents have an increase inside of MC that could be useful to identify these events. Also, the IMF behavior identified by wavelet coefficients as whether more quiescent or less quiescent signal helps to evaluate the MC region. After the identification of MC regions, the MVA method could be used to identify the boundaries in a more precise manner. The proposed methodology confirms to be very useful to identify the magnetic clouds as illustrated by the applications.

Identification of MC event at 07-08 October 2000

We select several events that were presented in Table A.1 to prove that the entropy index is a tool capable of identifying MCs. During the above test, we had the luck to found a MC. We begin to do a study in more details of the STE variations with some days before and after the event enumerated as 24 at Table A.1. The time series of the magnetic components B_y and B_z for MC have zero STE (see, Figure 6.1 event enumerated as 24) but B_x has nonzero STE. We selected data windows of 2500 records moving forward as 200 records until the end of the time series. In each temporal window the STE for B_x , B_y and B_z were calculated.

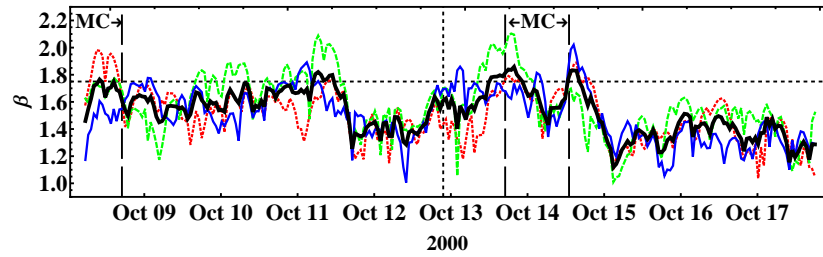
A study is done on the period including the 2000 October 12 – 14 event (presented

in Table A.1). The extended 10-day interval is informed in Table A.6. In Figure 6.19, with different lines (dotted line $\equiv x$, dashed line $\equiv y$, continuous thin line $\equiv z$) the STE values for each components as function of time are plotted. The black thick curve represents the IE calculated along the analyzed period. The MC around October 14 is plotted with three vertical dashed lines (the shock and cloud boundaries). The properties of this cloud are described by [Huttunen et al. \(2005\)](#): the MVA method gives $\lambda_2/\lambda_3 = 4$, $\chi = 62^\circ$ and $(\phi_C, \theta_C) = (33^\circ, -25^\circ)$, this bipolar MC has a flux-rope type NES and the observed angular variation of magnetic field is right-handed. During the passage of this MC, the B_y , B_z components have $STE = 0\%$ approximately in the first half of it, and the IE detects the presence of this MC. As expected, the STE method has once again demonstrated as useful and capable of producing valid results.

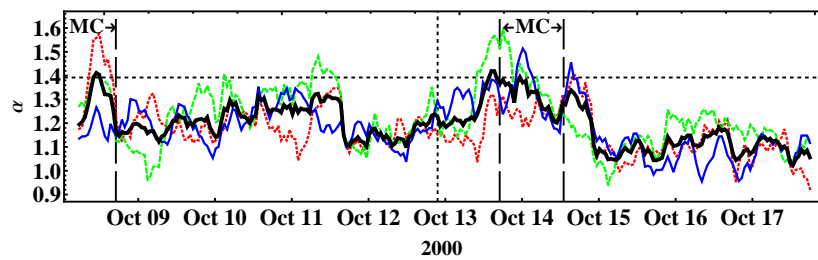
However, on October 8, the B_x , B_y components have STE value almost zero ($STE_x^{min} = 12\%$ and $STE_y^{min} = 4\%$). At this date, the presence of ICME was not reported. But a small magnetic structure where the field had a smooth variation can be noticed. The IE detects those kinds of small structures that are unnoticed in most of the studies.

Also, the persistence indices to identify the region of a MC can be used. Thus, in the Figure 6.20 shows the plot of the four persistences indices in the form as was explain in Subsection 5.2.4. The threshold is exceeded by the four indices at the same time only inside of the two MCs that shown in the Figure 6.20. With the idea of studying the magnetic field fluctuations, we also use the wavelet index ($WI \equiv \langle D_{d1} \rangle$) methodology explained in Subsection 5.2.5. In the Figure 6.21, we show the D_{d1} (*red* $\equiv x$, *green* $\equiv y$, *blue* $\equiv z$) values as a function of the time for times series of IMF B_x , B_y and B_z components in the SW. The WI is plotted by a black thick curve. Exist a decreasing in the cloud region, but it is not sufficient to identify the MC. The WI is plotted, because we want to compare the relationship between magnetic field fluctuations with the entropy and the persistence respectively.

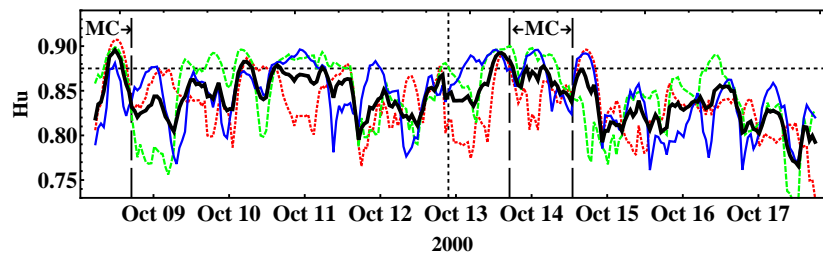
The correlation between IE , $\langle \beta \rangle$, $\langle \alpha \rangle$, $\langle H_u \rangle$, $\langle H_a \rangle$ and WI as form of correlation matrix were represented in the Table 6.2. The six indices are show in Figures 6.19, 6.20 and 6.21 respectively. As expected, exist a large anti-correlation between the persistence indices and the IE. However WI has low relationship with the other five index. Thus the solar wind intervals with large fluctuation has low memory and more randomness respectively.



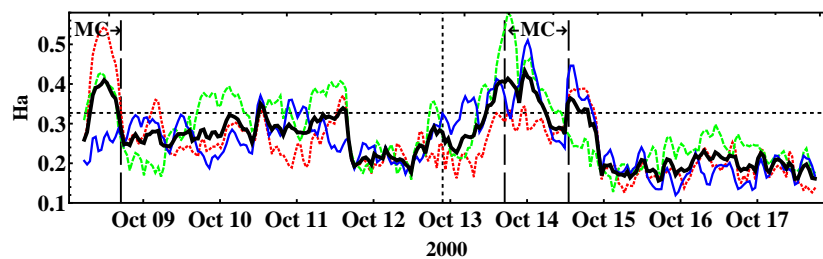
(a)



(b)



(c)



(d)

Figure 6.20 - Persistence exponents as a function of the time from B_x , B_y and B_z . In the four panels, the calculation of exponent in the components are shown as: *red* $\equiv x$, *green* $\equiv y$, *blue* $\equiv z$; the black thick curve represents the persistence indices calculated over the analyzed period. The shock, the start and end of the MC are represented by three vertical dotted lines. In all panels, the horizontal dotted line is the threshold value taken of the Figure 6.11(b).

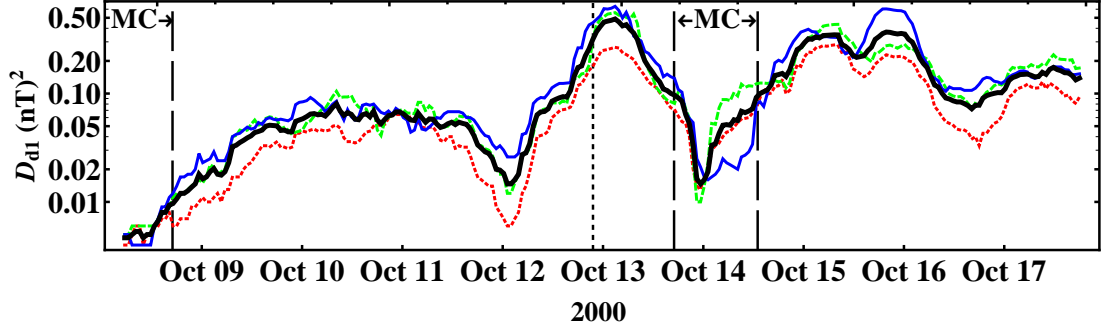


Figure 6.21 - We shows D_{d1} values as a function of the time for times series of IMF B_x , B_y and B_z components in the solar wind. D_{d1} values for B_x , B_y , and B_z are plotted with red dotted line, green dashed line, and blue continuum line respectively. The thick curve represents the Wavelet index (WI) calculated over the analyzed period.

Table 6.2 - Table in form of correlation matrix between the six studied tools that shown in Figures 6.19, 6.20 and 6.21 respectively.

	IE	$\langle\beta\rangle$	$\langle\alpha\rangle$	$\langle H_u\rangle$	$\langle H_a\rangle$	WI
IE	100					
$\langle\beta\rangle$	-85	100				
$\langle\alpha\rangle$	-94	88	100			
$\langle H_u\rangle$	-87	81	87	100		
$\langle H_a\rangle$	-93	85	95	79	100	
WI	41	-38	-38	-30	-42	100

The previous tools are not used to identify the boundaries of the MC. The combination between analysis of plasma data with the MVA method can be use to identified the boundaries. This methodology was explained in Subsection 5.2.3.

To identify MC boundaries, a combination between analysis of plasma data with the MVA method is usually applied. The data was measured by ACE from October 07 to 09, 2000 with 1 hour time resolution. So, Figure 6.22 is composed by six panels: (top panels) magnetic field strength and polar (B_{lat}) angles of the magnetic field vector in GSE coordinate system; (middle panels) azimuthal (B_{long}) angle and plasma beta; (bottom panels) maximum and minimum variance planes respectively. The plasma beta minimum value was $\beta_p = 2.7 \times 10^{-3}$ on 07 October at 23 : 00 UT. We used the magnetic field rotation confined to one plane, the plane of maximum

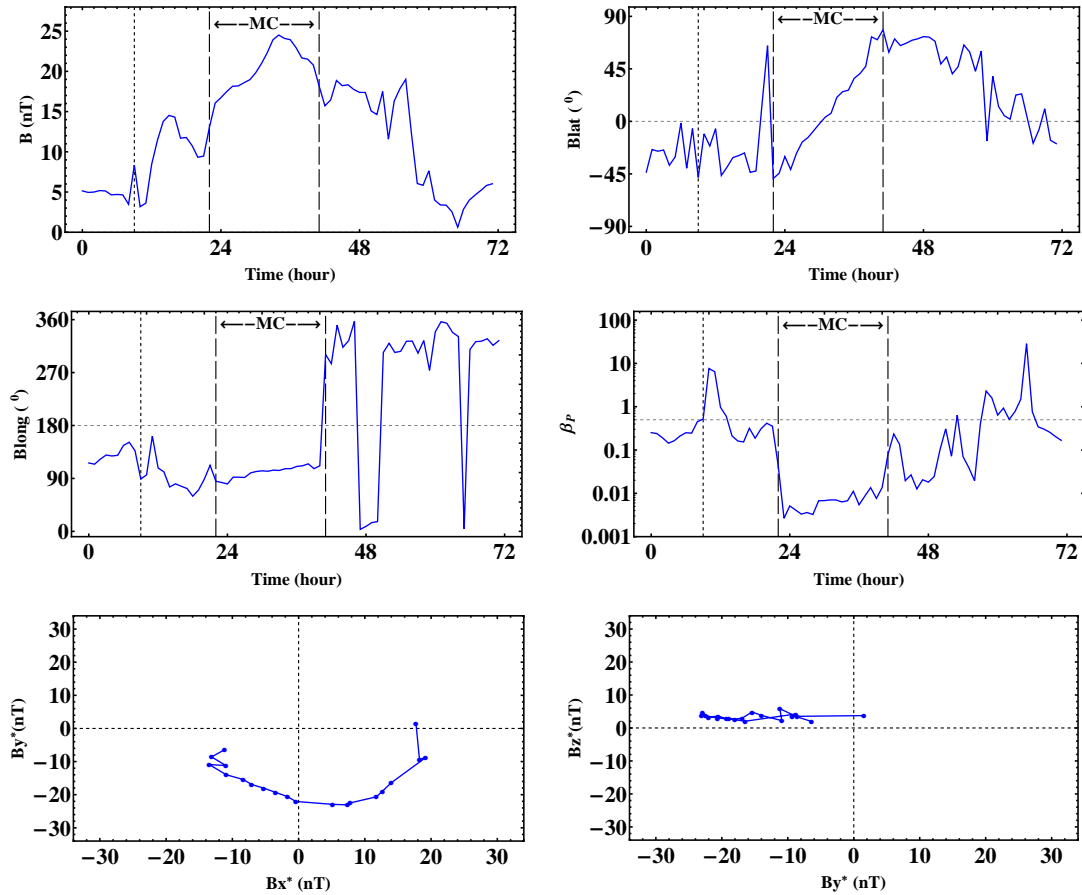


Figure 6.22 - The bipolar MC was observed by ACE on October 07 – 09, 2000 and identify in this work. The Figure is composed by six panels from (a) to (f): magnetic field strength, polar (B_{lat}) and azimuthal (B_{long}) angles of the magnetic field vector in GSE coordinate system; proton plasma beta; rotation of the magnetic field vector in the plane of maximum variance and rotation of the magnetic field vector in the plane of minimum variance.

variance ($B_x^*B_y^*$) to find the boundaries of the cloud, the dates were written in Table 6.3.

Table 6.3 - Magnetic cloud from 07 – 08 October 2000.

Year	Shock	MC, start	MC, stop
2000	07 Oct, 09 : 00	07 Oct, 22 : 00	08 Oct, 17 : 00

In all panels of Figure 6.22, the first vertical line indicates the shock, and the other two vertical lines indicate MC interval. The MVA method gives the eigenvalue ratio $\lambda_2/\lambda_3 = 47.5$, the angle between the first and the last magnetic field vectors $\chi = 148.4^\circ$, the orientation of the axis $(\phi_C, \theta_C) = (113.8^\circ, 7^\circ)$, the direction of minimum variance $(\phi_{min}, \theta_{min}) = (22^\circ, -10^\circ)$ and eigenvalues $[\lambda_1, \lambda_2, \lambda_3] = [124.6, 41.8, 0.9]$. This MC has a flux-rope type SEN as can be seen in the Figure 6.22, right top panel and left middle panel respectively. The observed angular variation of the magnetic field is left-handed. A MC event has been characterized. The entropy method demonstrates its usefulness, and its capable of producing new results (or, at least, interesting cases for studies).

Identification of MC event at 05-06 April 2010

On April 03, 2010, the Sun launched a cloud of material, known as a coronal mass ejection (CME), in a direction that reached the Earth. This CME was very fast with a speed of at least 800 km/s. The bulk of the CME passed south of Earth, but a piece of it hit the Earth's magnetosphere on April 05, causing a geomagnetic storm ($Dst_{min} = -73$ nT on 06 April at 15 : 00 UT).

This event was very recent and we wanted to use the technique to verify any possible MC occurrence. The ACE Magnetic Field Experiment data in level 2 (verified) were not available in April 2010 when the data were processed (April-May 2010). It was only possible to obtain such data for 16 second average IMF in RTN or GSE coordinates via anonymous ftp, from Caltech (<ftp://mussel.srl.caltech.edu/pub/ace/browse/MAG16sec>). For this reason, in Figure 6.23, the STE values are calculated using data in GSE coordinates. It is not a problem, because the choice of the coordinate system, *i.e.* GSE, GSM or RTN, does not affect this methodology for this study.

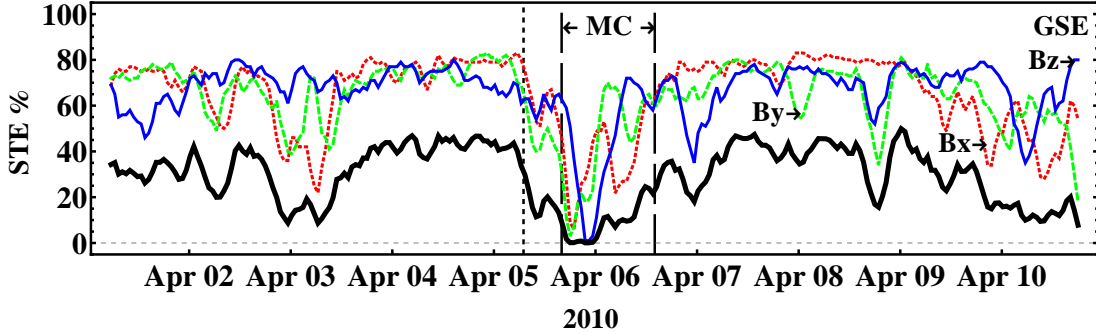


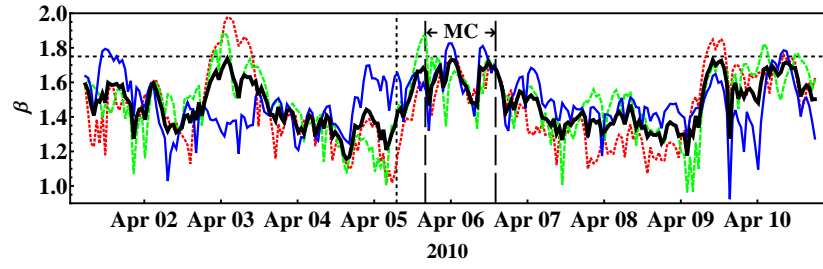
Figure 6.23 - It is plotted the IE as a function of the time for April 01 – 11, 2010. The shock and the MC boundaries are shown with three vertical lines, those dates were identified in this work. The format is the same as in Figure 5.5. The thick curve represents the IE calculated over the analyzed period. The MC is identified.

In the figure, STE values for the three IMF components are shown ($B_x \equiv$ dotted line, $B_y \equiv$ dashed line and $B_z \equiv$ continuous thin line). The thick curve represents the IE. We find minimum values of $STE = 1\%$ to B_z on 05 April at 21 : 33 : 20 and 22 : 26 : 40 UT. The B_x and B_y components had STE values less than 10% on 05 April from 18 : 00 : 00 to 18 : 53 : 20 UT respectively. Then, the IE has a minimum value less than 1% on day 05 from 18 : 00 : 00 to 23 : 20 : 00 UT. Thus the IE detects a structure with characteristics of a MC candidate.

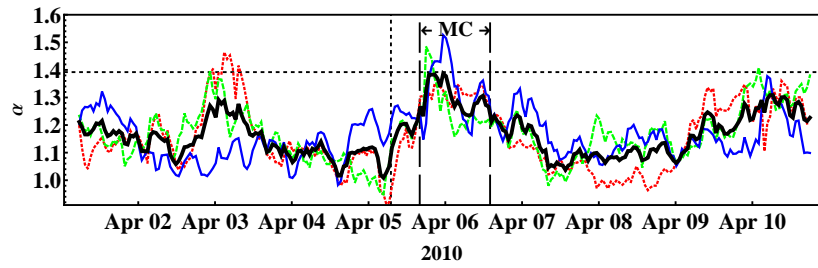
The four persistence exponents are shown in Figure 6.24. In the four panels of Figure 6.24, the increase of persistence occur around of April 6, which does not happen in other intervals of time. As the α -index ($\langle\alpha\rangle$) does not exceed the threshold, we think that the quality of the identification is not the best.

The WI is shown in the Figure 6.25. The largest WI values are at April 05, from 08 : 00 to 15 : 00 2010. This region could be the plasma sheath of the ICMEs. After that, the index has a rapidly decrease and may be the cloud region.

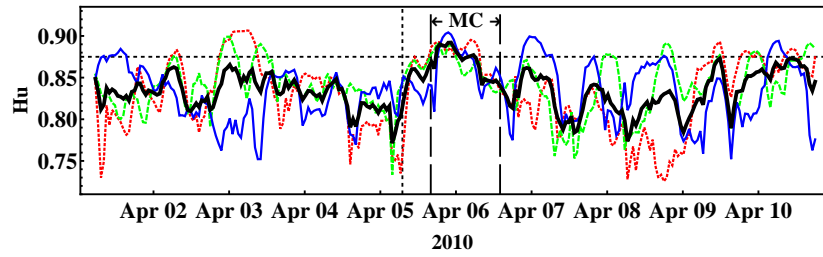
The six indices that are shown in the Figures 6.23, 6.24 and 6.25 were joined to calculate a correlation matrix as shows Table 6.4. The results are similar to those already discussed in Table 6.2. The four persistence indices have good correlations between them and with the IE (good-anticorrelation).



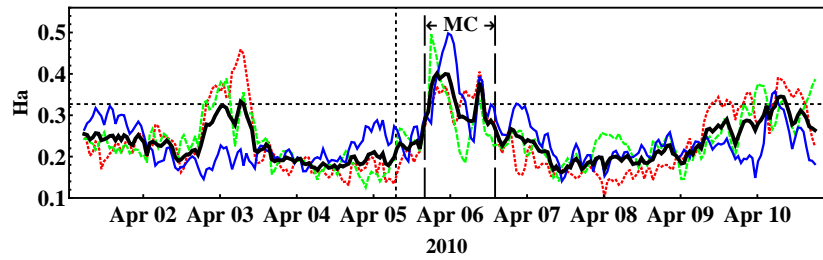
(a)



(b)



(c)



(d)

Figure 6.24 - Are shown values of persistence exponents, β, α, H_u, H_a on 01 – 11 October, 2010 as a function of the time for times series of IMF components ($(\beta, \alpha, H_u, H_a)$ in: $B_x \equiv$ Red, $B_y \equiv$ Green and $B_z \equiv$ Blue) in the solar wind. The thick curve represents the Persistence Indices ($\langle \beta \rangle, \langle \alpha \rangle, \langle H_u \rangle, \langle H_a \rangle$) calculated over the analyzed period.

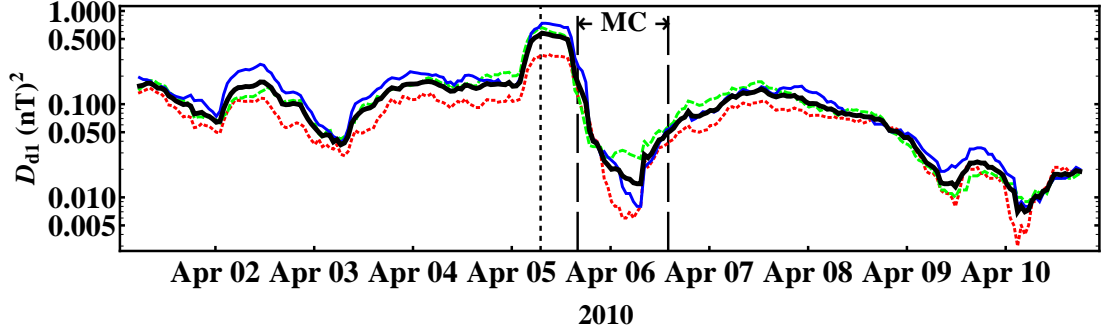


Figure 6.25 - We shows D_{d1} values as a function of the time for times series of IMF B_x , B_y and B_z components in the SW. D_{d1} values for B_x , B_y , and B_z are plotted with red dotted line, green dashed line, and blue continuum line respectively. The thick curve represents the wavelet index (WI) calculated over the analyzed period.

Table 6.4 - Table in form of correlation matrix between the six studied tools that shown in Figures 6.23, 6.24 and 6.25 respectively.

	IE	$\langle\beta\rangle$	$\langle\alpha\rangle$	$\langle H_u\rangle$	$\langle H_a\rangle$	WI
IE	100					
$\langle\beta\rangle$	-71	100				
$\langle\alpha\rangle$	-89	84	100			
$\langle H_u\rangle$	-82	70	82	100		
$\langle H_a\rangle$	-88	79	93	72	100	
WI	22	-31	-38	-23	-40	100

Up here, we think that exists a MC inside of this ICMEs. The methodology implemented in this work has identified a region with characteristic of MC in the magnetic field data. Using the earlier treatments, the boundaries found for the cloud-candidate is delimited in the data shown in Figure 6.26.

In Figure 6.26, the data were measured by ACE from April 01 to 11, 2010 with 1 h time resolution. The Figure has been composed by six panels: (top panels) magnetic field strength and polar (B_{lat}) angles of the magnetic field vector in GSE coordinate system; (middle panels) azimuthal angle (B_{long}) and plasma beta; (bottom panels) planes of maximum and minimum variance respectively. On 05 April 2010, at 07 : 00 UT, the proton density $N_p = 2.8 \text{ cm}^{-3}$, proton temperature $T_p = 2.4 * 10^5 \text{ K}$, ratio of $alphas/protons = 7 * 10^{-2}$, proton speed $V_p = 564.5 \text{ km/s}$, magnetic field

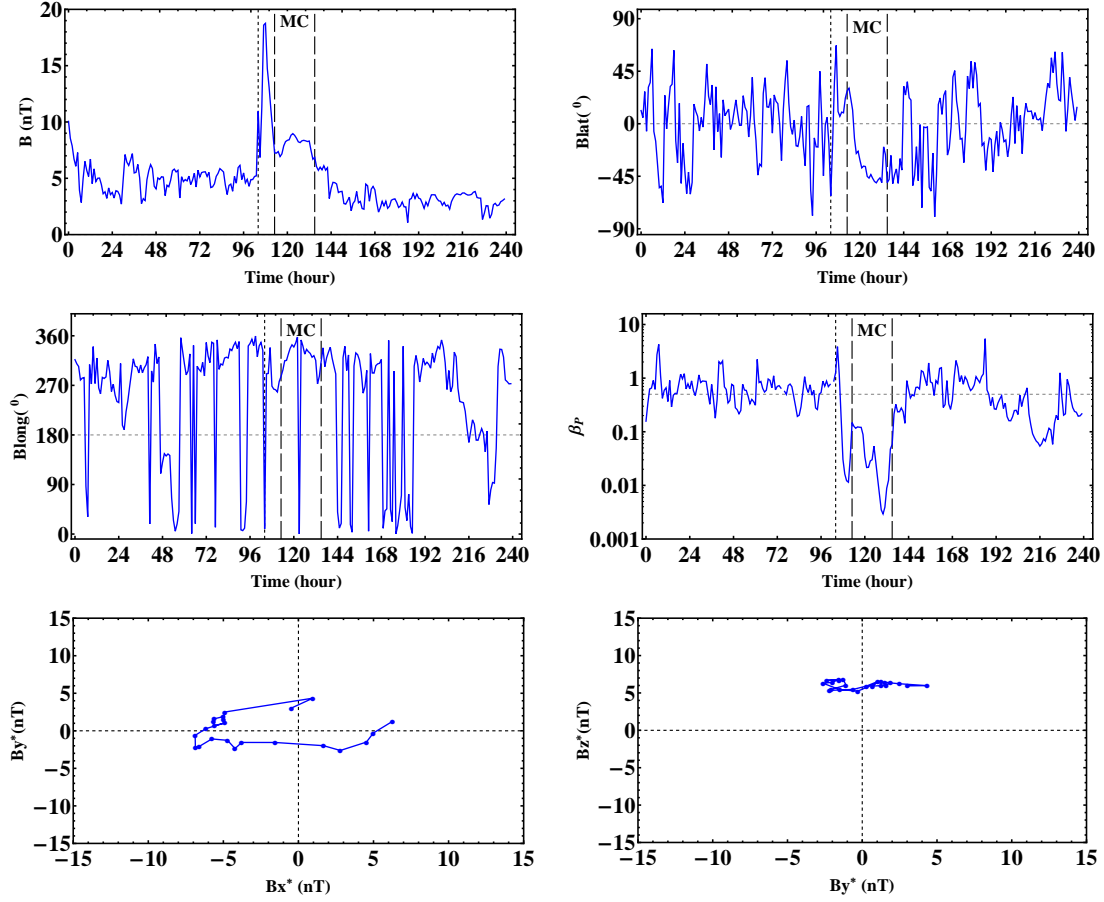


Figure 6.26 - The solar wind windows has been observed by ACE from April 01 to 10, 2010, in GSE coordinates system and with 1 h time resolution.

magnitude $B = 5.2$ nT and plasma beta $\beta_p = 0.9$. One hour later, some parameters have a change $N_p = 7.98 \text{ cm}^{-3}$, $T_p = 5.5 \times 10^5 \text{ K}$, $\alpha/\text{protons} = 1.7 \times 10^{-2}$, $V_p = 724.8 \text{ km/s}$, $B = 10.9 \text{ nT}$ and $\beta_p = 1.3$. It is easy to identify a shock because the velocity, density and magnetic field magnitude increase abruptly, and we believe that is related to the arrival of an event at ACE. Eight hours latter than the time of the shock, at 16 : 00 UT, the plasma beta decreases to $\beta_p = 3.2 \times 10^{-2}$, and it is the start of the MC.

The plasma beta minimum value were $\beta_p = 8.8 \times 10^{-3}$ on 06 April at 12 : 00 UT. We have used the magnetic field rotation confined to one plane, the maximum variance plane ($B_x^* B_y^*$), to find the boundaries of the MC. In Table 6.5, the dates are shown. The minimum variance plane ($B_y^* B_z^*$) has a problem, because the plot is not in $B_z^* = 0$ (there is an off set), and we report this MC as a mean quality in the identification.

Table 6.5 - Magnetic cloud from 05 – 06 April 2010.

Year	Shock	MC, start	MC, stop
2010	05 Apr, 07 : 00	05 Apr, 16 : 00	06 Apr, 14 : 00

Thus, in all panels of Figure 6.26, the first vertical line indicates the shock, and the other two vertical lines show the MC interval. The MVA method gives the eigenvalue ratio $\lambda_2/\lambda_3 = 16$, the angle between the first and the last magnetic field vectors $\chi = 48^\circ$, the orientation of the axis $(\phi_C, \theta_C) = (33^\circ, -32.6^\circ)$, the direction of minimum variance $(\phi_{min}, \theta_{min}) = (129^\circ, 9^\circ)$ and eigenvalues $[\lambda_1, \lambda_2, \lambda_3] = [16.8, 3.6, 0.2]$. This MC has a flux-rope type NWS as can be seen in Figures 6.26, right top panel and left middle panel, respectively. The observed angular variation of the magnetic field is left-handed. With proposed methodology we were able to identify a new MC.

By means of calculating of STE of magnetic structures, evaluated by an IE, the methodology proposed here allows identifying MC candidates, as well as unraveling some of them that present interesting features to further studies. The use of an easy computational technique to identify MC candidates seems better than performing an exhausting visual inspection of the data to find the candidates, as done with courage in many studies. Although there are other identification methodologies, other advantage of IE methodology is to deal only with the IMF data. At last, an emphasis should be done by us: this methodology is only an auxiliary identification tool, to be added to the others.

6.4 Part III: MC event analyses

Along the efforts to obtain a methodology, some appealing events have been discovered. Selected among them, two events are examined here in a more complete way to exemplify new results reached after the use of our methodology. It represents a result beyond the initial goal of this work. They are: (a) magnetic clouds in an electro-dynamical coupling, and (b) a MC event presenting a controversial interpretation in the literature.

6.4.1 Identification of a magnetic clouds with double rotations observed by the ACE spacecraft

The event of August 19 – 20, 1998 (Table A.5), is shown in the right panel of Figure 2 in the paper of Huttunen et al. (2005). Also, this MC was published by

NASA (http://wind.nasa.gov/mfi/mag_cloud_pub1.html), and also reported in the work of Cane and Richardson (2003). In those analyses, the MC is reported as a single flux-rope, (e.g. Cane and Richardson (2003)) detected one ICME classified as MC from August 19, 18 : 47 to August 21, 20 : 00, 1998, where $V_{ICME} = 300 \text{ km/s}$, $V_{max} = 340 \text{ km/s}$, and $B = 14 \text{ nT}$. Huttunen et al. (2005) used the MVA method, and the eigenvalue ratio $\lambda_2/\lambda_3 = 30$, the angle between the first and the last magnetic field vectors $\chi = 177^\circ$ and $(\phi_C, \theta_C) = (113^\circ, -16^\circ)$ are calculated. They reported the MC as bipolar cloud with a flux-rope type SWN and the observed angular variation of the magnetic field is right-handed. They calculated values using data with 1 *h* of time resolution, now 5 *min* is used. The observed SN-type MC had $B_z < 0$ for about eleven hours, with values of less than -10 nT . In the plasma sheath was observed $B_z < 0$ for more than seven hours and values close to $B_z = -11 \text{ nT}$. The *Dst* index shows two geomagnetic storms, the first with $Dst_{min} = -42 \text{ nT}$ caused by the plasma sheath, and the second with $Dst_{min} = -67 \text{ nT}$ caused by the MC (HUTTUNEN et al., 2005).

Initially, our motivation is test IE in a ten-day time window to verify if we can identify the mentioned MC. We select the period from August 15 to 24, 1998, as shown in Table A.6. The magnetic field data ($B_x \equiv \text{Red}$, $B_y \equiv \text{Green}$, $B_z \equiv \text{Blue}$) with time resolution of 16 *s* in GSM coordinates system are shown in Figure 6.27, at the top panel. Time data intervals of 2500 records moving forward as time steps of 200 records till the end of the time series are selected. Using the 2500-record intervals, the IE is calculated for each step.

In Figure 6.27, bottom panel, values of STE on 15 – 24 August, 1998 are shown as a function of time for time series of IMF components (*STE* in: $B_x \equiv \text{red dotted line}$, $B_y \equiv \text{green dashed line}$ and $B_z \equiv \text{blue continuous thin line}$) in the SW. The thick curve represents the IE calculated along the analyzed period. In Figure 6.27, the first, second, and third vertical dotted lines represent respectively the shock, the start, and end of the MC (designated by us as MC2) reported by Huttunen et al. (2005) (see event in Table A.5). Figure 6.27 shows that the B_x , B_y components have zero STE value during the plasma sheath of the MC, approximately at the end half of it. After that, approximately in the center of the MC2, the three components (B_x , B_y , B_z) have zero STE values. Thus, the IE is zero at the end of the sheath and again within the MC. We think that, maybe, there are two MCs, one after the other, because, so far, the IE was never zero outside of the

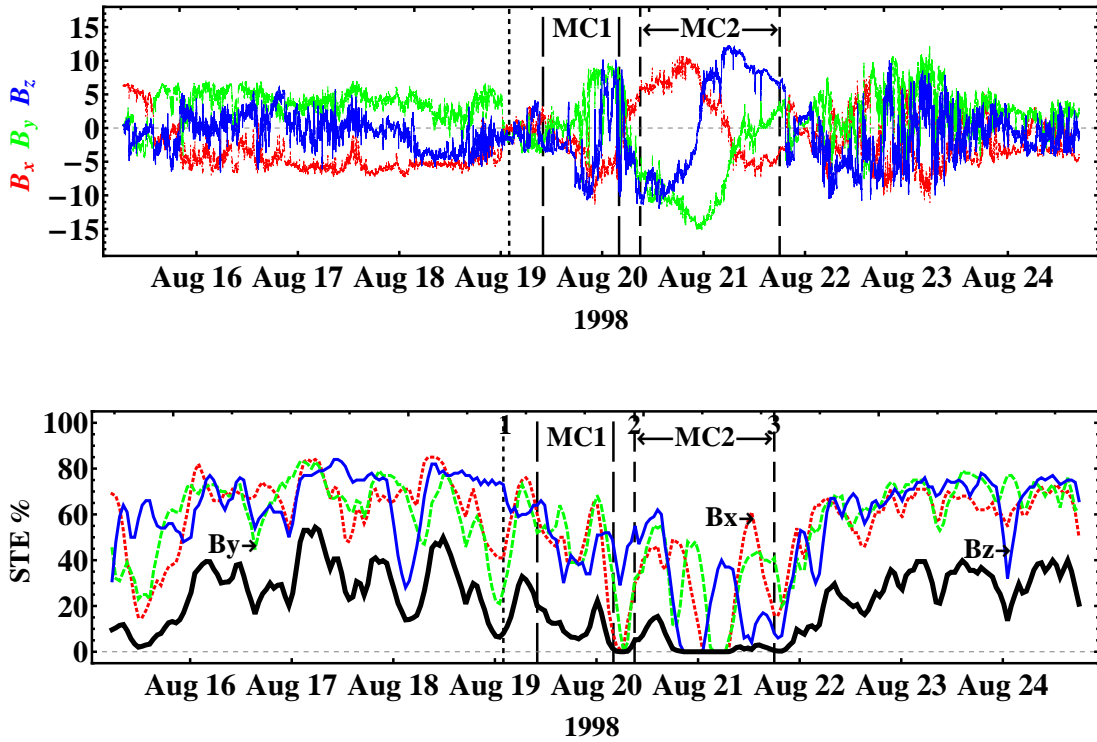


Figure 6.27 - (top panel) The magnetic field data ($B_x \equiv$ Red, $B_y \equiv$ Green, $B_z \equiv$ Blue) with time resolution of 16 s in GSM coordinates system are shown. (bottom panel) Are shown values of Spatio-Temporal Entropy on 15 – 24 August, 1998 as a function of the time for times series of IMF components (STE in: $B_x \equiv$ red dotted line, $B_y \equiv$ green dashed line and $B_z \equiv$ blue continuous thin line) in the solar wind. The thick curve represents the IE calculated over the analyzed period. The shock of the ICMEs, the start and end of the MC2 are represented by three vertical lines as is shown in Table A.5. We identify the first MC (MC1), the start and end of it are represented by two vertical lines according to the identification that was done.

cloud regions. The lower values of IE on August 15 is caused because the data has gaps and we done a linear interpolation.

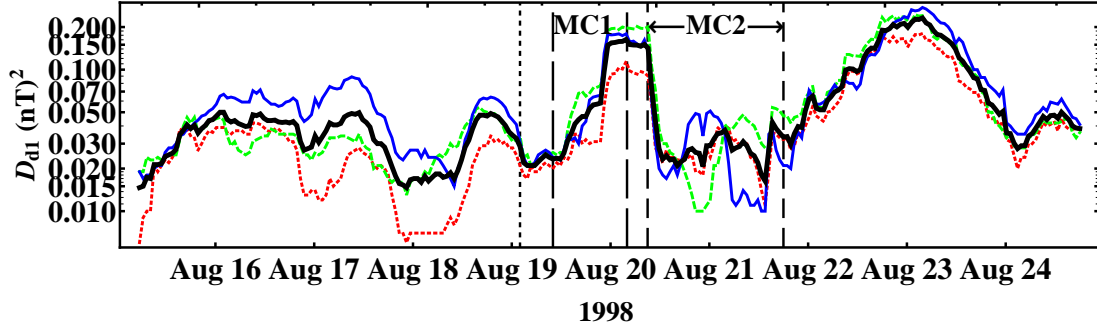
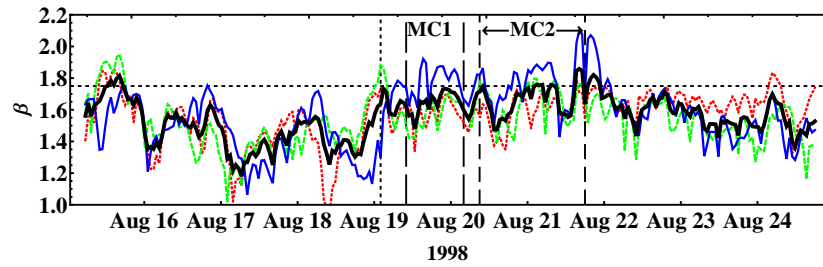


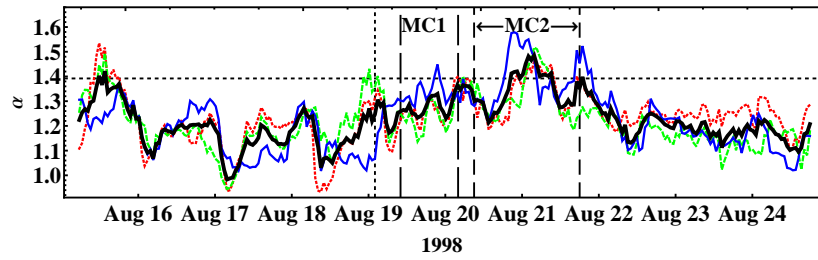
Figure 6.28 - Are shown values of average wavelet coefficients on 15 – 25 August, 1998 as a function of the time for times series of IMF components (D_{d1} in: $B_x \equiv$ Red, $B_y \equiv$ Green and $B_z \equiv$ Blue) in the solar wind. The thick curve represents the WI calculated overall interval.

We decided show the WI to clarify the doubts about the existence of a MC inside the plasma sheath. In the Figure 6.28 are shown values of average wavelet coefficients on 15 – 25 August, 1998 as a function of the time for times series of IMF components (D_{d1} in: $B_x \equiv$ Red, $B_y \equiv$ Green and $B_z \equiv$ Blue) in the SW. The thick curve represents the WI calculated overall interval. The WI is large between the end of plasma sheath and the start of the MC for the 20th of August. The WI is increased in this region and it had not been observed in the other studied cases, i.e. Figures 5.12(a), 5.12(b), 5.12(c), 6.21 and 6.25. We believe that this region is being compressed between two flux-tubes and it is the cause of the large IMF fluctuations.

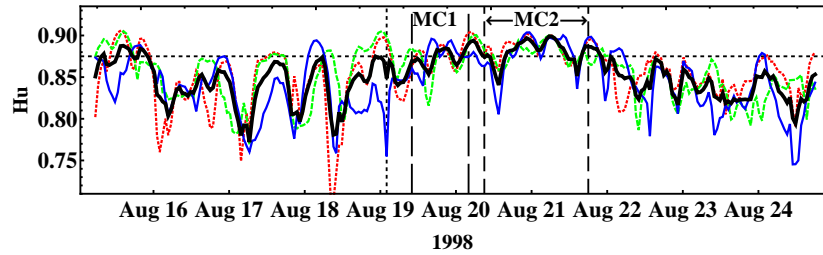
We continued to test the other tools. In Figure 6.29 are shown values of persistence exponents, β , α , H_u , H_a on 15 – 25 August, 1998 as a function of the time for times series of IMF components ($(\beta, \alpha, H_u, H_a)$ in: $B_x \equiv$ Red, $B_y \equiv$ Green and $B_z \equiv$ Blue) in the SW. The thick curve represents the persistence indices ($\langle\beta\rangle, \langle\alpha\rangle, \langle H_u\rangle, \langle H_a\rangle$). Not taking into account the day 15th due to the data gaps, then the Hurst ($\langle H_u\rangle$) and Hausdorff ($\langle H_a\rangle$) indices respectively, exceed the threshold only in the plasma sheath and in the cloud region, both regions identified in the work of Huttunen et al. (2005). The others two persistence indices do not exceed the threshold in the sheath but increase the persistence value in it. The results



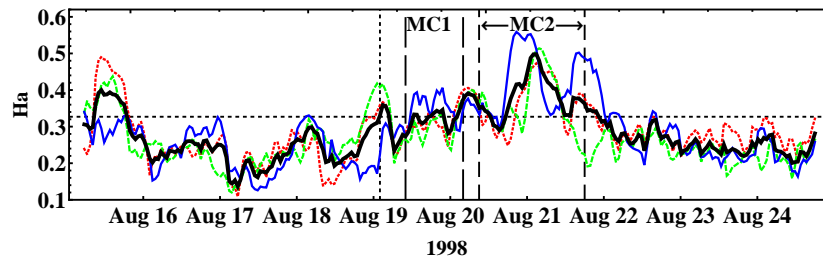
(a)



(b)



(c)



(d)

Figure 6.29 - Are shown values of persistence exponents, β , α , H_u , H_a on 15 – 25 August, 1998 as a function of the time for times series of IMF components ($(\beta, \alpha, H_u, H_a)$ in: $B_x \equiv$ Red, $B_y \equiv$ Green and $B_z \equiv$ Blue) in the SW. The thick curve represents the persistence indices ($\langle \beta \rangle$, $\langle \alpha \rangle$, $\langle H_u \rangle$, $\langle H_a \rangle$) calculated overall interval.

are not sufficient to identify another cloud in the plasma sheath, but it are not as clear as to conclude that there is not a MC.

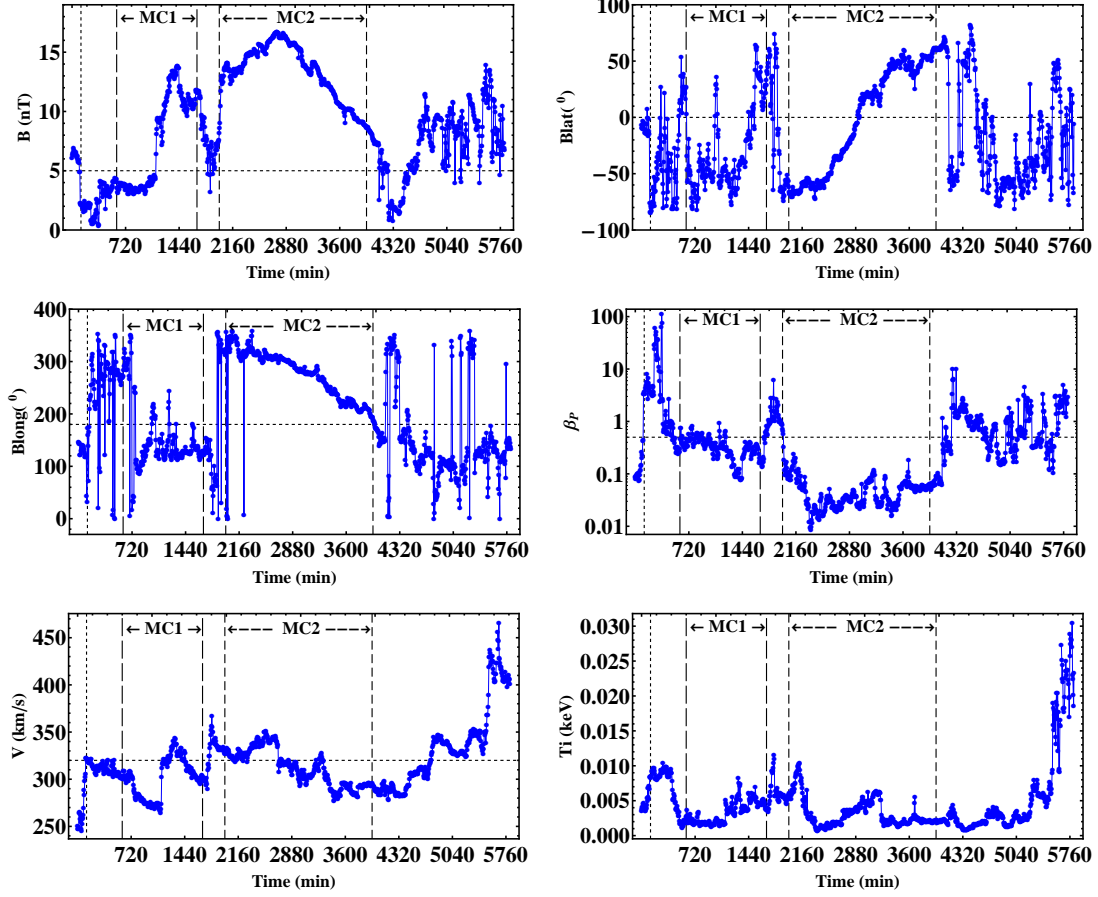


Figure 6.30 - The plot, obtained from OMNI data set in CDAWeb (http://cdaweb.gsfc.nasa.gov/istp_public/), are based on 5-min averaged ACE data in August 19-22, 1998 in GSE. The shock of the ICMEs, the start and end of the MC2 are represented by three vertical lines as is shown in Table A.5. We identify the first MC (MC1), the start and end of it are represented by two vertical lines according to the identification that was done.

The exact boundaries of the two MCs are found using plasma data and MVA method respectively. Figure 6.30 is composed by six panels: (top panels) magnetic field strength and polar (B_{lat}) angle of the magnetic field vector in GSE coordinate system; (middle panels) azimuthal (B_{long}) angle and plasma beta; (bottom panels) total velocity and temperature. On 19 August 1998, at 02 : 00 UT, the parameters were: proton density $N_p = 3.57 \text{ cm}^{-3}$, the proton temperature $T_p = 7.31 * 10^4 \text{ K}$, the ratio

of $\alpha/\text{protons} = 4.5 \times 10^{-3}$, the proton speed $V_p = 333.9$ km/s, magnetic field magnitude $B = 2.4$ nT and plasma beta $\beta_p = 1.6$. One hour later some parameters have a change to $N_p = 3.98$ cm $^{-3}$, $T_p = 7.1 \times 10^4$ K, $\alpha/\text{protons} = 6.1 \times 10^{-3}$, $V_p = 331.1$ km/s, $B = 0.57$ nT and $\beta_p = 29.8$.

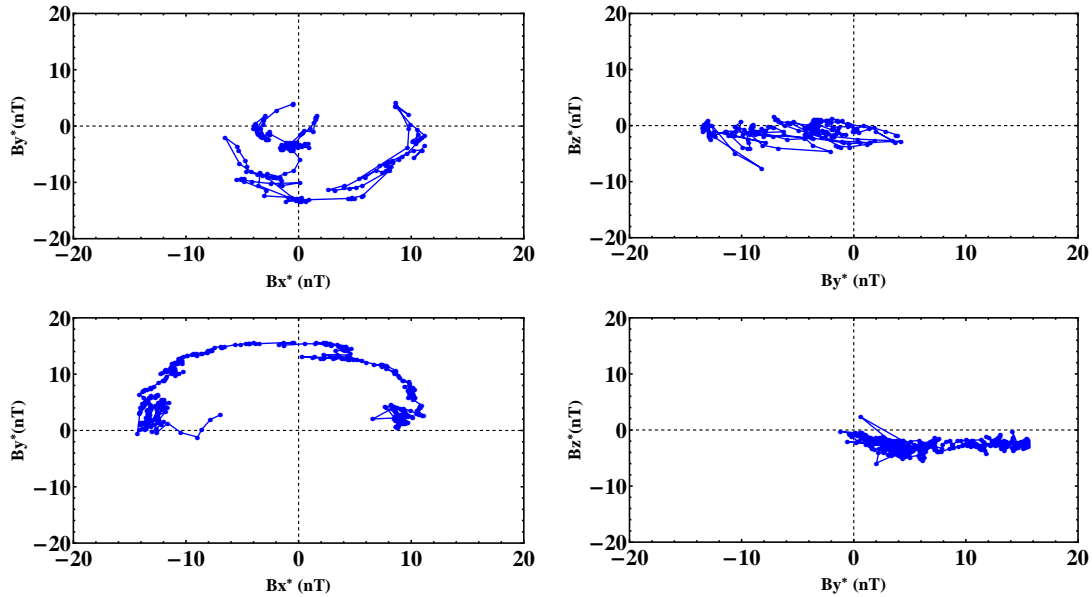


Figure 6.31 - In the panels are shown the magnetic hodograms for two magnetic clouds: (top panels) the first MC or MC1 was observed from August 19 – 20 10 : 00–04 : 00, 1998 while (bottom panels) the second MC or MC2 was observed from August 20 – 21 09 : 00 – 18 : 00, 1998. The magnetic field rotation confined to one plane, the plane of maximum ($B_x^*B_y^*$) and minimum ($B_y^*B_z^*$) variance are used to find the boundaries of the two clouds.

It is very difficult to identify a shock, but the plasma beta increased abruptly and we believe it was related to the arrival of an event. Two hours later, at 05 : 00 UT, the plasma beta decreased to $\beta_p = 0.58$. The plasma beta minimum value was $\beta_p = 7.8 \times 10^{-2}$ at 21 : 00 UT, where there was a maximum magnetic field magnitude of $B = 13.3$ nT. It is very difficult to detect the two MCs when a visual inspection of the data is performed. Someone could make a mistake in the interpretation of the cloud, and consider it as part of the plasma sheath of the other MC. To deal with the above hypothesis, we apply, with success, the same method (MVA) explained in Huttunen et al. (2005). The magnetic field rotation confined to one plane, the plane of maximum ($B_x^*B_y^*$) and minimum ($B_y^*B_z^*$) variance (see the two top panels of Figure 6.31) to find the boundaries of the first cloud (designated by us as MC1)

are used. In the two bottom panels of the Figure 6.31, the magnetic hodograms are shown for the second magnetic cloud or MC2.

Finally, we identify a bipolar MC observed by ACE from August 19, 10 : 00 UT to August 20, 04 : 00 UT. This MC has a flux-rope type SEN and the observed angular variation of the magnetic field is left-handed. The MVA method gives to MC1 $\lambda_2/\lambda_3 = 10.37$, $\chi = 111.96^\circ$, $(\phi_C, \theta_C) = (118.35^\circ, -38.98^\circ)$, the direction of minimum variance $(\phi_{min}, \theta_{min}) = (32.60^\circ, -5.23^\circ)$ and eigenvalues $[\lambda_1, \lambda_2, \lambda_3] = [21.00, 19.51, 1.88]$. In Table 6.6, we show the date of the two MCs, the time between the first and second MC is 5 *h* (sheath of the second MC). The results derived of MVA method described by Huttunen and collaborators are shown in Table 6.6.

The minimum speed in the first MC (MC1) was $V_{p1} = 272.9$ km/s at 15 : 00 UT, and in the beginning of the second MC (MC2) the maximum speed was $V_{p2} = 346.1$ km/s one day later, at 05 : 00 UT. Then, $V_{p2} > V_{p1}$, and the two events are very close to each other. Probably, there are other similar cases, where a MC was misunderstood and confused within the plasma sheath of the following prominent MC. The IE can help to identify the MCs in such kinds of cases and find the boundary of MC with MVA method. The IE is zero after the cloud (MC1) due to the adjustment in the time window for calculating the STE, and because this cloud is small.

We can see some properties in the interaction region (or contact region) between these two MC, maybe there are magnetic reconnection. In Figure 6.30, the absolute value of the magnetic field (B (*nT*)) decreases in the contact region. Also, the absolute value of the velocity (V (*km/s*)) decreases in the contact region as shown in Figure 6.30, left bottom panel. Such pairs of oppositely coupled changes in V and B provide observational support for magnetic reconnection exhausts in bifurcated current sheets in the SW (CHIAN; MUÑOZ, 2011). The modulus of the magnetic field $|B|$ in the Figure 6.30 (left top panel) is similar to that found in the vicinity of the magnetic boundary layer (MCBL), shown in Figure 2.7(a) at work of Chian and Muñoz (2011). They identified two current sheets in those boundaries. This signature is readily seen, and there are other important properties that reinforce the hypothesis of the magnetic reconnection in this region.

The magnetic field between two flux ropes with the same polarity may have opposite magnetic field. We can see in the Table 6.6, the first MC or MC1 has flux rope type SEN while MC2 has SWN, the magnetic field are opposite (N-S) in the interaction

Table 6.6 - Summary of results to MVA method (first part, rows 1-12) and Grad Shafranov reconstruction techniques (second part, rows 14-18) for two MCs. We show: (\hat{x}_i) the eigenvectors of the magnetic variance matrix; (λ_i) the corresponding eigenvalues; (λ_2/λ_3) the eigenvalue ratio; (ϕ_C, θ_C) MC axis orientation (longitudinal and latitudinal angles); (ϕ_{min}, θ_{min}) the direction of minimum variance; (χ) the angle between the first and the last magnetic field vectors; (Type) inferred flux-
rope type; (CH) handedness of the cloud (LH=left-handed, RH=right-handed); (\vec{V}_{HT}) deHoffman-Teller(HT) frame velocity; (cc_{all}) HT correlation coefficient; ($slope_{all}$) slope of the linear fit in deHoffman-Teller(HT) frame; ($cc_{all-Walen}$) Walén correlation coefficient; ($slope_{all-Walen}$) slope of the linear fit in the Walén analysis.

August, 1998		
Parameters	MC1 (19 – 20, 10 : 00 – 04 : 00)	MC2 (20 – 21, 09 : 00 – 18 : 00)
MVA		
\hat{x}_1, \hat{B}_x^*	(-0.40, 0.49, 0.77)	(-0.45, -0.03, 0.89)
\hat{x}_2, \hat{B}_y^*	(0.37, -0.68, 0.63)	(0.44, -0.88, 0.19)
\hat{x}_3, \hat{B}_z^*	(0.84, 0.54, 0.09)	(0.78, 0.48, 0.41)
$[\lambda_1, \lambda_2, \lambda_3]$	[21.00, 19.51, 1.88]	[97.20, 24.69, 0.96]
λ_2/λ_3	10.37	25.81
ϕ_C	118.35	116.88
θ_C	-38.98	-10.93
ϕ_{Min}	32.60	31.80
θ_{Min}	-5.23	-23.95
χ	111.96	155.61
Type	SEN	SWN
CH	LH	RH
Grad-Shafranov		
\vec{V}_{HT}	(-319.72; -2.45; 10.65)km/s	(-310.44, -2.94; -16.15)km/s
cc_{all}	0.998	0.999
$slope_{all}$	1.008	1.008
$cc_{all-Walen}$	-0.263	-0.256
$slope_{all-Walen}$	-0.165	-0.064

region. The WI can be detected the discontinuity in this contact region, i.e. it has large values there. The magnetic field has a jump in a short time interval to move from N(W) to S(E) or from S(E) to N(W). The WI becomes a tool for finding reconnection signatures in interaction regions between flux-ropes. That does not mean that other tools should not be used.

The generalization for the all cases, with or without magnetic reconnection are shown in Table 6.7. Following the terminology by Mulligan et al. (1998) the MCs with the axis lying near the ecliptic plane are called bipolar (low inclination), $\theta_C < 45^\circ$. On the other hand, the MCs that have the axis highly inclined to the ecliptic are called unipolar, (high inclination), $\theta_C > 45^\circ$. In all possible combinations of two bipolar MCs, the magnetic fields between them are antiparallel in eight cases SWN-SWN, SWN-SEN, SEN-SWN, SEN-SEN, NWS-NWS, NWS-NES, NES-NWS, NES-NWS as is shown in the first two rows of Table 6.7. If these clouds are interacting, then there is a magnetic reconnection between them. Also, exist eight bipolar MCs without magnetic reconnection as is shown in the rows 3–4 of Table 6.7. The above results can be apply for the unipolar MCs and are show in the rows 6–9 of Table 6.7.

According with the results showed in Table 6.7, the two MCs studied in this section (SEN-SWN) are reconnecting. The cross section of the magnetic flux-ropes of these clouds, could help to see the magnetic reconnection or X point. We can do this reconstruction with the Grad-Shafranov model.

Cross sections of double flux rope configuration

The GS reconstruction technique have been well documented in the Section 4.5 and others informations are shown in the Appendices C and D. We have worked with application in the magnetopause of it as explained in the work of Hau and Sonnerup (1999). One important step in the reconstruction is to calculate the invariant z axis. For magnetic flux ropes or MC the determination of z axis is determined by finding the direction, for which the data plot of $P_t(x_i, 0)$ versus $A(x_i, 0)$ display minimal scatter. The search for the invariant direction takes place numerically by trial and error. The final reconstruction interval is an output of the technique after several iterations that yields an optimal z axis. This application to MC at 1 AU have been well documented by Hu and Sonnerup (2002). There exist some variations of the basic method (see Sonnerup et al. (2006), and recent papers by (TEH; HAU, 2007)), however, we will be used the version of Hu and Sonnerup (2002).

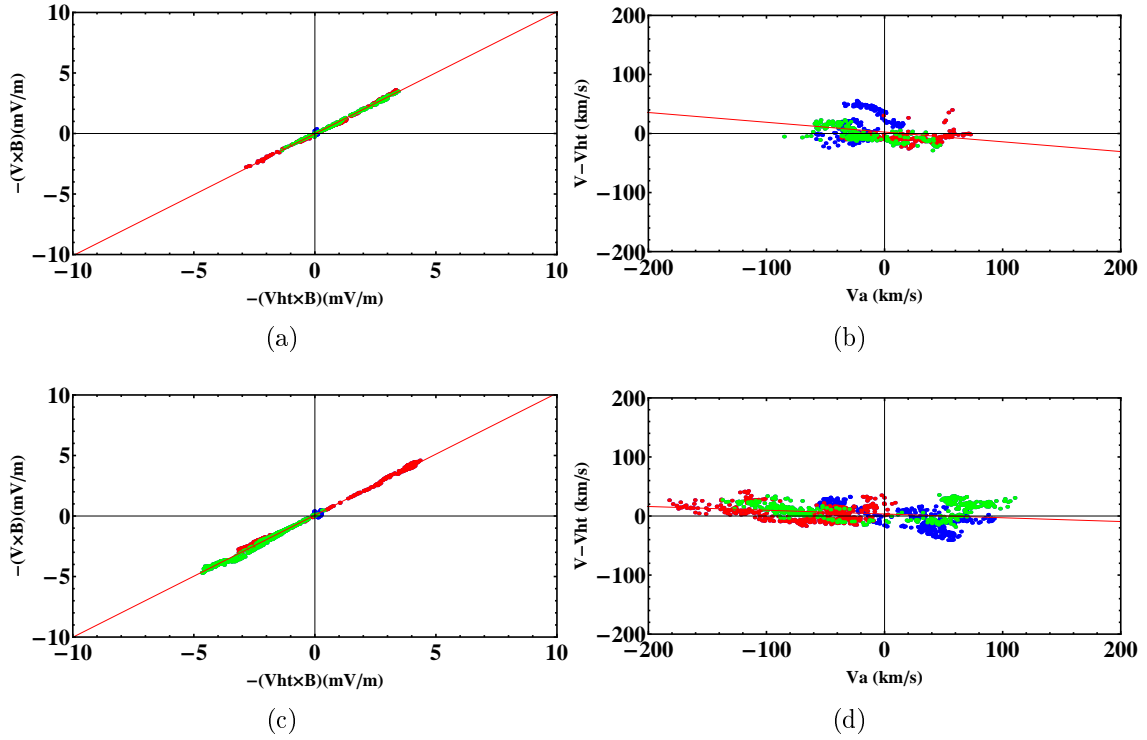


Figure 6.32 - In the panels (a) and (b) are plotted the results to MC1, Aug. 19-20 10:00-04:00, 1998 while in the panels (c) and (d) the results to MC2, Aug. 20-21 09:00-18:00, 1998 are plotted. In all panels, the colors represent the components, i.e., *red* $\equiv x$, *green* $\equiv y$, *blue* $\equiv z$. In (a) and (c) are illustrates that very good correlation of the convection electric field and the corresponding components of the HT electric field, the quantitative information is given in the Table 6.6. In (b) and (d) shows the correlation between GSE velocity components of the HT frame and the corresponding components of the Alfvén speed, the quantitative information is given in the Table 6.6.

Table 6.7 - Summary of the interaction between two magnetic cloud with different flux rope type.

Bipolar MC							
FR-Type		Reconnection?		WI	FR-Type		
S	(W or E)	N	-	-	S	(W or E)	N
↓	(← or ⇒)	↑	Yes	Large	↓	(← or ⇒)	↑
N	(W or E)	S	-	-	N	(W or E)	S
↑	(← or ⇒)	↓	Yes	Large	↑	(← or ⇒)	↓
S	(W or E)	N	-	-	N	(W or E)	S
↓	(← or ⇒)	↑	No	Small	↑	(← or ⇒)	↓
N	(W or E)	S	-	-	S	(W or E)	N
↑	(← or ⇒)	↓	No	Small	↓	(← or ⇒)	↑
Unipolar MC							
W	(N or S)	E	-	-	W	(N or S)	E
←	(↑ or ↓)	⇒	Yes	Large	←	(↑ or ↓)	⇒
E	(N or S)	W	-	-	E	(N or S)	W
⇒	(↑ or ↓)	←	Yes	Large	⇒	(↑ or ↓)	←
W	(N or S)	E	-	-	E	(N or S)	W
←	(↑ or ↓)	⇒	No	Small	⇒	(↑ or ↓)	←
E	(N or S)	W	-	-	W	(N or S)	E
⇒	(↑ or ↓)	←	No	Small	←	(↑ or ↓)	⇒

We used our programs to assess the quality of the HT frame and the residual flow velocity remaining in the frame (KHRABROV; SONNERUP, 1998). This is done in each of the clouds separately. The two top panels in Figure 6.31(top panels) (6.31(bottom panels)) show results from the minimum-variance analysis over the interval of MC1 (MC2) in the form of magnetic hodograms; quantitative information is given in the Table 6.6. In the Figure 6.32(a) (6.32(c)) is illustrates that very good correlation exists between the GSE components in the MC1 (MC2) of the convection electric field and the corresponding components of the HT electric field, $cc_{all} = 0.998$ ($cc_{all} = 0.999$), the quantitative information is given in the Table 6.6.

The Figure 6.32(b) (6.32(d)) shows the correlation between GSE velocity components in the MC1 (MC2) of the HT frame and the corresponding components of the Alfvén speed, $cc_{all} = -0.263$ ($cc_{all} = -0.256$) a new quantitative information is given in the Table 6.6. With the exception of a few points, in both MCs (MC1 and MC2) the velocities in the HT frame are smaller than Alfvén speed, $|\vec{V}_A|$, (and also sound speeds, c_s) and justify neglect of inertial terms in the momentum equation

and reducing it to a static balance as shown in the Equation 2.5.

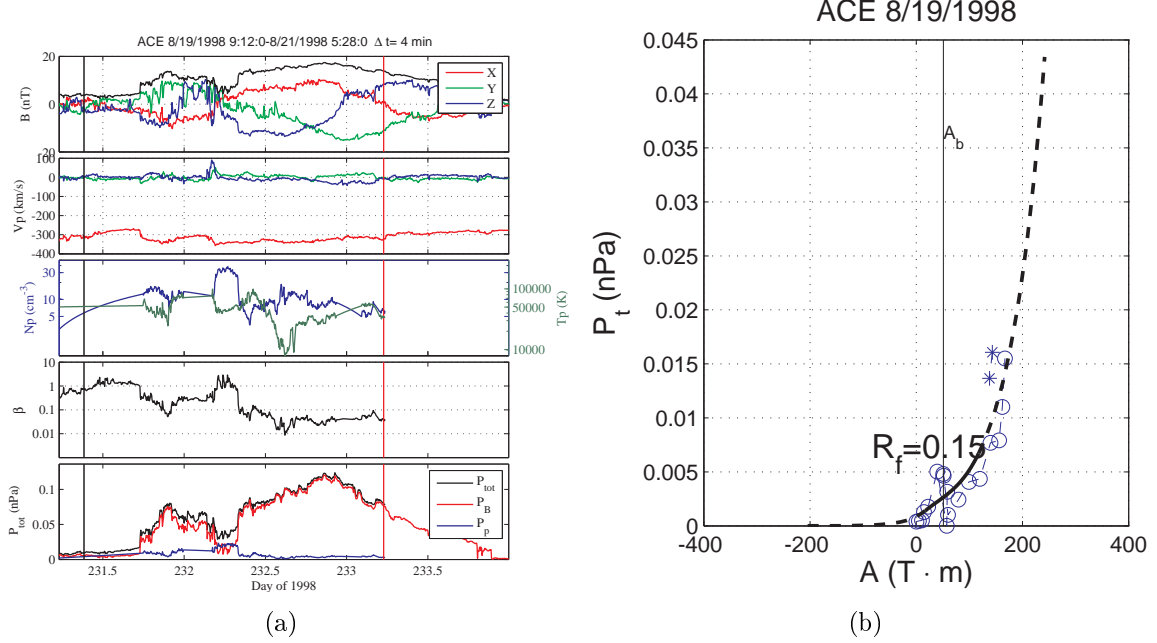


Figure 6.33 - a) From top to bottom panel: magnetic field components, B_x , B_y , B_z , in nT, proton velocity components, V_x , V_y , V_z , in km/s, proton density (in blue), N_p , in cm^{-3} join with proton temperature (in green), T_p , in K, plasma beta and in the last panel are plotted total pressure (in black), kinetic pressure (in blue) and magnetic pressure (in red). b) Plot of data $P_t(x, 0)$ versus $A(x, 0)$ along the x axis for the reconstruction interval and the fitted $P_t(A)$ function (black curve).

Figure 6.33(a) shows two MCs events observed by ACE from March 19 – 21, 1998 with 4 min of time resolution. (a) From top to bottom panel: magnetic field components, B_x , B_y , B_z , in nT, proton velocity components, V_x , V_y , V_z , in km/s, proton density (in blue), N_p , in cm^{-3} join with proton temperature (in green), T_p , in K, plasma beta and in the last panel the total pressure (in black), kinetic pressure (in blue) and magnetic pressure (in red) are plotted. Some interpolations were done in N_p and T_p to cover the gaps intervals. The vertical lines denote the analysis interval, from August 19, 09 : 12 : 00 to 21, 05 : 28 : 00.

The relationship between P_t and A in the Figure 6.33(b) shows scatter around the fitted polynomial curve (order 3) for $P_t(A)$ used in the reconstruction. The vertical line denoted by A_b marks the point on A axis where $A = A_b$ (HU et al., 2003). The

intervals $A \in [A_l, A_m]$ (see pag 4 Hu and Sonnerup (2002)) are the A valid values in the reconstruction. The value A_b is determined from P_t versus A plot, shown in Figure 6.33(b) as the point on the A axis beyond which the requirements that $P_t(A)$ be all functions of A alone are violated. In practice, A_b can be manually selected on the graph, doing trial and error. Meanwhile, a fitting residue, R_f , is calculated in the least squares sense as a quantitative evaluation of deviations from model assumptions by Hu et al. (2004) (see Equation C.45, Appendix C).

The integer N is the total of number of data samples, i.e., the total of points along the x axis represented at the yellow or green arrows in Figure 6.34 (top panel), also each of this point denotes the integer subscript, i . In Figure 6.33(b) is plotted data $P_t(x, 0)$ versus $A(x, 0)$ along the x axis for the reconstruction interval and the fitted $P_t(A)$ function (black curve). Circles are data along the spacecraft inbound path, while stars are along the outbound path. The vertical line denoted by A_b marks the point on A axis where $A = A_b$. The fitting residues $R_f = 0.15$ is defined in Equation C.45. In Figure 6.33(a) the vertical lines denote an interval that is utilized as initial input into the numerical solver of GS equation to recover the cross section of magnetic flux rope.

The reconstruction scheme is done with the invariant z axis, $z_s = [-0.6110, -0.7164, -0.3368]$. The archive “ALLCASE.par” contains all information necessary for controlling the programs, i.e. control the GS-solver program:

```

ACE_231_233_98
1
3
20 120 0
0 0.1 0.3

```

We do not explain the previous numbers, because with the program is provided help with a PDF archive (see Annex B).

In Figure 6.34 (top panel) is shown the recovered cross-section of the two MCs. The white thickened contour line is of value $A = A_b$ shown in Figure 6.33(b). The black contour lines show the transverse magnetic field lines (contours of $A(x, y)$), and the colors show the axial magnetic field, B_z , distribution (scales given by the color bar). White dot shows the magnetic field maximum in the center of the MC best

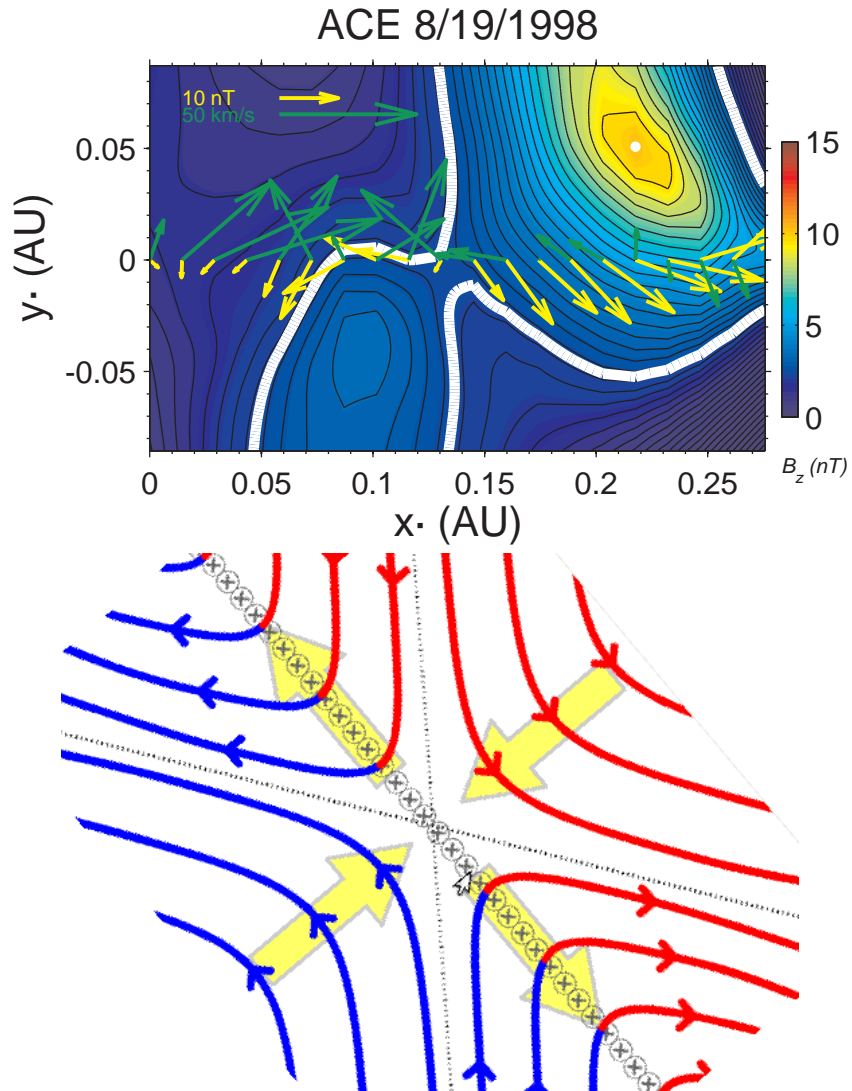


Figure 6.34 - (top panel) The recovered cross-section of the two MCs. In the X point, the spacecraft path seems to lie on top of the magnetic separatrix. (bottom panel) It is cross-section through four magnetic domains undergoing separator reconnection. The original figure was published in http://en.wikipedia.org/wiki/Magnetic_reconnection (November, 2012) and was rotated clockwise by an angle of 45° .

organized. The yellow arrows along $y = 0$ denote measured transverse magnetic field vectors, direction and magnitude measurements at ACE (scales given by the arrow in upper left corner of magnitude 10 nT) utilized as initial input into the numerical solver. The green arrows are residual velocities in the deHoffmann-Teller frame at ACE (scales given by the arrow in upper left corner of magnitude 50 km/s).

Figure 6.34 (top panel) the spacecraft crosses the X point and is observed the exact moment of the magnetic reconnection from 0.13 to 0.15 AU in x axis. In the opposite corners of the X point, the magnetic fields are antiparallel (see yellow arrows in this region). The residual velocity (green arrow in $y=0$) in the deHoffmann-Teller frame at ACE is perpendicular to the the magnetic field line in the reconnection region. We thought it was possible to adjust a two-dimensions model, the most common type of magnetic reconnection is separator reconnection, in which four separate magnetic domains exchange magnetic field lines. Figure 6.34, bottom panel, it is cross-section through four magnetic domains undergoing separator reconnection. Domains in a magnetic plasma are separated by separatrix surfaces or curved surfaces in space that divide different bundles of flux. Two separatrices divide space into four magnetic domains with a separator at the center of the figure. The magnetic field lines are flowing inward in opposite sides of the separator, reconnect, and spring outward in a perpendicular direction to above. The original figure was published in http://en.wikipedia.org/wiki/Magnetic_reconnection (November, 2012) and was rotated clockwise by an angle of 45° to do adjustment over X point that observed in the top panel. The green array in the top panel show a speed in the same direction as is predicted in the reconnection model (thick green arrow in the top corner panel).

Also, Figure 6.34 (top panel) confirm the initial hypothesis i.e. the existence of two magnetic cloud with reconnection between them. Still, for complete the results, current sheets need to be found.

Detection of Current Sheet Between two MCs

A methodology to find current sheets was presented in Section 4.6. Figure 6.35 shows the position of current sheets (red dots) found by the method fixing the critical angle $\theta = 60^\circ$ using four time scales $\tau = [4, 8, 16, 32] \text{ min}$. The magnetic field data is processed using 1 s time resolution with data obtained from the ACE home page (http://www.srl.caltech.edu/ACE/ASC/level2/lvl2DATA_MAG.html). Other current sheets are found in each scales, in the leading edge of the ejecta (ICME)

(along day 19th) as was observed in other event by Chian and Muñoz (2011), Muñoz (2011). Also in the rear edge of the ejection (at the end of day 21th), current sheets are found. From August 22 to 24 the magnetic field has large fluctuation and the number of current sheets found shows that is a turbulent region (MUÑOZ, 2011).

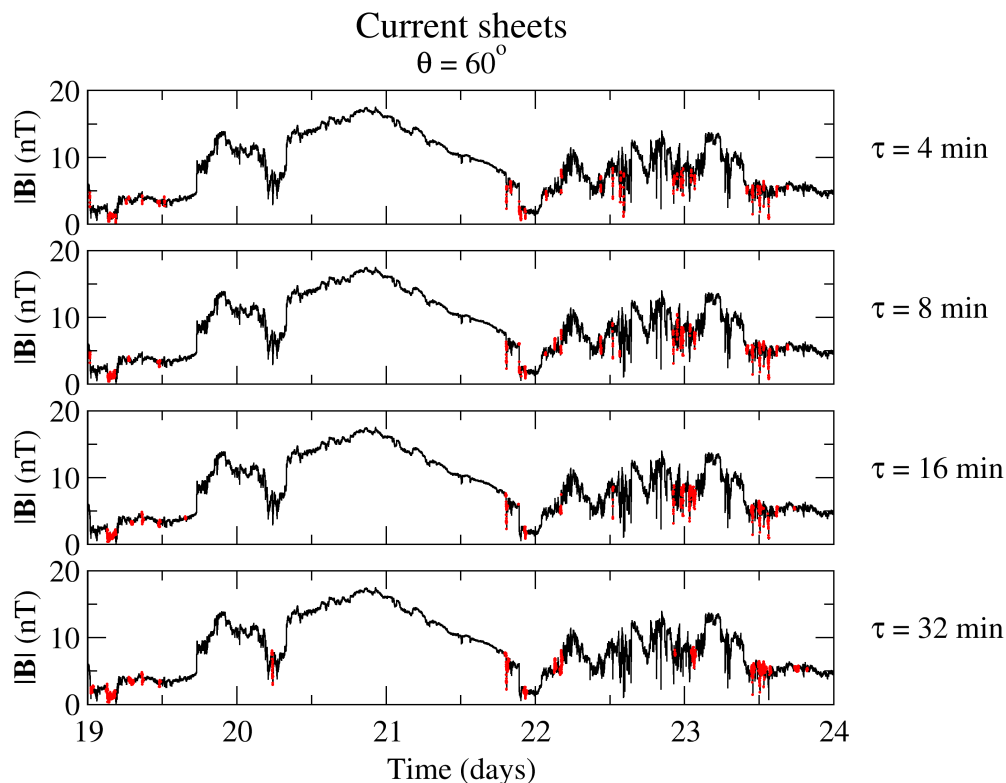


Figure 6.35 - Current sheets of size of $\theta = 60^\circ$ detected by the single-spacecraft method applied over the time series of \vec{B} (black line), using four typical size (scale) of the current sheets. The position of the currents sheets are marked by red dots. A current sheets is observed in the contact region between the two MCs.

At August 22, $\sim 06 : 00$, in the reconnection region between the two magnetic clouds observed in Figure 6.34, a current sheet is found only for the largest time scale, $\tau = 32 \text{ min}$. This result is important because it means that we have found a thick current sheet in that region. It is a perfect region to study transition to turbulence in a real case of scale change.

Finally, we has been used all the techniques presented in the methodological chapter

to identify a new cloud (a case very difficult to identify) and to characterize a reconnection region between the two clouds. This methodology allows a complete study of the magnetic clouds at 1 AU. And could be apply to find and study other similar cases that traditional methods have not identified.

6.4.2 A controversial event which has double magnetic field rotation

The event 27 in the Table A.1 is shown in the left panel of Figura 2 in the paper of Huttunen et al. (2005). They identified this event as a MC with a good magnetic organization on 19–21 March 2001. We reviewed other papers and found contradiction between the dates that this event was identified. Huttunen et al. (2005), Lynch et al. (2003), Cane and Richardson (2003) have classified this event as a single MC. On other hand, Nieves-Chinchilla et al. (2005) and NASA table² have classified this event as two independent clouds. A summary of the above works with the dates of identification of this event are shown in Table 6.8. The columns from the left to the right give: (MCs List) list of papers that studied clouds in this time interval; in the first cloud (MC1): MC start time (UT), MC end time (UT), “Q” is the quality(1 = Excellent, 2 = Good, 3 = Poor), in the second cloud (MC2) the same notation is used .

Table 6.8 - Summary of the five previous studies about MCs that identifies one or two magnetic clouds at 1 AU in the interval from 19 to 21 March. Two paper identified two clouds in this interval. However, the remaining papers (3) have identified a single MC.

March, 2001										
MCs List	MC1					MC2				
	Start	UT	End	UT	Q.	Start	UT	End	UT	Q.
Lepping et al. (1990) ³	19	23 : 18	20	18 : 18	1	20	17 : 48	22	14 : 48	3
Nieves-Chinchilla et al. (2005)	19	21 : 00	20	13 : 00	–	20	18 : 00	21	23 : 00	–
Huttunen et al. (2005)	19	22 : 00	–	–	–	–	–	21	23 : 00	1
Lynch et al. (2003)	19	19 : 00	–	–	–	–	–	21	17 : 00	1
Cane and Richardson (2003)	19	17 : 00	–	–	–	–	–	21	22 : 00	1

We are motivated to test our tools to study this contradictory result. Nieves-Chinchilla et al. (2005) has reported start time of the MC1 on March 19, 21 : 00 while

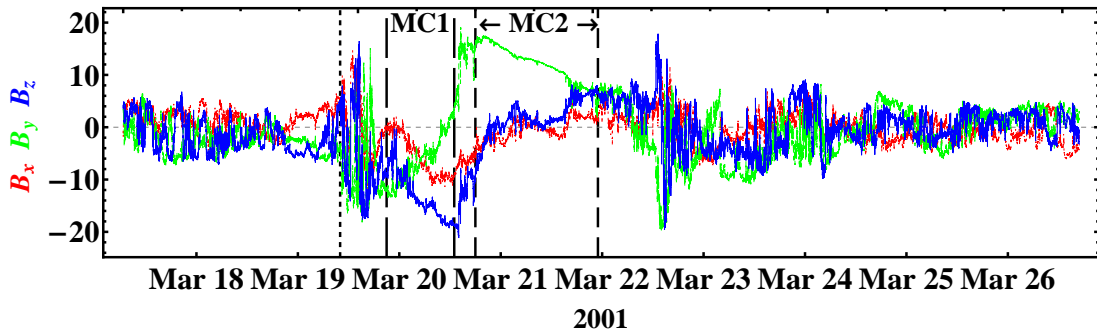
²(http://wind.nasa.gov/mfi/mag_cloud_pub1.html)

in Huttunen et al. (2005), the MC is identified one hour later, 22 : 00 *UT*. The end time of the MC2 is the same in both works, i.e., on March 21, 23 : 00. This allows see from the graphs, the event as one or two MCs. We select the period from March 17 to 27, 2001. The magnetic field data ($B_x \equiv$ Red, $B_y \equiv$ Green, $B_z \equiv$ Blue) with time resolution of 16 s in GSM coordinates system are shown in Figure 6.36. Over the intervals of 2500 records the IE, the persistence indices and WI are calculated. In all panels of the figure, the first vertical line represent the shock of the ICME as has reported by Huttunen et al. (2005); the other four vertical line are the boundaries of the two clouds as has published by Nieves-Chinchilla et al. (2005). Thus, between the first two vertical lines, the plasma sheath is located, and was reported by Huttunen et al. (2005). Furthermore, the MC is located between the two last vertical line. The two MCs have a temporal separation of 5 hours.

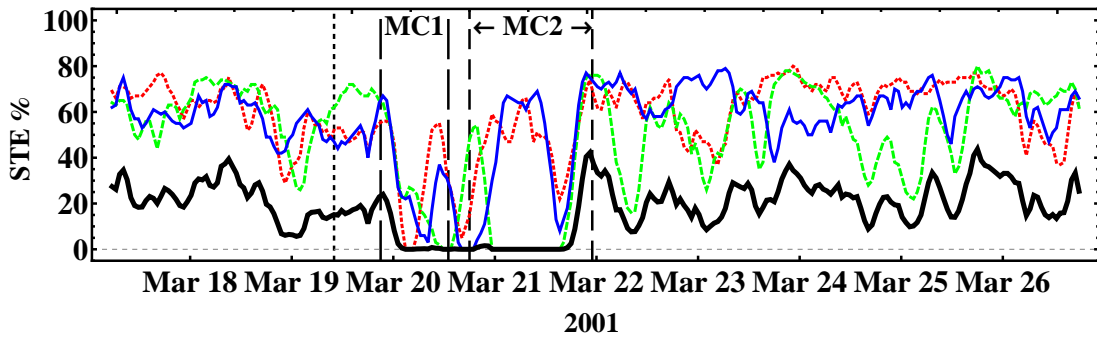
In the Figure 6.36(b) are shown values of STE on 17 – 27 March, 2001 as a function of the time for times series of IMF components (*STE* in: $B_x \equiv$ Red, $B_y \equiv$ Green and $B_z \equiv$ Blue) in the SW. The thick curve represents the IE calculation over all study interval. Figure 6.36(b) shows that the three components have zero STE value during the first MC (MC1). In the contact regions between the clouds also the three components have STE close to zero. The STE values of B_y have zero value within the second cloud (MC2). Thus, the IE is zero along the two clouds and with this tool is not possible to identify two MCs during this event.

In the Figure 6.36(c) are shown values of average wavelet coefficients on 17 – 27 March, 2001 as a function of the time for times series of IMF components (D_{d1} in: $B_x \equiv$ Red, $B_y \equiv$ Green and $B_z \equiv$ Blue) in the SW. The thick curve represents the WI calculation over all study interval. The WI is large in the plasma sheath as is shown in all cases that have been studied in this thesis. And as expected the WI decreases in the MC region. Unlike the case shown in Figure 6.28, in the interaction region between the two MCs, the WI is not increased. This fact makes it impossible to use the WI to identify the two MCs in this region. However, with this result, we conclude that although there are two MCs, then it are not reconnecting. The two clouds are a combination of flux-rope types as is shown in the Table 6.7 (rows 5 or 6 to bipolar MC; rows 10 or 11 to unipolar MC).

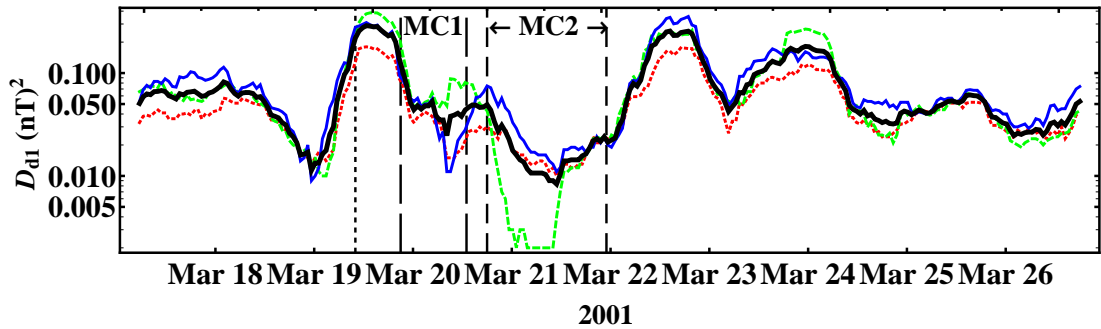
We continued to test the other tools. In the Figure 6.37 are shown values of persistence exponents, β , α , H_u , H_a on 17 – 27 March, 2001 as a function of the time for times series of IMF components ($(\beta, \alpha, H_u, H_a)$ in: $B_x \equiv$ Red, $B_y \equiv$



(a)

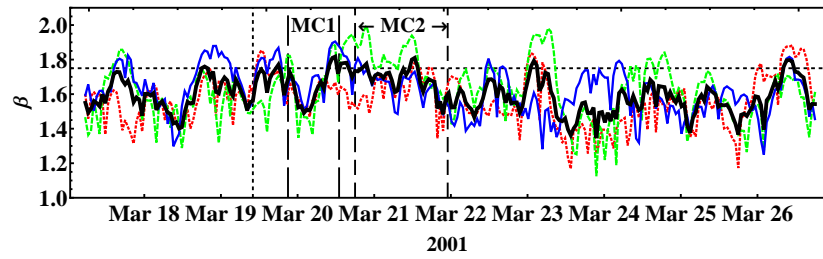


(b)

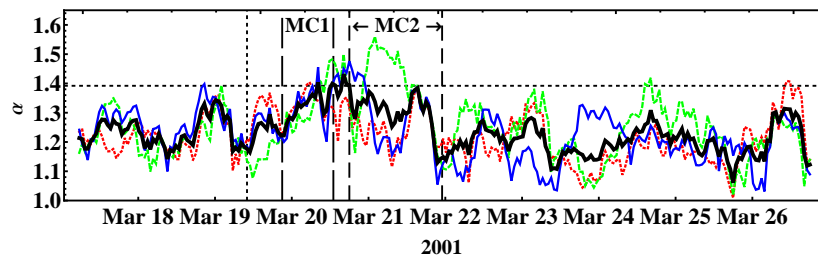


(c)

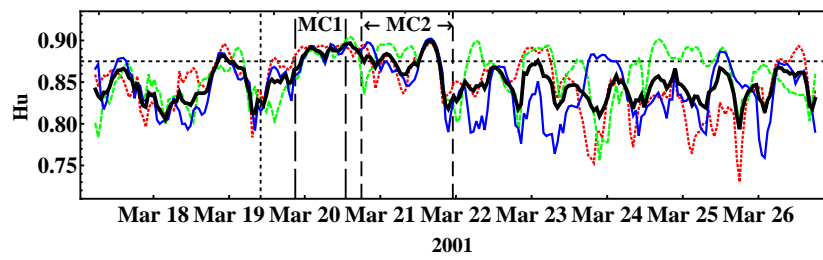
Figure 6.36 - (a) The magnetic field data ($B_x \equiv$ Red, $B_y \equiv$ Green, $B_z \equiv$ Blue) with time resolution of 16 s in GSM coordinates system are shown. (b) Are shown values of STE on 17 – 27 March, 2001 as a function of the time for times series of IMF components (STE in: $B_x \equiv$ Red, $B_y \equiv$ Green and $B_z \equiv$ Blue) in the SW. The thick curve represents the IE calculation over all study interval. We identify the MC1. (c) Are shown values of average wavelet coefficients on 17 – 27 March, 2001 as a function of the time for times series of IMF components (D_{d1} in: $B_x \equiv$ Red, $B_y \equiv$ Green and $B_z \equiv$ Blue) in the SW. The thick curve represents the WI calculation over all study interval.



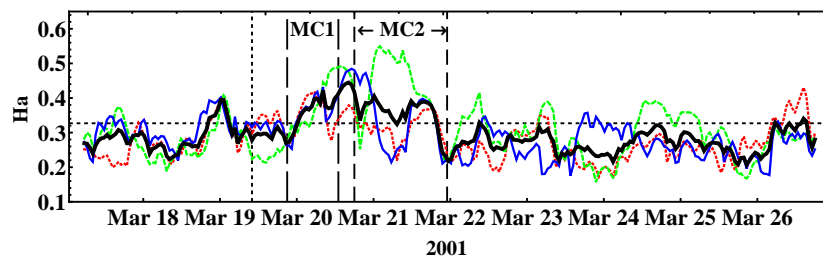
(a)



(b)



(c)



(d)

Figure 6.37 - Are shown values of persistence exponents, β , α , H_u , H_a on 17 – 27 March, 2001 as a function of the time for times series of IMF components ($(\beta, \alpha, H_u, H_a)$ in: $B_x \equiv \text{Red}, B_y \equiv \text{Green}$ and $B_z \equiv \text{Blue}$) in the SW. The thick curve represents the persistence indices ($\langle \beta \rangle, \langle \alpha \rangle, \langle H_u \rangle, \langle H_a \rangle$) calculation over all study interval.

Green and $B_z \equiv$ Blue) in the SW. The thick curve represents the persistence indices ($\langle\beta\rangle$, $\langle\alpha\rangle$, $\langle H_u\rangle$, $\langle H_a\rangle$) calculation over all study interval. The four indices are above the threshold for the two MCs. Thus, it is impossible to use the persistence indices to identify the two MCs in this region.

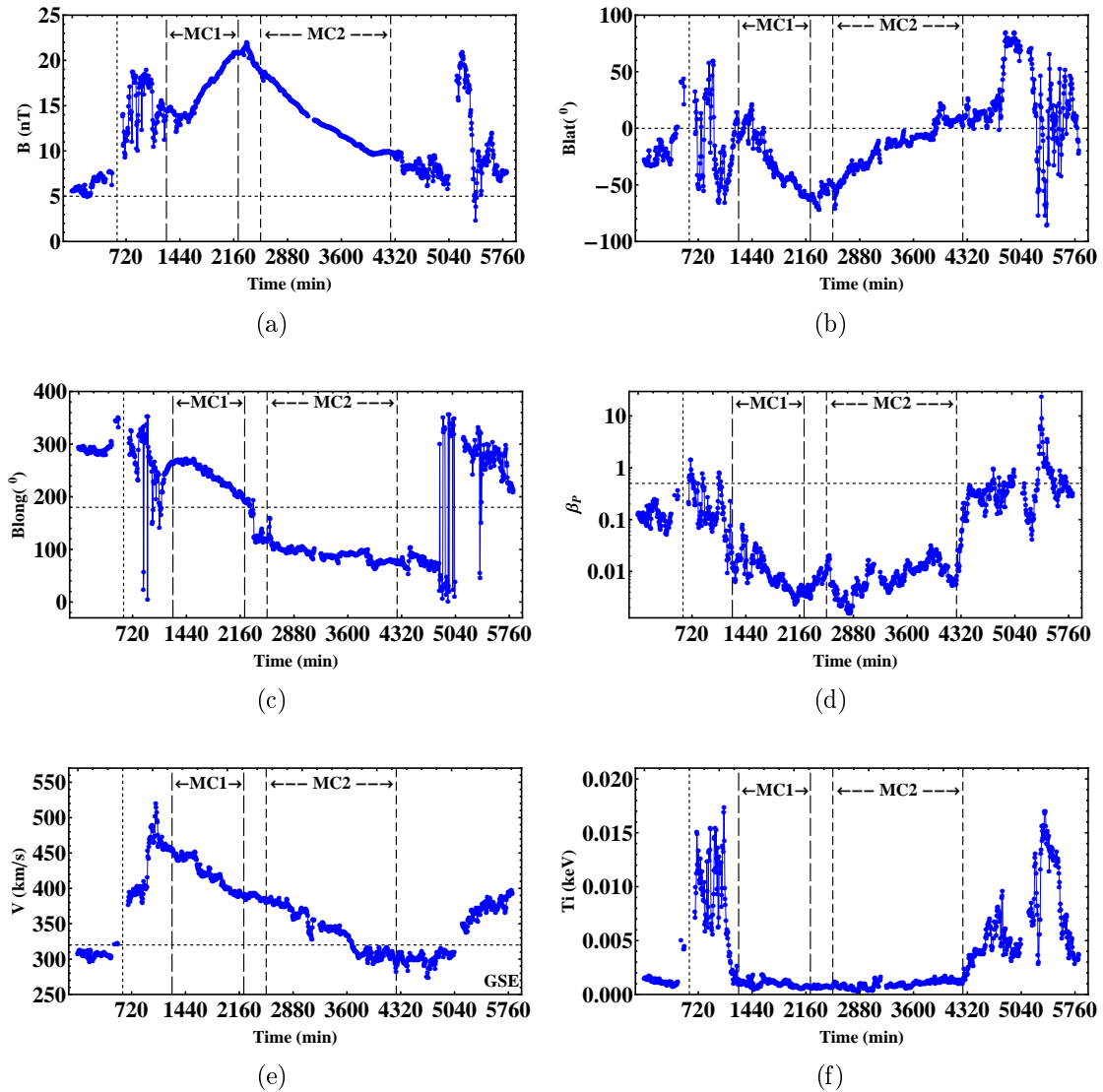


Figure 6.38 - The plot, obtained from OMNI data set in CDAWeb (http://cdaweb.gsfc.nasa.gov/istp_public/), are based on 5-min averaged ACE data in March 19-22, 2001 in GSE coordinates system.

As the above tools were not able to identify the two clouds, then the magnetic and plasma data are plotted to extract other informations about it. The data was

measured by ACE from March 19 to 22, 2001 in GSE with 5 min time resolution. Figure 6.38 is composed by six panels from (a) to (f): magnetic field strength, polar (B_{lat}) and azimuthal (B_{long}) angles of the magnetic field vector in GSE coordinate system, plasma beta, total velocity and temperature.

If the Figure 6.38(b and c) is only seen as a cloud, then this MC has a flux rope type WSE and the observed angular variation of the magnetic field is left-handed (HUTTUNEN et al., 2005). The kinds of variations of the magnetic field direction of MC can be reproduced by the force-free model as was shown in Figure 6.8. In that model, the magnetic field has a maximum in the axis of the MC and is expected a behavior of the average magnetic field $|\vec{B}|$ as is shown in Figure 6.38(a). The average magnetic field $|\vec{B}|$ has a maximum ~ 23 nT at March 20, $\sim 14 : 00$. The data shown in Figure 6.38 have no subject that allows us to identify two MCs in this event as was published by Nieves-Chinchilla et al. (2005) and NASA table. We only seen in the Figure 6.38(d) a small increase of the plasma beta in the contact region between the two MCs.

Despite the above results, we applied the MVA method for each clouds that were identified by Nieves-Chinchilla et al. (2005). The results are shown in the Figure 6.39. The magnetic field rotation confined to one plane, the plane of maximum ($B_x^*B_y^*$) and minimum ($B_y^*B_z^*$) variance to the first cloud or MC1 are shown in the Figures 6.39 (a and b). In the Figure 6.39 (c and d) the magnetic hodograms for the second magnetic cloud or MC2 are shown.

Finally, we have observed the bipolar MC1 detected by ACE from March 19, 21 : 00 UT to March 20, 13 : 00 UT. This MC has a flux-rope type NWS and the observed angular variation of the magnetic field is left-handed. The MVA method gives to MC1 the eigenvalue ratio $\lambda_2/\lambda_3 = 1.76$, the angle between the first and the last magnetic field vectors $\chi = 75.41^\circ$, the orientation of the axis $(\phi_C, \theta_C) = (80.20^\circ, -19.93^\circ)$, the direction of minimum variance $(\phi_{min}, \theta_{min}) = (1.70^\circ, 28.79^\circ)$ and eigenvalues $[\lambda_1, \lambda_2, \lambda_3] = [68.64, 2.21, 1.26]$. The low ratio of the intermediate eigenvalue λ_2 to the minimum eigenvalue λ_3 indicates that the eigenvectors are wrong defined. We required that λ_2/λ_3 is larger than 2, based on the analysis of Lepping and Behannon (1980). The MVA method gives to MC2 the eigenvalue ratio $\lambda_2/\lambda_3 = 3.70$, the angle between the first and the last magnetic field vectors $\chi = 68.27^\circ$, the orientation of the axis $(\phi_C, \theta_C) = (83.12^\circ, -4.31^\circ)$, the direction of minimum variance $(\phi_{min}, \theta_{min}) = (174.95^\circ, 22.96^\circ)$ and eigenvalues $[\lambda_1, \lambda_2, \lambda_3] =$

Table 6.9 - Summary of results to MVA method (first part, rows 1-12) and Grad Shafranov reconstruction techniques (second part, rows 14-18) for two MCs. We show: (\hat{x}_i) the eigenvectors of the magnetic variance matrix; (λ_i) the corresponding eigenvalues; (λ_2/λ_3) the eigenvalue ratio; (ϕ_C, θ_C) MC axis orientation (longitudinal and latitudinal angles); (ϕ_{min}, θ_{min}) the direction of minimum variance; (χ) the angle between the first and the last magnetic field vectors; (Type) inferred flux-rope type; (CH) handedness of the cloud (LH=left-handed, RH=right-handed); (\vec{V}_{HT}) deHoffman-Teller(HT) frame velocity; (cc_{all}) HT correlation coefficient; ($slope_{all}$) slope of the linear fit in deHoffman-Teller(HT) frame; ($cc_{all-Walen}$) Walén correlation coefficient; ($slope_{all-Walen}$) slope of the linear fit in the Walén analysis.

March, 2001		
Parameters	MC1 (19-20, 21:00-13:00)	MC2 (20-21, 18:00-23:00)
\hat{x}_1, \hat{B}_x^*	(-0.46, 0.38, -0.81)	(0.38, -0.12, 0.92)
\hat{x}_2, \hat{B}_y^*	(0.16, 0.93, 0.34)	(-0.12, -0.99, -0.08)
\hat{x}_3, \hat{B}_z^*	(0.88, 0.03, -0.48)	(-0.92, 0.08, 0.39)
$[\lambda_1, \lambda_2, \lambda_3]$	[68.64, 2.21, 1.26]	[28.66, 2.75, 0.74]
λ_2/λ_3	1.76	3.70
ϕ_C	80.20	83.12
θ_C	-19.93	-4.31
ϕ_{Min}	1.70	174.95
θ_{Min}	28.79	22.96
χ	75.41	68.27
Type	NWS	SEN
CH	LH	LH
Grad-Shafranov		
\vec{V}_{HT}	(-427.78; -26.01; -35.29)km/s	(-350.9, -36.2; 10.4)km/s
cc_{all}	0.999	0.999
$slope_{all}$	0.999	1.006
$cc_{all-Walen}$	-0.590	0.721
$slope_{all-Walen}$	-0.196	0.225

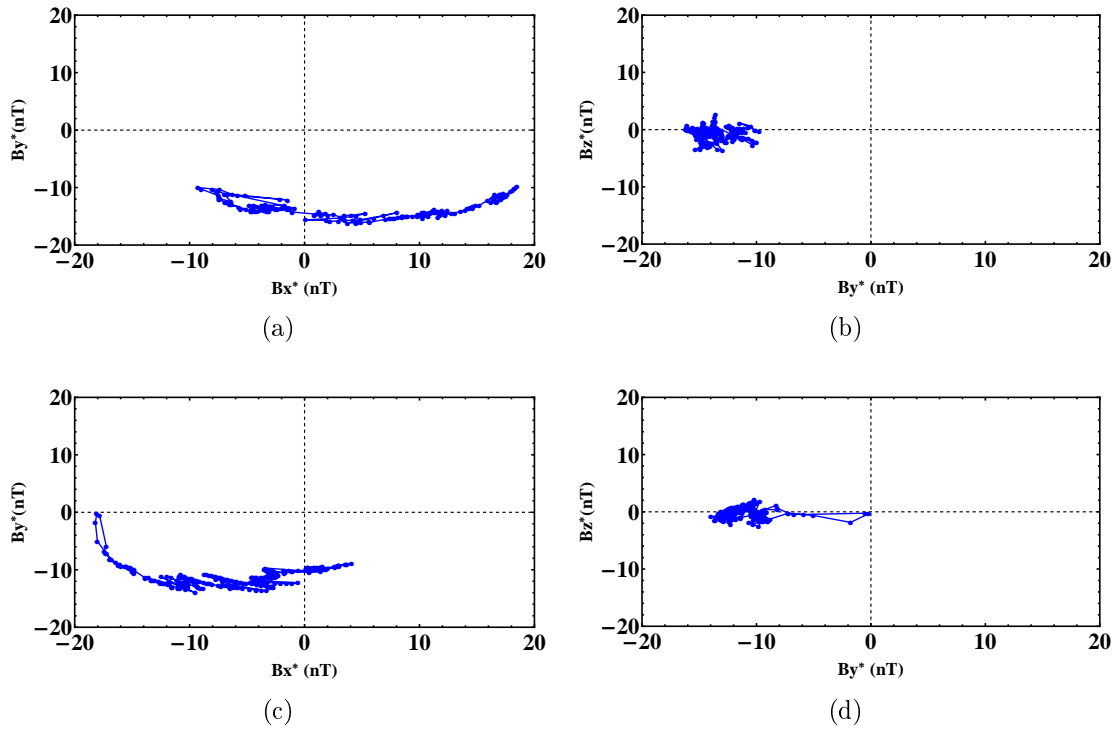


Figure 6.39 - In the panels are shown the magnetic hodograms for two magnetic clouds:(a and b) the first MC or MC1 was observed from March 19–20 21 : 00–13 : 00, 2001 while (c and d) the second MC or MC2 was observed from March 20–21 18 : 00–23 : 00, 2001. The magnetic field rotation confined to one plane, the plane of maximum ($B_x^*B_y^*$) and minimum ($B_y^*B_z^*$) variance are used to find the boundaries of the two clouds.

[28.66, 2.75, 0.74]. The large ratio of the intermediate eigenvalue λ_2 to the minimum eigenvalue λ_3 indicates that the eigenvectors are well defined. The results derived of MVA method are shown in the first 12 rows of the Table 6.9. If the results given in Table 6.7 are true, then in the interaction region between these two clouds is not form a X point. The flux-rope types are NWS-SEN (see row 6 in Table 6.7) in the interaction region between the two clouds, the magnetic fields are in south direction (S).

Reconstruction results of ACE March 19-21, 2001, magnetic clouds

The Grad-Shafranov reconstruction is the other technique that can be used to visualize, if indeed, there are two MCs in that interval. In the Figure 6.40(a) (6.40(c)) is illustrates that very good correlation exists between the GSE components in the MC1 (MC2) of the convection electric field and the corresponding components of

the HT electric field, $cc_{all} = 0.999$ ($cc_{all} = 0.999$), the quantitative information is given in the Table 6.9.

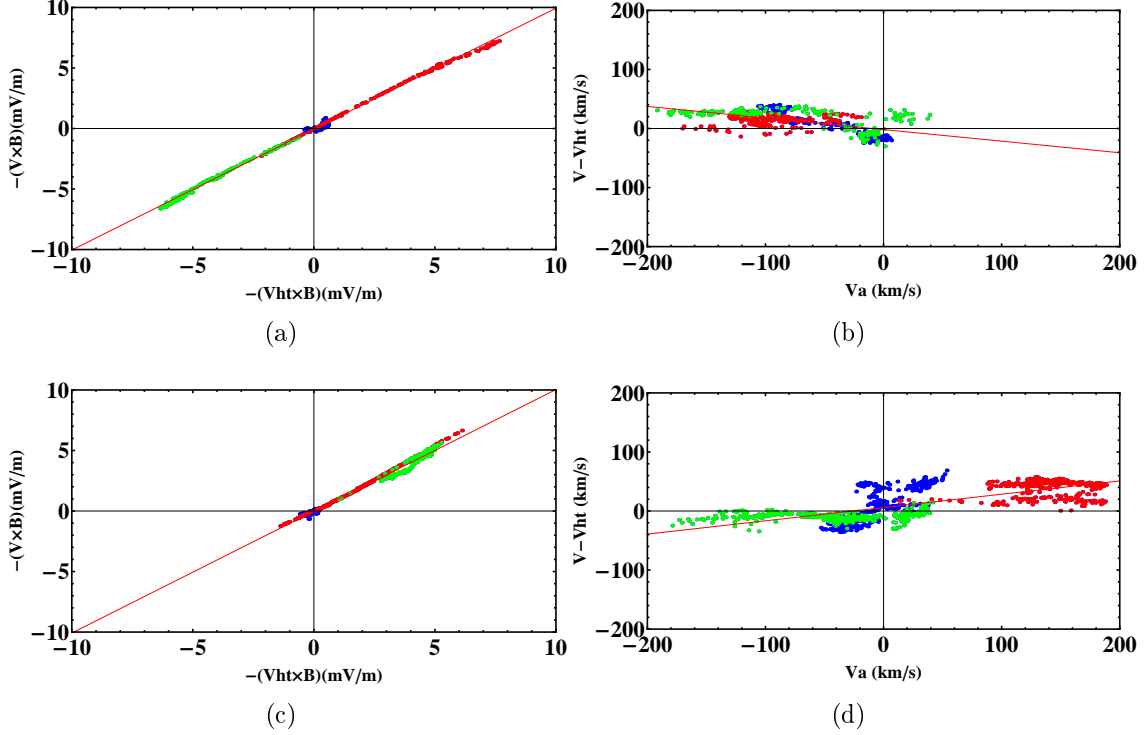


Figure 6.40 - In the panels (a) and (b) are plotted the results to MC1, March 19 – 20 21 : 00 – 13 : 00, 2001 while in the panels (c) and (d) are plotted the results to MC2, March 20 – 21 18 : 00 – 23 : 00, 2001. In all panels, the colors represent the components, *i.e.*, *red* $\equiv x$, *green* $\equiv y$, *blue* $\equiv z$. In (a) and (c) are illustrates that very good correlation of the convection electric field and the corresponding components of the HT electric field, the quantitative information is given in the Table 6.9. In (b) and (d) shows the correlation between GSE velocity components of the HT frame and the corresponding components of the Alfvén speed, the quantitative information is given in the Table 6.9.

The Figure 6.40(b) (6.40(d)) shows the correlation between GSE velocity components in the MC1 (MC2) of the HT frame and the corresponding components of the Alfvén speed, $cc_{all} = -0.590$ ($cc_{all} = 0.721$) anew quantitative information is given in the Table 6.9. With the exception of a few points, in both MCs (MC1 and MC2) the velocities in the HT frame are not smaller than Alfvén speed, $|V_A|$, (and also sound speeds, c_s) and not justified neglect of inertial terms in the momentum equation to reducing it to a static balance as shown in the Equation 2.5. Thus, the

use of the GS model is questionable, however, still can be used to view cross sections of the clouds.

From March 19, 17 : 16 to March 23, 00 : 04 are the analysis intervals used in the reconstruction scheme. The program read merged plasma and magnetic field data from ACE satellite obtained from ftp://nssdcftp.gsfc.nasa.gov/spacecraft_data/ace/4_min_merged_mag_plasma/, i.e. magnetic field components, B_x, B_y, B_z , in nT, proton velocity components, V_x, V_y, V_z , in km/s, proton density, N_p , in cm^{-3} , proton temperature, T_p , in K, plasma beta, total pressure, kinetic pressure and magnetic pressure. Some interpolations were done in N_p and T_p to cover the gaps intervals. The reconstruction scheme is done with the invariant z axis, $z_s = [0.4297, 0.0167, -0.9028]$. The archive “ALLCASE.par” contains all information necessary for controlling the programs, i.e., control the GS-solver program:

```

ACE_078_082_01
  1
  2
 20 120 0
 0 0.1 0.3

```

The relationship between P_t and A in the Figure 6.41 (left panel) shows scatter around the fitted polynomial curve (order 2) for $P_t(A)$ used in the reconstruction, with fitting residue $R_f = 0.12$. The value of $A = A_b$ marks the boundary point at which the inbound and outbound overlying branches of $P_t(x, 0)$ versus $A(x, 0)$ begin to separate.

The recovered cross section of the two magnetic clouds is shown in Figure 6.41 (right panel). The white thickened contour line is of value $A = A_b$ shown in the left panel. The black contour lines show the transverse magnetic field lines (contours of $A(x, y)$), and the colors show the axial magnetic field, B_z , distribution (scales given by the color bar). White dot shows the magnetic field maximum in the center of the MC best organized. The yellow arrows along $y = 0$ denote measured transverse magnetic field vectors, direction and magnitude measurements at ACE (scales given by the arrow in upper left corner of magnitude 10 nT) utilized as initial input into the numerical solver. The green arrows are residual velocities in the deHoffmann-Teller frame at ACE (scales given by the arrow in upper left corner of magnitude 50 km/s).

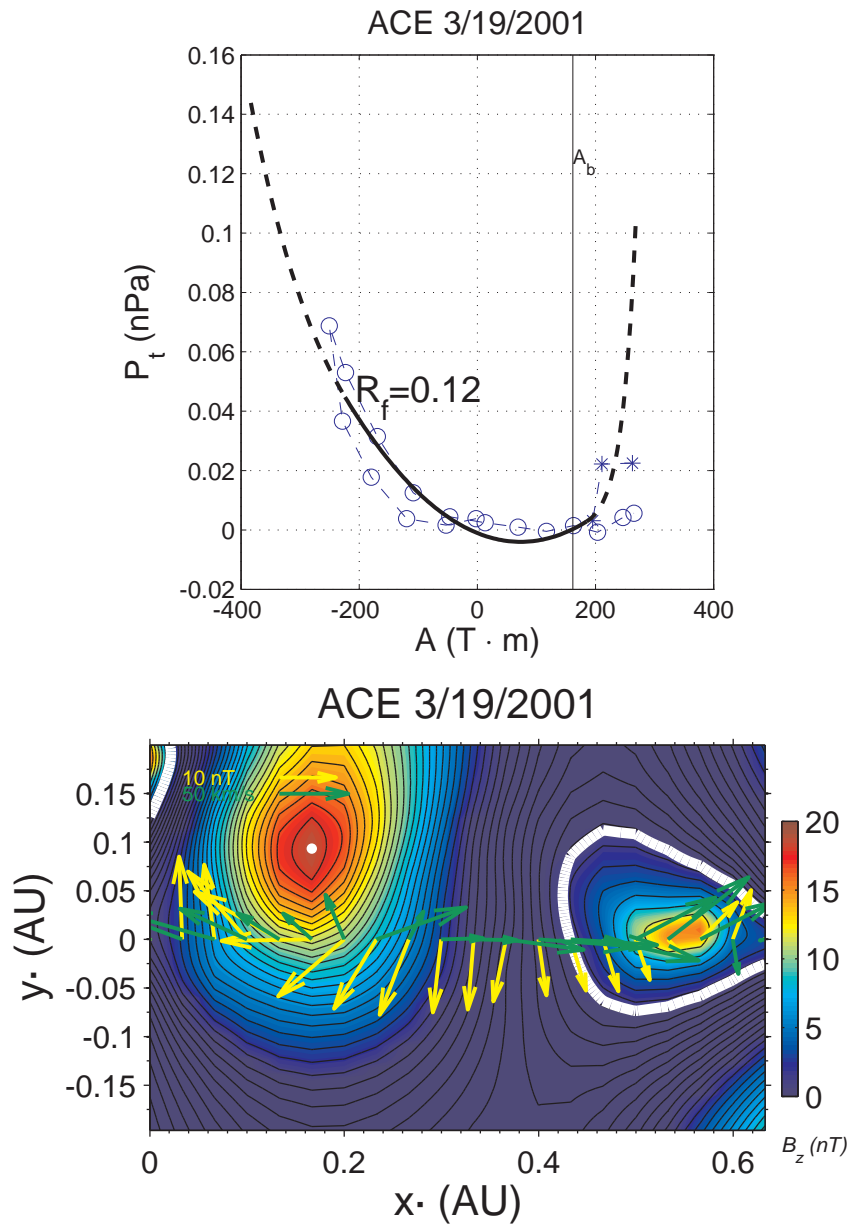


Figure 6.41 - The resulting $P_t(A)$ curve is shown in left panel with fitting residue $R_f = 0.12$. The value of $A = A_b$ marks the boundary point at which the inbound and outbound overlying branches of $P_t(x, 0)$ versus $A(x, 0)$ begin to separate. The recovered cross section of the two magnetic clouds is shown in right panel. The black contour lines show the transverse magnetic field lines (contours of $A(x, y)$), and the colors show the axial magnetic field, B_z , distribution (scales given by the color bar).

With the cross-section view, the two clouds can be identified. This allows to clarify the contradictions in the different studies shown in Table 6.8, the spacecraft saw two MCs in this SW interval. As announced, in the interaction region between the two clouds, the magnetic field is directed to the south. There is not form a X point and the magnetic reconnection is not observed.

The comparison between the Figures 6.41 (right panel) and 6.34 (top panel) is an important result of this work. In one case was observed magnetic reconnection. However, in the other case was not observed magnetic reconnection. We have proven that the summary shown in Table 6.7 is right.

6.5 Summary of the validation of the methodology

In Figure 6.42, a scheme with the methodology developed in this work is shown. In the part I, we start working with thye first technique, *i.e.* STE. The IMF data (in any reference system) with the best time resolution are acquired. Then Data in an arbitrary time interval are taken, using an interval large enough to contain a significant portion of the an eventual MC. After that, records from the data taken within a convenient time length (called window) are selected in each displacement under a constant time step till the end of the data series. Following, the STE value is calculated in each window for B_x , B_y , and B_z components respectively, that allows obtaining a time evolution to STE. If the IE time series has value equal zero then there is a cloud-candidate region and it could be examined in order to identify the MC boundaries.

In the part II is only used when the indexes derived from previous technique has identified a cloud candidate. The persistence exponents and discrete wavelet transform helps to characterize where was found the MC candidate. The MVA helps to identify the cloud boundaries. If exist plasma data then plasma beta is also used to identified the cloud boundaries.

In part III, we can proceed with the reconstruction. The GS reconstruction allow study the magnetic reconnection in double flux-rope MC at 1 AU. The study is completed by the possibility of finding plasma sheets throughout MC region.

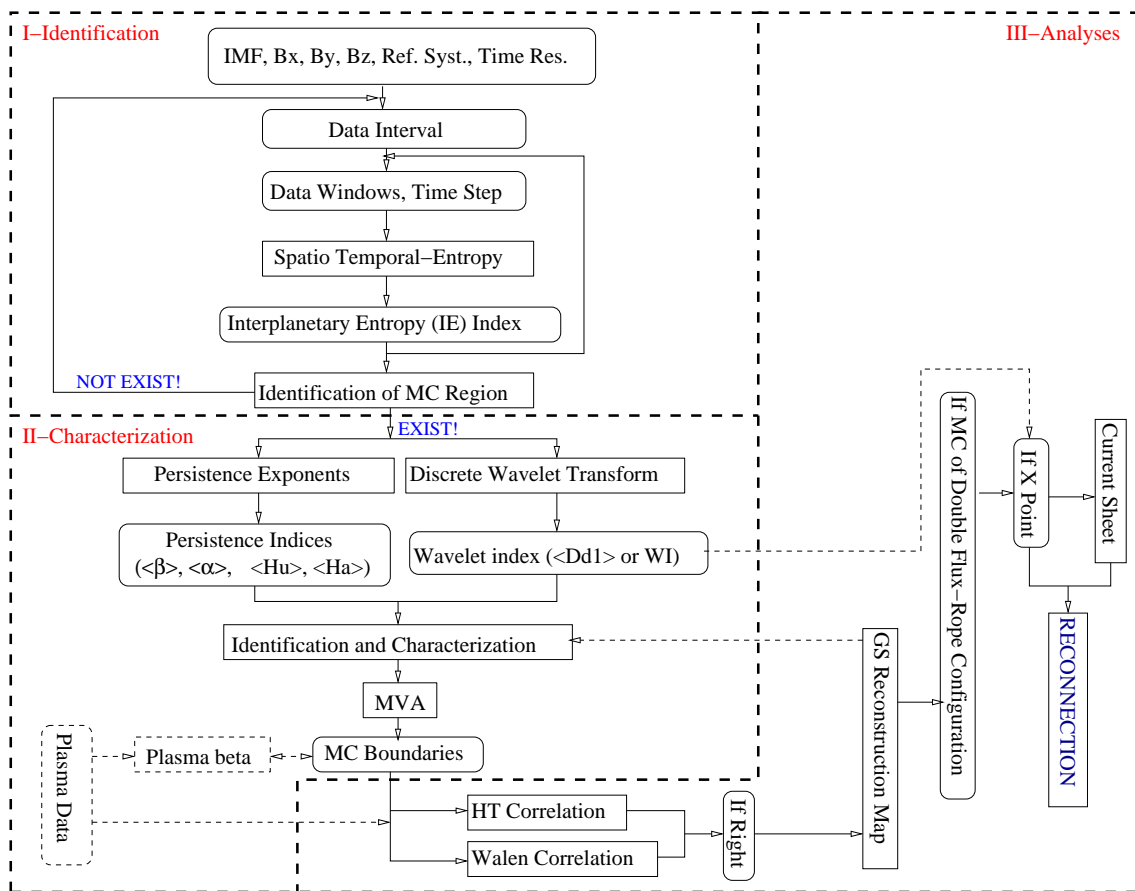


Figure 6.42 - Scheme to explain as the techniques were used. To identify and characterize a cloud, methodology is divided in three parts.

7 CONCLUSION

Dealing with the IMF data and plasma data, the most distinct studies on MC events are done. This work aims to improve a methodology able to help this studies but dealing with the IMF data. Although the potential use of this new tool is not restricted to the initial goal.

The physical bases for use of the techniques are the plasma features related to the MC processes. Several physical-mathematical techniques have been selected for their skills in order to allow the investigation on MC occurrences. Those techniques have been developed in an original approach to identify MC candidates in the SW data and characterize those events. They consist in techniques of spatio-temporal entropy (STE), persistence exponents (Hurst, Hausdorff, beta exponent from power-spectral density (Fourier) and alpha exponent from detrended fluctuation analysis) and wavelet coefficients. Those numerical tools have a great advantage by two characteristics. They are easy to implement with low computational cost and allow creating an automatic operation detection. Also, they can identify MC regions using as input data only the three components of the interplanetary magnetic field (IMF) measured by satellites at convenient space location, *e.g.*, the Lagrangian point $L1$.

The mentioned earlier tools are not able to define the precise boundaries of the MCs. Complementarily, the minimum variance analysis (MVA) technique are applied to delimit the MC location. Furthermore, this method allows characterizing the MC spatial structure. When plasma data are available, other interplanetary parameters are also calculated, as plasma beta, latitudinal and longitudinal rotational angles of magnetic field vector in relation to the ecliptic one, that allows to characterize the polarity as well as the inferred flux-rope type of the cloud.

We work mainly with data of B_x , B_y and B_z with temporal resolution of 16 s measured by the ACE, but divided in two different ways. Firstly, we work with a total of 41 MCs from the years 1998 to 2003, published in the paper of [Huttunen et al. \(2005\)](#). The criteria used to select these 41 cases was the existence of a plasma sheath in front of the MC, and in these cases clouds were well-identified. Secondly, a SW interval of ten days was selected to study the data continuously which were divided in subwindows with 2500 records, and then they were displaced by a convenient time step (here 200 records) from the beginning till the end of the data interval. Using the methodology, three new MCs were identified.

By means of STE calculation using recurrence plots, analyses on the IMF data were performed for a complete SW framework where a group of MCs exists. The developed analyses show that the STE values for MCs are lower than the ones for sheath region or the SW background. The reason is that in MC, the magnetic field strength is higher than average values on SW, the magnetic field direction rotates smoothly through a large angle. Then periods of MCs have more trend than sheaths region and quiet SW periods. The trend is the principal cause of the lower values of STE. It can be noticed that inside MC the IMF have less fluctuations and less noise than outside its boundary. MCs are more structured than sheath and quiet SW. This also collaborates for the decrease of STE within the MC region.

Also, the differences among the STE values for the three magnetic components in a MC give an idea about the anisotropy in the structure of MCs. Those features are related to the flux-rope structure orientation, based on concepts as presented by [Bothmer and Schwenn \(1994\)](#), [Bothmer and Schwenn \(1998\)](#). By using a force free model for IMF as presented by [Burlaga \(1988\)](#), a test considering the magnetic components, mainly the tangential component, of a cylindrically symmetric force-free field constructed analytically results zero STE value. It agrees with the physical assumption of finding zero STE values when studying experimental data in MC periods. The new feature just examined here adds to the usual features, as described in [Burlaga et al. \(1981\)](#), for the characterization of MCs. Thus, the STE calculation can be an auxiliary objective tool to identify flux-ropes associated with MCs, mainly during events with no available plasma data but only with IMF.

Also, we calculate the STE, as a function of time, for IMF components using magnetic records within a time windows corresponding approximately to 11.11 hours, displaced consecutively by a proper time step till the end of data series. The STE reaches values extremely close to zero at least for one of the IMF components during MC event, due to MC structure features. Not all the magnetic components in MCs have STE values equal zero at the same time. By that reason, we create a standardization index (called Interplanetary Entropy (IE) index). This representation is very convenient because it allows joining the STE results of the three IMF components in one estimate parameter, that presents an easy interpretation. IE close to zero indicates the occurrence of a MC-candidate, and its probable time location. By means of study case analyses, we verified and validated the methodology as an useful auxiliary tool to identify MC-candidates. Also, the use of IE index conjugated

with MVA analysis becomes also possible, using only the IMF data, to delimit the MC boundaries.

On the other hand, we have worked with four techniques to study persistence in the 41 ICMEs divided in three regions: plasma sheath, MC and post-cloud respectively. The persistence exponent values increased inside cloud regions, and it was possible select the following threshold values: $\langle\alpha\rangle = 1.392$; $\langle H_a\rangle = 0.327$; $\langle H_u\rangle = 0.875$. These values are useful as another test to evaluate the quality of the identification. After identifying a cloud, the persistence analysis can be performed in the full extent of temporal series of the three IMF components. If the cloud is well-structured, then the persistence exponents values exceed thresholds. With the previous idea, the persistence indices were calculated using the same earlier procedure. If $\langle\alpha\rangle$; $\langle H_a\rangle$; and $\langle H_u\rangle$ values exceed the thresholds, the occurrence is classified as an event in the magnetic cloud region from the diagram of the identification regions. The $\langle\beta\rangle$ index is not recommended to use.

We deal with the same 41 MC events in order to analyze the fluctuation of the IMF B_x , B_y and B_z components. The mathematical property chosen here was the statistical mean of the wavelet coefficients ($\langle D_{d1}\rangle$). It was obtained by applying the Discrete Wavelet Transform (Daubechies scale filters order 2) to the components of the IMF as recorded by the instruments of the MAG onboard of the ACE S/C at the L1 point. The results show that there apparently is a clear distinction between the values of the wavelet coefficients obtained along the different parts of the passing magnetic structure (ahead of the MC, *i.e.*, the sheath; the MC itself; and after the passage of the MC). The measurements show that the $\langle D_{d1}\rangle$ (wavelet index (WI)) exhibits the lower values during the passage of the MC. Also, we found the higher values in the sheaths.

Using assumptions that concern to the physics of MC, the analyses developed in this work show that a smoothed magnetic configuration (*i.e.*, few magnetic fluctuations) in MC is the main reason of the lower values of wavelet coefficients during it. This study is performed only for specific types of ICMEs, all of which were structures that appeared to be MCs. This tool permits comparing the IMF fluctuations at the clouds and its relationship with the neighbors regions, *i.e.*, the first region bounded by the shock front and leading edge, and second region selected after trailing edge. It also permits comparing the existing fluctuation of SW magnetic field, *i.e.*, B_x , B_y , and B_z , which it is not an easy task under simple visual inspection. The B_x component

has lower fluctuations, or singularities, and the B_z component the higher ones.

As a final result, when a complete SW dataset is available, MC events can be investigated in a deep way, mainly with the help of the methodology implemented here. Along the work, and beyond the initial scope, some new MC events were examined. The use of Grad-Shafranov reconstruction model allows to obtain a cross-section view of the flux-rope associated with the MC. Those kinds of information are very useful in the studies to identify and characterize MCs. Even an example of MC event involving an controversial event was studied to illustrate the potential of this methodology. A discrepancy related to 5 papers to indicate if one event is a single or double MC was solved. We observe two clouds in this case. They were measured on March 19 – 21, 2001.

With the methodology developed, an interacting process was found between two magnetic flux-ropes (events at 19 – 21 August 1998), where a single X point was formed between them. The WI detects an IMF discontinuity in this contact region, *i.e.* the WI has large values there. The magnetic field has a jump in a short time interval to move from N to S or vice-versa. The WI becomes a tool for finding reconnection signatures in interaction regions between flux-ropes. We propose the combination of eight flux tubes types, for which if there is interaction between them, the magnetic reconnection can be observed.

The major contribution of this work is the implementation of a methodology for the identification and characterization of MCs, adding new resources to the earlier tools. In a general sense, the proposed methodology can constitute the basis for an easy and automatic computational procedure for preliminary survey on MC occurrences for scientific goals, or even a convenient MC warning for the space weather purposes.

Future perspectives of work

We think that this work is an important continuation of what has been done so far for the study and prediction in space physics/weather. This work collected modern and traditional techniques to create a methodological procedure that could be used in a short time to study and prediction of space weather.

As future work, we suggest to continue this study, improving the identification and characterization in other interplanetary disturbances, such as, CIRs, heliospheric current sheath crossings or to ICMEs without MC signatures, respectively. Also, this

methodology will allow to identify other MCs in an historical SW data. Furthermore, the methodology may resolve discrepancies between some works where it is indicate if one event is a single or double MC. In the small group of MC, where the methodology does not work, we recommend to realize a detailed study of each case.

The technique can “open doors” for other applications. Maybe other applications for Space Physics Community uses will be found, mainly taking into account fluctuations that occur in several frequency ranges. Also to study relationship between SW and geomagnetic parameters, *i. e.*, geoeffectiveness.

REFERENCES

- ABRY, P. **Multirésolutions, algorithmes de décomposition, invariance d'échelles**. Paris: Diderot, 1997. (Ondelettes et turbulence). 58, 81
- BALASIS, G.; DAGLIS, I. A.; ANASTASIADIS, A.; EFTAXIAS, K. Detection of dynamical complexity changes in Dst; time series using entropy concepts and rescaled range analysis. In: LIU, W.; FUJIMOTO, M. (Ed.). **The dynamic magnetosphere**. Springer Netherlands, 2011, (IAGA special Sopron Book Series, v. 3). p. 211–220. ISBN 978-94-007-0501-2. Available from: http://dx.doi.org/10.1007/978-94-007-0501-2_12. 1
- BAME, S.; ASBRIDGE, J.; FELDMAN, W.; GOSLING, J.; ZWICKL, R. Bi-directional streaming of solar wind electrons greater than 80 eV - ISEE evidence for a closed-field structure within the driver gas of an interplanetary shock. **Geophysical Research Letters**, v. 8, p. 173–176, feb. 1981. 86
- BARONI, M. P. M. A.; WIT, A. D.; ROSA, R. R. Detrended fluctuation analysis of numerical density and viscous fingering patterns. **EPL**, v. 92, n. 6, p. 64002, 2010. Available from: <http://dx.doi.org/10.1209/0295-5075/92/64002>. 55
- BASHAN, A.; BARTSCH, R.; KANTELHARDT, J. W.; HAVLIN, S. Comparison of detrending methods for fluctuation analysis. **Physica A: Statistical Mechanics and its Applications**, v. 387, n. 21, p. 5080–5090, 2008. ISSN 0378-4371. Available from: <http://www.sciencedirect.com/science/article/pii/S0378437108003695>. 55
- BENFORD, G.; BOOK, D. L. Relativistic beam equilibria. **Advances in Plasma Physics**, v. 4, p. 125, 1971. 227
- BITTENCOURT, J. **Fundamentals of plasma physics**. Third. Verlag New York, Inc: Originally published by Pergamon Press, New York, 1986, 2004. ISBN 0-387-20975-1. 222, 224
- BOTHMER, V. Solar variability as an input to the earth's environment. In: WILSON, A. (Ed.). **Sources of magnetic helicity over the solar cycle**. Noordwijk:: ESA Publications Division, 2003, (ESA special publication, v. 535). p.

419–428. ISBN 92-9092-845-X. P. 419 – 428. International Solar Cycle Studies (ISCS) Symposium 2003, Tatranská Lomnica, Slovak Republic. 31, 32

BOTHMER, V.; RUST, D. M. The field configuration of magnetic clouds and the solar cycle. **Geophysical Monograph**, v. 99, p. 139–146, 1997. ISSN 0065-8448 CODEN : GPMGAD. AGU. Available from:
<[http://www.agu.org/login/no\\$_\\$license.shtml](http://www.agu.org/login/no$_$license.shtml)>. xxv, 9, 31, 33

BOTHMER, V.; SCHWENN, R. Eruptive prominences as sources of magnetic clouds in the solar wind. **Space Science Reviews**, v. 70, p. 215–220, oct. 1994. 10, 28, 29, 30, 176, 208, 209

_____. The structure and origin of magnetic clouds in the solar wind. **Annales Geophysicae**, Springer Berlin / Heidelberg, v. 16, p. 1–24, 1998. ISSN 0992-7689. 10.1007/s00585-997-0001-x. Available from:
<<http://dx.doi.org/10.1007/s00585-997-0001-x>>. xxv, 3, 9, 10, 27, 28, 29, 30, 31, 33, 63, 176, 206, 207, 208, 209, 210, 244

BULDYREV, S. V.; GOLDBERGER, A. L.; HAVLIN, S.; MANTEGNA, R. N.; MATSA, M. E.; PENG, C.-K.; SIMONS, M.; STANLEY, H. E. Long-range correlation properties of coding and noncoding dna sequences: Genbank analysis. **Phys. Rev. E**, American Physical Society, v. 51, p. 5084–5091, May 1995. Available from: <<http://link.aps.org/doi/10.1103/PhysRevE.51.5084>>. 55

BURLAGA, L.; BEHANNON, K. Magnetic clouds: Voyager observations between 2 and 4 AU. **Solar Physics**, v. 81, p. 181, 1982. Available from:
<<http://articles.adsabs.harvard.edu/full/1982SoPh...81..181B>>. 63, 206

BURLAGA, L. F. Magnetic clouds and force-free fields with constant alpha. **Journal of Geophysical Research**, v. 93, n. 7, p. 7217–7224, 1988. Available from: <<http://www.agu.org/pubs/crossref/1988/JA093iA07p07217.shtml>>. xviii, 1, 3, 8, 10, 16, 85, 115, 116, 130, 176

_____. Magnetic clouds. In: SCHWENN, R.; MARSCH, E. (Ed.). **Physics of the Inner Heliosphere Vol 2**. New York: Springer-Verlag, 1991. p. 1. Available from: <<http://adsabs.harvard.edu/full/1991pihp.book....1B>>. xv, 7, 18, 206

BURLAGA, L. F.; KLEIN, L. W. **Magnetic clouds in the solar wind**. [S.l.], mar. 1980. 1–15 p. Available from:

<http://ntrs.nasa.gov/archive/nasa/casi.ntrs.nasa.gov/19800013734_1980013734.pdf>.

8

BURLAGA, L. F.; SITTLER, E.; MARIANI, F.; SCHWENN, R. Magnetic loop behind an interplanetary shock: Voyager, Helios and IMP 8 observations. **Journal of Geophysical Research**, v. 86, p. 6673–6684, 1981. 1, 7, 8, 10, 91, 108, 129, 176, 205

CALZADILLA, M. A.; LAZO, B. Sheffield space plasma meeting: multipoint measurements versus theory. In: B. Warmbein (Ed.). **Inproceedings... ESA: Non-linear time series analysis of Dst geomagnetic index**, 2001. v. 492, p. 121–+. 2

CANE, H. V.; RICHARDSON, I. G. Interplanetary coronal mas ejections in the near-Earth solar wind during 1996-2002. **Journal of Geophysical Research**, v. 108, n. A4, p. 1156, 2003. 45, 88, 89, 91, 92, 145, 161

CARR, T. W.; SCHWARTZ, I. B. On measures of disorder in globally coupled oscillators. **Physica D: Nonlinear Phenomena**, v. 115, n. 3-4, p. 321–340, 1998. 50, 51

CASTILHO, J.; DOMINGUES, M. O.; MENDES, O.; PAGAMISSE, A. **Introdução ao mundo das wavelets**. São Paulo: SBMAC, 2012. 56

CELLETTI, A.; GIORGILLI, A. On the stability of the lagrangian points in the spatial restricted problem of three bodies. **Celestial Mechanics and Dynamical Astronomy**, v. 50, n. 1, p. 31–58, mar. 1990. ISSN 1572-9478. 35

CHARTFIELD, C. **The analysis of time series an introduction**. Sixth. [S.l.]: Taylor & Francis Library, 2009, 2003. (Chapman & Hall/CRC Texts in Statistical Science). ISBN 1-58488-317-0. 75, 76

CHIAN, A. C.-L.; KAMIDE, Y.; REMPEL, E. L.; SANTANA, W. M. On the chaotic nature of solar-terrestrial environment: Interplanetary alfvén intermittency. **Journal of Geophysical Research (Space Physics)**, v. 111, p. A07S03, jul. 2006. Available from:

<<http://www.agu.org/pubs/crossref/2006/2005JA011396.shtml>>. 1

CHIAN, A. C.-L.; MUÑOZ, P. R. Detection of current sheets and magnetic reconnections at the turbulent leading edge of an interplanetary coronal mass ejection. **The Astrophysical Journal Letters**, v. 733, n. 2, p. L34, 2011.

Available from: <<http://stacks.iop.org/2041-8205/733/i=2/a=L34>>. 1, 4, 72, 108, 151, 160

CID, C.; HIDALGO, M.; NIEVES-CHINCHILLA, T.; SEQUEIROS, J.; VIÑAS, A. Plasma and magnetic field inside magnetic clouds: A global study. **Solar Physics**, Springer Netherlands, v. 207, n. 1, p. 187–198, 2002. ISSN 0038-0938. 10.1023/A:1015542108356. Available from: <<http://dx.doi.org/10.1023/A:1015542108356>>. 10

COCCONI, G.; GREISEN, K.; MORRISON, P.; GOLD, T.; HAYAKAWA, S. The cosmic ray flare effect. **Il Nuovo Cimento(1955-1965)**, v. 8, p. 161–168, 1958. 7

Dal Lago, A.; GONZALEZ, W.; BALMACEDA, A.; L.E.A., V.; ECHER, E.; GUARNIERI, F.; SANTOS, J.; da Silva, M. R.; de Lucas, A.; GONZALEZ, A.; SCHWENN, R.; SCHUCH, N. The 17-21 October (1999) solar-interplanetary-geomagnetic event: Very intense geomagnetic storm associated with a pressure balance between interplanetary coronal mass ejection and a high-speed stream. **Journal of Geophysical Research**, v. 111, p. A07S14, 2006. xvi, 88, 90, 91, 96

DAL LAGO, A.; GONZALEZ, W.; GONZALEZ, A.; TSURUTANI, B. T. Magnetic field and plasma parameters for magnetic clouds in the interplanetary medium. **Geofísica Internacional**, v. 39, n. 1, p. 139–142, 2000. 205

Dal Lago, A.; GONZALEZ, W. D.; GONZALEZ, A.; VIEIRA, L. E. A. Compression of magnetic clouds in interplanetary space and increase in their geoeffectiveness. **Journal of Atmospheric and Solar-Terrestrial Physics**, v. 63, p. 451–455, mar. 2001. 205

Dal Lago, A.; SCHWENN, R.; GONZALEZ, W. Relation between the radial speed and the expansion speed of coronal mass ejections. **Advances in Space Research**, v. 32, n. 12, p. 2637–2640, 2003. ISSN 0273-1177. Available from: <<http://www.sciencedirect.com/science/article/pii/S0273117703800765>>. 209

Dal Lago, A.; SCHWENN, R.; HUTTUNEN, K.; GONZALEZ, W.; GONZALEZ, A.; VIEIRA, L.; ECHER, E.; GUARNIERI, F.; PRESTES, A.; BALMACEDA, L.; SCHUCH, N. Comparison between halo CME expansion speeds observed on the sun, their average propagation speeds to earth and their corresponding

counterparts near earth. In: **Proceedings...** Houston, USA: COSPAR SCIENTIFIC ASSEMBLY, 34., 2002., 2002. v. 34. 208

Dal Lago, A.; VIEIRA, L.; ECHER, E.; GONZALEZ, W.; de Gonzalez, A.; GUARNIERI, F.; SCHUCH, N.; SCHWENN, R. Comparison between halo cme expansion speeds observed on the Sun, the related shock transit speeds to Earth and corresponding ejecta speeds at 1 AU. **Solar Physics**, Springer Netherlands, v. 222, n. 2, p. 323–328, 2004. ISSN 0038-0938.

10.1023/B:SOLA.0000043566.21049.82. Available from:

<<http://dx.doi.org/10.1023/B:SOLA.0000043566.21049.82>>. 209

DASAN, J.; RAMAMOCHAN, T. R.; SINGH, A.; NOTT, P. R. Stress fluctuations in sheared stokesian suspensions. **Physical Review E**, v. 66, n. 2, p. 021409, 2002. 50

DASSO, S.; MANDRINI, C.; DÉMOULIN, P.; LUONI, M.; GULISANO, A. Large scale mhd properties of interplanetary magnetic

clouds. **Advances in Space Research**, v. 35, n. 5, p. 711–724, 2005. Available from:

<<http://www.sciencedirect.com/science/article/pii/S027311770500462X>>. 7, 10, 14, 28

DAUBECHIES, I. **Ten lectures on wavelets**. Philadelphia, PA, USA: Society for Industrial and Applied Mathematics, 1992. ISBN 13: 978-0-89871-274-2. Available from: <<http://dx.doi.org/10.1137/1.9781611970104>>. 57, 58

DÉMOULIN, P.; DASSO, S. Causes and consequences of magnetic cloud expansion. **Astronomy and Astrophysics**, v. 498, n. 2, p. 551–566, may 2009. 1, 27, 206, 209, 210

DEPRIT, A.; Deprit-Bartholome, A. Stability of the triangular Lagrangian points. **The Astrophysical Journal**, v. 72, n. 2, p. 173–179, mar. 1967. 35

DOMINGUES, M. O.; KAIBARA, M. Wavelets biortogonais. **Revista Brasileira de Ensino de Física**, v. 34, n. 3, p. 3701, 2012. 56

DOMINGUES, M. O.; MENDES, O.; Mendes da Costa, A. On wavelet techniques in atmospheric sci-

ences. **Advances in Space Research**, v. 35, n. 5, p. 831–842, 2005. Available from:

<<http://www.sciencedirect.com/science/article/pii/S0273117705004680>>. 3, 56, 57

DU, D.; WANG, C.; HU, Q. Propagation and evolution of a magnetic cloud from ACE to Ulysses. **Journal of Geophysical Research**, v. 112, n. A9, sep. 2007. ISSN 0148-0227. Available from: <<http://dx.doi.org/10.1029/2007JA012482>>. 3, 4

ECHER, E.; ALVES, M.; GONZALEZ, W. A statistical study of magnetic cloud parameters and geoeffectiveness. **Journal of Atmospheric and Solar-Terrestrial Physics**, v. 67, n. 10, p. 839–852, 2005. Available from: <<http://www.sciencedirect.com/science/article/pii/S136468260500060X>>. 31, 32, 205

ECKMANN, J.; KAMPHORST, S.; RUELLE, D. Recurrence plots of dynamical systems. **Europhysics Letters**, v. 4, n. 9, p. 973–977, 1987. Available from: <<http://iopscience.iop.org/0295-5075/4/9/004>>. 49, 84

FACCHINI, A.; MOCENNI, C.; VINICIO, A. Generalized recurrence plots for the analysis of images from spatially distributed systems. **Physica D**, v. 238, p. 162–169, 2009. 49

FADEEV, V.; KVABTSKHAVA, I.; KOMAROV, N. Self-focusing of local plasma currents. **Nuclear Fusion**, v. 5, n. 202, p. 202–209, 1965. 228, 229

FARGE, M. Wavelet transforms and their applications to turbulence. **Annual Review of Fluid Mechanics**, v. 24, p. 395–457, 1992. 56

FARRUGIA, C. J.; JANOO, L. A.; TORBERT, R. B.; QUINN, J. M.; OGILVIE, K. W.; LEPPING, R. P.; FITZENREITER, R. J.; STEINBERG, J. T.; LAZARUS, A. J.; LIN, R. P.; LARSON, D.; DASSO, S.; GRATTON, F. T.; LIN, Y.; BERDICHEVSKY, D. A uniform-twist magnetic flux rope in the solar wind. In: HABBAL, S. R.; ESSER, R.; HOLLWEG, J. V.; ISENBERG, P. A. (Ed.). **Proceedings...** [S.l.]: American Institute of Physics Conference Series, 1999. (American Institute of Physics Conference Series, v. 471), p. 745–748. 10

FARRUGIA, C. J.; OSHEROVICH, V. A.; BURLAGA, L. Magnetic flux rope versus the spheromak as models for interplanetary magnetic clouds. **Journal of Geophysical Research**, v. 100, n. A7, p. 12293–12306, 1995. ISSN 0148-0227. Available from: <<http://www.agu.org/pubs/crossref/1995/95JA00272.shtml>>. 10, 205

FRÄNZ, M.; HARPER, D. Heliospheric coordinate systems. **Planetary and Space Science**, v. 50, n. 2, p. 217–233, 2002. ISSN 0032-0633. 36

FRASER-SMITH, A. C. Centered and eccentric geomagnetic dipoles and their poles, 1600 - 1985. **Reviews of Geophysics**, v. 25, p. 1–16, 1987. 38

FRICK, P.; GROSSMANN, A.; TCHAMITCHIAN, P. Wavelet analysis of signals with gaps. **Journal of Mathematical Physics**, v. 39, p. 4091–4107, aug. 1998. 56

GOLDSTEIN, H. On the field configuration in magnetic clouds. **Solar Wind Five**, p. 731, 1983. Available from:

<<http://adsabs.harvard.edu/abs/1983NASCP.2280.731G>>. 8, 10, 15, 28

GONZALEZ, W. D.; dal Lago, A.; GONZALEZ, A.; VIEIRA, L. E. A.; TSURUTANI, B. T. Prediction of peak-dst from halo cme/magnetic cloud-speed observations. **Journal of Atmospheric and Solar-Terrestrial Physics**, v. 66, n. 2, p. 161–165, jan. 2004. ISSN 1364-6826. Available from:

<<http://www.sciencedirect.com/science/article/pii/S1364682603002141>>. 209

GONZALEZ, W. D.; TSURUTANI, B. T. Criteria of interplanetary parameters causing intense magnetic storms ($dst < -100nt$). **Planetary and Space Science**, v. 35, n. 9, p. 1101–1109, 1987. ISSN 0032-0633. Available from:

<<http://www.sciencedirect.com/science/article/pii/0032063387900158>>. 205

GOSLING, J. Coronal mass ejections and magnetic flux ropes in interplanetary space. In: RUSSEL, C. T.; PRIEST, E. R.; LEE, L. C. (Ed.). **Physics of Magnetic Flux Ropes**. [S.l.]: AGU Geophys. Monogr., 1990. p. 343. 1, 86

GOUPILLAUD, P.; GROSSMANN, A.; MORLET, J. Cycle-octave and related transforms in seismic signal analysis. **Geoexploration**, v. 23, n. 1, p. 85–102, oct. 1984. Available from: <[http://dx.doi.org/10.1016/0016-7142\(84\)90025-5](http://dx.doi.org/10.1016/0016-7142(84)90025-5)>.

56

GRAD, H.; RUBIN, H. Hydromagnetic equilibria and force free fields. In: **Proceedings...** United Nations, Geneva: 2nd U.N. conference on the peaceful uses of atomic energy, 1958. v. 31, n. IAEA, p. 190–197. 20

GROSSMANN, A.; MORLET, J. Decomposition of Hardy functions into square integrable wavelets of constant shape. **SIAM Journal on Mathematical Analysis**, v. 15, p. 723–736, jul. 1984. ISSN 0036-1410. 56

Haggerty, D. K.; Roelof, E. C.; Smith, C. W.; Ness, N. F.; Skoug, R. M.; Tokar, R. L. Two distinct plasma and energetic ion distributions within the June 1998 magnetic cloud. In: Mewaldt, R. A.; Jokipii, J. R.; Lee, M. A.; Möbius, E.; Zurbuchen, T. H. (Ed.). **Inproceedings...** American Institute of Physics: Acceleration and Transport of Energetic Particles Observed in the Heliosphere, 2000. (American Institute of Physics Conference Series, v. 528), p. 266–269. 102

HAPGOOD, M. A. Space physics coordinate transformations: A user guide. **Planetary and Space Science**, v. 40, n. 5, p. 711–717, 1992. ISSN 0032-0633.

Available from:

<<http://www.sciencedirect.com/science/article/pii/003206339290012D>>. 36, 37, 38, 39, 40

HARRIS, E. G. On a plasma sheath separating regions of oppositely directed magnetic field. **Il Nuovo Cimento**, Springer, v. 23, n. 1, p. 115–121, 1962. ISSN 00296341. Available from:

<<http://www.springerlink.com/index/10.1007/BF02733547>>. 226, 227, 229

HASEGAWA, H.; NAKAMURA, R.; FUJIMOTO, M.; SERGEEV, V. A.; LUCEK, E. A.; REME, H.; KHOTYAINTSEV, Y. Reconstruction of a bipolar magnetic signature in an earthward jet in the tail : Flux rope or 3D guide-field reconnection? **Journal of Geophysical Research**, v. 112, n. A11, p. A11206–, 2007. 4

HASEGAWA, H.; SONNERUP, B.; OWEN, C.; KLECKER, B.; PASCHMANN, G.; BALOGH, A.; REME, H. The structure of flux transfer events recovered from cluster data. **Ann Geophys-Germany**, EUROPEAN GEOSCIENCES UNION, v. 24, n. 2, p. 603 – 618, 2006. Available from:

<<http://discovery.ucl.ac.uk/153183/>>. 4

HASEGAWA, H.; SONNERUP, B. U. Ö.; KLECKER, B.; PASCHMANN, G.; DUNLOP, M. W.; REME, H. Optimal reconstruction of magnetopause structures from Cluster data. **Annales Geophysicae**, v. 23, p. 973–982, mar. 2005. 4

HAU, L.-N.; SONNERUP, B. U. Ö. Two-dimensional coherent structures in the magnetopause: Recovery of static equilibria from single-spacecraft data. **Journal**

of Geophysical Research, v. 104, n. A4, p. 6899–6917, 1999. ISSN 0148-0227. Available from: <<http://dx.doi.org/10.1029/1999JA900002>>. xxii, xxiii, xxvi, 3, 20, 21, 64, 66, 67, 68, 69, 71, 153, 229, 230, 233, 235, 236, 238, 243, 244, 245, 246, 247, 248, 249, 250, 253, 254

HENEGHAN, C.; MCDARBY, G. Establishing the relation between detrended fluctuation analysis and power spectral density analysis for stochastic processes. **Phys Rev E Stat Phys Plasmas Fluids Relat Interdiscip Topics**, Digital Signal Processing Research Group, University College Dublin, Belfield, Dublin 4, Ireland., v. 62, n. 5 Pt A, p. 6103–6110, nov. 2000. ISSN 1063-651X. Available from: <<http://view.ncbi.nlm.nih.gov/pubmed/11101940>>. 55

HIDALGO, M.; CID, C.; VINAS, A.; SEQUEIROS, J. A non-force-free approach to the topology of magnetic clouds in the solar wind. **Journal of Geophysical Research**, v. 107, n. A1, p. 1002–1009, jan. 2002. ISSN 0148-0227. Available from: <<http://dx.doi.org/10.1029/2001JA900100>>. 10

HIDALGO, M. A. A study of the expansion and distortion of the cross section of magnetic clouds in the interplanetary medium. **Journal of Geophysical Research**, v. 108, n. A8, 2003. Available from: <<http://www.agu.org/pubs/crossref/2003/2002JA009818.shtml>>. 9

_____. Correction to “A study of the expansion and distortion of the cross section of magnetic clouds in the interplanetary medium”. **Journal of Geophysical Research (Space Physics)**, v. 110, p. 3207, mar. 2005. 9

HOLSCHNEIDER, M. Inverse Radon transforms through inverse wavelet transforms. **Inverse Problems**, v. 7, n. 6, p. 853, 1991. 58

HU, K.; IVANOV, P. C.; CHEN, Z.; CARPENA, P.; STANLEY, H. E. Effect of trends on detrended fluctuation analysis. **Phys. Rev. E**, American Physical Society, v. 64, p. 011114, Jun 2001. Available from: <<http://link.aps.org/doi/10.1103/PhysRevE.64.011114>>. 55

HU, Q.; CHARLES, W.; SMITH, C. W.; NESS, N. F. Double flux-rope magnetic cloud in the solar wind at 1 AU. **Geophysical Research Letters**, v. 30, n. 7, p. 1385, 2003. xvii, 20, 102, 103, 105, 156

HU, Q.; SMITH, C. W.; NESS, N. F.; SKOUG, R. M. Multiple flux rope magnetic ejecta in the solar wind. **Journal of Geophysical Research (Space Physics)**, v. 109, p. 3102, mar. 2004. 20, 102, 157

HU, Q.; SONNERUP, B. Reconstruction of magnetic clouds in the solar wind: Orientations and configurations. **Journal of Geophysical Research**, v. 107, n. A7, p. 1142, 15 PP, jul. 2002. ISSN 0148-0227. Available from: <<http://www.agu.org/pubs/crossref/2002/2001JA000293.shtml>>. 4, 64, 65, 68, 69, 70, 72, 102, 153, 157, 238, 240

HU, Q.; SONNERUP, B. U. Ö. Magnetopause transects from two spacecraft: A comparison. **Geophysical Research Letters**, v. 27, n. 10, p. 1443–1446, may 2000. 69

_____. Reconstruction of magnetic flux ropes in the solar wind. **Geophysical Research Letters**, v. 28, n. 3, p. 467–470, 2001. Available from: <<http://www.agu.org/pubs/crossref/2001/2000GL012232.shtml>>. 3, 4, 10, 64, 65, 68, 69, 70

HU, Q.; SONNERUP, B. U. Ö. Reconstruction of two-dimensional structures in the magnetopause: Method improvements. **Journal of Geophysical Research**, v. 108, n. A1, p. 1011 (9 pp), 2003. Available from: <<http://www.agu.org/pubs/crossref/2003/2002JA009323.shtml>>. 3, 4, 238, 253, 254

HUBBARD, B. B. **The world according to wavelets: The story of a mathematical technique in the making.** [S.l.]: A K Peters Ltd, 1997. 56

HURST, H. E. Long-term storage capacity of reservoirs. **Trans. Amer. Soc. Civil Eng.**, v. 116, p. 770–808, 1951. 53, 211

HURST, H. E.; BLACK, R. P.; SIMAIKA, Y. M. Book. **Long-term storage : an experimental study.** [S.l.]: Constable, London, 1965. 145 p. : p. 2, 53, 211

HUTTUNEN, K. E. J.; SCHWENN, R.; BOTHMER, V.; KOSKINEN, H. E. J. Properties and geoeffectiveness of magnetic clouds in the rising, maximum and early declining phases of solar cycle 23. **Annales Geophysicae**, v. 23, n. 2, p. 625–641, 2005. Available from: <<http://www.ann-geophys.net/23/625/2005/>>. xvi, xxv, xxvi, 9, 30, 31, 42, 44, 45, 84, 88, 89, 92, 93, 94, 95, 126, 132, 135, 144, 145, 147, 150, 161, 162, 166, 175, 205, 206, 209, 259, 267

- IVANOV, K.; HARSHILADZE, A. Dynamics of hydromagnetic clouds from powerful solar flares. **Solar Physics**, v. 92, p. 351, 1984. Available from: <http://adsabs.harvard.edu/abs/1984SoPh...92..351I>. 8, 10, 12, 18, 19
- IVANOV, K. G.; HARSHILADZE, A. F.; EROSHENKO, E. G.; Stiazhkin, V. A. Configuration, structure, and dynamics of magnetic clouds from solar flares in light of measurements on broad vega 1 and vega 2 in january-february 1986. **Solar Physics**, v. 120, p. 407–419, sep. 1989. 18, 19, 20
- JAFFARD, S.; MEYER, Y.; RYAN, R. D. **Wavelets. Tools for science and technology**. [S.l.]: Society for Industrial and Applied Mathematics, 1987. 256 p. ISBN 9780898714487. 56
- KAN, J. Non-linear tearing structures in equilibrium current sheet. **Planetary and Space Science**, v. 27, n. 4, p. 351–354, 1979. ISSN 0032-0633. Available from: <http://www.sciencedirect.com/science/article/pii/0032063379901120>. 226
- KANE, R. P. How good is the relationship of solar and interplanetary plasma parameters with geomagnetic storms? **Journal of Geophysical Research**, v. 110, n. A2, p. A02213, feb. 2005. ISSN 0148-0227. Available from: <http://dx.doi.org/10.1029/2004JA010799>. 209
- KANTELHARDT, J. W.; ZSCHIEGNER, S. A.; KOSCIELNY-BUNDE, E.; HAVLIN, S.; BUNDE, A.; STANLEY, H. E. Multifractal detrended fluctuation analysis of nonstationary time series. **Physica A Statistical Mechanics and its Applications**, v. 316, p. 87–114, dec. 2002. 55
- KAY, S.; MARPLE, S. J. Spectrum analysis - a modern perspective. **Proceedings of the IEEE**, v. 69, n. 11, p. 1380–1419, nov. 1981. ISSN 0018-9219. 55
- KHRABROV, A. V.; SONNERUP, B. U. Ö. DeHoffmann-Teller analysis. **ISSI Scientific Reports Series**, v. 1, p. 221–248, 1998. Available from: <http://www.issibern.ch/forads/sr-001-09.pdf>. 68, 69, 70, 71, 155, 246, 247, 248, 249
- KLEIN, L. W.; BURLAGA, L. F. Interplanetary magnetic clouds at 1 au. **Journal of Geophysical Research**, v. 87, p. 613–624, feb. 1982. 1, 7, 8, 27, 29, 90, 93, 130, 205

KUMAR, A.; RUST, D. M. Interplanetary magnetic clouds, helicity conservation, and current-core flux-ropes. **Journal of Geophysical Research**, v. 101, p. 15667–15684, jul. 1996. 28

LEPPING, R.; BURLAGA, L.; SZABO, A.; OGILVIE, K.; MISH, W. The wind magnetic cloud and events october 18-20, 1995: interplanetary properties and as triggers for geomagnetic activity. **Journal of Geophysical Research**, v. 102, n. A7, p. 14,049–14,063, 1997. Available from:
<<http://www.agu.org/journals/ja/v102/iA07/97JA00272/97JA00272.pdf>>. 18

LEPPING, R. P.; ACÛNA, M. H.; BURLAGA, L. F.; FARRELL, W. M.; SLAVIN, J. A.; SCHATTEN, K. H.; MARIANI, F.; NESS, N. F.; NEUBAUER, F. M.; WHANG, Y. C.; BYRNES, J. B.; KENNON, R. S.; PANETTA, P. V.; SCHEIFELE, J.; WORLEY, E. M. The Wind magnetic field investigation. **Space Science Reviews**, v. 71, p. 207–229, feb. 1995. 42, 89

LEPPING, R. P.; BEHANNON, K. W. Magnetic field directional discontinuities. 1: Minimum variance errors. **Journal of Geophysical Research**, v. 85, n. A9, p. 4695–4703, jun. 1980. 8, 63, 166

LEPPING, R. P.; BERDICHEVSKY, D.; PANDALAI, S. G. Interplanetary magnetic clouds: Sources, properties, modeling, and geomagnetic relationship. **Recent Research Developments in Geophysics**, p. 77–96, 2000. Eng. Available from: <<http://www.refdoc.fr/Detailnotice?idarticle=24766023>>. 205

LEPPING, R. P.; BURLAGA, L. F.; JONES, J. A. Magnetic field structure of interplanetary magnetic clouds at 1 AU. **Journal of Geophysical Research**, v. 951, p. 11957–11965, aug. 1990. Available from:
<<http://www.agu.org/pubs/crossref/1990/JA095iA08p11957.shtml>>. 9, 10, 16, 17, 27, 70, 126, 161

LI, G. Identifying current-sheet-like structures in the solar wind. **The Astrophysical Journal Letters**, v. 672, p. L65–L68, jan. 2008. 4, 71

LIPKIE, D. **A coordinate system for a non-spherical Earth-oblate spheroidal coordinates**. apr. 2001.

[Http://www.lipkie.com/oceanography/oscoord.pdf](http://www.lipkie.com/oceanography/oscoord.pdf). Available from:
<<http://www.lipkie.com/oceanography/oscoord.pdf>>. 18, 19

LITTLE, M.; MCSHARRY, P.; MOROZ, I.; ROBERTS, S. Nonlinear, biophysically-informed speech pathology detection. In: **Inproceedings...** Toulouse, France: Acoustics, Speech and Signal Processing, 2006. ICASSP 2006 Proceedings. 2006 IEEE International Conference on Acoustics, Speech and Signal Processing, 2006. v. 2, p. II–II. ISSN 1520-6149. 55, 79

LITTLE, M. A.; MCSHARRY, P. E.; J., R. S.; COSTELLO, D. A.; MOROZ, I. M. Exploiting nonlinear recurrence and fractal scaling properties for voice disorder detection. **BioMedical Engineering OnLine**, v. 6, n. 23, p. 1–19, 2007. 50

LUCAS, A. D. **A study of shock wave front's and magnetic cloud's extent in the inner Heliosphere using onservations from multi-spacecraft**. PhD Thesis (PhD) — INPE, 2009. 3

LUCAS, A. D.; dal Lago, A.; SCHWENN, R.; de Gonzalez, A. L. C. Multi-spacecraft observed magnetic clouds as seen by helios mission. **Journal of Atmospheric and Solar Terrestrial Physics**, v. 73, n. 11-12, p. 1361–1371, 2011. ISSN 1364-6826. Available from: <http://www.sciencedirect.com/science/article/pii/S1364682611000538>. 3, 208

LUI, A. T. Y. Grad-Shafranov reconstruction of magnetic flux ropes in the near-Earth space. **fr**, v. 158, p. 43–68, jan. 2011. 4, 64, 68

LUI, A. T. Y.; SIBECK, D. G.; PHAN, T.; ANGELOPOULOS, V.; MCFADDEN, J.; CARLSON, C.; LARSON, D.; BONNELL, J.; GLASSMEIER, K.-H.; FREY, S. Reconstruction of a magnetic flux rope from THEMIS observations. **Geophysical Research Letters**, v. 351, p. 17, apr. 2008. 3, 4, 64, 230

LUNDQUIST, S. Magnetohydrostatic fields. **Ark Fys**, v. 2, p. 361–365, 1950. xv, 8, 10, 16, 17, 115

_____. On the stability of magneto-hydrostatic fields. **Physical Review**, v. 83, p. 307–311, jul. 1951. Available from: <http://adsabs.harvard.edu/abs/1951PhRv...83..307L>. 8, 115

LYNCH, B.; ZURBUCHEN, T.; FISK, L.; ANTIOCHOS, S. Internal structure of magnetic clouds: Plasma and composition. **Journal of Geophysical Research**, v. 108, n. A6, p. 1239–1253, 2003. ISSN 0148-0227. Available from:

<<http://www.agu.org/pubs/crossref/2003/2002JA009591.shtml>>. xxv, 9, 161

MA, Y.; ZHANG, H. Detecting motion object by spatial-temporal entropy. In: **Proceedings...** [S.l.]: Multimedia and Expo, 2001. ICME. IEEE International Conference..., 2001. p. 265–268. 2

MALAMUD, B. D.; TURCOTTE, D. L. Self-affine times series: 1. generation and analyses. In: DMOWSKA, R.; SALTZMAN, B. (Ed.). **Long-range persistence in geophysical time series**. Elsevier, 1999. (Advances in Geophysics, v. 40), p. 1–90. ISBN 0080547400. Available from:

<<http://www.sciencedirect.com/science/article/pii/S0065268708602939>>. xv, 52, 53, 54, 79, 211, 215

MALLAT, S. G. Multiresolution approximations and wavelet orthonormal bases of $L^2(R)$. v. 315, n. 1, p. 69–87, sep. 1989. 56, 57

Mandelbrot, B. B. **The fractal geometry of nature /Revised and enlarged edition/**. [S.l.: s.n.], 1983. 52

MANDELROT, B. B.; NESS, J. W. V. Fractional brownian motions, fractional noises and applications. **SIAM Review**, Society for Industrial and Applied Mathematics, v. 10, n. 4, p. pp. 422–437, 1968. ISSN 00361445. Available from: <<http://harrisd.net/papers/Id/MandelbrotVanNess1968SIAM.pdf>>. 53

MANDELROT, B. B.; WALLIS, J. R. Some long-run properties of geophysical records. **Water Resources Research**, v. 5, n. 2, p. 321–340, 1969. Available from: <<http://www.agu.org/pubs/crossref/1969/WR005i002p00321.shtml>>. 2

MARTIN, S. F.; BILIMORIA, R.; TRACADAS, P. W. Magnetic field configurations basic to filament channels and filaments. In: Rutten, R. J.; Schrijver, C. J. (Ed.). **Solar Surface Magnetism**. [s.n.], 1994. p. 303. Available from: <<http://adsabs.harvard.edu/abs/1994ssm..work..303M>>. 32

MARUBASHI, K. Structure of the interplanetary magnetic clouds and their solar origins. **Advances in Space Research**, v. 6, n. 6, p. 335–338, 1986. ISSN 0273-1177. Available from:

<<http://www.sciencedirect.com/science/article/pii/0273117786901729>>.

8

_____. Interplanetary magnetic flux ropes and solar filaments. **Geophysical Monograph Series**, v. 99, n. AGU, p. 147–156, 1997. ISSN 0-87590-081-X. Available from: <<http://dx.doi.org/10.1029/GM099p0147>>. 20, 28

MCCOMAS, D. J.; BAME, S. J.; BARKER, P.; FELDMAN, W. C.; PHILLIPS, J. L.; RILEY, P.; GRIFFEE, J. W. Solar wind electron proton alpha monitor (SWEPAM) for the advanced composition explorer. **Space Science Reviews**, v. 86, p. 563–612, jul. 1998. 35, 36, 44

MCSHARRY, P. E.; MALAMUD, B. D. **Quantifying self-similarity in cardiac inter-beat interval time series**. 2005. [Http://people.maths.ox.ac.uk/mcsharry/papers/cinc2005mm.pdf](http://people.maths.ox.ac.uk/mcsharry/papers/cinc2005mm.pdf). 79

Mendes da Costa, A.; Oliveira Domingues, M.; Mendes, O.; Marques Brum, C. G. Interplanetary medium condition effects in the south atlantic magnetic anomaly: A case study. **Journal of Atmospheric and Solar-Terrestrial Physics**, v. 73, p. 1478–1491, jul. 2011. 3, 82

MENDES, O. J. **A origem iunterplanetária e o desenvolvimento da fase principal das tempestades geomagnéticas mederadas (1978-1979)**. PhD Thesis (PhD) — Instituto Nacional de Pesquisas Espaciais, 1992. 37

MENDES, O. J.; DOMINGUES, M. O.; Mendes da Costa, A.; GONZALEZ, A. Wavelet analysis applied to magnetograms: Singularity detections related to geomagnetic storms. **Journal of Atmospheric and Solar-Terrestrial Physics**, v. 67, p. 1827–1836, 2005. ISSN 1364-6826. Available from: <<http://www.sciencedirect.com/science/article/pii/S1364682605001550>>. 3, 82

MENEVEAU, C. Analysis of turbulence in the orthonormal wavelet representation. **Journal of Fluid Mechanics**, v. 232, p. 469–520, 1991. ISSN 1469-7645. Available from: <<http://dx.doi.org/10.1017/S0022112091003786>>. 56

MIELNICZUK, J.; WOJDYLLO, P. Estimation of Hurst exponent revisited. **Computational Statistics and Data Analysis**, v. 51, n. 9, p. 4510–4525, May 2007. Available from: <<http://ideas.repec.org/a/eee/csdana/v51y2007i9p4510-4525.html>>. 79

MILLER, G.; TURNER, L. Force free equilibria in toroidal geometry. **Physics of Fluids**, v. 24, p. 363–365, feb. 1981. Available from:

<<http://adsabs.harvard.edu/abs/1981PhFl...24..363M>>. 18, 19, 20

MIURA, A. Anomalous transport by magnetohydrodynamic kelvin-helmholtz instabilities in the solar wind-magnetosphere interaction. **Journal of Geophysical Research**, American Geophysical Union, v. 89, n. A2, p. 801–818, 1984. Available from:

<<http://www.agu.org/pubs/crossref/1984/JA089iA02p00801.shtml>>. 1

MORLET, J. Sampling theory and wave propagation. In: CHEN, C. (Ed.). **Acoustic Signal/Image Processing and Recognition**. [S.l.]: in NATO ASI. Springer-Verlag. New York, 1983. v. 1, p. 233–261. 56

MORRISON, P. Solar-connected variations of the cosmic rays. **Physical Reviews**, v. 95, p. 646, 1954. 7

MÖSTL, C. **Modeling magnetic clouds using multi-spacecraft observations**. PhD Thesis (PhD) — Institut für Physik Institutsbereich Geophysik, Astrophysik und Meteorologie, oct. 2009. Available from:

<http://www.uni-graz.at/~moestlc/moestl_thesis.pdf>. 4, 64

MULLIGAN, T.; RUSSEL, C. T. Multispacecraft modeling of the flux rope structure of interplanetary coronal mass ejections: Cylindrically symmetric versus nonsymmetric topologies. **Journal of Geophysical Research**, v. 106, n. A6, p. 10581–10596, 2001. Available from:

<<http://www.agu.org/pubs/crossref/2001/2000JA900170.shtml>>. 10

MULLIGAN, T.; RUSSEL, C. T.; LUHMANN, J. Solar cycle evolution of the structure of magnetic clouds in the inner heliosphere. **Geophysical Research Letters**, v. 25, n. 15, p. 2959–2962, 1998. Available from:

<<http://dx.doi.org/10.1029/98GL01302>>. xxv, 9, 29, 30, 31, 32, 153

MUÑOZ, P. R. **Edge structures and turbulence in space plasmas**. PhD Thesis (PhD) — INPE, São Jose dos Campos-SP Brasil, 2011. 4, 72, 160

NAROCK, T. W.; LEPPING, R. P. Anisotropy of magnetic field fluctuations in an average interplanetary magnetic cloud at 1 AU. **Journal of Geophysical Research**, v. 112, n. A06108, p. 6, 2007. Available from:

<<http://dx.doi.org/10.1029/2006JA011987>>. 80

NEUGEBAUER, M.; LIEWER, P. C.; GOLDSTEIN, B.; ZHOU, X.;
STEINBERG, J. T. Solar wind stream interaction regions without sector
boundaries. **Journal of Geophysical Research**, v. 109, n. A10102, p. 102, oct.
2004. 109

NIEVES-CHINCHILLA, T.; HIDALGO, M.; SEQUEIROS, J. Magnetic clouds
observed at 1 AU during the period 2000–2003. **Solar Physics**, Springer
Netherlands, v. 232, p. 105–126, 2005. ISSN 0038-0938. 10.1007/s11207-005-1593-5.
Available from: <<http://dx.doi.org/10.1007/s11207-005-1593-5>>. xxv, 9,
94, 161, 162, 166

OJEDA, G. A.; CALZADILLA, M. A.; LAZO, B.; ALAZO, K.; SAVIO, O.
Analysis of behavior of solar wind parameters under different IMF conditions using
nonlinear dynamics techniques. **Journal of Atmospheric
and Solar-Terrestrial Physics**, v. 67, n. 17-18, p. 1859–1864, 2005. Available from:
<<http://www.sciencedirect.com/science/article/pii/S1364682605001598>>.
2, 90, 108

OJEDA, G. A.; MENDES, O.; CALZADILLA, M. A.; DOMINGUES, M. O.
Spatio-temporal entropy analysis of the magnetic field to help magnetic cloud
characterization. **Journal of Geophysical Research**, jan. 2013. 90

Osherovich, V. A.; Fainberg, J.; Stone, R. G. Multi-tube model for interplanetary
magnetic clouds. **Geophysical Research Letters**, v. 26, p. 401–404, 1999. 102

PEACOCK, J. A. Two-dimensional goodness-of-fit testing in astronomy. **Royal
Astronomical Society**, v. 202, n. 1983, p. 615–627, feb. 1983. Available from:
<<http://adsabs.harvard.edu/abs/1983MNRAS.202..615P>>. 50

PELLETIER, J. D.; TURCOTTE, D. L. Self-affine times series: 2. applications
and models. In: DMOWSKA, R.; SALTZMAN, B. (Ed.). **Long-range
persistence in geophysical time series**. [S.l.]: Elsevier, 1999. (Advances in
Geophysics, v. 40), p. 91–166. ISBN 0080547400. 52

PENG, C.-K.; BULDYREV, S. V.; HAVLIN, S.; SIMONS, M.; STANLEY, H. E.;
GOLDBERGER, A. L. Mosaic organization of dna nucleotides. **Phys. Rev. E**,
American Physical Society, v. 49, p. 1685–1689, Feb 1994. Available from:
<<http://link.aps.org/doi/10.1103/PhysRevE.49.1685>>. 54, 55

PERCIVAL, D. B.; WALDEN, A. T. Book. **Spectral analysis for physical applications : multitaper and conventional univariate techniques / Donald B. Percival and Andrew T. Walden.** Cambridge University Press, Cambridge ; New York, N.Y., U.S.A. :, 1993. xxvii, 583 p. : p. ISBN 0521355320521435412. Available from:
<<http://www.loc.gov/catdir/toc/cam021/92045862.html>>. 81

PIDDINGTON, J. H. Interplanetary magnetic field and its control of cosmic-ray variations. **Physical Reviews**, v. 112, p. 589, 1958. Available from:
<[http://prola.aps.org/pdf/PR/v112/i2/p589\\$_\\$1](http://prola.aps.org/pdf/PR/v112/i2/p589$_$1)>. 7

PRICE, C. P.; NEWMAN, D. E. Using the r/s statistic to analyze ae data. **Journal of Atmospheric and Solar-Terrestrial Physics**, v. 63, n. 13, p. 1387–1397, 2001. ISSN 1364-6826. Available from:
<<http://www.sciencedirect.com/science/article/pii/S1364682600002406>>. 2

PRIESTLEY, M. B. Spectral analysis and time series / m.b. priestley. Academic Press, London ; New York :, p. 2 v. (xvii, [45], 890 p.) :, 1981. 52, 81

QIU, J.; HU, Q.; TIMOTHY, A. H.; YURCHYSHYN, V. B. On the magnetic flux budget in low-corona magnetic reconnection and interplanetary coronal mass ejections. **The Astrophysical Journal**, v. 659, n. 1, p. 758–772, apr. 2007. 4

REMYA, R.; UNNIKRIISHNAN, K. Chaotic behaviour of interplanetary magnetic field under various geomagnetic conditions. **Journal of Atmospheric and Solar-Terrestrial Physics**, v. 72, n. 9-10, p. 662–675, 2010. ISSN 1364-6826. 1

RICHARDSON, I. G.; CANE, H. V. Regions of abnormally low proton temperature in the solar wind (1965 – 1991) and their association with ejecta. **Journal of Geophysical Research**, v. 100, p. 23397, 1995. 1

ROBERTS, D. A.; GOLDSTEIN, M. L.; KLEIN, L. W.; MATTHAEUS, W. H. Origin and evolution of fluctuations in the solar wind- helios observations and helios-voyager comparisons. **Journal of Geophysical Research**, v. 92, n. A11, p. 12023–12035, nov. 1987. Available from:
<<http://www.agu.org/pubs/crossref/1987/JA092iA11p12023.shtml>>. 1

ROMASHETS, E.; VANDAS, M. Force-free field inside a toroidal magnetic cloud. **Geophysical Research Letters**, v. 30, n. 20, p. 2065, 2003. Available from: <<http://www.agu.org/pubs/crossref/2003/2003GL017692.shtml>>. 17, 18, 20

RUST, D. M. Spawning and shedding helical magnetic fields in the solar atmosphere. **Geophysical Research Letters**, v. 21, n. 4, p. 241–244, 1994. Available from: <<http://dx.doi.org/10.1029/94GL00003>>. 28

RUST, D. M.; KUMAR, A. Helical magnetic fields in filaments. **Solar Physics**, v. 155, p. 69–97, nov. 1994. Available from: <<http://www.springerlink.com/content/q130902227k6x747/>>. 32

RUZMAIKIN, A.; FEYNMAN, J.; ROBINSON, P. Long-term persistence of solar activity. **Solar Physics**, Springer Netherlands, v. 149, n. 2, p. 395–403, 1994. ISSN 0038-0938. 10.1007/BF00690625. Available from: <<http://dx.doi.org/10.1007/BF00690625>>. 2

SCHWENN, R. Space weather: The solar perspective. **Living Reviews in Solar Physics**, v. 3, n. 2, p. 1–72, 2006. 1, 27

SCHWENN, R.; Dal Lago, A.; HUTTUNEN, K. E. J.; GONZALEZ, W. D. The association of coronal mass ejections with their effects near the Earth. **Annales Geophysicae**, v. 23, p. 1033–1059, 2005. 209

SHAN, L.-H.; GOERTZ, C.; SMITH, R. A. On the embedding-dimension analysis of ae and al time series. **Geophysical Research Letters**, v. 18, n. 8, p. 1647–1650, aug. 1991. 1

SHAN, L.-H.; HANSEN, P.; GOERTZ, C. K.; SMITH, R. A. Chaotic appearance of the ae index. **Geophysical Research Letters**, v. 18, n. 2, p. 147–150, feb. 1991. Available from: <<http://www.agu.org/pubs/crossref/1991/90GL02477.shtml>>. 1

SIMOES, M. C. **Identification of disturbances in magnetograms due to geomagnetic storms using wavelets**. Master Thesis (Mestrado) — Instituto Nacional de Pesquisas Espaciais, Ave Dos Astronautas, SJC,SP, Brasil, apr. 2011. 3

SISCOE, G. L.; SUEY, R. W. Significance criteria for variance matrix applications. **Journal of Geophysical Research**, v. 77, p. 1321–1322, 1972. 63

SKOUG, R. M.; FEDMAN, W.; GOSLING, J.; MCCOMAS, D. J.; REISENFELD, D.; SMITH, C. W.; LEPPING, R. P.; BALOGH, A. Radial variation of solar wind electrons inside a magnetic cloud observed at 1 and 5 AU. **Journal of Geophysical Research**, v. 105, n. A12, p. 27,269, 2000. 102

SMITH, C. W.; L'HEUREUX, J.; NESS, N. F.; ACUÑA, M. H.; BURLAGA, L. F.; SCHEIFELE, J. The ACE magnetic fields experiment. **Space Science Reviews**, v. 86, p. 613–632, jul. 1998. 35, 42, 43

SONNERUP, B.; CAHILL, L. Magnetopause structure and attitude from Explorer 12 observations. **Journal of Geophysical Research**, v. 72, p. 171, 1967.

Available from:

<<http://www.agu.org/pubs/crossref/1967/JZ072i001p00171.shtml>>. 8, 9, 29, 60, 70, 244

SONNERUP, B. U. Ö.; GUO, M. Magnetopause transects. **Geophysical Research Letters**, v. 23, n. 25, p. 3679–3682, 1996. ISSN 0094-8276. Available from: <<http://dx.doi.org/10.1029/96GL03573>>. 3, 20, 21, 64, 65, 66, 69, 250

SONNERUP, B. U. Ö.; HASEGAWA, H.; PASCHMANN, G. Anatomy of a flux transfer event seen by cluster. **Geophysical Research Letters**, v. 31, p. L11803–L11803, 2004. ISSN 0094-8276. 4

SONNERUP, B. U. Ö.; HASEGAWA, H.; TEH, W.-L.; HAU, L.-N. Grad-Shafranov reconstruction: An overview. **Journal of Geophysical Research**, v. 111, n. A09204, p. 12 PP, 2006. 153

SONNERUP, B. U. Ö.; PAPAMASTORAKIS, I.; PASCHMANN, G.; LUEHR, H. Magnetopause properties from AMPTE/IRM observations of the convection electric field - Method development. **Journal of Geophysical Research**, v. 92, p. 12137–12159, nov. 1987. 70

SONNERUP, B. U. Ö.; SCHEIBLE, M. Minimum and maximum variance analysis. **ISSI Scientific Reports Series**, v. 1, p. 185–220, 1998. xv, 3, 29, 60, 61, 62, 64, 65, 70, 244

TAKENS, F. Detecting strange attractors in turbulence. **Lecture Notes in Mathematics**, v. 898, p. 366–381, 1981. 49, 84

TAPIERO, C.; VALLOIS, P. Run length statistics and the hurst exponent in random and birth-death random walks. **Chaos, Solitons and Fractals**, v. 7, n. 9, 1996. 54, 212

TEH, W.-L. **A study of two-Dimensional magnetopause structure based on Grad-Shafranov reconstruction method**. PhD Thesis (PhD) — Institute of Space Science, National Central University, jan. 2007. 4, 64, 65

TEH, W.-L.; HAU, L.-N. Evidence for pearl-like magnetic island structures at dawn and dusk side magnetopause. **Earth, Planets, and Space**, v. 56, p. L681, jul. 2004. 3, 4

_____. Triple crossings of a string of magnetic islands at duskside magnetopause encountered by AMPTE/IRM satellite on 8 August 1985. **Journal of Geophysical Research**, v. 102, n. A8, p. A08207, 2007. ISSN 0148-0227. Available from: <<http://dx.doi.org/10.1029/2007JA012294>>. 3, 4, 153

TSURUTANI, B. T.; GONZALEZ, W. D. Great magnetic storms. **Geophysical Research Letters**, v. 19, n. 1, p. 73–76, 1992. Available from: <<http://www.agu.org/pubs/crossref/1992/91GL02783.shtml>>. 205

TSURUTANI, B. T.; GONZALEZ, W. D.; TANG, F.; AKASOFU, S. I.; SMITH, E. J. Origin of interplanetary southward magnetic fields responsible for major magnetic storms near solar maximum (1978-1979). **Journal of Geophysical Research**, v. 93, p. 8519–8531, 1988. 205

TURCOTTE, D. L. **Fractals and chaos in geology and geophysics**. 2nd revised edition. ed. [S.l.]: Cambridge University Press, 1997. ISBN 0521567335. 52

VAN DEN BERG, J. **Wavelets In physics**. [S.l.]: Cambridge University, 2004. (Cambridge University). ISBN 9788177648508. 56

VAN YEN, R. N.; CASTILLO-NEGRETE, D. del; SCHNEIDER, K.; FARGE, M.; CHEN, G. Wavelet-based density estimation for noise reduction in plasma simulations using particles. **Journal of Computational Physics**, v. 229, n. 8, p. 2821–2839, 2010. ISSN 0021-9991. Available from: <<http://www.sciencedirect.com/science/article/pii/S0021999109006810>>. 56

Vandas, M.; Fischer, S.; Geranios, A. Double flux rope structure of magnetic clouds? In: Suess, S. T.; Gary, G. A.; Nerney, S. F. (Ed.). **American Institute of Physics Conference Series**. [S.l.: s.n.], 1999. (American Institute of Physics Conference Series, v. 471), p. 127–130. 102

VANDAS, M.; ODSTRCIL, D.; WATARI, S. Three-dimensional mhd simulation of a loop-like magnetic cloud in the solar wind. **Journal of Geophysical Research**, v. 107, n. A9, p. 1236, sep. 2002. ISSN 0148-0227. Available from: <<http://dx.doi.org/10.1029/2001JA005068>>. 7, 20

VANOUPINES, P. Rescaled range analysis and the fractal dimension of p. In: **University Library**. 1050 Brussels, Belgium: Free University Brussels, Pleinlaan 2, 1995. Available from: <<http://ftp.vub.ac.be/~pvouplin/pi/pi.ps>>. 53

VASSILIADIS, D.; SHARMA, A. S.; PAPADOPOULOS, K. Lyapunov exponent of magnetospheric activity from al time series. **Geophysical Research Letters**, v. 18, p. 1643–1646, aug. 1991. 1

VERONESE, T.; ROSA, R.; BOLZAN, M.; FERNANDES, F. R.; SAWANT, H.; KARLICKY, M. Fluctuation analysis of solar radio bursts associated with geoeffective X-class flares. **Journal of Atmospheric and Solar-Terrestrial Physics**, v. 73, n. 11-12, p. 1311–1316, 2011. ISSN 1364-6826. Available from: <<http://www.sciencedirect.com/science/article/pii/S1364682610002907>>. 55, 120, 123

VOSS, R. F. Random fractal forgeries. In: EARNSHAW, R. A. (Ed.). **Fundamental Algorithms for computer Graphics**. [S.l.]: Springer-Verlag, 1985. (NATO ASI, F17), p. 805–835. 52

_____. Random fractals: Characterization and measurement. In: R., P.; A., S. (Ed.). **Scaling Phenomena in Disordered System**. [S.l.]: Plenum Press, 1985. (Plenum Press), p. 1–11. 52

_____. Characterization and measurement of random fractals. **Physica Scripta**, T13, n. 27, p. 27–32, 1986. Available from: <<http://iopscience.iop.org/1402-4896/1986/T13/004>>. 52

WALKER, G. W. Some problems illustrating the forms of nebulae. **Royal Society of London Proceedings Series A**, v. 91, p. 410–420, jul. 1915. Available from: <<http://www.jstor.org/stable/93512>>. 227

WANG, Y. M.; WANG, S.; YE, P. Z. Multiple magnetic clouds in interplanetary space. **Solar Physics**, v. 211, p. 333–344, dec. 2002. 20

WEBBER, C. L.; ZBILUT, L. P. Dynamical assessment of physiological systems and state using recurrence plot strategies. **Journal of Applied Physiology**, v. 76, p. 965–973, 1994. Available from:
<<http://jap.physiology.org/content/76/2/965.abstract>>. 49

WEI, H. L.; BILLINGS, S. A.; BALIKHIN, M. Analysis of the geomagnetic activity of the d_{st} index and self-affine fractals using wavelet transforms. **Nonlinear Processes in Geophysics**, v. 11, p. 303–312, jun. 2004. 2

WU, C.-C.; LEPPING, R. P. Effect of solar wind velocity on magnetic cloud-associated magnetic storm intensity. **Journal of Geophysical Research**, v. 107, n. A11, p. 1346–1350, nov. 2002. ISSN 0148-0227. Available from:
<<http://www.agu.org/pubs/crossref/2002/2002JA009396.shtml>>. 205

_____. Effects of magnetic clouds on the occurrence of geomagnetic storms: The first 4 years of wind. **Journal of Geophysical Research**, v. 107, n. A10, p. 1314–1322, oct. 2002. ISSN 0148-0227. Available from:
<<http://www.agu.org/pubs/crossref/2002/2001JA000161.shtml>>. 205

WU, C.-C.; LEPPING, R. P.; GOPALSWAMY, N. Variations of magnetic clouds and CMEs with solar activity cycle. In: Wilson, A. (Ed.). **Solar Variability as an Input to the Earth's Environment**. [s.n.], 2003. (ESA Special Publication, v. 535), p. 429–432. ISBN 92-9092-845-X. Available from:
<<http://adsabs.harvard.edu/abs/2003ESASP.535..429W>>. xxv, 9

YOON, P. H.; LUI, A. T. Y. A class of exact two-dimensional kinetic current sheet equilibria. **Journal of Geophysical Research**, v. 110, n. A1, p. A01202, jan. 2005. ISSN 0148-0227. Available from:
<<http://www.agu.org/pubs/crossref/2005/2003JA010308.shtml>>. 225, 228, 229

ZBILUT, L. P.; WEBBER, C. L. Embeddings and delays as derived from quantification of recurrence plots. **Physics Letters A**, v. 171, n. 3-4, p. 199–203, 1992. Available from:
<<http://www.sciencedirect.com/science/article/pii/037596019290426M>>. 49

ZHANG, G.; BURLAGA, L. F. Magnetic clouds, geomagnetic disturbances and cosmic ray decreases. **Journal of Geophysical Research**, v. 88, p. 2511, 1988. 1, 130

ZHENG, H.; SONG, W.; WANG, J. Detrended fluctuation analysis of forest fires and related weather parameters. **Physica A: Statistical Mechanics and its Applications**, v. 387, n. 8-9, p. 2091–2099, 2008. ISSN 0378-4371. Available from: <<http://www.sciencedirect.com/science/article/pii/S0378437107012204>>. 55

ZWICKL, R.; ASBRIDGE, J.; BAME, S.; FELDMAN, W.; GOSLING, J.; SMITH, E. Plasma properties of driver gas following interplanetary shocks observed by isee-3. In: NEUGEBAUER, M. (Ed.). **in Solar Wind Five**. [S.l.]: NASA Conf. Publ., 1983. v. 2280, p. 711. 1

APPENDIX A - GEOEFFECTIVENESS AND EXPANSION OF MAGNETIC CLOUDS

MCs are an important source of southward interplanetary magnetic field (e. g. NS, SN and S polarity), the relation between MCs and geomagnetic storms have been investigated by several authors (BURLAGA et al., 1981; KLEIN; BURLAGA, 1982; GONZALEZ; TSURUTANI, 1987; TSURUTANI et al., 1988; TSURUTANI; GONZALEZ, 1992; FARRUGIA et al., 1995; LEPPING et al., 2000; DAL LAGO et al., 2000; Dal Lago et al., 2001; WU; LEPPING, 2002b; WU; LEPPING, 2002a). In the work of Echer et al. (2005) a large number of magnetic clouds, 149, were analyzed during the 1966–2001 period, from the whole data set of MCs, 51 are of the NS type, 83 are of the type SN and 15 are unipolar. They did a statistical study of MC parameters and geoeffectiveness that was determined by classifying the number of MCs followed by intense, moderate and weak magnetic storms, and by calm periods. They found that around 77% of the magnetic clouds with $Dst \leq -50/nT$ are geoeffective. And considering also weak storms ($-50/nT \leq Dst \leq -30/nT$), 97% of MCs were followed by geomagnetic activity.

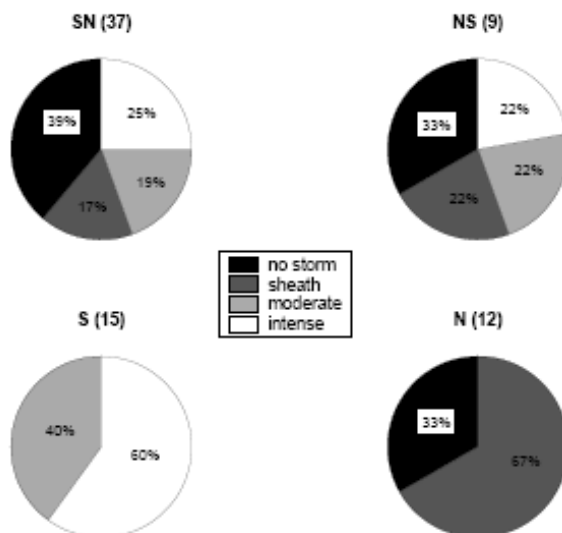


Figure A.1 - The effect of the flux rope type to the geoeffectivity. Numbers in the parentheses show the total numbers of MCs identified in each category. Different colors demonstrate the different geomagnetic response: no storm at all, $Dst > -50/nT$ (black); sheath region generated a storm (dark gray); MC caused a moderate storm (light gray); MC caused an intense storm (white). SOURCE: Huttunen et al. (2005).

Other example is the work of [Huttunen et al. \(2005\)](#), they studied the geomagnetic response of MCs using the $1 - h$ Dst index. They focused on whether the storm was caused by sheath fields or by the MC itself. They found that the geomagnetic response of a MC depends greatly on its flux-rope type. In the [Figure A.1](#) different colors demonstrate the different geomagnetic response: no storm at all, $Dst > -50/nT$ (black); sheath region generated a storm (dark gray); MC caused a moderate storm (light gray); MC caused an intense storm (white). The pie-diagrams in the top part of the figure show the distribution for bipolar MCs. If the MC is geoeffective then the SN type MCs caused more intense storms than moderate storms. For bipolar MCs the respond depends clearly on the direction of the magnetic field on the axis. As seen from [Figure A.1](#) all of 15 identified S-type MCs caused a storm, nine of them an intense storm. But from the 12 identified N-type MCs none caused a storm, but for eight of these MCs the sheath region was geoeffective.

Inside ICMEs, the measured plasma velocity typically has a linear variation along the spacecraft trajectory. A much higher velocity is present in the front than in the back, indicating expansion ([DÉMOULIN; DASSO, 2009](#)). [Burlaga and Behannon \(1982\)](#) found consistency between the expansion speed estimated from in situ observations and the increase of their typical size, obtained from measurements with different spacecraft located between 2 and 4 AUs. As the magnetic field strength is higher than the average inside a MC. This means that the magnetic pressure $B^2/(2\mu_0)$ is higher than the plasma pressure inside the structure. A gradient in pressure would make the MC expand unless an external force prevents the expansion ([BURLAGA, 1991](#)). The simple and universal law found ([DÉMOULIN; DASSO, 2009](#)) for the radial expansion of flux ropes in the SW predicts the typical size, magnetic structure, and radial velocity of MCs at various solar distances.

[Bothmer and Schwenn \(1998\)](#) investigated the expansion of magnetic clouds in the Heliosphere. The authors conducted a study using four spacecraft, Helios 1/2 at 0.3 – 1 AU and Voyager 1/2 2.6 AU. An example observed by Helios 1 at 0.9 AU on days 61, 01 : 00 UT -62, 01 : 00 UT, Voyager 1 at 2.6 AU on days 66, 08 : 00 UT - 68, 11 : 00 UT and Voyager 2 at 2.6 AU on days 66, 02 : 00 UT - 68, 02 UT, march 1978 was presented by [Bothmer and Schwenn \(1998\)](#). The previous case was shown in [Figure A.2](#). The right side of [Figure A.2](#) shows the results of the MVA for the magnetic field data that was shown in the left side. Note the striking similarity of the directional changes of the magnetic field vector at all three spacecraft, which

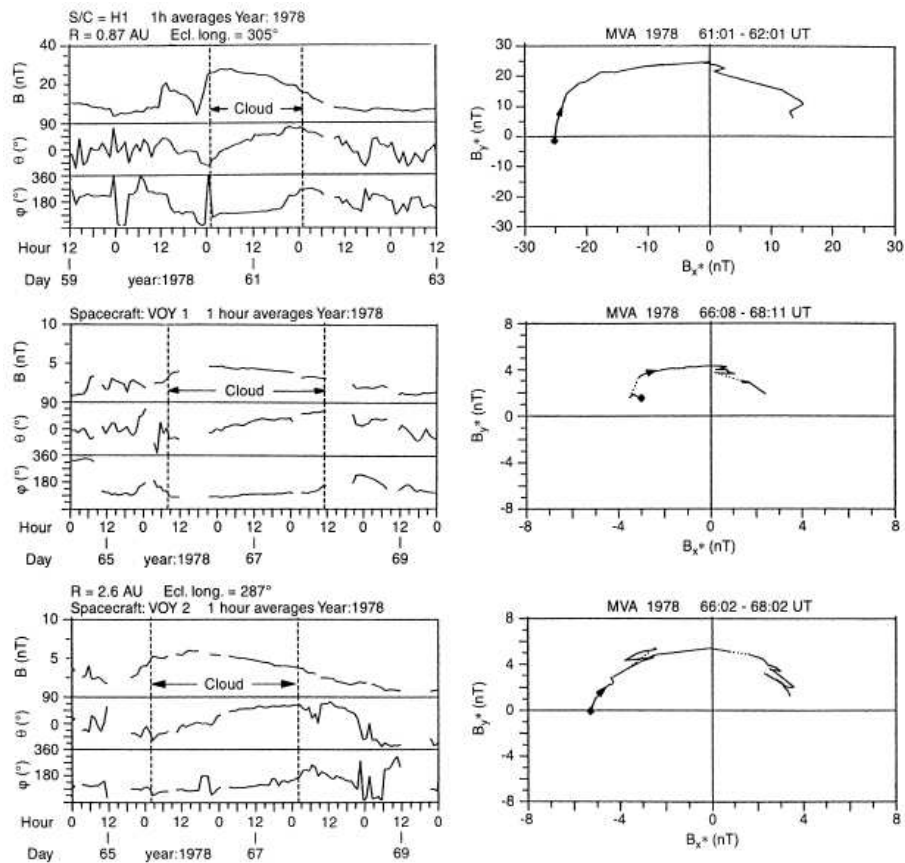


Figure A.2 - Magnetic field data and results of the MVA for a MC (vertical dashed lines) that passed Helios 1 at 0.9 AU on days 61, 01 : 00 UT - 62, 01 : 00 UT, Voyager 1 at 2.6 AU on days 66, 08 : 00 UT - 68, 11 : 00 UT and Voyager 2 at 2.6 AU on days 66, 02 : 00 UT - 68, 02 UT, march 1978. The Helios 1 and Voyager 1/2 were separated by 18° in solar longitude and by 1.6 AU in solar distance. Note the longer time duration of MC at Voyager 1/2. SOURCE: Bothmer and Schwenn (1998).

all detected a SEN-type MC. The propagation velocity of the cloud (~ 446 km/s) was estimated of plasma speed in Helios 1 at 0.9 AU. The cloud showed a much longer time-duration at the position of Voyager 1 ($t = 50$ h) and Voyager 2 ($t = 48$ h) compared to Helios 1 ($t = 24$ h), thus giving direct evidence for the expansion of this MC. The MVA yielded similar results for the orientation of the cloud's axis at all three spacecraft (BOTHMER; SCHWENN, 1998).

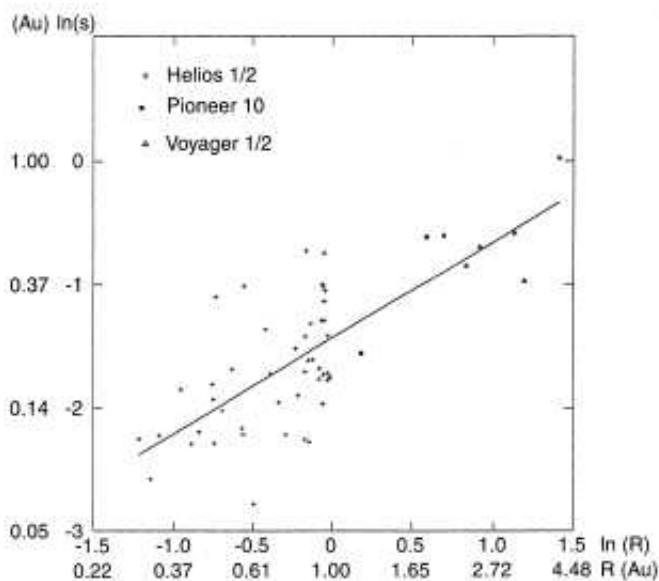


Figure A.3 - Log-log plot showing the radial sizes, s , of MCs observed by Helios 1/2 (with +-symbol), Voyager 1/2 (with Δ -symbol), Pioneer 10 (with *-symbol) between 0.3 and 4.2 AU versus solar distance, R (from (BOTHMER; SCHWENN, 1994)). The *straight line* was obtained by linear regression: $s(R) = (0.24 \pm 0.01) \times R^{(0.78 \pm 0.10)}[AU]$. SOURCE: Bothmer and Schwenn (1998).

Bothmer and Schwenn (1998) also conducted a study about the radial sizes of MCs between 0.3 and 4.2 AU obtained from Helios 1/2, Voyager 1/2, and Pioneer 10 data (see the log-log plot that is shown in Figure A.3). From linear regression it is found that the radial size $s(R)$ in AU, of MCs increases with radial distance, R from the Sun as $s(R) = (0.24 \pm 0.01) \times R^{(0.78 \pm 0.10)}[AU]$. The expansion of MCs has a dependence on the radial distance from the Sun (LUCAS et al., 2011), confirming that radial expansion is a common feature of MCs in the heliosphere. Dal Lago et al. (2002) have used solar and interplanetary observations from January 1997 to April 2001 to correlate the interplanetary speed (v_p) near 1 AU with the expansion speed

(v_e) of halo CMEs (GONZALEZ et al., 2004). Using the previous study, a prediction scheme for peak Dst , based on halo CME-expansion speed observation near the Sun and associated with magnetic clouds, was suggested for the first time by Gonzalez et al. (2004). Dal Lago et al. (2004) compared the lateral expansion speeds of these halo CMEs and the corresponding ejecta speeds near Earth. They found that there is a high correlation between these two speeds. In the works of Dal Lago et al. (2003), Schwenn et al. (2005), Huttunen et al. (2005), Kane (2005) also it is proposed a method to calculate MC-expansion speed (e.g. see figure 8 pag 10 of Huttunen et al. (2005)).

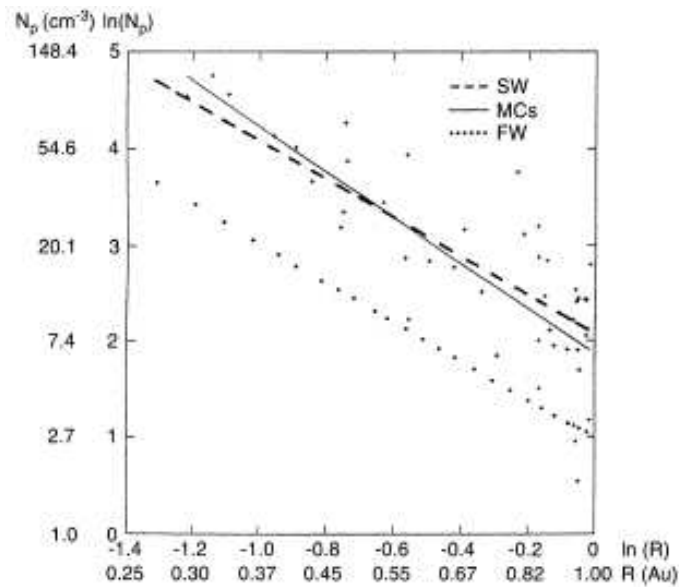


Figure A.4 - Log-log plot showing the average proton density ($\langle N_p \rangle$) inside MCs observed by Helios 1/2 between 0.3 and 1 AU during (1974–1981) versus solar distance, R (from (BOTHMER; SCHWENN, 1994)). The *straight line* was obtained by linear regression: $N_p(R) = (6.47 \pm 0.85) \times R^{(-2.4 \pm 0.3)} \text{cm}^{-3} [\text{R em AU}]$. The other two lines were measured by the Helios probes in slow (S) and fast (F) solar wind-streams in the inner heliosphere. SOURCE: Bothmer and Schwenn (1998).

Self-similar models are useful to study the expansion of flux rope. Some consider only a radial expansion, while others consider an isotropic expansion (DÉMOULIN; DASSO, 2009, and reference therein). The main problem of the first group of models is that, even taking a force-free configuration at some point of the evolution, the only radial expansion implies the creation of strong unbalanced magnetic force during the

evolution. Then, the force-free state is singular in these models, happening only at one single time during the evolution, while observations show that MCs typically have a low β_p plasma. A self-similar isotropic expansion does not change the force balance, so the second group of models are expected to be a better approximation. However, it is not obvious that the expansion could be isotropic since the magnetic force is anisotropic in a flux rope (DÉMOULIN; DASSO, 2009). Démoulin and Dasso (2009) analyzed the expansion of flux ropes in SW with a complementary approach to self-similar expansion models and to the MHD simulations.

The MCs closer to the Sun compared to 1 AU had higher plasma densities than the surrounding solar wind. Thus, the density inside the flux tubes has a rapid decrease with the increasing distance from the Sun where the cloud undergoes a radial expansion. Figure A.4 shows in a log-log plot N_p versus R (BOTHMER; SCHWENN, 1998). From linear regression Bothmer and Schwenn (1998) found that the density of MCs decreases with increasing radial distance, R , as: $N_p = (6.47 \pm 0.85) \times R^{(-2.4 \pm 0.3)} \text{cm}^{-3} [\text{R em AU}]$. Figure A.4 shows that the density in MCs is generally higher than that of the average fast solar wind and that it is also generally higher than that of the slow solar wind at closer distances to the Sun. Bothmer and Schwenn (1998) observed that MCs in which the densities are found to be considerably lower compared to that of the ambient slow solar wind should have undergone strong expansion on their way out from the Sun.

APPENDIX B - TOOL OF PERSISTENCE ANALYSIS AND SOURCE CODE IMPLEMENTED

B.1 Rescaled-Range (R/S) Analysis

We will be presented a theory summary of Rescaled-Range (R/S) Analysis discussed by [Malamud and Turcotte \(1999\)](#). Also, A source code is presented for running in Octave, a free software of high-level interactive language.

An alternative approach to the quantification of correlations in time series was developed by Harold E. Hurst ([HURST, 1951](#); [HURST et al., 1965](#)). He considered a Nile River flow as a time series and determined the storage limits in an idealized reservoir. Based on these studies, he introduced empirically the concept of rescaled-range (R/S) analysis. Where the range $R(T')$ is defined to be the difference between the maximum volume of water V_{max} and the minimum volume of water V_{min} ([HURST, 1951](#)) during the period T' . $S(T')$ is the standard deviation of the flow $Q(t)$ during the period T' .

[Hurst \(1951\)](#) and [Hurst et al. \(1965\)](#) found empirically that many data sets in nature satisfy the power-law relation:

$$\left[\frac{R_\tau}{S_\tau} \right]_{av} = \left(\frac{\tau}{2} \right)^{H_u}, \quad (\text{B.1})$$

where H_u is known as the Hurst exponent and if T' denote the period, it can be broken up into subintervals τ . For $\tau = 2$, $R_\tau/S_\tau = 1$ by definition.

The R/S analysis is easily extended to a discrete time series, Y_n , $n = 1, 2, 3, \dots, N$. The running sum, Y_m of the time series, y_n relative to its mean is:

$$y_m = \sum_n^m (y_n - \bar{y}_N) = \left(\sum_{n=1}^m y_n \right) - m\bar{y}_N. \quad (\text{B.2})$$

The range is defined by:

$$R_N = (y_m)_{max} - (y_m)_{min} \quad (\text{B.3})$$

with

$$S_N = \sigma_N \quad (\text{B.4})$$

where \bar{y}_N and σ_N are the mean and standard deviation of all N values in the time

series, y_n . We are interested in how (R/S) varies with successive subintervals τ of N , we substitute τ for N in Equations B.2 to B.4. The Hurst exponent, H_u , is obtained from B.1

For example, if 64 values of y_n are available for a time series, the R_N and S_N for $N = 64$ are obtained. Then the data are broken into two parts, each with $\tau = 32$ (1, 2, \dots , 32 and 33, 34, \dots , 64. The values for R_{32} and S_{32} are obtained for the two parts. The two values of R_{32}/S_{32} are then averaged to give $(R_{32}/S_{32})_{av}$. This process is continued for $\tau = 16$, $\tau = 8$, and $\tau = 4$ to give $(R_{16}/S_{16})_{av}$, $(R_8/S_8)_{av}$ and $(R_4/S_4)_{av}$. The values of $\log(R_\tau/S_\tau)_{av}$ are plotted against $\log(\tau/2)$ and the best-fit straight line gives H_u from Equation B.1. In practice, there is generally some curvature of $(R/S)_{av}$ for small values of $\tau/2$ and they are therefore omitted (TAPIERO; VALLOIS, 1996).

Implementation

If we installed GNU/Octave in Ubuntu, a computer operating system based on the Debian distribution and distributed as free and open source software, then a *hurst(x)* function is created for example in */usr/share/octave/3.0.1/m/signal/*. This function is an estimate the Hurst parameter of sample X via the rescaled range statistic in Octave. This program is not correspond with the previous theory. The running sum is only realized on higher scale.

```
function H = hurst(x)
if (nargin != 1)
print_usage();
endif
if (isscalar(x)) error ("hurst : xmustnotbeascalar")
elseif (isvector(x))
x = reshape(x, length(x), 1);
endif
[xr, xc] = size(x);
s = std(x);
w = cumsum(x - mean(x));
RS = (max(w) - min(w))./s;
H = log(RS)/log(xr);
endfunction
```


We perform a implementation using the R/S theory, that was presented.

Mean function:

```
function Hu = MeanHurst(Yn)
%LEFT
sLeft = HurstRSPotLeft(Yn);
XLeft = sLeft(:, 1);
YLeft = sLeft(:, 2);
[HuLeft, R1Left] = RegressionLinear(log10(XLeft), log10(YLeft));
plot(log10(XLeft), log10(YLeft))
%RIGHT
sRight = HurstRSPotRight(Yn);
XRight = sRight(:, 1);
YRight = sRight(:, 2);
[HuRight, R1Right] = RegressionLinear(log10(XRight), log10(YRight));
Hu = (HuLeft + HuRight)/2;
endfunction
```

```
function RSPoint = HurstRSPotLeft(Yn)
n = length(Yn);
np = floor(log2(n));
Yn1 = Yn(1 : 2^np);
pointGraf = ones(np - 1, 2);
for i = 2 : np
Yn2 = reshape(Yn1, 2^i, length(Yn1)/2^i);
RSave = 0;
cont = 0;
for k1 = 1 : length(Yn2(1, :))
if std(Yn2(:, k1)) > 0
cont = cont + 1;
[RS] = hurst1(Yn2(:, k1));
RSave = RSave + RS;
endif
endfor
RSave = RSave/cont;
pointGraf(i - 1, :) = [2^i/2RSave];
```

```

endfor
RSPoint = pointGraf;
endfunction

function RSPoint = HurstRSPotRight(Yn)
n = length(Yn);
np = floor(log2(n));
Yn1 = Yn(n - 2^np + 1 : n);
pointGraf = ones(np, 2);
for i = 2 : np
Yn2 = reshape(Yn1, 2^i, length(Yn1)/2^i);
RSave = 0;
cont = 0;
for k1 = 1 : length(Yn2(1, :))
if std(Yn2(:, k1)) > 0
cont = cont + 1;
[RS] = hurst1(Yn2(:, k1));
RSave = RSave + RS;
endif
endifor
RSave = RSave/cont;
pointGraf(i - 1, :) = [2^i/2RSave];
endifor
RSPoint = pointGraf;
endfunction

```

```

function RS = hurst1(x)
if (nargin != 1)
print_usage();
endif
if (isscalar(x))
error("hurst : xmustnotbeascalar");
elseif (isvector(x))
x = reshape(x, length(x), 1);
endif
[xr, xc] = size(x);

```

```

s = std(x);
w = cumsum(x - mean(x));
RS = (max(w) - min(w))./s;
endfunction

function [a, R] = RegresionLinear(xi, yi)
n1 = size(xi, 2);
a = (n1 * sum(xi .* yi) - sum(xi) * sum(yi))/(n1 * sum(xi.^2) - sum(xi)^2);
b = (sum(yi) - a * sum(xi))/n1;
R = ((sum(xi.*yi) - (sum(xi)*sum(yi))/n1)^2)/((sum(xi.^2) - (sum(xi)^2)/n1)*
(sum(yi.^2) - (sum(yi)^2)/n1));
end

```

B.2 Autocorrelations and Semivariograms

A summary taken from [Malamud and Turcotte \(1999\)](#) is presented here. In many cases the persistence (or antipersistence) of a time series can be quantified by using the correlation function. The autocorrelation function, $r(s)$, at lag s , measures the correlation of a time series with itself, $y(t+s)$ compare with $y(t)$, at increasing values of s . This is given by:

$$r(s) = \frac{c(s)}{c(0)}, \quad (\text{B.5})$$

with the autocovariance function, $c(s)$, given by

$$c(s) = \frac{1}{(T' - s)} \int_0^{T'-s} [y(t+s) - \bar{y}] [y(t) - \bar{y}] dt$$

and the autocovariance function at 0 lag, $c(0)$, given by

$$c(0) = \frac{1}{T'} \int_0^{T'} [y(t) - \bar{y}]^2 dt = Va$$

The time series, $y(t)$, is prescribed over the interval $0 \leq t \leq T'$. The average and variance of $y(t)$ over the interval T' are \bar{y} and Va . The autocorrelation function, $r(s)$, is dimensionless and does not depend on the units of $y(t)$ or t . With $s = 0$ we have $c(s) = c(0) = Va$, the variance of time series over the period T' , resulting in $r(s) = 1$. With increasing lag, s , the values of $r(s)$ become smaller as the statistical correlations of $y(t+s)$ with $y(t)$ decrease. The plot of $r(s)$ versus s is known as **correlogram**.

Although the autocorrelation, Equation B.5, at a particular lag, s , can give insight into the data, one is generally more interested in the overall structure of the autocorrelation function taken over a range of lags. Large values of $r(s)$ indicate a strong correlation between those points in the time series that are separated by lag s , small values of $r(s)$ indicate weak correlation, and values of $r(s) = 0$ indicate no correlation (white noise). Persistence here can be defined as a sequence of $r(s)$ that have positive values. If the values of $r(s)$ are large, but then quickly drop to $r(s) = 0$, we have an example of strong persistence over a short range of values. If the values of $r(s)$ are small (nonzero) and continue to stay small for very large lags, then the persistence is weak and long-range.

For a discrete time series, the autocorrelation function, r_k , is given by:

$$r_k = \frac{c_k}{c_0} \quad (\text{B.6})$$

with the autocovariance, c_k , given by:

$$c_k = \frac{1}{(N-k)} \sum_{n=1}^{N-k} (y_{n+k} - \bar{y})(y_n - \bar{y}) \quad (\text{B.7})$$

and the autocovariance at 0 lag (the variance) given by:

$$c_0 = \frac{1}{N} \sum_{n=1}^N (y_n - \bar{y})^2 = Va. \quad (\text{B.8})$$

If the mean or variance vary with the length of the interval considered, then the time series is nonstationary. It is **inappropriate to use correlograms for nonstationary time series**, because the autocorrelation function, $r(s)$, has the mean, \bar{y} , in its definition. An alternative way to measure long-range correlation, which is valid for both stationary and nonstationary time series, is the **semivariogram** γ . Like the autocorrelation function, the semivariogram measures the dependence of values in a time series that are separated by a lag, s .

For a discrete time series, the semivariogram, $\gamma(s)$, is given by:

$$\gamma_k = \frac{1}{2}(N-k) \sum_{n=1}^{N-k} (y_{n+k} - y_n)^2 \quad (\text{B.9})$$

Increasing values of s or k correspond to increasing lag. The plot of γ_k vs k is known as a semivariogram. For a stationary time series, the semivariogram, γ_k , and the autocorrelation function, r_k , are related. The mean of the time series, \bar{y} , can be added and subtracted within the summation in Equation B.9 to give:

$$\gamma_k = \frac{1}{2(N-k)} \sum_{n=1}^{N-k} [(y_{n+k} - \bar{y}) - (y_n - \bar{y})]^2.$$

When expanded this gives:

$$\gamma_k = \frac{1}{2(N-k)} \left[\sum_{n=1}^{N-k} (y_{n+k} - \bar{y})^2 + \sum_{n=1}^{N-k} (y_n - \bar{y})^2 - \sum_{n=1}^{N-k} 2(y_{n+k} - \bar{y})(y_n - \bar{y}) \right]. \quad (\text{B.10})$$

Provided the time series is stationary, two of the terms in Equation B.10 are equivalent to the variance in Equation B.8, giving:

$$\gamma_k = Va - \frac{1}{(N-k)} \sum_{n=1}^{N-k} (y_{n+k} - \bar{y})(y_n - \bar{y}). \quad (\text{B.11})$$

Substituting the definition for c_k from B.7 into B.11 and using the definitions of c_0 from Equation B.8 and r_k from B.6, we find:

$$\gamma_k = (Va - c_k) = \left(V - V \frac{c_k}{c_0} \right) = V(1 - r_k) \quad (\text{B.12})$$

For an uncorrelated time series we have $r_k = 0$ and $\gamma_k = Va$. Both the autocorrelation function and semivariograms have been applied by a number of authors to synthetic time series that exhibit long-range persistence.

Implementation

Using the definition for the semivariogram, γ_k , given in Equation B.9,

function [Ha, R1] = Semivariogram(y)

N1 = size(y, 1);

potencia2 = floor(log2(N1));

gammaT_k = 1 : potencia2;

```

xi = 1 : potencia2;
for i = 1 : potencia2
k = 2^i;
contador = 0;
for n = 1 : (N1 - k)
contador = contador + (y(n + k) - y(n))^2;
end
gam_k = (1/(N1 - k)) * contador;
gammaT_k(i) = gam_k;
xi(i) = k;
end
yi = gammaT_k;
[a, R] = RegresionLinear(log10(xi), log10(yi));
Ha = a/2; %Because  $\gamma_k^2 H_a$  where  $H_a$  is the Hausdoff exponent
R1 = R;
end

```

```

function [a, R] = RegresionLinear(xi, yi)
n1 = size(xi, 2);
a = (n1 * sum(xi .* yi) - sum(xi) * sum(yi)) / (n1 * sum(xi.^2) - sum(xi)^2);
b = (sum(yi) - a * sum(xi)) / n1;
R = ((sum(xi .* yi) - (sum(xi) * sum(yi)) / n1)^2) / ((sum(xi.^2) - (sum(xi)^2) / n1) *
(sum(yi.^2) - (sum(yi)^2) / n1));
end

```

B.3 Power spectrum, implementation

beta = powspecscale(x, pflag) calculates the power spectral density, $S(f)$, scaling coefficient, β , satisfying $S(f) \propto f^{-\beta}$. A Welch window is used to reduce spectral leakage. The bin size is given by the distance between the first two points. A log-log plot of $S(f)$ against f is provided when $pflag=1$. Default: $pflag=0$. Copyright (c) 2005 Patrick E. McSharry (patrick@mcsarry.net)

```

function beta = powspecscale(x, pflag) if nargin < 2
pflag = 0;
end

```

```
N = length(x);
```

```
Ensure data has a mean of zero
```

```
x = x - mean(x);
```

```
Welch window
```

```
w = 1 - (([1 : N]' - N/2)/(N/2)).2;
```

```
Wss = mean(w.2);
```

```
calculate the spectrum
```

```
k = round(N/2);
```

```
s0 = (1/Wss) * (2/N) * abs(fft(w.*x)).2;
```

```
s = s0(1 : k);
```

```
f = [1 : k]'/N;
```

```
lf = log10(f);
```

```
S = log10(s);
```

```
estimate bin size as distance between first two points on log  
frequency scale
```

```
lf1 = log10(f(1));
```

```
lf2 = log10(f(2));
```

```
lfk = log10(f(k));
```

```
dlfb = lf2 - lf1;
```

```
bin the data
```

```
lfrange = lfk - lf1;
```

```
Nlfb = ceil(lfrange/dlfb);
```

```
lfb = lf1 - 0.5 * dlfb + [1 : Nlfb] * dlfb;
```

```
ind = find((lfb(1) - 0.5 * dlfb <= lf) & (lf <= lfb(1) + 0.5 * dlfb));
```

```
nind(1) = length(ind);
```

```
Slfb(1) = mean(S(ind));
```

```

fori = 2 : Nlfb - 1
ind = find((lfb(i) - 0.5 * dlfb < lf) & (lf <= lfb(i) + 0.5 * dlfb));
nind(i) = length(ind);
Slfb(i) = mean(S(ind));
end
ind = find((lfb(Nlfb) - 0.5 * dlfb < lf));
nind(Nlfb) = length(ind);
Slfb(Nlfb) = mean(S(ind));

```

fit a line to the log-log plot

```

A = ones(Nlfb, 2);
A(:, 2) = lfb';
a = pinv(A) * Slfb';
Slfbpred = A * a;
ifpflag == 1
figure;
loglog(f, s, 'b.-');
holdon;
loglog(10.^lfb, 10.^Slfb, 'k.', 'MarkerSize', 14);
loglog(10.^lfb(1):lfb(Nlfb), 10.^Slfbpred(1):Slfbpred(Nlfb), 'k');
xlabel('f');
ylabel('S(f)');
title(['S(f) f-β with β = ' num2str(-a(2))]);
end
beta = -a(2);

```


APPENDIX C - GRAD SHAFRANOV EQUATION USING KINETIC THEORY. ANALYTICAL SOLUTION

The number density, $n_j(\vec{r}, t)$, is a macroscopic variable defined in configuration space as the number of particles of type j , per unit volume, irrespective of velocity.

$$n_j(\vec{r}, t) = \frac{1}{d^3r} \int_v d^6 N_j(\vec{r}, \vec{v}, t). \quad (\text{C.1})$$

Let $d^6 N_j(\vec{r}, \vec{v}, t)$ denote the number of particles of type j that, at the instant t , are situated within the volume element $d^3r d^3v$ of phase space, about the coordinates (\vec{r}, \vec{v}) . The *distribution function* in phase space, $f_j(\vec{r}, \vec{v}, t)$, is defined as the *density* of representative points of j -type particles of phase space, that is:

$$f_j(\vec{r}, \vec{v}, t) = \frac{d^6 N_j(\vec{r}, \vec{v}, t)}{d^3r d^3v} \quad (\text{C.2})$$

It is assumed that the density of representative points in phase space does not vary rapidly from one element of volume to the neighboring element, so that $f_j(\vec{r}, \vec{v}, t)$ can be considered as a continuous function of its arguments. According to its definition $f_j(\vec{r}, \vec{v}, t)$ is also a positive and finite function at any instant of time. In a volume element $d^3r d^3v$, whose velocity coordinates (v_x, v_y, v_z) are very large, the number of representative points is relatively small since, in any macroscopic system, there must be relatively few particles with very large velocities. Physical considerations require therefore that $f_j(\vec{r}, \vec{v}, t)$ must tend to zero as the velocity becomes infinitely large.

The distribution function is, in general, a function of the position vector \vec{r} . When this is the case the corresponding plasma is said to be *inhomogeneous*. In the absence of external forces, however, a plasma initially inhomogeneous reaches, in the course of time, an equilibrium state as a result of the mutual particle interactions. In this *homogeneous* state the distribution function does not depend on \vec{r} .

In velocity space the distribution function can be *anisotropic*, when it depends on the orientation of the velocity vector \vec{v} , or *isotropic*, when it does not depend on the orientation of \vec{v} but only on its magnitude, i.e., on the particle speed $v = |\vec{v}|$. A plasma in thermal equilibrium, for example, is characterized by a homogeneous, isotropic, and time-independent distribution function. In a statistical sense the dis-

tribution function provides a complete description of the system under consideration. Knowing $f_j(\vec{r}, \vec{v}, t)$ we can deduce all the macroscopic variables of physical interest for the type j species.

The dependence of the distribution function on the independent variables \vec{r}, \vec{v} and t is governed by an equation known as the *Boltzmann equation*. Let the Equation C.2:

$$d^6 N_j(\vec{r}, \vec{v}, t) = f_j(\vec{r}, \vec{v}, t) d^3 r d^3 v \quad (\text{C.3})$$

Suppose that each particle is subjected to an *external* force \vec{F} . In the absence of particles interactions, a particle of type j with coordinates about (\vec{r}, \vec{v}) in phase space, at the instant t , will be found after a time interval dt about the new coordinates (\vec{r}', \vec{v}') such that

$$\vec{r}'(t + dt) = \vec{r}(t) + \vec{v} dt \quad (\text{C.4})$$

$$\vec{v}'(t + dt) = \vec{v}(t) + \vec{a} dt \quad (\text{C.5})$$

where $\vec{a} = \vec{F}/m_j$ is the particle acceleration and m_j its mass. Thus, all particles of type j inside the volume element $d^3 r d^3 v$ of phase space, about (\vec{r}, \vec{v}) at the instant t , will occupy a new volume element $d^3 r' d^3 v'$, about (\vec{r}', \vec{v}') after the interval dt . Since we are considering the same particles at t and $t + dt$, we must have, in the absence of collisions,

$$f_j(\vec{r}', \vec{v}', t + dt) d^3 r' d^3 v' = f_j(\vec{r}, \vec{v}, t) d^3 r d^3 v. \quad (\text{C.6})$$

The element of volume $d^3 r d^3 v$ may become distorted in shape as a result of the particles motion. The relation between the new element of volume and the initial one is given by

$$d^3 r' d^3 v' = |\mathcal{J}| d^3 r d^3 v$$

where \mathcal{J} stands for the Jacobian of the transformation from the initial coordinates (\vec{r}, \vec{v}) to the final ones (\vec{r}', \vec{v}') . For the transformation defined by the equations C.4 and C.5 we have $|\mathcal{J}| = 1$ (see pages 132-133 on Bittencourt (2004)), so that

$$d^3 r' d^3 v' = d^3 r d^3 v \quad (\text{C.7})$$

and C.6 becomes:

$$[f_j(\vec{r}', \vec{v}', t + dt) - f_j(\vec{r}, \vec{v}, t)] d^3 r d^3 v = 0. \quad (\text{C.8})$$

The first term on the left-hand side of C.8 can be expanded in a Taylor series about $f_j(\vec{r}, \vec{v}, t)$ as follows:

$$f_j(\vec{r} + \vec{v}dt, \vec{v} + \vec{a}dt, t + dt) = f_j(\vec{r}, \vec{v}, t) + \left[\frac{\partial f_j}{\partial t} + \left(v_x \frac{\partial f_j}{\partial x} + v_y \frac{\partial f_j}{\partial y} + v_z \frac{\partial f_j}{\partial z} \right) + \left(a_x \frac{\partial f_j}{\partial v_x} + a_y \frac{\partial f_j}{\partial v_y} + a_z \frac{\partial f_j}{\partial v_z} \right) \right] dt, \quad (\text{C.9})$$

neglecting terms of order $(dt)^2$ and higher. Using the operator notation nabla in the space of spatial (∇) coordinates and velocities coordinates (∇_v) respectively:

$$\nabla = \hat{x} \frac{\partial}{\partial x} + \hat{y} \frac{\partial}{\partial y} + \hat{z} \frac{\partial}{\partial z} \quad (\text{C.10})$$

$$\nabla_v = \hat{x} \frac{\partial}{\partial v_x} + \hat{y} \frac{\partial}{\partial v_y} + \hat{z} \frac{\partial}{\partial v_z}. \quad (\text{C.11})$$

We obtain from Equation C.9

$$f_j(\vec{r} + \vec{v}dt, \vec{v} + \vec{a}dt, t + dt) - f_j(\vec{r}, \vec{v}, t) = \left[\frac{\partial f_j(\vec{r}, \vec{v}, t)}{\partial t} + \vec{v} \cdot \nabla f_j(\vec{r}, \vec{v}, t) + \vec{a} \cdot \nabla_v f_j(\vec{r}, \vec{v}, t) \right] dt. \quad (\text{C.12})$$

Substituting this result into C.8 gives the *the Boltzmann equation in absence of collisions*:

$$\frac{\partial f_j(\vec{r}, \vec{v}, t)}{\partial t} + \vec{v} \cdot \nabla f_j(\vec{r}, \vec{v}, t) + \vec{a} \cdot \nabla_v f_j(\vec{r}, \vec{v}, t) = 0. \quad (\text{C.13})$$

This equation can be rewritten as:

$$\frac{\mathcal{D}f_j(\vec{r}, \vec{v}, t)}{\mathcal{D}t} = 0, \quad (\text{C.14})$$

where the operator \mathcal{D} is:

$$\frac{\mathcal{D}}{\mathcal{D}t} = \frac{\partial}{\partial t} + \vec{v} \cdot \nabla + \vec{a} \cdot \nabla_v \quad (\text{C.15})$$

represents the *total derivative* with respect to time, in phase space. Equation C.14 is a statement of the conservation of the density of representative points (f_j) in phase space. If we move along with a representative point *alpha* in phase space and observe the density of representative points $f_j(\vec{r}, \vec{v}, t)$ in its neighborhood, we find that this density remains constant in time. This result is known as *Liouville's theorem*. Note that this result applies only to the special case which collisions, as well

as radiation losses, processes of production, and loss of particles, are unimportant (BITTENCOURT, 2004).

C.1 The Vlasov equation

A very useful approximate way to describe the dynamics of a plasma is to consider that the plasma particle motions are governed by the applied *external* fields *plus* the macroscopic *average internal* fields, smoothed in space and time, due to the presence and motion of all plasma particles. The problem of obtaining the macroscopic (smoothed) internal electromagnetic fields, however, is still a complex one and requires that a *self-consistent* solution be obtained (BITTENCOURT, 2004).

The Vlasov equation is a partial differential equation that describes the time evolution of the distribution function in phase space and that directly incorporates the smoothed macroscopic internal electromagnetic fields (BITTENCOURT, 2004). It may be obtained from the Boltzmann equation C.13 with the collision term $(\delta_j/\delta t)_{coll}$ equal to zero, but including the *internal smoothed fields* in the force term,

$$\frac{\partial f_j}{\partial t} + \vec{v} \cdot \nabla f_j + \frac{1}{m_j} [\vec{F}_{ext} + q_j(\vec{E}_i + \vec{v} \times \vec{B}_i)] \cdot \nabla_v f_j = 0. \quad (\text{C.16})$$

Here \vec{F}_{ext} represents the external force, including the Lorentz force associated with any *externally* applied electric and magnetic fields, and \vec{E}_i and \vec{B}_i are *internal* smoothed electric and magnetic fields due to the presence and motion of all charged particles inside the plasma. In order that the internal macroscopic electromagnetic fields \vec{E}_i and \vec{B}_i be consistent with the macroscopic charge and current densities existing in the plasma itself, they must satisfy Maxwell equations

$$\nabla \cdot \vec{E}_i = \frac{\rho}{\epsilon_0} \quad (\text{C.17})$$

$$\nabla \cdot \vec{B}_i = 0 \quad (\text{C.18})$$

$$\nabla \times \vec{E}_i = -\frac{\partial \vec{B}_i}{\partial t} \quad (\text{C.19})$$

$$\nabla \times \vec{B}_i = \mu_0 \left(\vec{J} + \epsilon_0 \frac{\partial \vec{E}_i}{\partial t} \right) \quad (\text{C.20})$$

with the plasma charge density ρ and the plasma current density \vec{J} given by the

expressions:

$$\rho(\vec{r}, t) = \sum_j q_j n_j(\vec{r}, t) = \sum_j q_j \int_{\mathbf{v}} f_j(\vec{r}, \vec{v}, t) d^3v \quad (\text{C.21})$$

$$\vec{J}(\vec{r}, t) = \sum_j q_j n_j(\vec{r}, t) \vec{u}_j(\vec{r}, t) = \sum_j q_j \int_{\mathbf{v}} \vec{v} f_j(\vec{r}, \vec{v}, t) d^3v \quad (\text{C.22})$$

the summations being over the different charged particle species in the plasma. Here $\vec{u}_j(\vec{r}, t)$ denotes the macroscopic *average velocity* for the particles of type j . Equations C.16 to C.22 constitute a complete set of *self-consistent* equations to be solved simultaneously.

Formal Solution to Equilibrium Vlasov Equation

We may also arrive at the Grad-Shafranov equation 2.40 using kinetic theory, and following the work of Yoon and Lui (2005) an exact solution can be obtained. We will rewrite in this subsection a part of the work of Yoon and Lui (2005), changing the magnetic field orientation, that is $\vec{B} = B_x(x, y)\hat{x} + B_y(x, y)\hat{y}$. The class of kinetic current sheet equilibrium to be discussed in the present subsection is a solution of the equilibrium Vlasov kinetic equation derived from C.16, C.20 and C.22:

$$[\vec{v} \cdot \nabla + (q_j/m_j c)(\vec{v} \times \vec{B}) \cdot (\partial/\partial \vec{v})] f_j(x, y, \vec{v}) = 0 \quad (\text{C.23})$$

$$\nabla \times \vec{B} = 4\pi \vec{J}/c, \quad \vec{J} = \sum_j q_j \int \vec{v} f_j(x, y, \vec{v}) d\vec{v} \quad (\text{C.24})$$

We are further interested in a class of distributions which satisfy the current neutrality condition along x ($\sum_j q_j \int v_x f_j(x, y, \vec{v}) d\vec{v} = 0$) and y ($\sum_j q_j \int v_y f_j(x, y, \vec{v}) d\vec{v} = 0$) axes and are charge neutral ($\sum_j q_j \int f_j(x, y, \vec{v}) d\vec{v} = 0$). If we introduce the vector potential, then one can see that only the z component remains nonzero, $\vec{B} = \nabla \times \vec{A}$, where $\vec{A} = A(x, y)\hat{z}$. Then the solution to equilibrium Vlasov equation is any function of the characteristics:

$$P_j = m_j v_z + q_j A(x, y)/c = \text{const}, \quad (\text{C.25})$$

$$H_j = m_j \vec{v}^2/2 = \text{const}, \quad (\text{C.26})$$

are available. These are the canonical momentum and the total Hamiltonian. From this, we may construct the solution f_j as any arbitrary function of P_j and H_j . Of

infinitely many possible choices, we select the Gaussian functional form, from [Harris \(1962\)](#),

$$f_j(P_j, H_j) = N_j \exp [-(H_j - V_j P_j + m_j V_j^2/2)/T_j], \quad (\text{C.27})$$

where N_j , V_j , and T_j are multiplicative constants, which are related to the number density n_j , and isotropic kinetic temperature T_j , for species labeled j ($j = i$ for the ions and e for the electrons), through the definitions:

$$n_j = n_{0j} \exp (q_j V_j A / c T_j), \quad (\text{C.28})$$

$$v_{T_j}^2 = 2T_j / m_j \quad (\text{C.29})$$

$$n_{0j} = \pi^{3/2} v_{T_j}^3 N_j. \quad (\text{C.30})$$

Physically, v_{T_j} is the thermal speed, m_j and q_j are the mass and charge, respectively, and V_j corresponds to the cross-field (diamagnetic) drift speed. Note that the solution [C.27](#) will satisfy the (x and y component) current and charge neutrality only if $n_{0e} = n_{0i} = n_0$ and $V_i/T_i = -V_e/T_e$ (also see [Kan \(1979\)](#)). We assume such a condition henceforth.

Inserting the distribution function f_j to the field equation in [C.24](#) with [2.34](#) ($\vec{A} = A(x, y)\hat{z}$), we obtain

$$c\left(\frac{\partial^2 A}{\partial x^2} + \frac{\partial^2 A}{\partial y^2}\right) = -4\pi \sum_j q_j n_{0j} V_j \exp (q_j V_j A / c T_j), \quad (\text{C.31})$$

Let us introduce two constants, $B_0^2 = 8\pi n_0(T_e + T_i)$ and $L = 2cT_i/(qB_0V_i)$, where B_0 will turn out to be the asymptotic ($y^2 \rightarrow \infty$) magnetic field strength and L is the characteristic scale length associated with the current sheet. We further introduce dimensionless quantities,

$$X = x/L, \quad Y = y/L, \quad \Psi = -A/(LB_0), \quad (\text{C.32})$$

where Ψ is the *normalized vector potential*. Then the Equation [C.31](#) or equilibrium Ampere's law (Grad-Shafranov equation) becomes,

$$\frac{\partial^2 \Psi}{\partial X^2} + \frac{\partial^2 \Psi}{\partial Y^2} = e^{-2\Psi}. \quad (\text{C.33})$$

Note that the density is given in term of Ψ by $n = n_i = n_e = n_0 e^{-2\Psi}$. Thus the problem of obtaining exact two-dimensional current sheet equilibrium solutions boils

down to solving the above Grad-Shafranov equation for $\Psi(X, Y)$.

The general solution in terms of complex variable, $\Upsilon = X + \iota Y$, was obtained by Walker (1915). He first notes that any complex function of the form $w(\Upsilon) = g(\Upsilon) + h(\Upsilon^*)$, where the asterisk denotes the complex conjugate, satisfies the homogeneous equation, $\partial^2 w / \partial X^2 + \partial^2 w / \partial Y^2 = 0$. He then proceeds to write down an inhomogeneous solution,

$$\Psi(X, Y) = \frac{1}{2} \ln \left[-\frac{w^2}{(\partial w / \partial X)^2 + (\partial w / \partial Y)^2} \right],$$

the validity of which can be checked by the inserting the previous solution to C.33. For a specific choice of $h(\Upsilon^*)$. Walker (1915) selects $h(\Upsilon^*) = 1/g^*(\Upsilon)$. Then by writing $g(\Upsilon) = u(X, Y) + \iota \nu(X, Y)$, where u and ν are real functions, one can show that:

$$w^2 = \frac{1 + u^2 + \nu^2}{(u - \iota \nu)^2},$$

$$\left(\frac{\partial w}{\partial X} \right)^2 = \left(\frac{\partial w}{\partial Y} \right)^2 = \frac{-4(u_X^2 + \nu_Y^2)}{(u - \iota \nu)^2}.$$

Here, $u_X = \partial u / \partial X$ and $\nu_X = \partial \nu / \partial X$. Since $\partial \nu / \partial X = -\partial u / \partial Y$ and $\partial u / \partial X = -\partial \nu / \partial Y$, Walker (1915) thus obtains the formal solution to C.33 as follows:

$$e^{-2\Psi} = \frac{4|g'|^2}{(1 + |g|^2)^2}, \quad (\text{C.34})$$

where $g' = dg(\Upsilon)/d\Upsilon$. This result, which forms the basis for the reconstruction of specific current sheet model, is also widely used in the theory of relativistic beam equilibrium (BENFORD; BOOK, 1971). All that remains is the choice of specific functional form for generating function $g(\Upsilon)$. There are infinite varieties of $g(\Upsilon)$ in a purely mathematical sense, but not all choice will turn out to be useful from a physical perspective.

Harris Solution

Harris model (HARRIS, 1962) can be obtained if we choose the generating function as

$$g(\Upsilon) = \exp(\iota \Upsilon). \quad (\text{C.35})$$

Then, the specific solution becomes (with $\cosh x = (e^x + e^{-x})/2 = (e^{2x} + 1)/(2e^x)$)

$$n/n_0 = e^{-2\Psi} = \operatorname{sech}^2 Y, \quad \Psi = -A(X, Y)/LB_0 = \ln(\cosh Y). \quad (\text{C.36})$$

This is a one-dimensional model ($X = 0$), since $B_y = 0$ and $B_x = B_0 \tanh Y$. The profile of the cross-field current across Y is dictated by the density profile, $J_z/[qn_0 V_i(1 + T_e/T_i)] = \operatorname{sech}^2 Y$, but the current density is uniform across X .

Fadeev solution

Fadeev model (FADEEV et al., 1965) represents a filamentary current sheet, or equivalently, an infinite chain of magnetic X -line. The generating function which results in the Fadeev solution is

$$g(\Upsilon) = w + \sqrt{1 + w^2} \exp(\iota \Upsilon). \quad (\text{C.37})$$

When $w = 0$ one recovers the Harris model. With C.37, the solution are

$$e^{-2\Psi} = \frac{n}{n_0} = \frac{J_z}{qn_0 V_i(1 + T_e/T_i)} = \frac{1}{w \cos X + \sqrt{1 + w^2} \cosh Y}$$

$$\Psi = -\frac{A(X, Y)}{LB_0} = \ln\left(w \cos X + \sqrt{1 + w^2} \cosh Y\right) \quad (\text{C.38})$$

Two values of $w = 0.5$ and $w = 5.0$ can be used to plot the normalized vector potential, Ψ , for Fadeev model. The filamentary current density structure along X axis are formed, and the nested closed magnetic field lines (O lines or magnetic islands). Between every pair of magnetic islands is the magnetic null, or X point.

C.2 BENCHMARK CASE. RESULTS FOR GRAD-SHAFRANOV EQUATION

Also a special form of the (suitably normalized, $\Psi = -A/(LB_0)$) GS equation, namely,

$$\nabla A(\tilde{x}, \tilde{y}) = e^{-2A(\tilde{x}, \tilde{y})}, \quad (\text{C.39})$$

can be used (YOON; LUI, 2005). If we choose \tilde{x} and \tilde{y} along the current sheet and to be perpendicular to the current sheet respectively, then analytical solution is (see Equation C.38¹):

$$A(\tilde{x}, \tilde{y}) = \ln\{\tilde{\alpha} \cos \tilde{x} + \sqrt{1 + \tilde{\alpha}^2} \cosh \tilde{y}\}, \quad (\text{C.40})$$

¹where $w = \tilde{\alpha}$, $X = \tilde{x}$, $Y = \tilde{y}$ and $\Psi = A(\tilde{x}, \tilde{y})$

The parameter $\tilde{\alpha}$ describe a string of nonlinear magnetic islands separated by X -type neutral point (YOON; LUI, 2005). The solution shown in C.40 was derived of the Harris model (HARRIS, 1962) by Fadeev et al. (1965) (Fadeev solution). A map of the exact solution $A(\tilde{x}, \tilde{y})$ with $\tilde{\alpha} = 0.225$ is:

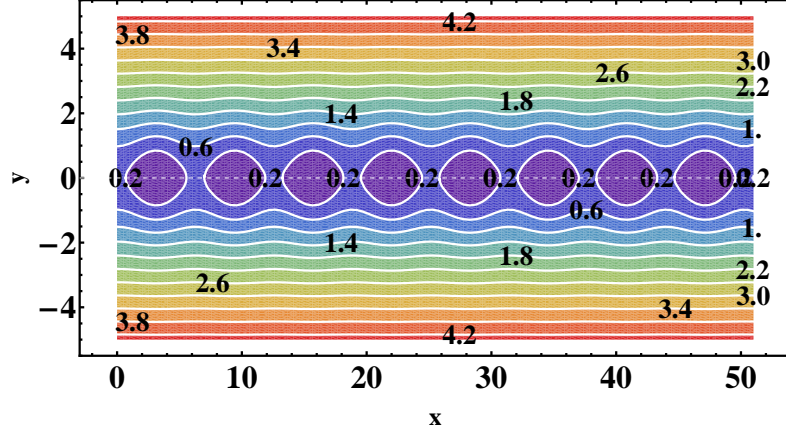


Figure C.1 - Map of exact analytical solution (or benchmark solution). Field lines are separated by equal flux.

In Figure C.1 was plotted Equation C.40 in a grid of $\tilde{x}_{min} = 0$ and $\tilde{x}_{max} = 51$ with a total of 101 equidistant samples, separated by $\Delta\tilde{x} = 51/101$, in the other axis $\Delta\tilde{y} = 0.1\Delta\tilde{x}$ with $\tilde{y}_{min} = -5$ and $\tilde{y}_{max} = 5$. The analytical solutions to $B_{\tilde{x}}, B_{\tilde{y}}, B_{\tilde{z}}$ are:

$$B_{\tilde{x}} = \frac{\partial A}{\partial \tilde{y}} = \frac{\sqrt{1 + \tilde{\alpha}^2} \sinh \tilde{y}}{\tilde{\alpha} \cos \tilde{x} + \sqrt{1 + \tilde{\alpha}^2} \cosh \tilde{y}}; \quad (\text{C.41})$$

$$B_{\tilde{y}} = -\frac{\partial A}{\partial \tilde{x}} = \frac{\tilde{\alpha} \sin \tilde{x}}{\tilde{\alpha} \cos \tilde{x} + \sqrt{1 + \tilde{\alpha}^2} \cosh \tilde{y}}; \quad (\text{C.42})$$

$$B_{\tilde{z}} = \sqrt{\frac{e^{-2A}}{3}} = \frac{1}{\sqrt{3}(\tilde{\alpha} \cos \tilde{x} + \sqrt{1 + \tilde{\alpha}^2} \cosh \tilde{y})}; \quad (\text{C.43})$$

In Figure C.2, a total of 51 equidistant measurements of each $B_{\tilde{x}}, B_{\tilde{y}}, B_{\tilde{z}}, A(\tilde{x}, \tilde{y})$ versus \tilde{x} at $\tilde{y} = 0$ are plotted. The dataset were interpolated by use of a cubic spline to obtain a total of 101 equidistant samples, separated by $\Delta\tilde{x}$, idem to Hau and Sonnerup (1999).

We check out the code to solve the GS equation using the Benchmark case given by

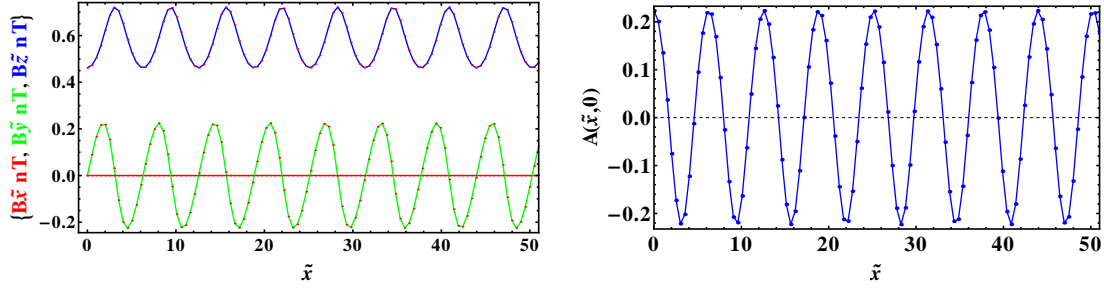


Figure C.2 - Plot of $(B_{\tilde{x}}, B_{\tilde{y}}, B_{\tilde{z}}$ and $A(\tilde{x}, \tilde{y}))$ versus \tilde{x} at $\tilde{y} = 0$.

Hau and Sonnerup (1999) recalculated by Lui et al. (2008). The theoretical model is given by the partial differential Equation C.39 of magnetic vector potential $A(\tilde{x}, \tilde{y})$ where $\tilde{\alpha} = 0.225$, $p = e^{-2A}/(3\mu_0)$, and $B_z = e^{-A}/\sqrt{3}$. A map of exact analytical solution given by Equation C.40 was shown in Figure C.1.

For testing, a frame velocity vector $-V_{HT} = 0.8\hat{\tilde{x}} + 0.08\hat{\tilde{y}} + 0.16\hat{\tilde{z}}$ onto the $\tilde{x}\tilde{y}$ plane was selected, as was proposed by Hau and Sonnerup (1999). The $\tilde{x}\tilde{y}$ coordinate system is rotated relative to the xy system by an angle of 5.7° ($\tan^{-1}(0.08/0.8) = 5.7^\circ$). To rotate a figure counterclockwise around the origin by some angle $\theta = 5.7^\circ$ is equivalent to replacing every point with coordinates (\tilde{x}, \tilde{y}) by the point with coordinates (x, y) :

$$\begin{aligned}\tilde{x} &= x \cos \theta - y \sin \theta \\ \tilde{y} &= x \sin \theta + y \cos \theta.\end{aligned}$$

Thus, the coordinates (\tilde{x}, \tilde{y}) are changes by new coordinates xy in the exact solution, $A(\tilde{x}, \tilde{y})$:

$$A(x, y) = \ln\{\tilde{\alpha} \cos[x \cos \theta - y \sin \theta] + \sqrt{1 + \tilde{\alpha}^2} \cosh[x \sin \theta + y \cos \theta]\}. \quad (\text{C.44})$$

The map of the solution C.44 was shown in Figure C.3(a). We used a grid of $x_{min} = 0$ and $x_{max} = 51$ with a total of 101 equidistant samples, separated by $\Delta x = 51/101$, in the other axis $\Delta y = 0.1\Delta x$ with $y_{min} = -5$ and $y_{max} = 5$. Also, seven plasma

parameters can be written in the xy coordinates system, *i. e.*,

$$B_x = \frac{\partial A}{\partial y} = \frac{\tilde{\alpha} \sin[x \cos \theta - y \sin \theta] \sin \theta + \sqrt{1 + \tilde{\alpha}^2} \sinh[x \sin \theta + y \cos \theta] \cos \theta}{\tilde{\alpha} \cos[x \cos \theta - y \sin \theta] + \sqrt{1 + \tilde{\alpha}^2} \cosh[x \sin \theta + y \cos \theta]},$$

$$B_y = -\frac{\partial A}{\partial x} = \frac{\tilde{\alpha} \sin[x \cos \theta - y \sin \theta] \cos \theta - \sqrt{1 + \tilde{\alpha}^2} \sinh[x \sin \theta + y \cos \theta] \sin \theta}{\tilde{\alpha} \cos[x \cos \theta - y \sin \theta] + \sqrt{1 + \tilde{\alpha}^2} \cosh[x \sin \theta + y \cos \theta]},$$

$$B_z = \sqrt{\frac{e^{-2A(x,y)}}{3}} = \frac{1}{\sqrt{3}(\tilde{\alpha} \cos[x \cos \theta - y \sin \theta] + \sqrt{1 + \tilde{\alpha}^2} \cosh[x \sin \theta + y \cos \theta])},$$

$$p = \frac{1}{3\mu_0(\tilde{\alpha} \cos[x \cos \theta - y \sin \theta] + \sqrt{1 + \tilde{\alpha}^2} \cosh[x \sin \theta + y \cos \theta])^2},$$

$$P_t = p + \frac{B_z^2}{2\mu_0} = \frac{1}{2\mu_0} e^{-2A},$$

$$J_z = \frac{d(p + B_z^2/(2\mu_0))}{dA} = -\frac{1}{\mu_0} e^{-2A},$$

$$P_{Total} = p + \frac{B^2}{2\mu_0} = \frac{1}{3\mu_0} e^{-2A} + \frac{B_x^2 + B_y^2 + B_z^2}{2\mu_0},$$

where, B_x, B_y, B_z are the magnetic field components; p is the plasma pressure; P_t is the transverse pressure; J_z is the axial current; P_t is the total pressure; μ_0 is permeability of free space; $\theta = 5.7^\circ$; the parameter $\tilde{\alpha} = 0.225$ is a separation constant which determines the properties of the solution. The Maps of above equations are given in Figure C.3. In panel (a) is show the Map of exact analytical solution, $A(x, y)$ in xy plane. In the other panels are show the exact solution in xy plane of the others seven plasma parameters: (b) B_x ; (c) B_y ; (d) B_z ; (e) p with normalization 10^5 ; (f) P_t with normalization 10^5 ; (g) J_z with normalization 10^5 ; (h) P_{Total} with normalization 10^5 .

The map of the function $A(x, y)$ has been determined from the initial condition at points $y = 0$, *i. e.*, $A(x, 0) = -\int_0^x B_y(x'', 0) dx''$, $B_x(x, 0), p(x, 0)$ and $[d(p + B_z^2/2\mu_0)/dA]_{x,0}$. The plot of B_x, B_y, B_z at $y = 0$ as function of x are shown in Figure C.4(a). Panel (b) shows the plot of A at $y = 0$ as function of x while in panel (c) is plot the plasma pressure, $p(x, 0)$. Figure C.4(d) shows the curve of measured values of $P_t(x, 0) = (p + B_z^2/2\mu_0)$ versus their corresponding $A(x, 0)$ values, the curve fitting is $P_t(x, 0) = 0.398e^{-2A(x,0)}$.

The map of numerical solution of Grad-Shafranov equation is shown in Figure C.5(a). Figure C.5 has the same format that C.3 but it was obtained of the numerical solution of Grad-Shafranov equation. In all panels, on the bottom right corner is the highest error observed.

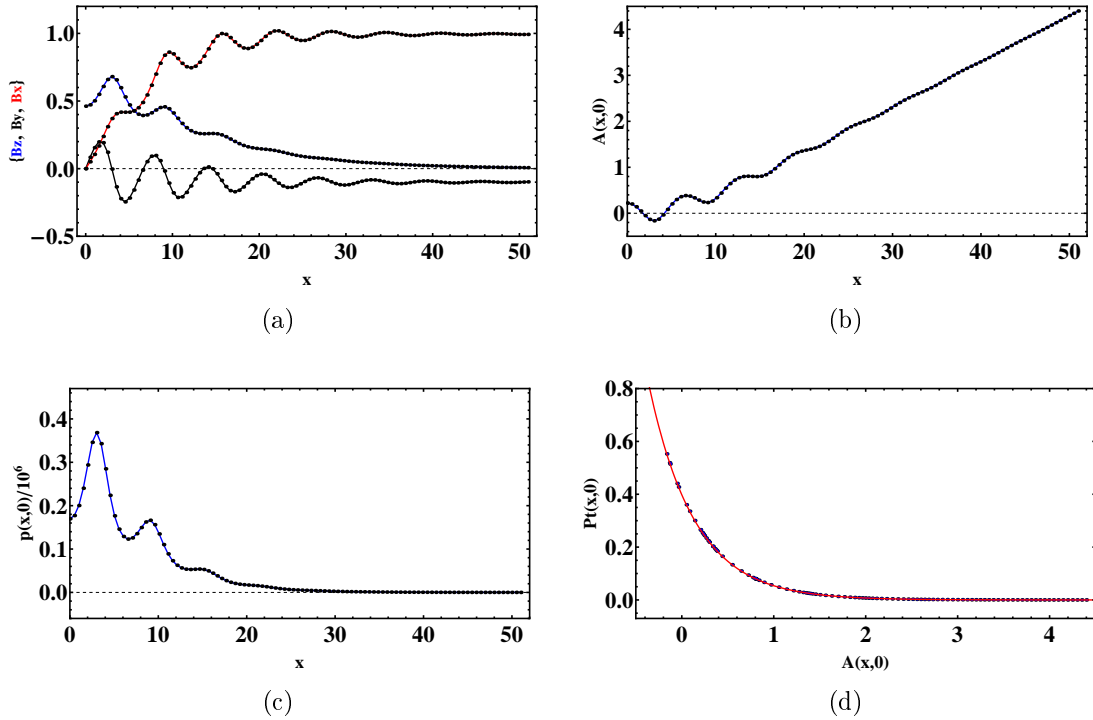


Figure C.4 - Reconstruction of Benchmark case with invariant (z) axis rotates around $\theta = 5.7^\circ$. (a) B_x, B_y, B_z at $y = 0$ as function of x ; (b) A at $y = 0$ as function of x ; (c) p at $y = 0$ as function of x ; (d) P_t as function of A at $y = 0$, the curve fitting is $P_t(A) = 0.398e^{-2A}$.

C.3 Improved numerical resolution

Plots of magnetic field lines for benchmark solution similar to Figure 1 in the paper of Hau and Sonnerup (1999) is obtained by us. Thus, Figure C.6 shows: (a) is the same graphic shows in the Figure C.3(a) i.e., map of exact solution $A(x,y)$; (b) the numerical solution derived from the initial condition, as shown in the Figure C.4. The integration domain was extended to 51 points in the x axis and from -5 to 5 in y axis, since in Hau and Sonnerup (1999) the domain is $0 < x < 40$ and $-2.5 < y < 2.5$. Panel (c) is the contours of constant error, $(A_{calc} - A_{exact})/|A|$,

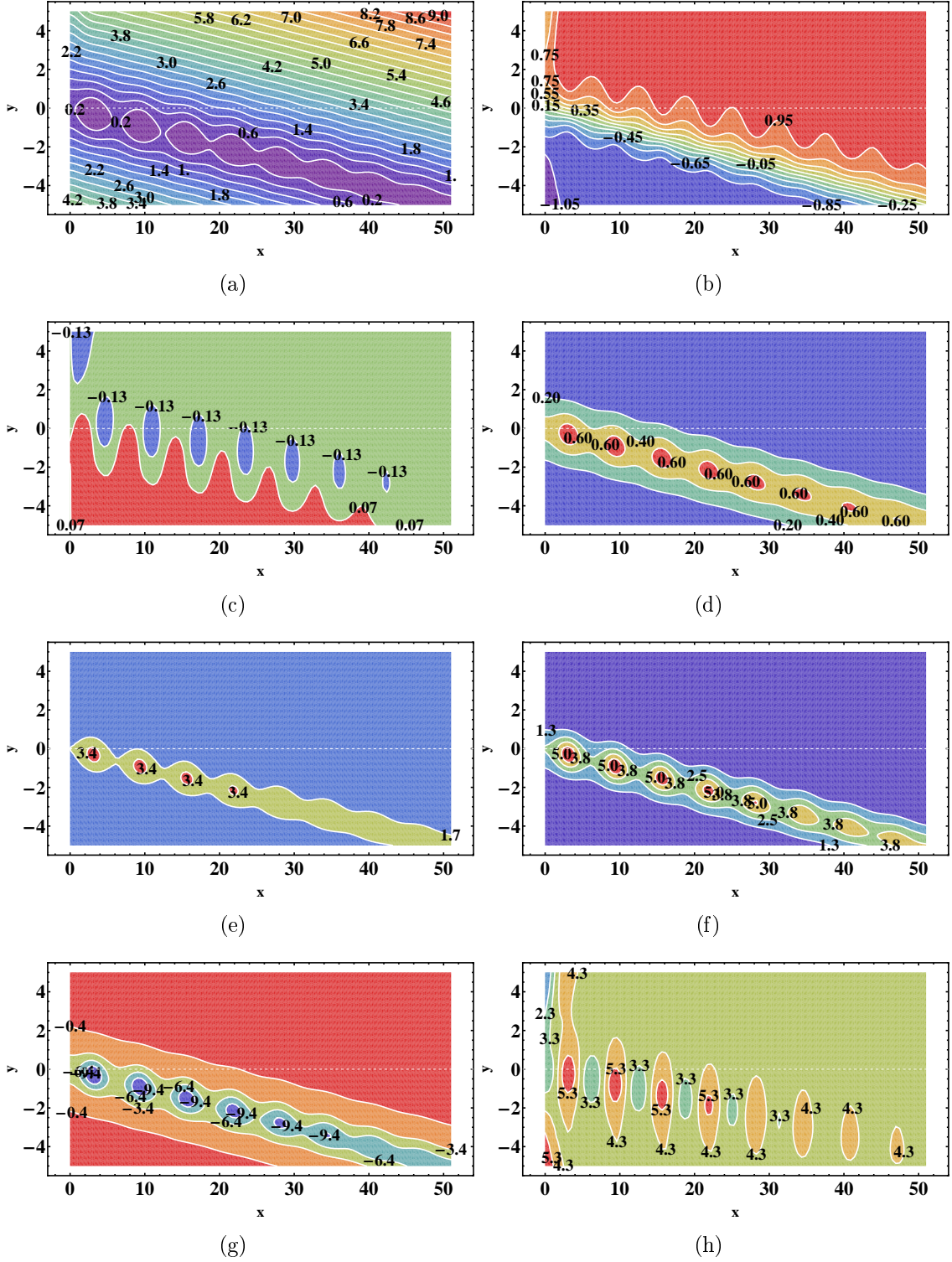


Figure C.5 - (a) Map of numerical solution, $A(x,y)$ in xy plane. The $\tilde{x}\tilde{y}$ coordinate system is rotated relative to the xy system by an angle of 5.7° . Field lines are separated by equal flux. In the other panels are shown the numerical solution in xy plane of the other seven plasma parameters: (b) B_x ; (c) B_y ; (d) B_z ; (e) p with normalization 10^5 ; (f) P_t with normalization 10^5 ; (g) J_z with normalization 10^5 ; (h) P_{Total} with normalization 10^5 .

where $\langle |A| \rangle$ is the average of the magnitude of A over the map. Panel (d) is a zoom of (c), so that is equal to Figure 1 (bottom panel) of Hau and Sonnerup (1999).

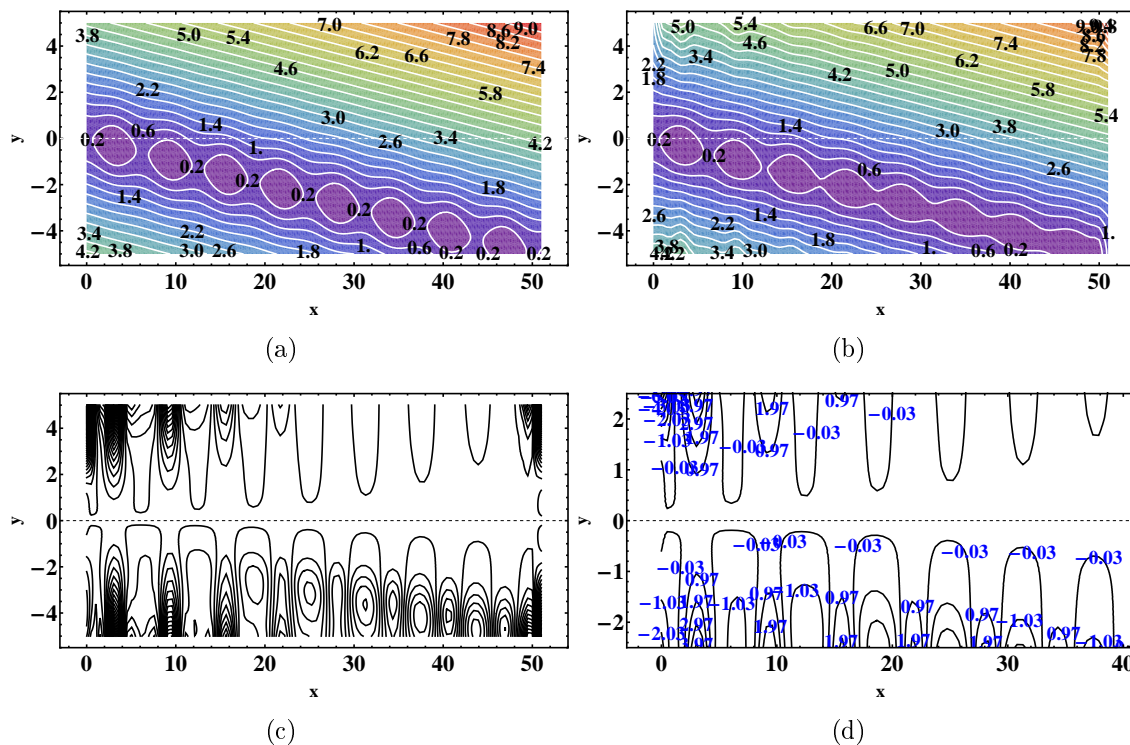


Figure C.6 - Contours of constant error, $(A_{calc} - A_{exact})/\langle |A| \rangle$, where $\langle |A| \rangle$ is the average of the magnitude of A over the map. Error contours are separated by 1%. (a) Analytical solution map of $A(x, y)$; (b) numerical solution map of $A(x, y)$; (c) contours of constant error; (d) zoom of contours of constant error, idem to shown in Figure 1 of Hau and Sonnerup (1999).

We propose some changes in the resolution scheme of the Grad-Shafranov equation to improve the solution. We will be talking about four methods:

- 1) (HS99 method) The solution is idem as explain in the paper of Hau and Sonnerup (1999). In the version of Hau and Sonnerup (1999) GS solver, they attempt to suppress the development of the singularities associated with the shortest wavelengths by doing running an filter (see Equations 10 and 11 in that paper or Equations 4.32 and 4.33 in this thesis) in $A(x, \Delta y)$ for each integration step. The previous numerical solution map with its contours of constant error map are shown in the panels of Figure C.6. The more important information is that here,

$B_x(x, \Delta y)$ is not filtered (see Figure C.7(b)) and in the difference scheme at each step Δy second-order Taylor expansion with second order of accuracy was used.

- 2) (first method) During the integration scheme at the same time are filtered $A(x, \Delta y)$ and $B_x(x, \Delta y)$ (see Figure C.7(c)) respectively.
- 3) (second method) $B_x(x, \Delta y)$ is not filtered. The derivative $\partial^2 A / \partial x^2$ is calculated numerically, using a central difference scheme at each step Δy of the integration, resulting in the rectangular box by writing it at the i point, a second-order Taylor expansion with sixth order of accuracy (Hau and Sonnerup (1999) used second order of accuracy): $(\partial^2 A / \partial x^2)_i = (\frac{1}{90}A_{i-3} - \frac{3}{30}A_{i-2} + \frac{3}{2}A_{i-1} - \frac{49}{18}A_i + \frac{3}{2}A_{i+1} - \frac{3}{20}A_{i+2} + \frac{1}{90}A_{i+3}) / (\Delta x)^2 + O(\Delta x^2)$.
- 4) (third method) It is a combination of the first and second methods respectively.

The Figure C.7(a) shows the exact solution map of B_x . The panels (b) and (d) shows numerical solution map of B_x without filter it; in both panels are used “HS99 method” and “second method” respectively. The panel (c) shows map of B_x using the first method (B_x is filtered) and improve the numerical solution. In panel (e) the third method is used, and it is improved the numerical solution. Grad-Shafranov equation has the nonlinearity in the term $d(P_t)/dA$, during the integration scheme B_x values are obtained from the first order Taylor expansion,

$$B_x(x, \pm \Delta y) \cong B_x(x, 0) \pm (\partial^2 A / \partial y^2)_{x,0} \Delta y,$$

and the second derivative in the above equation can be evaluated from GS equation,

$$\left(\frac{\partial^2 A}{\partial y^2} \right)_{x,0} = - \left(\frac{\partial^2 A}{\partial x^2} \right)_{x,0} - \mu_0 \frac{dP_t(A(x, 0))}{dA}.$$

This justifies the need to filter B_x during the integration scheme.

After obtaining the solution is reduces the integration domain to remove the influence of the boundaries. Thus, in Figure C.8 the maps of $A(x, y)$ are shown in a grid of $5 \lesssim x \lesssim 45$ and $-4.5 \lesssim y \lesssim 4.5$. In each pair of panels from top to bottom are shown: (a) the exact solution map and (b) contours of constant error, $(A_{calc} - A_{exact}) / \langle |A| \rangle$, using the HS99 method; (c) and (d) the numerical solution map using the first method and contours of constant error; (e) and (f) are similar to (c) and (d) but for second method; (g) and (h) are similar to (c) and (d) but for

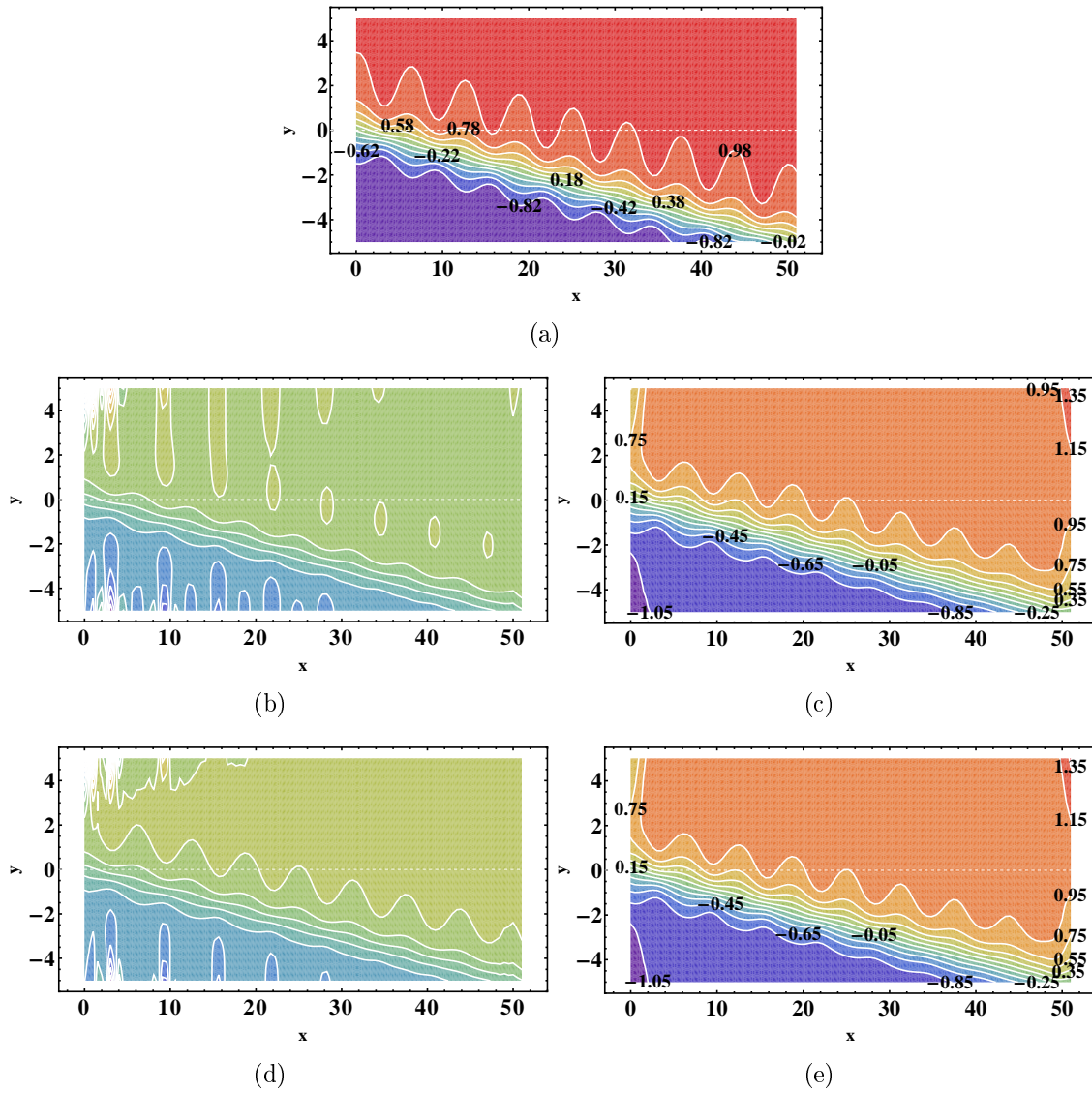


Figure C.7 - (a) Map of exact analytical solution, $B_x(x, y)$ in xy plane. The other panels show numerical solution maps of B_x , where are used the following methods: (b) HS method; (c) first method; (d) second method; (e) third method.

third method. The panels of contours of constant error are compared with the panel (b). The solution greatly improves when we use the first method (see panel (d)). On the other hand, there is not improvement when using the second method (see panel (f)). The third method also improves the solution and is the best method (see panel (h)). Summary, the solution in the paper of [Hau and Sonnerup \(1999\)](#) was improved with these proposals. Other method to improve the GS solver are presented by the same authors in [Hu and Sonnerup \(2003\)](#), Appendix A.

C.4 Orientation of Magnetic flux ropes

Taken from [Hu and Sonnerup \(2002\)](#): The right panel of Figure C.9 illustrates a plot of $P_t(x, 0)$ versus $A(x, 0)$, obtained by using an incorrect z axis (rotated around the true x axis by 3°), for the Lundquist flux-rope, a cross section of which is shown in the left panel. The small circles starting at $A = 0$ represent the data points collected by a virtual spacecraft along the first half of its trajectory, projected along the x axis, when it penetrates the structure from its left edge toward the center. After it passes the point of closest approach, where the value $A = A_m$ is reached, the data along the second half of the spacecraft trajectory are represented by the stars. They drop to lower P_t values, passing the value $A = A_l$ ($A_l = 0$ in this case) again, while the spacecraft is moving away from the center of the structure toward its right edge. However, the stars do not follow the curve through the circles from the first half of the data interval.

The separation between the curves, threaded by the circles and stars, respectively, is an indication that the z axis chosen is not right. For the correct z axis the magnetic field lines having potentials between A_l and A_m are crossed exactly twice by the spacecraft, in the first half and the second half of its trajectory, separately. The data from the two halves ought to have exactly the same P_t value for the same A value. In other words, for the correct choice of z axis all the circles and stars in the right panel of Figure C.9 should lie on one single-valued curve representing $P_t(A)$.

The arrow tip of the trial axis varies on a hemisphere, representing all possible directions in 3-D space. A fitting residue for $P_t(A)$, associated with each trial axis, is also calculated. The precise definition of this residue will be given below. The optimal invariant direction is the minimum-residue direction.

The plot between $A = A_l$ and $A = A_m$ in the right panel of Figure C.9 provides an

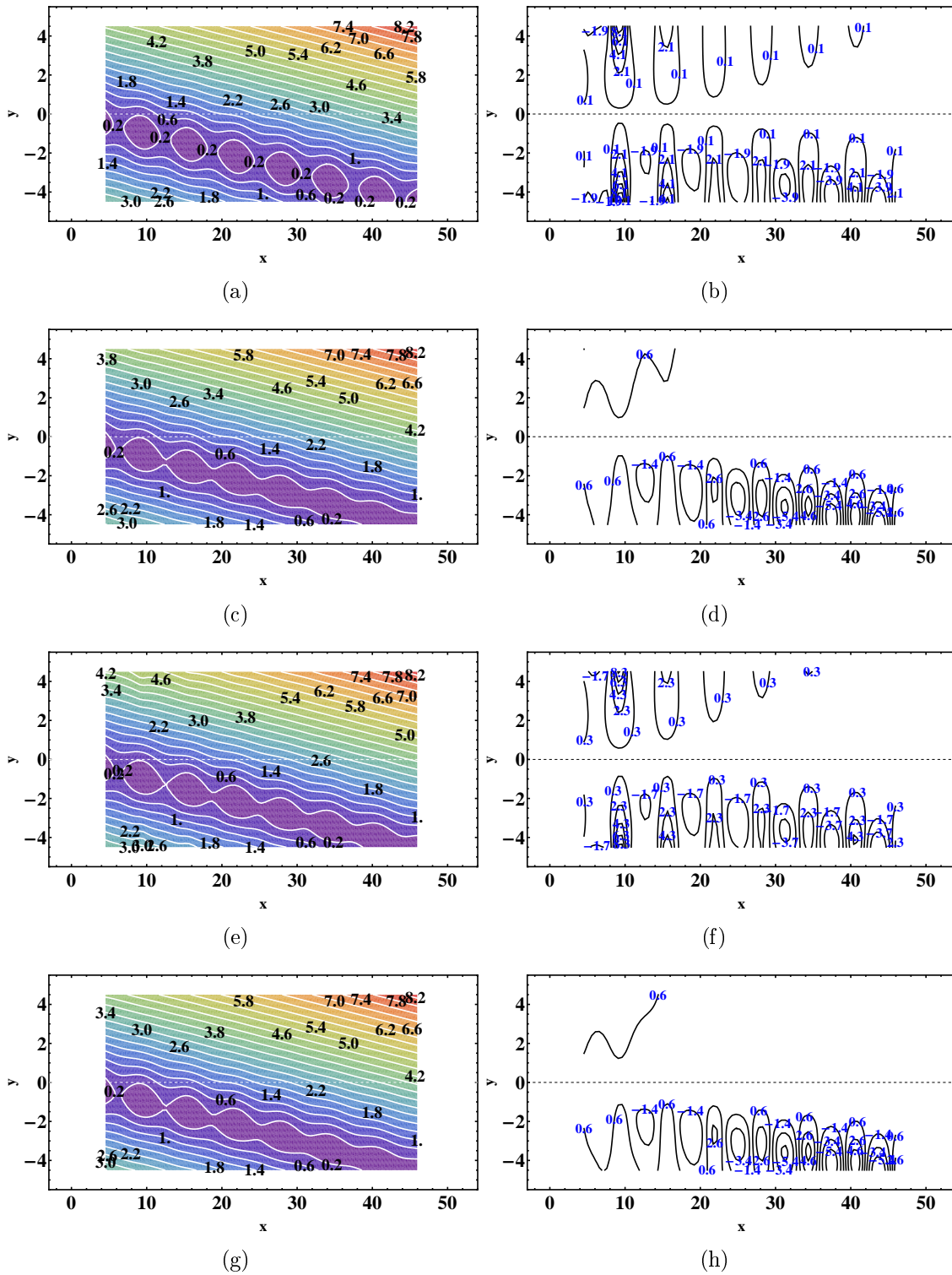


Figure C.8 - In each pair of panels from top to bottom are shown: (a) the exact solution map and (b) contours of constant error, $(A_{calc} - A_{exact})/|A|$, using the HS99 method; (c) and (d) the numerical solution map using the first method and contours of constant error; (e) and (f) are similar to (c) and (d) but for second method; (g) and (h) are similar to (c) and (d) but for third method.

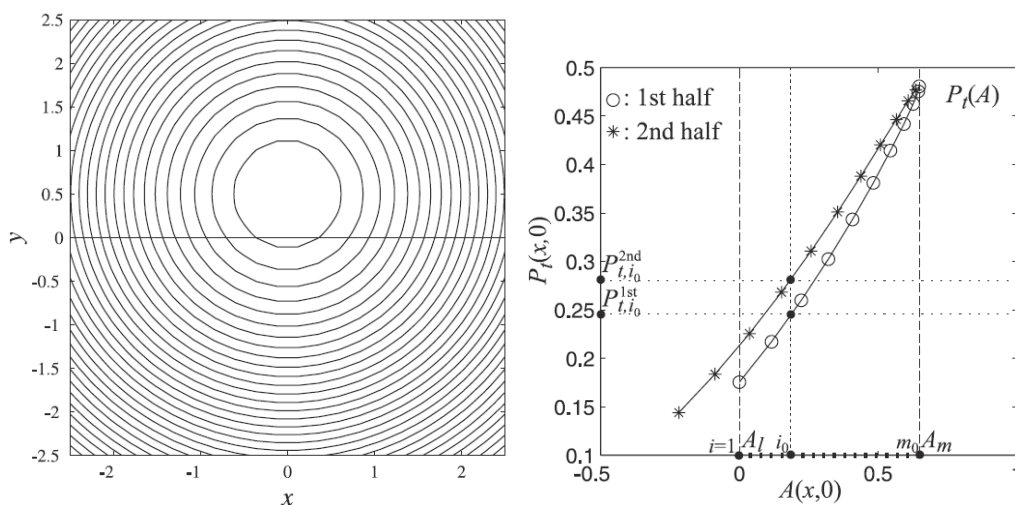


Figure C.9 - Illustration of behavior of $P_t(A)$ for an incorrect z axis orientation. (left) Cross section of Lundquist flux rope for $\tilde{\alpha}L_0 = 0.55$ (L_0 being the length normalization), centered at $(x, y) = (0, 0.5)$, with the correct z axis. The x axis ($y = 0$) denotes the projected spacecraft trajectory. (right) Scatter plot of $P_t(x, 0)$ versus $A(x, 0)$ for an incorrect z axis. See the text for an explanation of the symbols. SOURCE: Hu and Sonnerup (2002).

example for the chosen trial axis. That data interval is utilized in the calculation of the fitting residue. The data from the first half and the second half of the adaptive interval, respectively, are interpolated onto a stencil of uniformly spaced grid points along the A axis, between its minimum and maximum values. For example, in the right panel of Figure C.9 the interval $A \in [A_l, A_m]$ is uniformly divided by m_0 points with integer index, $i \in [1, \dots, m_0]$, to form such a stencil. Then components of an m_0 -dimensional residue vector are obtained by pair-wise subtraction of the interpolated first-half data from their second-half counterparts. The fitting residue, $\mathcal{RES} = R_f$, is calculated by taking the 2-norm of the residue vector and then normalizing it by $|\max(P_t) - \min(P_t)|$, i.e.,

$$\mathcal{RES} = \left[\sum_{i=1}^{m_0} (P_{t,i}^{1st} - P_{t,i}^{2nd})^2 \right]^{\frac{1}{2}} / |\max(P_t) - \min(P_t)|. \quad (\text{C.45})$$

One pair of such interpolated data at $i = i_0$, with corresponding transverse pressure value, $P_{t,i}^{1st}$ and $P_{t,i}^{2nd}$, is illustrated in the right panel of Figure C.9. The minimum-residue direction is the direction along which the residue calculated from Equation C.45 has its absolute minimum. The normalization in Equation C.45 by the

range of P_t is necessary to avoid obtaining an erroneous axis direction such that the slope of $P_t(A)$ is nearly zero, which would be equivalent to nearly zero axial current density.

APPENDIX D - REVIEW OF THE GRAD-SHAFRANOV EQUATION
USEFUL IN THE RECONSTRUCTION OF TWO-DIMENSIONAL
COHERENT STRUCTURES IN THE MAGNETOPAUSE

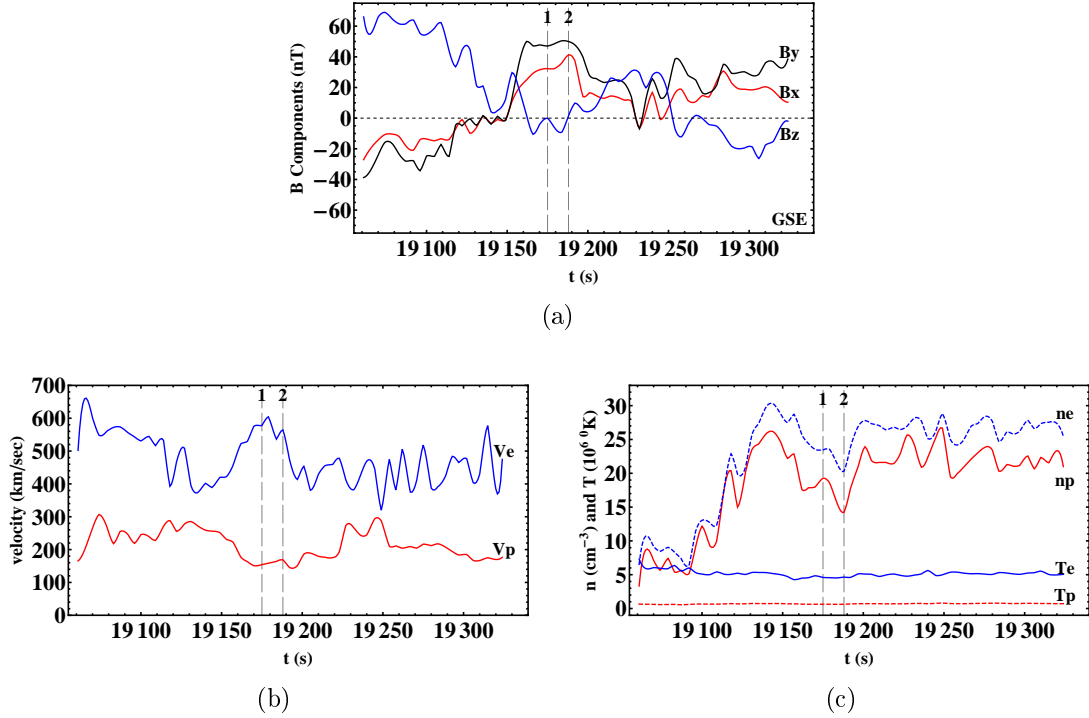


Figure D.1 - Time series of AMPTE/IRM measurements during magnetopause crossing, October 19, 1984, in the interval 05 : 17 : 41 – 05 : 22 : 03 UT. The vertical dashed lines number 1 and 2 correspond at the dates 05 : 19 : 35 and 05 : 19 : 48 respectively. (a) B_x, B_y, B_z in nT (GSE); (b) Electron velocity and proton velocity; (c) number proton density, number electron density, electron temperature and proton temperature.

The procedures used in the reconstruction scheme following the work of (HAU; SONNERUP, 1999) are (Note that all figures to be presented were obtained by us):

1) **Input Data:**

The data analysis utilizes a set of \tilde{K} measured values, at constant time intervals, of GSE components of magnetic field (B_X, B_Y, B_Z), plasma velocity (v_X, v_Y, v_Z) in GSE to electron and proton, plasma density $N = N_e + N_p$, and temperature $T = (T_p + T_e)/2$. Plots of GSE magnetic field components, plasma number density, and temperature versus time (with 4.37 s of resolution) for the spacecraft

AMPTE/IRM¹ crossing the magnetopause, October 19, 1984, in the interval 05 : 17 : 41 – 05 : 22 : 03 UT , are shown in Figure D.1 (HAU; SONNERUP, 1999). The vertical dashed lines number 1 and 2 correspond at the dates 05 : 19 : 35 and 05 : 19 : 48 respectively. In the first interval (05 : 17 : 41 – 05 : 19 : 35 UT) have been calculated the eigenvalues and eigenvectors derived from MVA. To capture more of the magnetopause structure, the interval used in the reconstruction was extended to 05 : 17 : 41 – 05 : 19 : 48 UT by Hau and Sonnerup (1999) and contained $\tilde{K} = 30$ original data points. These data will be useful to calculate deHoffman - Teller frame and the plasma pressure to resolve the GS equation.

2) **Use minimum-variance analysis** (SONNERUP; CAHILL, 1967; SONNERUP; SCHEIBLE, 1998; BOTHMER; SCHWENN, 1998):

We used MVA on the measured magnetic field vectors (B_X, B_Y, B_Z) in GSE, to determine \vec{n} , the vector normal to the magnetopause. In this chapter a detailed study about the MVA was presented. The magnetic field components which were used correspond to October 19, 1984, in the interval 05 : 17 : 41 – 05 : 19 : 35 UT. The figure D.2(a) and D.2(b) show results from MVA over this data intervals (27 data points) in the form of magnetic hodograms (HAU; SONNERUP, 1999). The eigenvalues of the magnetic variance matrix are $\lambda_1, \lambda_2, \lambda_3$, in order of declining size and the corresponding normalized eigenvectors, $\hat{x}_1 = \hat{B}_L, \hat{x}_2 = \hat{B}_M, \hat{x}_3 = \hat{B}_N$ in which eigenvector $\hat{x}_3 = \hat{B}_N$ is the magnetopause normal: $\hat{x}_3 = \hat{B}_N = \vec{n}$. A comparison of our results with those of the Hau and Sonnerup (1999) are shown in Table D.1 where can be see the quantification information. In the paper appear an incorrect eigenvalue of $\lambda_3 = 9.6$, but the correct eigenvalue is $\lambda_3 = 7.6$; we prove that is a digitalization error, in the subsequent results was used $\lambda_3 = 7.6$. Note that, the two top panels in Figure 5 of Hau and Sonnerup (1999) are the hodograms in the interval 05 : 17 : 41 – 05 : 19 : 48 UT, and not correspond with was wrote by the authors in the caption (the interval 05 : 17 : 41 – 05 : 19 : 35 UT). In the last four rows of Table D.1 the values for the extended interval are shown. These values are not used in subsequent reconstruction because exist a physical problem that we will be explained in the following item.

3) **Determine the deHoffman - Teller frame velocity:**

The deHoffman-Teller velocity is a velocity where the residual electric field is minimized. The existence of an HT frame indicates that a coherent quasi-

¹<http://www-ssg.sr.unh.edu/index.html?tof/Missions/Ampte-irm/amptemain.html>

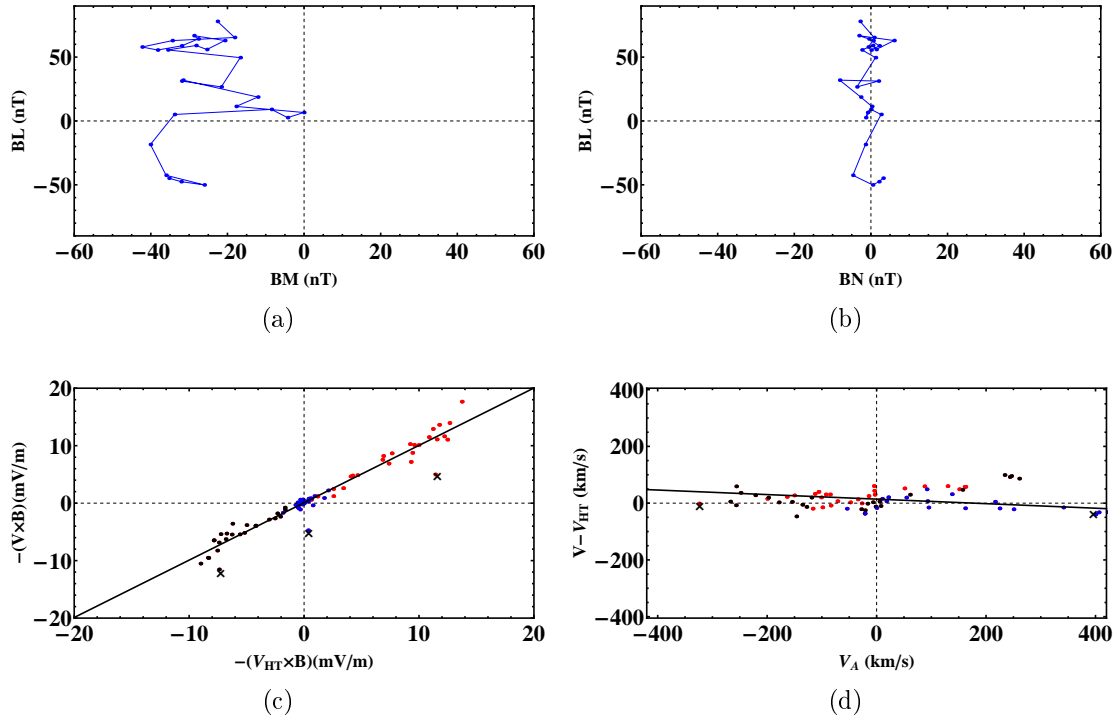


Figure D.2 - Analysis results for AMPTE/IRM event, October 19, 1984, in the interval 05 : 17 : 41–05 : 19 : 35 UT. The eigenvalues and eigenvectors of the magnetic hodogram pair from MVA, in the two top panels, are shown in the first rows of Table D.1. In the two bottom panels, the colors represent the components, i.e., *red* $\equiv x$, *black* $\equiv y$, *blue* $\equiv z$. The crosses are to identify points that were eliminated by [Hau and Sonnerup \(1999\)](#) to calculate the correlation coefficient (cc_{all}) and the slope ($slope_{all}$) of the linear fit. (a) Maximum Variance; (b) Minimum Variance; (c) HT correlation with $cc_{all} = 0.974$ and $slope_{all} = 0.998$; (d) Walén correlation. with $cc_{all} = -0.433$, $slope_{all} = -0.080$.

Table D.1 - The eigenvalues of the magnetic variance matrix are $\lambda_1, \lambda_2, \lambda_3$, in order of declining size and the corresponding normalized eigenvectors, $\hat{x}_1 = \hat{B}_L$, $\hat{x}_2 = \hat{B}_M$, $\hat{x}_3 = \hat{B}_N$. Our results, shown in the third column, are consistent with the second column. The different results (λ_3) are shown in red.

October 19,1984, 0517:41-0519:35		
Parameters	Hau and Sonnerup (1999)	Our implementation
\hat{x}_1, \hat{B}_L	(-0.4095; -0.6698; 0.6194)	(-0.4095; -0.6698; 0.6194)
\hat{x}_2, \hat{B}_M	(-0.3195; -0.5306; -0.7851)	(-0.3195; -0.5306; -0.7851)
\hat{x}_3, \hat{B}_N	(0.8545; -0.5194; 0.0033)	(0.8545; -0.5194; 0.0033)
$[\lambda_1, \lambda_2, \lambda_3]$	[1530.4, 114.7, 9.6]	[1530.4, 114.7, 7.6]
October 19,1984, 0517:41-0519:48		
\hat{x}_1, \hat{B}_L	-	(-0.4377; -0.6757; 0.5931)
\hat{x}_2, \hat{B}_M	-	(-0.3419; -0.4850; -0.8049)
\hat{x}_3, \hat{B}_N	-	(0.8316; -0.5551; -0.0188)
$[\lambda_1, \lambda_2, \lambda_3]$	-	[1929.3, 109.997, 9.6]

stationary pattern of magnetic field and plasma velocity such as a wave or current layer, is present. If the electric field measured in the instrument frame is \vec{E} , then the electric field in the HT frame, assuming such a frame exist, is $\vec{E}' = \vec{E} + \vec{V}_{HT} \times \vec{B} = 0$ (KHRABROV; SONNERUP, 1998). The Faraday's law evaluated in the HT frame is $\nabla \times \vec{E}' = -(\partial \vec{B} / \partial t)' = 0$. The existence of the HT frame implies that the magnetic field structure sampled is stationary when viewed in that frame. When the data to be analyzed have been collected within regions and structures where ideal MHD is approximately valid so that $\vec{E} + \vec{v} \times \vec{B} \cong 0$, then the convective electric field, $-\vec{v} \times \vec{B}$, can be used as a proxy for the electric field (KHRABROV; SONNERUP, 1998). To obtain an approximation to V_{HT} from a set of M experimental data (following the work of Khrabrov and Sonnerup (1998)), the mean square of the electric field (denoted by $D(\vec{V})$) is as small as possible for the given set of M measurements:

$$D(\vec{V}) = \frac{1}{M} \sum_{m=1}^M \left| \vec{E}'^{(m)} \right|^2 = \frac{1}{M} \sum_{m=1}^M \left| (\vec{v}^{(m)} - \vec{V}) \times \vec{B}^{(m)} \right|^2.$$

The HT velocity is the value of the frame velocity, \vec{V} , that minimizes $D(\nabla_{\vec{V}} D = 0)$. The solution is (KHRABROV; SONNERUP, 1998):

$$\vec{V}_{HT} = K_0^{-1} \langle K^{(m)} \vec{v}^{(m)} \rangle, \quad (\text{D.1})$$

Table D.2 - Applying the formula D.1 in the two intervals gives the components of the \vec{V}_{HT} in GSE coordinates. Its component along the outward directed magnetopause normal, $\hat{n} = \hat{x}_3 = (0.8545; -0.5194; 0.0033)$ ($\hat{n} = \hat{x}_3 = (0.8316; -0.5551; -0.0188)$) in GSE, taken from the first (second) interval, is -9.08 km/s (1.1 km/s). The correlation coefficients (cc_{all}) are different with the paper because the point represented with crosses (\times) in Figure D.2(d) were eliminated by Hau and Sonnerup (1999) to do the calculations.

October 19,1984, 0517:41-0519:35		
Parameters	Hau and Sonnerup (1999)	Our implementation
\vec{V}_{HT}	$(-142; -215; 72)km/s$	$(-141.9, -215.5; 72.5)km/s$
$\vec{V}_{HT} \cdot \hat{n} = \vec{V}_{HT} \cdot \hat{x}_3$	$-9km/s$	$-9.08km/s$
cc_{all}	0.994	0.974
$slope_{all}$	-	0.998
$cc_{all-Walen}$	-	-0.433
$slope_{all-Walen}$	-	-0.080
October 19,1984, 0517:41-0519:48		
\vec{V}_{HT}	-	$(-142.2, -217.5; 77.3)km/s$
$\vec{V}_{HT} \cdot \hat{n} = \vec{V}_{HT} \cdot \hat{x}_3$	-	$1.1km/s$
cc_{all}	0.987	0.973
$slope_{all}$	-	1.001

the angle brackets $\langle \dots \rangle$ denote an average of an enclosed quantity over the set of M measurements, and $K_0 \equiv \langle K^{(m)} \rangle$ with K_0 is non-singular matrix. In these expressions, each $K^{(m)}$ is the matrix of projection, $P^{(m)}$, into a plane perpendicular to $\vec{B}^{(m)}$, multiplied by $B^{(m)2}$:

$$K_{\mu\nu}^{(m)} = B^{(m)2} \left(\delta_{\mu\nu} - \frac{B_{\mu}^{(m)} B_{\nu}^{(m)}}{B^{(m)2}} \right) \equiv B^{(m)2} P_{\mu\nu}^{(m)}. \quad (D.2)$$

We wrote a program to calculate V_{HT} according to the Equations D.1 and D.2, in Table D.2, the results for the two intervals are shown. Its component along the outward directed magnetopause normal, \hat{n} in GSE, taken from the first (second) interval, is -9.08 km/s (1.1 km/s). In the second interval the inconsistency is that V_{HT} , the HT frame velocity, *has a small positive component along \hat{n}* , whereas the sense of the traversal, from the magnetosphere to the magnetosheath, requires this component to be negative. This discrepancy is within error bounds when allowance is made for the estimated uncertainties in the plasma measurements, in the normal vector, and in \vec{V}_{HT} (KHRABROV; SONNERUP, 1998). In that study,

Hau and Sonnerup (1999) used the HT - frame derived from the first interval, where $V_{HT} < 0$, and extend this interval in the reconstruction. In the following step, we must prove that a very good HT frame exists for this interval.

4) deHoffman - Teller correlation:

In a tangential discontinuity (TD) is where no magnetic field along the normal component, $\langle \vec{B} \rangle \cdot \hat{n} = 0$, nor any plasma transport across the discontinuity. In a rotational discontinuity (RD) is where a finite magnetic field component along the normal, $\langle \vec{B} \rangle \cdot \hat{n} \neq 0$, and plasma flow across the boundary. To give an impression of the quality of the HT frame, the two electric fields $E^{(m)} = -\vec{v}^{(m)} \times \vec{B}^{(m)}$ and $\vec{E}_{HT}^{(m)} = -\vec{V}_{HT} \times \vec{B}^{(m)}$ are plotted against each other, component by component, in Figure D.2(c). The correlation between these two field is seen to be very good: the correlation coefficients is $cc_{all} = 0.974$. The slope of the linear fit is $slope_{all} = 0.998$. To compare this results with Hau and Sonnerup (1999) see Table D.2. The correlation coefficients (cc_{all}) are different with the paper because the point represented with crosses (\times) in Figure D.2(c) were eliminated by Hau and Sonnerup (1999) to do the calculations. A high correlation mean existence of a TD, where in the simple two-fluid model, the magnetic field is frozen into the plasma fluid ($\vec{E}' = 0$) (KHRABROV; SONNERUP, 1998). The cross section of the the magnetopause appears to be that of a basic TD, where the structures in the transverse magnetic field were generated by the tearing mode (HAU; SONNERUP, 1999).

5) Walén correlation:

If we examine the plasma velocity, $\vec{V}' = \vec{V} - V_{HT}$, in the HT frame and their relation to the local measured Alfvén velocity ($\vec{V}_A = \vec{B}(\mu_0\rho_0)^{-1/2}$), the plasma velocity is small compared to the corresponding Alfvén and sound speeds. A component by component scatter plot of these two velocities, referred to as a Walén plot, is shown in Figure D.2(d). In magnetopause reconnection events where \vec{V}' is proportional to V_A the magnetopause had the structure of a large-amplitude Alfvén wave or RD for which $\langle \vec{B} \rangle \cdot \hat{n} \neq 0$ and $\vec{V}' = \pm \vec{V}_A$, where the sign on the right-hand side is the same as the sign of the product, $(\langle \vec{V}' \rangle \cdot \hat{n})(\langle \vec{B} \rangle \cdot \hat{n})$ (KHRABROV; SONNERUP, 1998). For such structures, the data points in the scatter plot fall along one of the diagonals in a Walén plot, that is not the case in a HT-frame. For the data set in Figure D.2(d), the Walén test is not successful: the correlation coefficients is $cc_{all-Walén} = -0.433$ while the slope of

Table D.3 - The results from the GS coordinate system are shown here, using the trial angle, and the optimal angle of -40° chosen by Hau and Sonnerup (1999).

October 19,1984, 0517:41-0519:35		
GS System	$\theta = 0^\circ$	$\theta = -40^\circ$
$\hat{x}'_1 =$	(0.410; 0.670; -0.619)	(0.108; 0.172; -0.979)
$\hat{x}'_2 =$	(0.855; -0.519; 0.003)	(0.855; -0.519; 0.003)
$\hat{x}'_3 =$	(-0.320; -0.531; -0.785)	(-0.508; -0.837; -0.203)
$V_{HTt} =$	247.49 km/s	123.75 km/s
$\hat{x} =$	(0.441; 0.650; -0.619)	(0.171; 0.133; -0.976)
$\hat{y} =$	(0.839; -0.544; -0.026)	(0.844; -0.531; 0.075)
$\hat{z} =$	(-0.320; -0.531; -0.785)	(-0.508; -0.837; -0.203)

the linear fit is $slope_{all-Walen} = -0.080$, the data are clustered around $V' = 0$. The conclusion can be drawn that the magnetopause structure examined here was that of a TD, rather than that of a RD. In the practice, the current layer did not have purely one-dimensional structure, substantial fluctuations in the individual values, $\vec{B} \cdot \hat{n}$ are presented. If a good HT frame exists, these fluctuations can be interpreted as being caused by 2-D or 3-D quasi-stationary structures moving past the spacecraft with the HT velocity (KHRABROV; SONNERUP, 1998). Also, the exist of a TD justified the neglect of inertial terms in the momentum equation and reducing it to a static balance that was shown in equation 2.5.

6) Grad-Shafranov coordinate system:

When we found a convecting 2D structure, one may proceed to define the normal to the GS plane. Let us denote the axes from the MVA by $(\hat{x}_1, \hat{x}_2, \hat{x}_3)$, corresponding to minimum, intermediate and maximum variance directions. To define the two axes on the GS plane. We make two adjustments. The first is a rotation about the x_3 axis by an angle θ to give the new coordinate system $\hat{x}'_1, \hat{x}'_2, \hat{x}'_3$, i.e., $\hat{x}'_2 = \hat{x}_3, \hat{x}'_3 = \hat{x}_2 \cos(\theta) - \hat{x}_1 \sin(\theta)$. A trial angle is used initially. The second is the projection of deHoffman-Teller velocity onto the $x'_1 x'_2$ plane, i.e. $V_{HTt} = (V_{HT} \cdot \hat{x}'_1) \hat{x}'_1 + (V_{HT} \cdot \hat{x}'_2) \hat{x}'_2$. The final GS coordinate system $(\hat{x}, \hat{y}, \hat{z})$ is formed with this projection, i. e., $\hat{x} = -V_{HTt}/|V_{HTt}|, \hat{z} = \hat{x}'_3, \hat{y} = \hat{z} \times \hat{x}$ (HAU; SONNERUP, 1999). The results from the GS coordinate system (xyz) are shown in Table D.3, using the trial angle and the optimal angle of -40° chosen by Hau and Sonnerup (1999). These results are not shown by the aforementioned authors.

7) Distance along x axis:

If we observed in the HT frame, the spacecraft moves with speed $|V_{HTt}|$ along the x axis, toward increasing x values, during the magnetopause traversal (HAU; SONNERUP, 1999). The data points, magnetic field and plasma pressure, are separated by distances $V_{HTt}\tau$ along x , where τ is the time between consecutive data samples. The conversion of time t to distance x along the x axis is $x = |V_{HTt}|t$. In the studied time interval, october 19, 1984, 05 : 17 : 41 – 05 : 19 : 48, time series for distance x is (0, 123.7, 247.45, . . . , 15592.2, 15715.97) km with $\tilde{K} = 30$ original data point. The distance x is normalize by $x_0 = 482$ km (HAU; SONNERUP, 1999). In the Figure D.3(a) B_X, B_Y, B_Z projection in GS system (xyz) vs x are shown. The distance x was normalized by $x_0 = 482$ km (HAU; SONNERUP, 1999) while field components by $B_0 = 81.2$ nT.

8) **Compute** $A(x, 0)$:

Due to time-independence and constant V_{HT} , time intervals can be directly converted into spatial distances with $dx = -V_{HT}\hat{x}dt$. The vector potential $A(x, 0)$ along x is obtained using the equation (5) of Hau and Sonnerup (1999) paper (see a best explication in Sonnerup and Guo (1996)):

$$A(x, 0) = - \int_0^x B_y(x'')dx'',$$

where $B_y(x'')$ (x'' is a dummy variable) is the projection of magnetic field in the GS system (xyz). To use the above expression, the structure is assumed time stationary. Here was used the extended data intervals, 05 : 17 : 41 – 05 : 19 : 48. Extrapolating functions are used in regions of the integration domain which are not covered by observations, commonly taken as second or third-order polynomial functions. Vector potential A at $y = 0$ as a function of x was shown in Figure D.3(b) (idem to Figure 6 shown by Hau and Sonnerup (1999)).

9) **Compute the pressures:** P_t and p :

The other initial conditions to do the GS reconstruction are derived of the pressures, P_t and p . The plasma pressure is $p = K_0NT$ [Pa], where $N = (ne + np) 10^6$ [1/m³] is the plasma density, $T = ((T_e + T_p)/2) 10^6$ [K] is the temperature, and $k_0 = 1.380603 10^{-23}$ [J · m · K⁻¹ = Pa · m³ · K⁻¹] is the Boltzmann constant. The transverse pressure, $P_t = (p + B_z^2/2\mu_0)$ [Pa] with B_z [T] is the projection onto the GS coordinates system, $\mu_0 = 4\pi 10^{-7}$ [N/A²] permeabil-

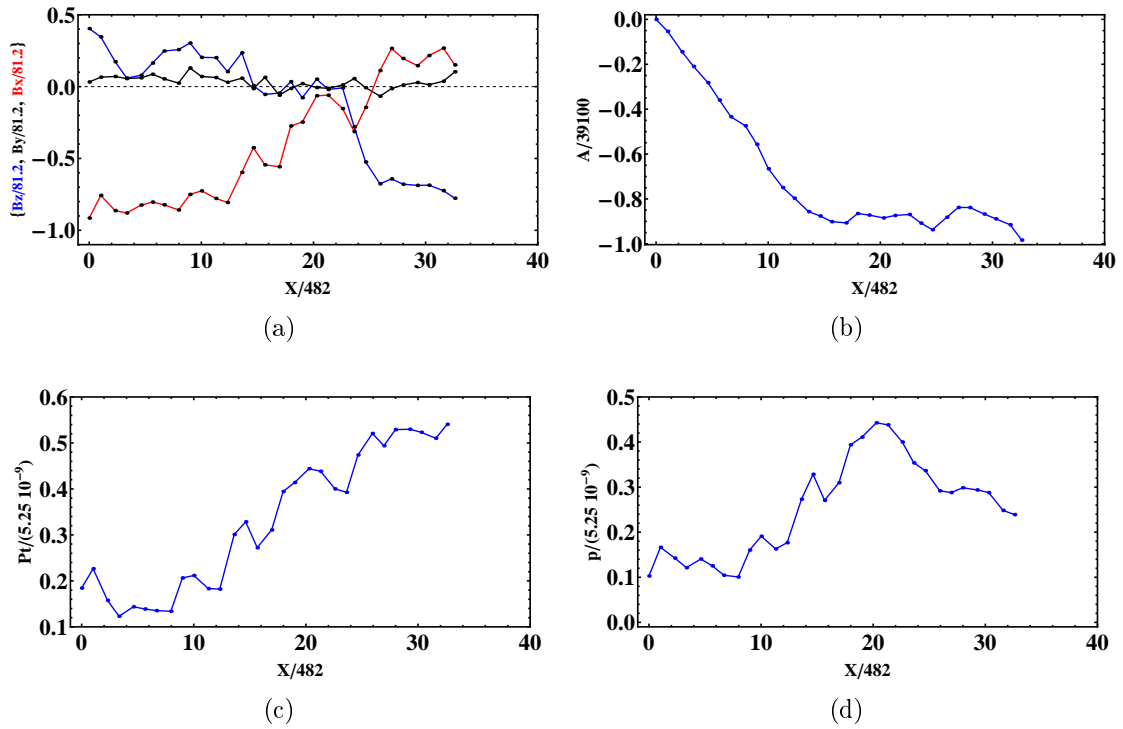


Figure D.3 - Analysis results for AMPTE/IRM event, October 19, 1984, in the interval 05 : 17 : 41 – 05 : 19 : 48 UT for optimal angle, $\theta = -40^\circ$, of invariant (z) axis. Normalizations in the four panels are as follows. For distance x : $x_0 = 482$ km. For vector potential A : $A_0 = 39100$ Tm. For pressures p and P_t : $p_0 = 5.25 \cdot 10^{-9}$ Pa. For field components: $B_0 = 81.2$ nT. (a) B_X, B_Y, B_Z projection in GS system (xyz) vs x ; (b) A at $y = 0$ as a function of x ; (c) Transverse pressure P_t as a function of x ; (d) Plasma pressure p as a function of x .

ity of free space. Plasma pressure and transverse pressure at $y = 0$ as a function of x were shown in Figures D.3(d) and D.3(c) respectively.

10) **Plot P_t vs $A(x, 0)$ and fit a function:**

The Grad-Shafranov equation 4.29 at $y = 0$ is transformed as:

$$\left(\frac{\partial^2 A}{\partial y^2}\right)_{x,0} = -\left(\frac{\partial^2 A}{\partial x^2}\right)_{x,0} - \mu_0 \frac{dP_t(A(x, 0))}{dA},$$

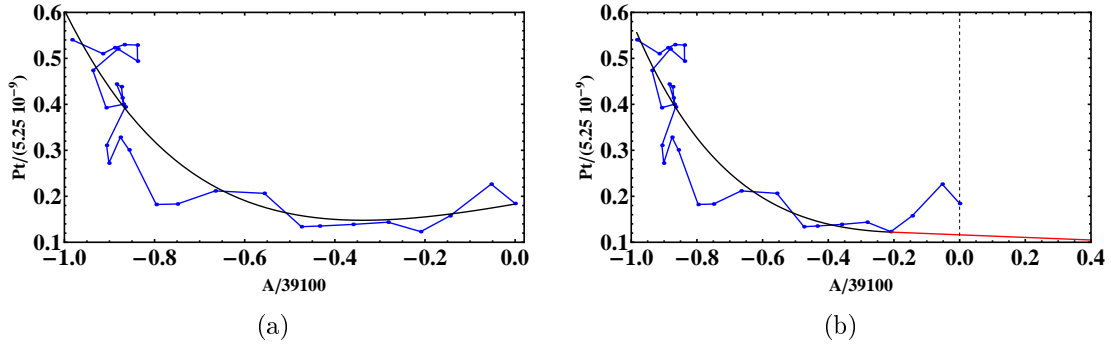


Figure D.4 - a) $P_t(x, 0)$ as function of $A(x, 0)$ where $P_t(A) = 0.51 + 0.10e^{-\frac{5}{2}A} - 0.43e^{-A}$.
b) $P_t(x, 0)$ as function of $A(x, 0)$ with linear tail where $P_t(A) = 0.29 + 0.08e^{-\frac{5}{2}A} - 0.25e^{-A}$ and $P_t(A) = -0.03A + 0.12$.

The second term in the right hand is a first order derivative. An analytic function, $P_t(A)$ is needed to solve it. One way to do this, is prepare a plot of $P_t(x, 0)$ versus $A(x, 0)$ and fit an exponential curve used in the reconstruction as was shown in Figure D.4(a).

The first derivative of the exponential function is an initial condition that is used along all reconstruction. In Figure D.4(a) the curve shown as a solid black line represents a least squares fitting polynomial exponential function. The fitted exponential function was $P_t(A) = 0.51 + 0.10e^{-\frac{5}{2}A} - 0.43e^{-A}$. But, the great values of P_t could create singular points (the problem is ill-posed), affecting to make a correct reconstruction. Then, starting with the last value of $A(x, 0)$, from the right plot, we set a sequence of tangent lines to the curve until the slope has a negative value. Thus, in Figure D.4(b) was presented a fitted by an exponential polynomial (black line: $P_t(A) = 0.29 + 0.08e^{-\frac{5}{2}A} - 0.25e^{-A}$) with linear tails (red

line: $P_t(A) = -0.03A + 0.12$). Similar to Hau and Sonnerup (1999) the adjust shown in Figure D.4(b) was used in this reconstruction. However, the adjusting mathematical expressions are not offered by them. The way to make this adjust has been improved in subsequent articles (HU; SONNERUP, 2003), but that issue is not addressed here.

11) Interpolation using cubic splines:

Interpolation of the data is performed by use of a cubic spline to generate spatial increments Δx suitable for the integration. $\Delta x = |(x_0 - x_N)|/\tilde{N}$ where $\tilde{N} = 128$ is the number of interpolation points between each original sample. The interpolations using the cubic spline was shown in Figure D.5. Format of the Figure D.5 is the same as in Figure D.3.

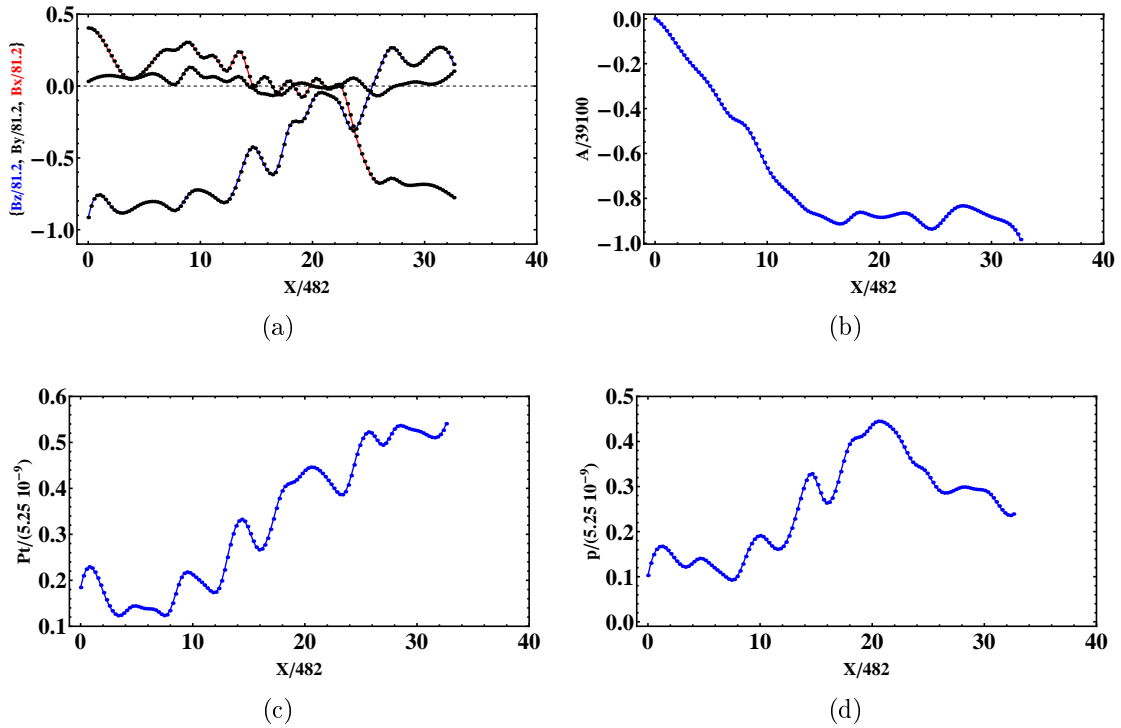


Figure D.5 - Analysis results for AMPTE/IRM event, October 19, 1984, in the interval 05 : 17 : 41 – 05 : 19 : 48 UT for optimal angle, $\theta = -40^\circ$, of invariant (z) axis. Format is the same as in Figure D.3, but an interpolation ($\tilde{N} = 128$) of the data is performed by use of a cubic spline to generate spatial increments Δx suitable for the integration. (a) B_X, B_Y, B_Z projection in GS system (xyz) vs x ; (b) A at $y = 0$ as a function of x ; (c) Transverse pressure P_t as a function of x ; (d) Plasma pressure p as a function of x .

12) **Grad-Shafranov Solver:**

The Grad-Shafranov equation with $A(x, 0)$, $(\partial A/\partial x)_{x,0} = -B_y(x, 0)$, $(\partial^2 A/\partial x^2)_{x,0}$, $(\partial A/\partial y)_{x,0} = B_x(x, 0)$, and $[d(p + B_z^2/2\mu_0)/dA]_{x,0}$ as input data can be resolved. The GS solver generates a map of $A(x, y)$ around the spacecraft trajectory (x axis) with $-y_{max} < y < y_{max}$. In Appendix C a detailed discussion about the numerical resolution of GS equation using an analytical solution is presented. The improvement of the error in the numerical solution is a novel result presented in this thesis (see Appendix C).

13) **Optimal choice of rotation angle (θ):**

Apply the criteria for optimal choice of z axis, as described at the end of section 2.2 of Hau and Sonnerup (1999) and improvement in Hu and Sonnerup (2003). If these criteria appear to be poorly met, return to step 6, select a new angle θ for rotation of \hat{z} about the normal vector \vec{n} , and repeat the calculation (HAU; SONNERUP, 1999).

APPENDIX E - FINITE DIFFERENCES SCHEME

The approximation of derivatives by finite differences plays a central role in finite difference methods for the numerical solution of differential equations. If the spacing Δx is constant. If the 4th-order Taylor expansion with $x_i = i\Delta x$ is used. A forward differences to A_{i+1} , A_{i+2} and A_{i+3} with $x - x_0 = (\Delta x, 2\Delta x, 3\Delta x)$ in i are respectively:

$$\begin{aligned} A_{i+1} &= A_i + A_x|_i \Delta x + \frac{1}{2} A_{xx}|_i \Delta x^2 + \frac{1}{6} A_{xxx}|_i \Delta x^3 + O(\Delta x^4) \\ A_{i+2} &= A_i + 2A_x|_i \Delta x + \frac{4}{2} A_{xx}|_i \Delta x^2 + \frac{8}{6} A_{xxx}|_i \Delta x^3 + O(\Delta x^4) \\ A_{i+3} &= A_i + 3A_x|_i \Delta x + \frac{9}{2} A_{xx}|_i \Delta x^2 + \frac{27}{6} A_{xxx}|_i \Delta x^3 + O(\Delta x^4). \end{aligned}$$

The above equations can be written as a system of equations:

$$\begin{aligned} \frac{1}{6} A_{xxx}|_i \Delta x^3 + A_x|_i \Delta x + \frac{1}{2} A_{xx}|_i \Delta x^2 &= A_{i+1} - A_i + O(\Delta x^4) \\ \frac{8}{6} A_{xxx}|_i \Delta x^3 + 2A_x|_i \Delta x + \frac{4}{2} A_{xx}|_i \Delta x^2 &= A_{i+2} - A_i + O(\Delta x^4) \\ \frac{27}{6} A_{xxx}|_i \Delta x^3 + 3A_x|_i \Delta x + \frac{9}{2} A_{xx}|_i \Delta x^2 &= A_{i+3} - A_i + O(\Delta x^4). \end{aligned}$$

To solve the system, it can be written in matrix form:

$$\left[\begin{array}{ccc|c} 1/6 & 1 & 1/2 & A_{i+1} - A_i + O(\Delta x^4) \\ 8/6 & 2 & 4/2 & A_{i+2} - A_i + O(\Delta x^4) \\ 27/6 & 3 & 9/2 & A_{i+3} - A_i + O(\Delta x^4). \end{array} \right]$$

After adding and subtracting rows of the matrix, the system is:

$$\left[\begin{array}{ccc|c} 1/6 & 1 & 1/2 & A_{i+1} - A_i + O(\Delta x^4) \\ 0 & 6 & 4/2 & 8A_{i+1} - 7A_i - A_{i+2} + O(\Delta x^4) \\ 0 & 0 & -1 & 5A_{i+1} - 4A_{i+2} + A_{i+3} - 2A_i + O(\Delta x^4), \end{array} \right]$$

then the 3th row is the second-order Taylor expansion for forward differentiation at point i :

$$(\partial^2 A / \partial x^2)_i = (2A_i - 5A_{i+1} + 4A_{i+2} - A_{i+3}) / (\Delta x)^2 + O(\Delta x^2) \quad (\text{E.1})$$

On the other hand a backward differences to A_{i-1} , A_{i-2} and A_{i-3} with $x - x_0 =$

$(-\Delta x, -2\Delta x, -3\Delta x)$ in i are respectively:

$$\begin{aligned} A_{i-1} &= A_i - A_x|_i \Delta x + \frac{1}{2} A_{xx}|_i \Delta x^2 - \frac{1}{6} A_{xxx}|_i \Delta x^3 + O(\Delta x^4) \\ A_{i-2} &= A_i - 2A_x|_i \Delta x + \frac{4}{2} A_{xx}|_i \Delta x^2 - \frac{8}{6} A_{xxx}|_i \Delta x^3 + O(\Delta x^4) \\ A_{i-3} &= A_i - 3A_x|_i \Delta x + \frac{9}{2} A_{xx}|_i \Delta x^2 - \frac{27}{6} A_{xxx}|_i \Delta x^3 + O(\Delta x^4). \end{aligned}$$

Similarly to the previous case:

$$\left[\begin{array}{ccc|c} -1/6 & -1 & 1/2 & A_{i-1} - A_i + O(\Delta x^4) \\ -8/6 & -2 & 4/2 & A_{i-2} - A_i + O(\Delta x^4) \\ -27/6 & -3 & 9/2 & A_{i-3} - A_i + O(\Delta x^4), \end{array} \right]$$

$$\left[\begin{array}{ccc|c} -1/6 & -1 & 1/2 & A_{i-1} - A_i + O(\Delta x^4) \\ 0 & 6 & -4/2 & A_{i-2} - 8A_{i-1} + 7A_i + O(\Delta x^4) \\ 0 & 0 & -1 & A_{i-3} - 4A_{i-2} + 5A_{i-1} - 2A_i + O(\Delta x^4), \end{array} \right]$$

then the 3th row is the second-order Taylor expansion for backward differentiation at point i :

$$(\partial^2 A / \partial x^2)_i = (2A_i - 5A_{i-1} + 4A_{i-2} - A_{i-3}) / (\Delta x)^2 + O(\Delta x^2) \quad (\text{E.2})$$

To obtain the central difference of 2th-order for A_x and A_{xx} at point i , we add and subtract the following equations:

$$\begin{aligned} A_{i+1} &= A_i + A_x|_i \Delta x + \frac{1}{2} A_{xx}|_i \Delta x^2 + \frac{1}{6} A_{xxx}|_i \Delta x^3 + O(\Delta x^4) \\ A_{i-1} &= A_i - A_x|_i \Delta x + \frac{1}{2} A_{xx}|_i \Delta x^2 - \frac{1}{6} A_{xxx}|_i \Delta x^3 + O(\Delta x^4) \end{aligned}$$

The results are:

$$(\partial A / \partial x)_i = (A_{i+1} - A_{i-1}) / (2\Delta x) + O(\Delta x^2) \quad (\text{E.3})$$

$$(\partial^2 A / \partial x^2)_i = (A_{i+1} - 2A_i + A_{i-1}) / (\Delta x)^2 + O(\Delta x^2) \quad (\text{E.4})$$

We listed in the Table E.1 the coefficients of the finite difference formula until second order derivative, and eighth order of accuracy for a discrete function at point i .

Table E.1 - Coefficients of central finite difference formulas on uniform grid.

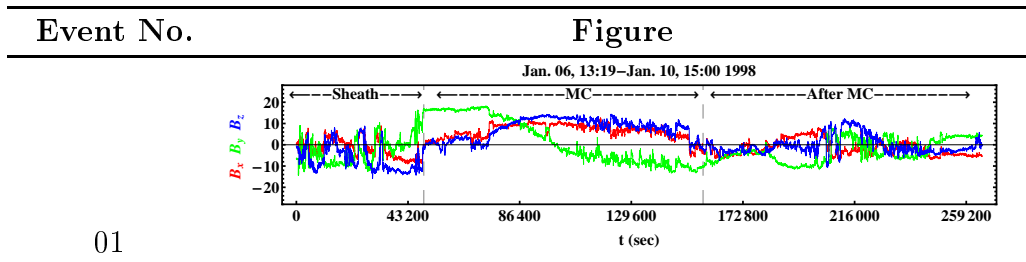
	$i-4$	$i-3$	$i-2$	$i-1$	i	$i+1$	$i+2$	$i+3$	$i+4$
<i>1st derivative</i>									
2				$-\frac{1}{2}$	0	$\frac{1}{2}$			
4			$\frac{1}{12}$	$-\frac{2}{3}$	0	$\frac{2}{3}$	$-\frac{1}{12}$		
6		$-\frac{1}{60}$	$\frac{3}{20}$	$-\frac{3}{4}$	0	$\frac{3}{4}$	$-\frac{3}{20}$	$\frac{1}{60}$	
8	$\frac{1}{290}$	$-\frac{1}{105}$	$\frac{1}{5}$	$-\frac{4}{5}$	0	$\frac{4}{5}$	$-\frac{1}{5}$	$\frac{60}{105}$	$-\frac{1}{280}$
<i>2nd derivative</i>									
2				1	-2	1			
4			$-\frac{1}{12}$	$\frac{4}{3}$	$-\frac{5}{2}$	$\frac{4}{3}$	$-\frac{1}{12}$		
6		$\frac{1}{90}$	$-\frac{20}{3}$	$\frac{3}{8}$	$-\frac{49}{205}$	$\frac{3}{8}$	$-\frac{1}{3}$	$\frac{1}{90}$	
8	$-\frac{1}{560}$	$\frac{90}{315}$	$-\frac{1}{5}$	$\frac{2}{5}$	$-\frac{18}{72}$	$\frac{2}{5}$	$-\frac{1}{5}$	$\frac{90}{315}$	$-\frac{1}{560}$

ANNEX A - LISTS OF MCs STUDIED

Table A.1 - Solar wind data studied (from Huttunen et al. (2005)).

No.	Year	Shock	UT	MCstart	UT	MCstop	UT	AfterMC	UT
01	1998	06 Jan	13:19	07	03:00	08	09:00	10	15:00
02		03 Feb	13:09	04	05:00	05	14:00	06	23:00
03		04 Mar	11:03	04	15:00	05	21:00	07	03:00
04		01 May	21:11	02	12:00	03	17:00	04	22:00
05		13 Jun	18:25	14	02:00	14	24:00	15	22:00
06		19 Aug	05:30	20	08:00	21	18:00	23	04:00
07		24 Sep	23:15	25	08:00	26	12:00	27	16:00
08		18 Oct	19:00	19	04:00	20	06:00	21	08:00
09		08 Nov	04:20	08	23:00	10	01:00	12	02:00
10		13 Nov	00:53	13	04:00	14	06:00	15	08:00
11	1999	18 Feb	02:08	18	14:00	19	11:00	20	08:00
12		16 Apr	10:47	16	20:00	17	18:00	18	16:00
13		08 Aug	17:45	09	10:00	10	14:00	11	18:00
14	2000	11 Feb	23:23	12	12:00	12	24:00	13	12:00
15		20 Feb	20:57	21	14:00	22	12:00	23	10:00
16		11 Jul	11:22	11	23:00	13	02:00	14	05:00
17		13 Jul	09:11	13	15:00	13	24:00	14	09:00
18		15 Jul	14:18	15	19:00	16	12:00	17	05:00
19		28 Jul	05:53	28	18:00	29	10:00	30	02:00
20		10 Aug	04:07	10	20:00	11	08:00	11	20:00
21		11 Aug	18:19	12	05:00	13	02:00	13	23:00
22		17 Sep	17:00	17	23:00	18	14:00	19	05:00
23		02 Oct	23:58	03	15:00	04	14:00	05	13:00
24		12 Oct	21:36	13	17:00	14	13:00	15	09:00
25		28 Oct	09:01	28	24:00	29	23:00	30	22:00
26		06 Nov	09:08	06	22:00	07	15:00	08	08:00
27	2001	19 Mar	10:12	19	22:00	21	23:00	23	24:00
28		27 Mar	17:02	27	22:00	28	05:00	28	12:00
29		11 Apr	15:18	12	10:00	13	06:00	14	02:00
30		21 Apr	15:06	21	23:00	22	24:00	24	01:00
31		28 Apr	04:31	28	24:00	29	13:00	30	02:00
32		27 May	14:17	28	11:00	29	06:00	30	01:00
33		31 Oct	12:53	31	22:00	02	04:00	03	10:00
34	2002	23 Mar	10:53	24	10:00	25	12:00	26	14:00
35		17 Apr	10:20	17	24:00	19	01:00	20	02:00
36		18 May	19:44	19	04:00	19	22:00	20	16:00
37		01 Aug	23:10	02	06:00	02	22:00	03	14:00
38		30 Sep	07:55	30	23:00	01	15:00	02	07:00
39	2003	20 Mar	04:20	20	13:00	20	22:00	21	07:00
40		17 Aug	13:41	18	06:00	19	11:00	20	16:00
41		20 Nov	07:27	20	11:00	21	01:00	22	15:00

Table A.2 - Graphics of events shown in Table A.1.



(Continues)

Table A.2 - Continuation

No.	Figure
02	
03	
04	
05	
06	
07	
08	

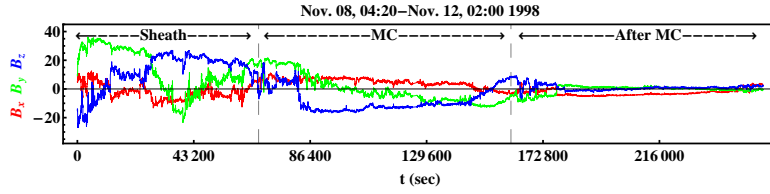
(Continues)

Table A.2 - Continuation

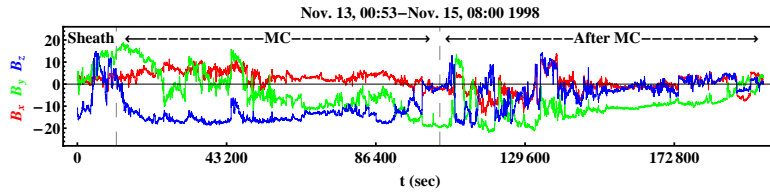
No.

Figure

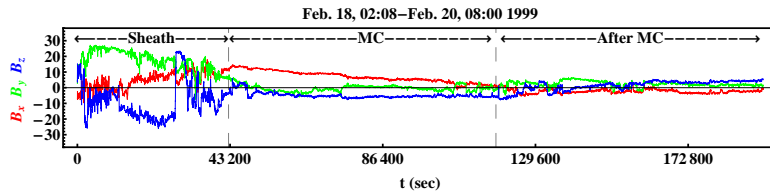
09



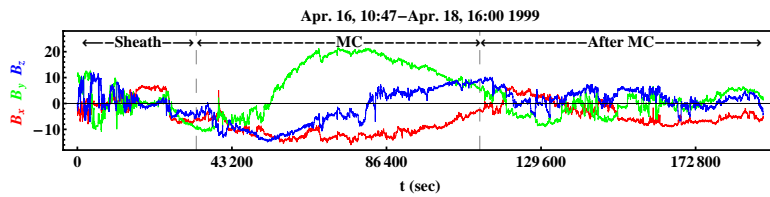
10



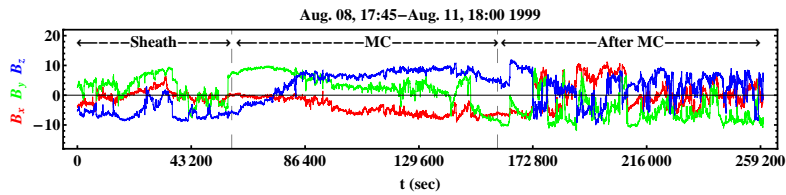
11



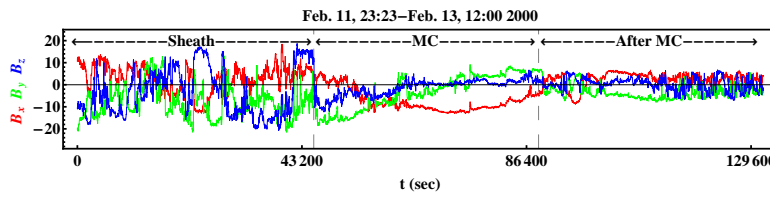
12



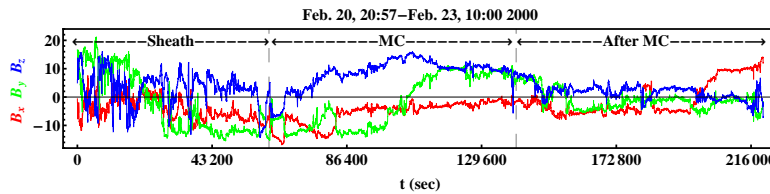
13



14



15



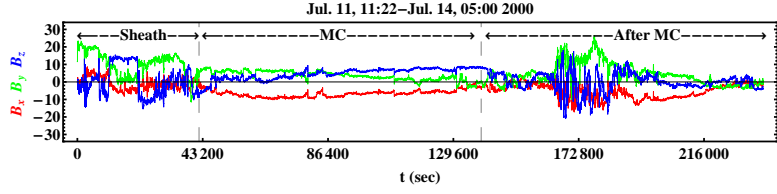
(Continues)

Table A.2 - Continuation

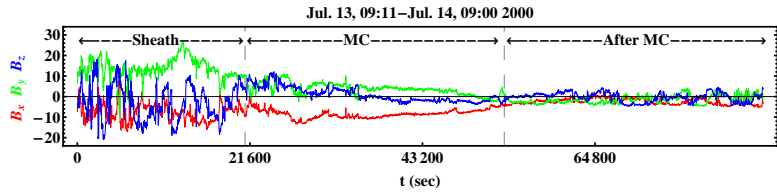
No.

Figure

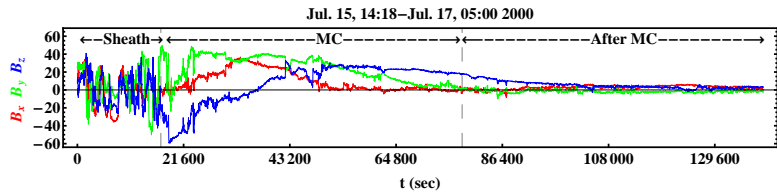
16



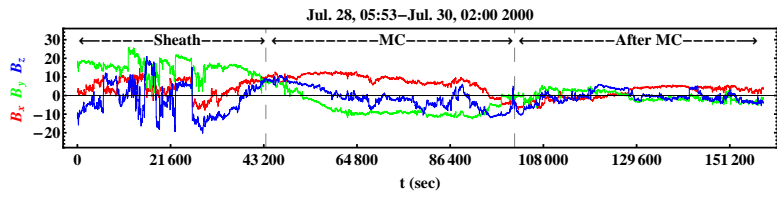
17



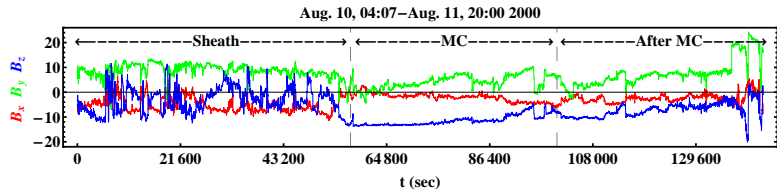
18



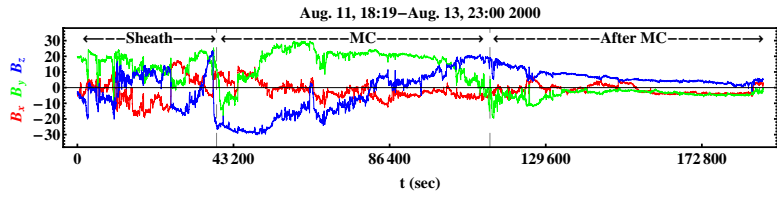
19



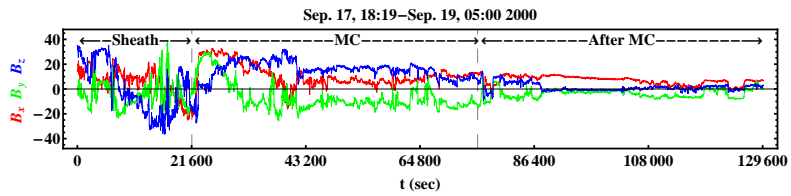
20



21



22



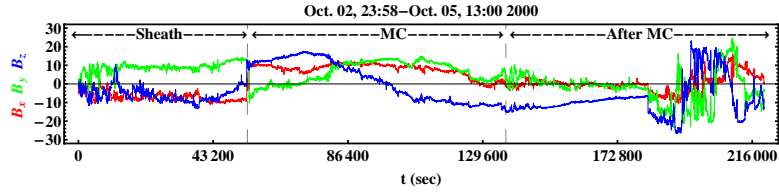
(Continues)

Table A.2 - Continuation

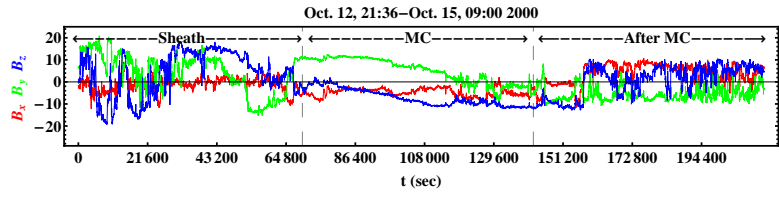
No.

Figure

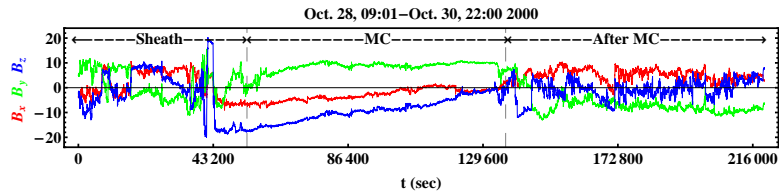
23



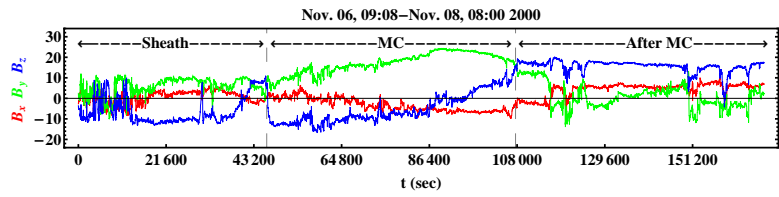
24



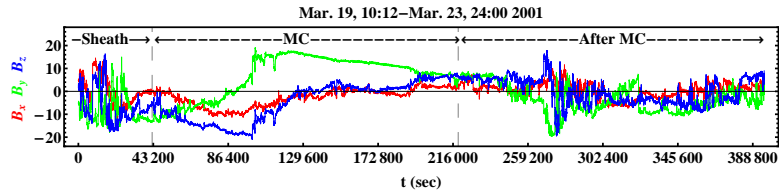
25



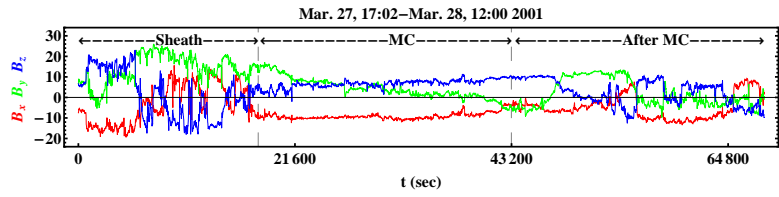
26



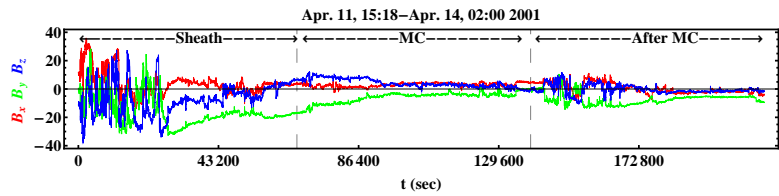
27



28



29

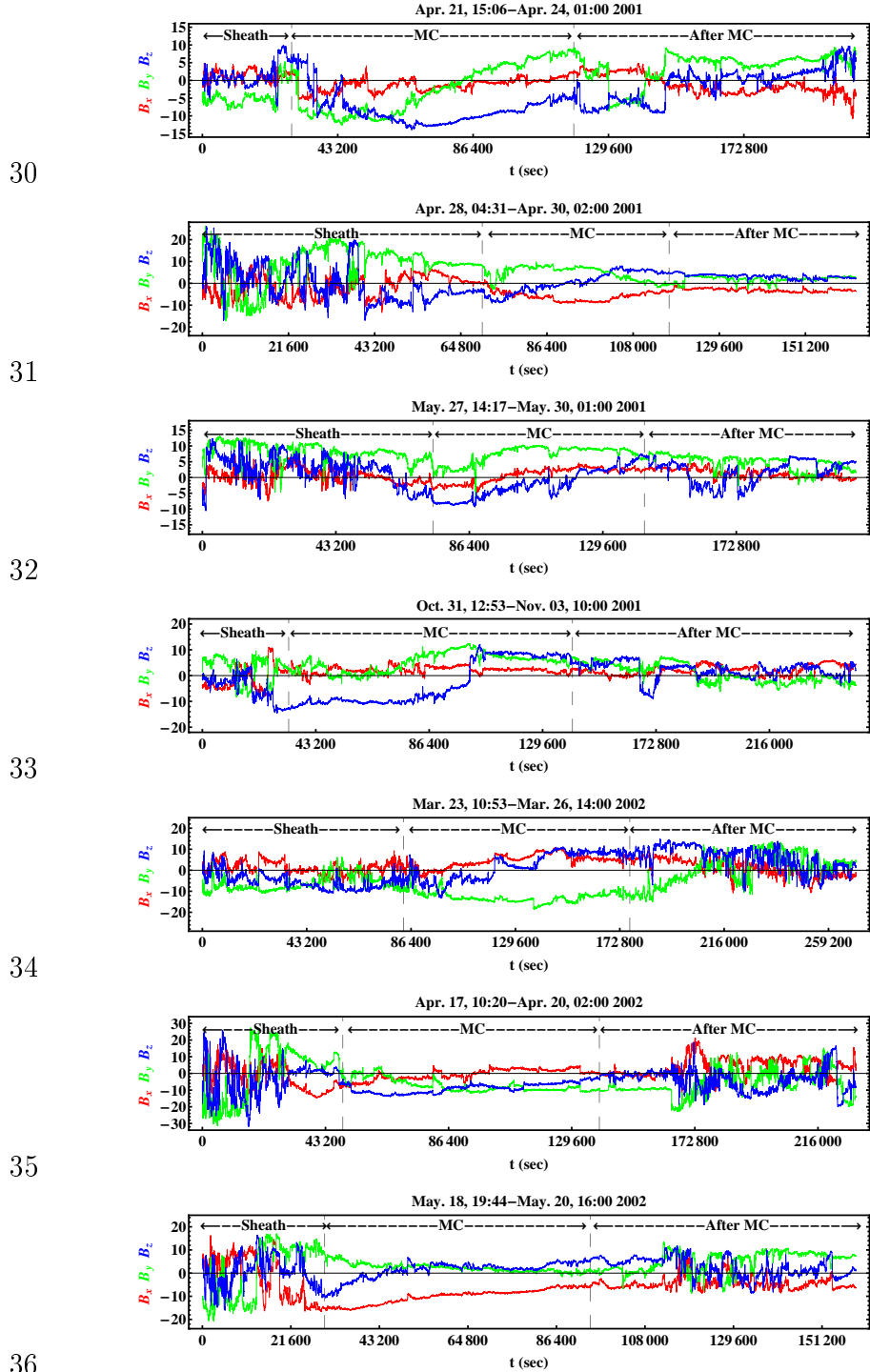


(Continues)

Table A.2 - Continuation

No.

Figure

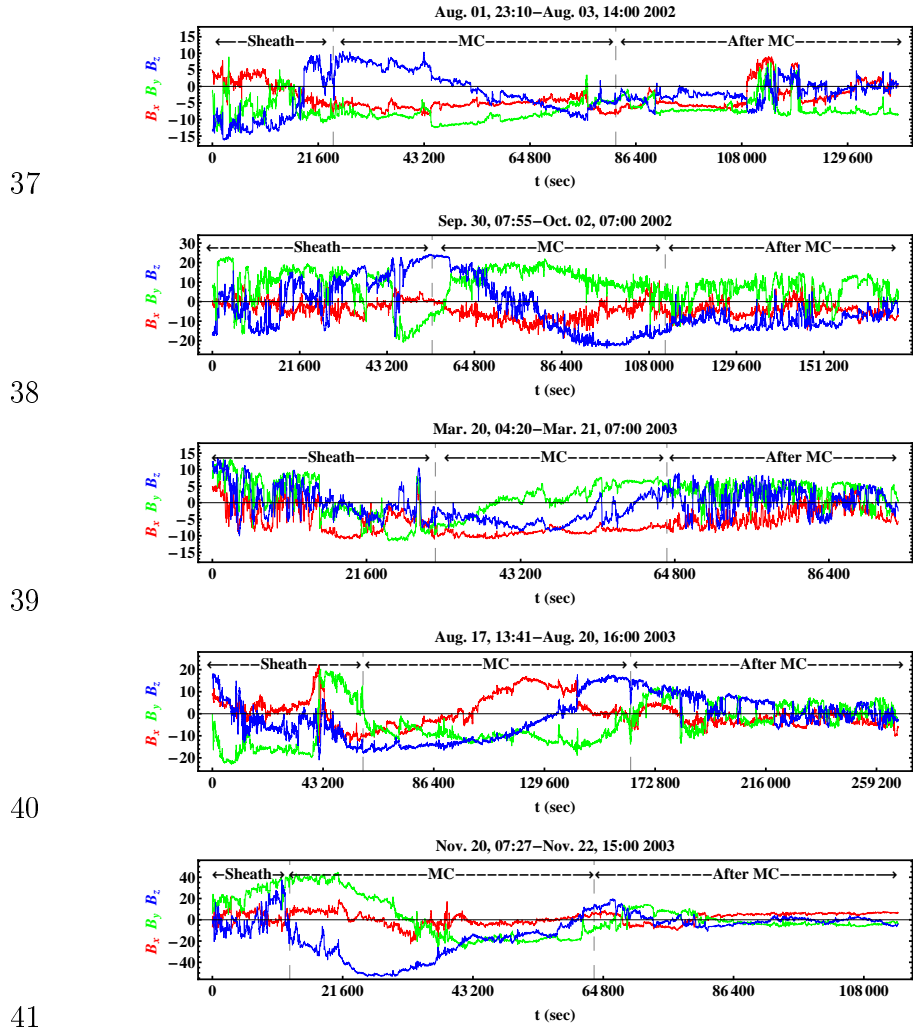


(Continues)

Table A.2 - Continuation

No.

Figure



END

Table A.3 - MC events measured by WIND (not examined). Letter “Q” denotes whether the event was an MC (l) or cloud candidate (cl).

No.	Year	Shock, UT	MC start, UT	MC stop, UT	Q
01	1997	10 Jan, 00:20	10 Jan, 05:00	11 Jan, 02:00	l
02		09 Feb, 23:43	10 Feb, 03:00	10 Feb, 19:00	cl
03		10 Apr, 12:57	11 Apr, 08:00	11 Apr, 16:00	l
04		-	21 Apr, 17:00	22 Apr, 24:00	cl
05		15 May, 00:56	15 May, 10:00	15 May, 24:00	l
06		-	15 May, 07:00	16 May, 16:00	l
07		26 May, 09:10	26 May, 16:00	27 May, 19:00	l
08		-	09 Jun, 06:00	09 Jun, 23:00	l
09		19 Jun, 00:12	19 Jun, 06:00	19 Jun, 16:00	l
10		-	15 Jul, 09:00	16 Jul, 06:00	l
11		-	03 Aug, 14:00	04 Aug, 02:00	l
12		-	18 Sep, 03:00	19 Sep, 21:00	l
13		-	22 Sep, 01:00	22 Sep, 18:00	l
14		01 Oct, 00:20	01 Oct, 15:00	02 Oct, 22:00	l
15		10 Oct, 15:48	10 Oct, 23:00	12 Oct, 01:00	l
16		06 Nov, 22:07	07 Nov, 05:00	08 Nov, 03:00	l
17		22 Nov, 08:55	22 Nov, 19:00	23 Nov, 12:00	l

Table A.4 - MC events not preceded by shock waves. Letter “Q” denotes whether the event was an MC (l) or cloud candidate (cl).

No.	Year	Shock, UT	MC start, UT	MC stop, UT	Q
01	1998	-	17 Feb, 10:00	18 Feb, 04:00	l
02		-	02 Jun, 10:00	02 Jun, 16:00	l
03		-	24 Jun, 12:00	25 Jun, 16:00	l
04	1999	-	25 Mar, 16:00	25 Mar, 23:00	l
05		-	21 Apr, 12:00	22 Apr, 13:00	l
06		-	22 Aug, 12:00	23 Aug, 06:00	l
07		-	21 Sep, 20:00	23 Sep, 05:00	l
08		-	14 Nov, 01:00	14 Nov, 09:00	cl
09		-	16 Nov, 09:00	16 Nov, 23:00	l
10	2000	-	15 Jul, 05:00	15 Jul, 14:00	cl
11		-	31 Jul, 22:00	01 Aug, 12:00	l
12	2001	-	04 Mar, 16:00	05 Mar, 01:00	l
13		-	18 Jun, 23:00	19 Jun, 14:00	l
14		-	10 Jul, 17:00	11 Jul, 23:00	l
15		03 Oct, 08:??	03 Oct, 01:00	03 Oct, 16:00	l
16		-	24 Nov, 17:00	25 Nov, 13:00	cl
17	2002	-	28 Feb, 18:00	01 Mar, 10:00	l
18		-	19 Mar, 22:00	20 Mar, 10:00	l
19		-	20 Apr, 13:00	21 Apr, 15:00	l
20		23 May, 10:15	23 May, 22:00	24 May, ??:??	cl
21	2003	-	27 Jan, 01:00	27 Jan, 15:00	l
22		-	29 Oct, 12:00	30 Oct, 01:00	l

Table A.5 - Four MCs events identified by [Huttunen et al. \(2005\)](#). In this work, we studied these events. The columns from the left to the right give: year, month, shock time (UT), MC start time (UT), MC end time (UT), inferred flux-rope type, direction of the MC axis (ϕ_C , θ_C).

Year	Mon	Shock	Start	Stop	type	ϕ_C	θ_C
1998	Jan	06,13:19	07,03:00	08,09:00	ENW	21	52
1998	Aug	19,05:30	20,08:00	21,18:00	SWN	113	-16
1999	Feb	18,02:08	18,14:00	19,11:00	NWS	96	6
2000	Oct	12,21:36	13,17:00	14,13:00	NES	33	-25

Table A.6 - The date of solar wind intervals studied in this work. The intervals are presented in the order that it appear in the paper. The columns from the left to the right give: year, month, solar wind star time interval, solar wind stop time interval, coordinates system, total of windows of 11.11 hours in the intervals.

Year	Month	Start	Stop	Sist	Windows
1998	Jan	03,00:00	12,23:59	GSM	258
1999	Oct	20,00:00	25,23:59	GSM	150
1999	Feb	14,00:00	23,23:59	GSM	258
1998	Aug	15,00:00	24,23:59	GSM	258
2000	Oct	08,00:00	17,23:59	GSM	258
2010	Apr	01,00:00	10,23:59	GSE	258

ANNEX B - HANDBOOK FOR GRAD-SHAFRANOV RECONSTRUCTION OF MAGNETIC FLUX ROPES

Handbook for Grad-Shafranov reconstruction of magnetic flux ropes

Christian Möstl¹ and Charles J. Farrugia²

¹Space Research Institute, Graz, Austria, <http://www.uni-graz.at/~moestlc/>

²University of New Hampshire, NH, USA

based on the code by Qiang Hu, now at University of Alabama at Huntsville

last update: 12 November 2010

1. Introduction	2
2. Quick start	4
3. Example for analysing a new event.....	0
4. Literature.....	10

The MATLAB program package can be downloaded as a zip file (~6 MB) from:

ftp://ftp.iwf.oeaw.ac.at/pub/moestl/public_gs_code/

For a Quickstart to MATLAB, take a look at the tutorials in the program help or online at

<http://www.mathworks.com/help/techdoc/index.html>

Please mail questions to christian.moestl@oeaw.ac.at

if they are of general interest I will put them here, including the answers:

(Question space ;-)

If this code is to be used as part of a scientific publication, please include us as co-authors.

Introduction

The **Grad-Shafranov (GS) reconstruction method** has recently become widely used in the space physics community in different contexts. It has been invented about 10 years ago by a group around Prof. Sonnerup at Dartmouth University and has since become widely accepted. It has been often used on structures in space plasmas which can be described in the approximation of magnetohydrostatics such as the magnetopause, flux transfer events, flux ropes in the Earth's magnetotail, as well as magnetic flux ropes and magnetic clouds in the solar wind. Its main point is to assume **invariance and time-independency** so the MHD equations in equilibrium, including plasma pressure, can simply be numerically integrated as an initial

value problem. There exist some variations of the basic method (see Sonnerup, 2006, JGR, and recent papers by e.g. Teh et al.), however, this document is restricted to its use on magnetic flux ropes in the solar wind in the version of Hu and Sonnerup (2002).

Where the programs come from

In this document a program package in MATLAB is described as a basis for learning the method and for future reference and deals with the use of the method on in situ data of any kind of magnetic flux ropes. These programs are based on those used by Qiang Hu for his 2002 JGR paper (for references see below) which were part of his PhD thesis at Dartmouth university. They were extended by Christian Möstl (Space Research Institute, Graz, Austria) during his PhD thesis (finished in 2009) to include a graphical user interface (GUI), which makes it easy to apply the reconstruction method for a single event after the satellite data have been put into a proper format. For a quick start, there are some events included in this package to play around with, so you can omit the next step if you want.

If you want to use your own events:

A program to read merged plasma and magnetic field data from the ACE satellite is provided: "getace.m".

This program converts the ACE data files obtained from

ftp://nssdcftp.gsfc.nasa.gov/spacecraft_data/ace/4_min_merged_mag_plasma/

to a proper format which can be read by the reconstruction programs. By all means please take a look at the readme file provided with these data! To keep the file size of the package low, please download the ACE data yourself (~230 MB) from the source above into the directory "ACEDATA\4_min_merged_mag_plasma" relative to the "root" path. I have included in this package the merged ACE Data for the **years 2003 and 2004 only**. The files produced by "getace.m" are saved as MATLAB internal data files ".mat" in the subdirectory "ACEDATA" relative to the root.

Current state of research

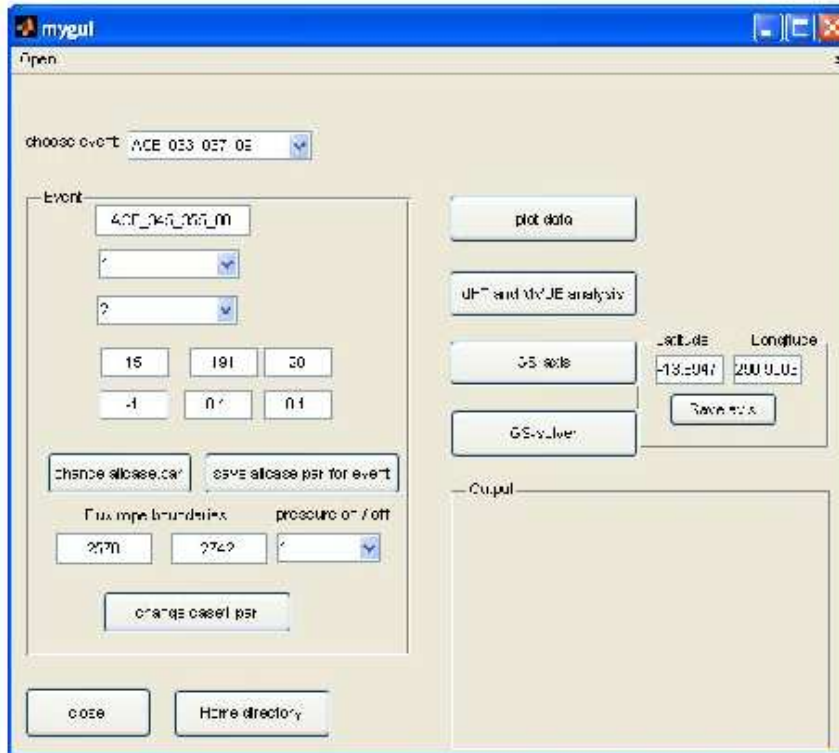
The technique has been introduced for MCs/MFRs (magnetic clouds and magnetic flux ropes) in the solar wind, applied to many MC/MFR events (including multiple ropes) and extended to multi-spacecraft observations. Research is under way on its application to magnetic clouds for a full solar cycle and extensive testing using different numerical and analytical solutions has started. Additionally, this code presented here serves as a basis to make 2 necessary future extensions:

(1) including the often observed expansion of MCs (2) making the 2.5D invariant model a bent flux rope in 3D.

Quick start

The programs can be unzipped to any desired folder. **The path to this folder, lets call it the "root", should then be added to the MATLAB paths under "File"-> "Set Path" without subfolders (this is important).** Be sure to change directory inside MATLAB to the "root" folder before running the gui. A graphical user interface can now be started by **typing "mygui" in the MATLAB command line.**

A window pops up which looks like this:



Under the menu point "open" another gui (acegui) can be opened to plot data from ACE and create new events (see below how to use getace.m)

Choose Event: This scroll down menu shows a list of all the folders which have the correct name format in the present directory.
 Select the event which you would like to analyse further - switching between different events is thus very easy.
 The format is always "spacecraft_day of year (begin)_day of year (end)_ year (two digits)."
 If a new event directory has been generated by using "the

getace.m program",
the gui has to be started again (click the close button and restart).

Try to choose the event ACE_323_325_03 for a start; the run all the programs beginning from "plot data" downwards with the pre-installed parameters so you see how a good reconstruction looks like.

Event: This box shows all information necessary for controlling the programs to the right.

The parameters in the upper part, i.e.

1
2
15 191 20
-1 0.1 0.1

control the GS-solver program (see below).

The flux rope boundaries (in data points) can be adjusted in the bottom part.

Also the pressure can be set to on/off by setting the pulldown menu to 1 or 0.

You need to press "change case1.par" to make the changes effective.

(Example: press "plot data"; try changing the boundaries; press "change case1.par" ; press "plot data" again.)

The boundaries are selected by clicking twice while using the getace program (in write mode, see below).

Plot data: plots a data figure onscreen as well as a an eps output of this figure.

dhT and MVUB analysis: carries out these analyses of course (i.e. deHoffmann Teller and Minimum Variance) ;-)

The minimum variance direction is the first approximation to search for the GS axis.

GS axis This is basically the core of the method and the most complex part. The Pt(A) function is searched to be single-valued. This orientation is then the subsequent flux rope axis. Wait until a residue map is generated. (see Hu and Sonnerup, 2002).

Click left on the plot to check a given direction. Click right anywhere and the direction with the black dot is used.

(Note: if you want any other direction than the "black dot" click left, note the orientation (command window) and click right; you can then "force" the GS solver to use your own axis by typing it into "Latitude" and "Longitude" on the right in mygui.)

GS-Solver: Creates a magnetic field map perpendicular to the invariant axis and a nice version of the Pt(A) plot as .eps files.

To control this program some parameters in the Event box can be set manually:

```
1          % if the reconstruction should be done with
plasma pressure (1) or without (0); default=0
2          % the order of the fitting polynomial for Pt(A)
- usually 2 (experience showed that its better to use a lower one).
15 191 20   %15 is the grid size in the x direction; 191 in
the y direction (can be varied); 20 is an offset of the spacecraft
-1 0.1 0.1  % -1/0/1 controls the boundary Ab ; 0.1 and
0.1 control the overlapping of the polynomial with the exponential functions
          % i.e. higher values result in suppressing the
polynomial more and more (play with it).
```

see also Möstl et al. 2009 (Solar Physics) for more info.

The boundary Ab is the white contour in the magnetic field map and indicates where the single-valuedness of Pt(A) breaks down.

0: lets you set the boundary with a left-click of the mouse

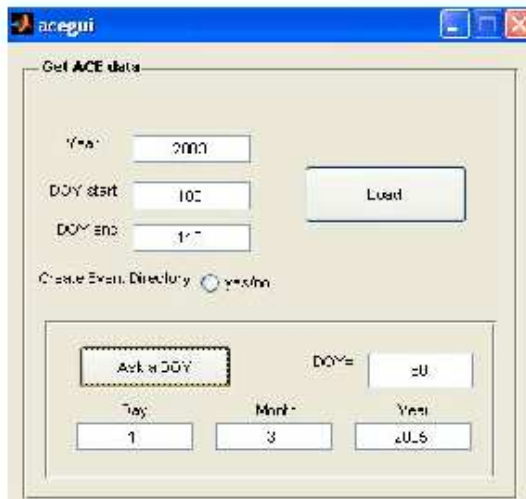
1: indicates that for calculating the axial flux and the axial current everything to the right of Ab is counted.

-1: flux and current calculated but everything left of Ab (in Pt(A)) is counted

(This just says that if the maximum of Pt is positive/negative in A, Ab has to be set to +1/-1, respectively, to get the correct flux and current)

How to use getace.m:

you can either use this nice GUI by using Ctrl+A or the open tab in mygui:



here you can ask for a DOY if you know the date but not the DOY of a particular event.

or directly in the command line, type for example

```
>> getace(2004,312,316,0)
```


to see an in situ plot from the year 2004 from days of year 312-316 of 2 magnetic clouds unleashed by the same active region on the Sun in November 2004 (if you want to know what was going on there, check out the paper

Harra et al. 2007, Solar Physics, DOI 10.1007/s11207-007-9002-x). If you want to check your reconstruction results for one of these magnetic clouds, take a look at Qiu et al. (2007, ApJ, see below).

Setting the last variable to **"0"** means that **only the figure is created and nothing is saved. A "1" setting indicates that an event directory (in this "ACE_312_316_04") created for further reconstruction** using the GUI and that the converted data is saved in the "DATA" directory. Then you must also set boundaries of the magnetic flux rope interval by clicking with the left mouse button, first to the left, then to the right. This can be changed later again by using the same command with which you called "getace.m". If you now start the GUI, you should be able to see the event in the "choose event" scroll down menu.

try
>> help getace
to see a summary.

Typical error handling:

- If the gui does not start, check if you are in the "root" directory. It might be necessary to type

```
>> cd ..
```

to change the directory back to the root for the next try.

- if something doesn't work after clicking a button, try clicking "Home directory" at the bottom.

- If you kill a figure manually while a program runs, it crashes and maybe you are left in the wrong directory.

Then the next program will crash if it looks for a file which isn't there.

In any other case, kill the gui and restart. Restart MATLAB in tough cases ;-).

**- if there are too many open windows, type
>> close all**

Typing

>> help mygui

results in a quick start help.

Literature

The central paper which describes in detail everything that's necessary to know about GS reconstruction on flux ropes is

Q. Hu and B. U. Ö. Sonnerup. "Reconstruction of magnetic clouds in the solar wind: Orientations and configurations". *Journal of Geophysical Research (Space Physics)* 107 (2002) 10–1.

A selected list of refereed papers in major journals where the technique has been introduced for MCs/MFRs in the solar wind, applied to many MC/MFR events (including multiple ropes) and extended to multi-spacecraft observations:

Q. Hu and B. U. Ö. Sonnerup. "Reconstruction of magnetic flux ropes in the solar wind". *Geophys. Res. Lett.* 28 (2001) 467–470.

Q. Hu, C. W. Smith, N. F. Ness, and R. M. Skoug. "Multiple flux rope magnetic ejecta in the solar wind". *Journal of Geophysical Research (Space Physics)* 109 (2004) 3102.

Q. Hu, C. W. Smith, N. F. Ness, and R. M. Skoug. "On the magnetic topology of October/November 2003 events". *Journal of Geophysical Research (Space Physics)* 110 (2005).

J. Qiu, Q. Hu, T. A. Howard, and V. B. Yurchyshyn. "On the Magnetic Flux Budget in Low-Corona Magnetic Reconnection and Interplanetary Coronal Mass Ejections". *ApJ* 659 (2007) 758–772.

Y. Liu, J. G. Luhmann, K. E. J. Huttunen, R. P. Lin, S. D. Bale, C. T. Russell, and A. B. Galvin. "Reconstruction of the 2007 May 22 Magnetic Cloud: How Much Can We Trust the Flux-Rope Geometry of CMEs?" *ApJL* 677 (2008) L133–L136.

C. Möstl, C. Miklenic, C. J. Farrugia, M. Temmer, A. Veronig, A. B. Galvin, B. Vrsnak, and H. K. Biernat. "Two-spacecraft reconstruction of a magnetic cloud and comparison to its solar source". *Annales Geophysicae*, 26 (2008) 3139–3152.

C. Möstl, C. J. Farrugia, H. K. Biernat, M. Leitner, E. K. J. Kilpua, A. B. Galvin, and J. G. Luhmann. "Optimized Grad-Shafranov Reconstruction of a Magnetic Cloud Using STEREO- Wind Observations". *Sol. Phys.* 256 (2009) 427–441.

C. Möstl, C. J. Farrugia, M. Temmer, C. Miklenic, A. M. Veronig, A. B. Galvin, M. Leitner, and H. K. Biernat. "Linking Remote Imagery of a Coronal Mass Ejection to Its In Situ Signatures at 1 AU". *ApJL* 705 (2009) L180–L185.

Möstl, C., C. J. Farrugia, C. Miklenic, M. Temmer, A. B. Galvin, J.G. Luhmann, K.E.J. Huttunen, M. Leitner, T. Nieves-Chinchilla, A. Veronig and H.K. Biernat, Multi-spacecraft recovery of a magnetic cloud and its origin from magnetic reconnection on the Sun, *Journal of Geophysical Research (Space Physics)*, 114, A04102, doi:10.1029/2008JA013657, 2009.

E. K. J. Kilpua, P. C. Liewer, C. Farrugia, J. G. Luhmann, C. Möstl, Y. Li, Y. Liu, B. J. Lynch, et al. "Multispacecraft Observations of Magnetic Clouds and Their Solar Origins between 19 and 23 May 2007". *Sol. Phys.* 254 (2009) 325–344.

ANNEX C - PUBLISHED ABSTRACT SUMMARY IN CONFERENCES/CONGRESS/SCHOOL/MEETINGS PROCEEDINGS

1- Geomagnetic Disturbance Identification Using Discrete Wavelet Decomposition. A Preliminary Study

Ojeda, G. A., Correa M. S., Klausner, V., Denardini, C. M., Papa, A. R., Domingues, M.O., Mendes, O.

Summer school.

PUC-Rio de Janeiro, Brazil. 02-06 Feb 2009.

Abstract

In this work, we analyze the global geomagnetic disturbance using simultaneous satellite and ground observations. In order to study such phenomena, the wavelet technique (Daubechies orthogonal wavelet transform) has been chosen because of its ability to analyze non-stationary signals and time-frequency localization (Domingues et, al., 2005). The geomagnetic activity during April 2001 will be study in this paper using ACE satellite, magnetograms (to five station) and geomagnetic indices data. The first three levels of the wavelet coefficients of the discrete wavelet transform was calculated to previous data. Mendes et. al., (2005) used this methodology only applied to H or X component of the Earths magnetic field for six day temporal windows. In April 2001 happened seven sudden storm commencing (SSC) identified in the Dst Index. The higher amplitude of the wavelet coefficients (H or X component and geomagnetic indices) occurred during the main phase of the geomagnetic storms. The discrete wavelet transform (Daubechies) as an alternative way to predict the global geomagnetic disturbance and it can using how a sophisticated space weather tool still in development.

2- Orthogonal discrete wavelet decomposition: Part 1. Using ACE satellite data

Ojeda, G. A., Correa M. S., Klausner, V., Domingues, M.O., Mendes, O., Papa, A. R.

DINCON 2009.

Universidade Estadual Paulista Julio de Mesquita Filho - Unesp, in Bauru city, Brazil. 18-22 Maio de 2009.

Abstract

We analyze geomagnetic disturbance using ACE satellite and Dst data (April 2001). The Daubechies orthogonal wavelet transform has been chosen because of its ability to

analyze non-stationary signals and time-frequency localization. The wavelet coefficients thresholds allow the singularity detection in the solar wind component associate with a future geomagnetic storm.

3- Orthogonal discrete wavelet decomposition Part 2: Analysis of magnetometer data.

Klausner, V., Correa M. S., Ojeda, G. A., Domingues, M.O., Mendes, O., Papa, A. R.
DINCON 2009.

Universidade Estadual Paulista Julio de Mesquita Filho - Unesp, in Bauru city, Brazil.
18-22 Maio de 2009.

Abstract

This work analyzes the magnetogram data of four selected stations using discrete wavelet decomposition. We used the H or the X component of the Earth's magnetic field as it was available for each station in data centers. The main phase of geomagnetic storms is identified by this technique.

4- Analysis on Spatio Temporal Entropy for Magnetic Clouds of solar Cycle 23.

Ojeda, A. G., Mendes, O., Domingues, M. O., Calzadilla A. M.
International Living with a star.
Ubatuba, SP, Brazil .04-09/10 de 2009.

Abstract

Nonlinear evolving dynamical systems, such as solar wind plasma, generate complex fluctuations in the detect signals that can be investigated with techniques adopted from the nonlinear dynamics theory, for example the Spatio-Temporal Entropy (STE). The time series of Interplanetary Magnetic Field (bx, by, bz) for a group of Interplanetary coronal mass ejection (ICME), separating the shock wave and magnetic cloud (MC) identified by Huttunen et al. (*Annales Geophysicae Vol. 23, pp. 1 - 17, 2005*) were used. It was composed by 57 magnetic clouds (1998 - 2003) observed by the ACE satellite in solar cycle 23. The results of this work, lower value close to zero were found for the STE similar to Ojeda et al. (*JASTP, Vol. 67, pp. 1859-1864, 2005*). It is a new feature but the usual features (the magnetic field strength is higher than the average, the magnetic field direction rotates smoothly through a large angle, and the proton temperature is

low) established to the MCs. The MCs also have lower STE values than the shock wave. The efficiencies of the magnetic reconnection will be studied related to the feature of the magnetic cloud reaching the Earth magnetosphere. It is motivate due to low STE establishes a topological magnetic configuration well structured.

5- Cálculo da entropia espaço temporal janelada em variáveis do vento solar.

Ojeda, G. A., Mendes, O., Calzadilla, M. A., e Domingues, M. O.

III Simpósio Brasileiro de Geofísica Espacial e Aeronomia.

Armação dos Búzios - RJ, Brasil. 01 a 03 de setembro de 2010.

Resumo

A geometria de uma nuvem magnética (MC) durante a movimentação no meio interplanetário é considerada como uma corda de fluxo onde o campo magnético está livre de força. O valor do ângulo de inclinação do eixo da nuvem em relação ao plano da eclíptica deriva em oito tipos de cordas de fluxo: os bipolares SWN, SEN, NWS, NES ($\theta_C < 45^0$) e os unipolares WSE, WNE, ESW, ENW ($\theta_C > 45^0$). A maioria das nuvens magnéticas é precedida por choques, quando a velocidade de deslocamento da nuvem é superior ao meio (vento solar). Nos dados experimentais, as características de um choque são: o aumento brusco (similar a uma descontinuidade) da intensidade do campo magnético, da densidade do plasma e da temperatura do vento solar, respectivamente. Neste trabalho estudam-se series temporais de nuvens magnéticas imersas no vento solar, com uma ferramenta (Entropia Espaço-Temporal) de dinâmica não-linear. A técnica consiste em fazer o gráfico de recorrência (RP) de uma série temporal e obter medida da sua estrutura com o cálculo da entropia. A Entropia Espaço-Temporal (STE) mede a “estrutura” da imagem nos domínios do espaço e tempo. Essencialmente, compara-se a distribuição global de cores sobre todo o gráfico de recorrência (RP) com a distribuição de cores sobre cada linha diagonal no próprio gráfico. Fisicamente, comparam-se as distribuições de distancias entre todos os pares de vetores no espaço de fase reconstruído com a distribuição de distancias entre diferentes orbitas que evoluem no tempo. O resultado é normalizado e apresentado como uma porcentagem da máxima entropia (aleatoriedade). O calculo da STE não é significativo em uma serie temporal com tendências. Sendo assim, as series temporais das variáveis no vento solar tem tendências, então não é possível utilizar a STE para estudar as não-linearidades. No entanto notou-se que a maioria das nuvens magnéticas tem uma tendência muito marcada nas componentes do campo magnético e o calculo da STE apresenta um valor de 0% só no intervalo da nuvem. A técnica permite detectar rapidamente a presença de uma MC dos dados de vento solar se calcularmos a

STE continuamente em janelas de vento solar. O valor de STE próximo a 0% é uma nova característica das MCs.

6- The windowed spatio-temporal entropy, automatic tool to detect magnetic clouds.

Ojeda, G. A., Mendes, O., Calzadilla, M. A., and Domingues, M. O.
Summer School.

“Estación Astronómica Carlos U. Cesco” del Observatorio Astronómico Félix Aquilar de la Universidad Nacional de San Juan, parque nacional “El Leoncito”, Barreal, Argentina. 7-14/february/2011.

Abstract

We studied time series of magnetic clouds immersed in the solar wind, with a tool (Spatio-Temporal Entropy) of nonlinear dynamics. Spatio-Temporal Entropy (STE) measures the image “structureness” in both space and time domains. Essentially, it compares the global distribution of colors over the entire recurrence plot with the distribution of colors over each diagonal line of the recurrence plot. This quantity compares the distribution of distances between all pairs of vectors in the reconstructed state space with that of distances between different orbits evolving in time. If there is a trend in the time series, you might want to consider removing it by differencing the original time series before calculating STE. The time series of IMF components has a trend, then it is not possible to use STE to study the nonlinearities. But, the magnetic clouds have characterized by enhanced magnetic fields that rotate slowly through a large angle, and the big trend causes $STE = 0\%$ inside of the cloud. The tool (STE) allows detection of MCs in solar wind windows because values of STE close to 0% is a new characteristic of MCs. As not all the magnetic components have zero entropy at the same time, we create an standardization index (Entropy Index (EI)) to allow joining the result of the three variable (Bx, By, Bz). The index is the result of multiplying the values of entropy of the three variables at the same time t normalized by 10^4 . We used the EI and minimum variance analysis method to identify two news magnetic clouds, arriving at the ACE spacecraft on 19 August 1998 at 10:00 UT and 05 April 2010 at 16:00 UT.

7- A wavelet tool to identify the occurrence of interplanetary magnetic clouds: preliminary results

Ojeda, G. A., Mendes, O., Domingues, M. O., Kaibara, M.K.
DINCON 2011.

Hotel Majestic, Águas de Lindóia. From 19/08 to 02/10, 2011.

Abstract

This work aims to provide a wavelet based methodology to be used as tool to identify and study magnetic cloud (MC) events in the solar wind. This methodology uses the interplanetary magnetic field (IMF) time series and the amplitude of their wavelet coefficients to perform this identification. The results obtained are very promising, some case analyses demonstrate its usefulness.

8- Review of the Grad-Shafranov Equation Useful in the Reconstruction of Two-Dimensional Coherent Structures in the Magnetopause.

Ojeda, G. A., Mendes, O., and Domingues, M. O.

IV Simpósio Brasileiro de Geofísica Espacial e Aeronomia.

Universidade Presbiteriana Mackenzie Escola de Engenharia, CRAAM, São Paulo. 10-14/09/2012.

Abstract

Nowadays some important studies on space plasmas are based on the investigation of two fundamental questions: (1) what means exactly an electromagnetic confinement? (2) How is the evolution of plasmas within a such confinement? Those kinds of studies involve basically nonlinear elliptic partial differential equations with free boundary conditions and can be performed using the Grad-Shafranov (GS) equation in regions with toroidal symmetry. However, Sonnerup, B. U.O. et al. (1996, GRL, v. 23, n. 25, pp 3679-3682) and Hau, L.-N. et al. (1999, JGR, v. 104, n. A4, pp 6899-6917) developed a method for recovering two-dimensional structures in the magnetopause, from the GS equation, in an ideal MHD formulation. The method is called Grad-Shafranov or GS reconstruction. Using the spacecraft measurements as initial values, this approach can treat the problem as a Cauchy problem - although it is ill-posed - and it can be solved numerically. Those authors found several small magnetic islands embedded into the magnetopause edge, which are presumably caused by resistive tearing mode instability. In order to test the accuracy of the numerical procedure a special case with an exact solution of the GS equation has been used. Thus, in this work a detailed, software-aided study of the Hau, L.-N. et al. (1999, JGR, v. 104, n. A4, pp 6899-6917) paper was performed. We review the results and we are presenting some equations and figures that are not shown by the authors. We are also showing results obtained in the works of Hau, L.-N. et al. (2003, JGR, v. 108, n. A1, pp 1011-1021) and Lui A. T.Y. (2008, JGR, v. 35, n. L17S05, 1-7). Currently, the technique also has been developed by us to be applied in surveys

of flux transfer events, flux ropes in the Earth's magnetotail, as well as magnetic flux ropes and magnetic clouds in the solar wind (Lui A. T.Y. 2011 Space Sci Rev, v. 158, 43-68).

9- Characterization of a double flux-rope magnetic cloud observed by ACE spacecraft on August 19-21, 1998

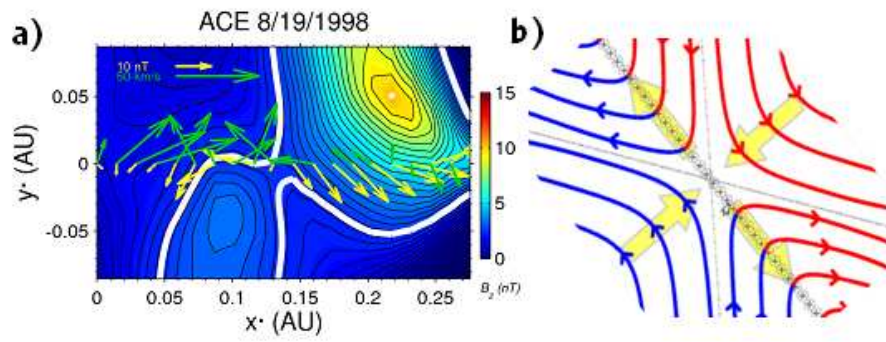
Ojeda, G. A., Mendes, O., Domingues, M. O., Möstl, C., Farrugia, C. J., Gonzalez, W. D.,

Abstract submitted to AGU Meeting of the Americas
Cancun, Mexico, 14-17 May 2013.

Abstract

Investigations have studied MC cases of double flux rope configuration with apparent asymmetry. Grad-Shafranov reconstruction technique allows deriving the local magnetic structure from data of a single spacecraft. The results obtained show two cylindrical flux ropes next to each other, where a single X point forms between them. In all possible combinations of two bipolar MCs, the magnetic field between them is antiparallel in eight cases SWN-SWN, SWN-SEN, SEN-SWN, SEN-SEN, NWS-NWS, NWS-NES, NES-NWS, NES-NWS. If clouds are under magnetic coupling, reconnection evidences are expected from the interaction between them. In this work, we examine the event that occurred at Aug. 19-21, 1998 using solar wind measurements collected by ACE. In Fig. C a) presents the recovered cross-section of the two bipolar MCs (SEN-SWN). The black contour lines show the transverse magnetic field lines (calculated as the contours of the magnetic potential function $A(x,y)$), and the colors show the axial magnetic field B_z distribution. The yellow arrows along $y=0$ denote measured transverse magnetic field vectors, direction and magnitude measurements at ACE utilized as initial input into the numerical solver. The green arrows are residual velocities in the deHoffmann-Teller frame at ACE. The spacecraft crosses the X point and observes the exact moment of the magnetic reconnection, from 0.13 to 0.15 AU in x axis. In the opposite corners of the X point, the magnetic fields are antiparallel (see yellow arrows in this region). The residual velocity (green arrow in $y=0$) in the deHoffmann-Teller frame at ACE is perpendicular to the magnetic field line in the reconnection region. In principle, it is possible to adjust a two-dimension model considering the most common separator reconnection, in which four separate magnetic domains exchange magnetic field lines. In Fig. C b), the cross-section through four magnetic domains undergoing separator reconnection is represented. The green array in the top panel shows a speed in the same direction as the prediction in the reconnection model. Also, the magnetic configuration reconstructed confirms the initial hypothesis, i.e., the existence of two bipolar MCs (SEN-SWN) with reconnection between

them. Based on the analyses done by nonlinear mathematical tools, this work considers some other instigating features.



ANNEX D - ARTICLES IN SCIENTIFIC JOURNALS

1- The Daubechies wavelet as a tool to study interplanetary magnetic field fluctuations

Ojeda, G. A., Mendes, O., and Domingues, M. O.

Abstract

Many geoeffective space phenomena, among them the magnetic clouds (MCs), require extensive studies to understand the physical processes. To do that, examinations of Interplanetary Magnetic Field (IMF) data together solar wind plasma data are essential. However, many times the IMF are the only available data from satellites in the solar wind. Efforts to develop new ways to deal with this kind of data aiming to help diagnose purposes could be very useful. Thus, by using the Daubechies wavelet coefficients, an analysis methodology was implemented in order to study a wide set of MCs. The aim is to characterize the magnetic field at the three difference regions around an Interplanetary Coronal Mass Ejection (ICME) event: plasma sheath, MC, and after the MC. The analysis of this work is based on the application of wavelets techniques to three different regions, relating it with the behavior of the three regions. The wavelet coefficients have the property that their amplitudes are related to the local regularity of the analyzed data (where the data present a smooth behavior, the wavelet coefficients are smaller, and vice-versa). This is the basic idea of data compression and the application we are doing here. The wavelet coefficients amplitudes are also related to the analyzing wavelet order and the scale level. There is not a perfect wavelet choice for a certain data analysis, however one can follow certain criteria to provide a good choice. We choose the Daubechies scaling function of order 2 (db2), with that choice the wavelet function locally reproduces linear polynomial. With this choice, to reproduce well the interplanetary magnetic cloud disturbances is possible, and therefore the wavelet coefficients in that regions are very small. On one hand, high order analyzing Daubechies functions are not adding a better local reproduction of the MC disturbances data, and on the other hand, the analyzing function of order 1 does not reproduce well these disturbance. We also observed that just one decomposition level is enough for the energy analysis methodology that we study, level which corresponds to a pseudo-period of 48 seconds. A *zoom in* made in the magnetic fluctuations help to separate features related to different disturbance processes, *i. e.*, to allow identifying magnetic cloud. The results achieved here confirm the promising use of this methodology as an auxiliary tool to identify boundaries (with human help) in the solar wind, specifically, the shock wave and leading edge of ICMEs. This methodology is not still tested to identify some specific fluctuation patterns at IMF to any other interplanetary disturbances, such as, CIRs, heliospheric current sheath crossings or to

ICMEs without MC signatures respectively. In our opinion, as it is by the first time applied to the IMF data with this purpose, the presentation of this approach for the Space Physics Community is the most important contribution of this work.

Keywords: Space weather, Space Electrodynamics, Magnetic Clouds, Time Series Analysis, Wavelet Transform.

Current Stage - Manuscript accepted for publication in the "Geofísica Internacional" (2013).

2- Spatio-Temporal Entropy Analysis Of The Magnetic Field To Help Magnetic Cloud Characterization

Ojeda, G. A., Mendes, O., Calzadilla, M. A., and Domingues, M. O.

Abstract

A subset of Interplanetary Coronal Mass Ejections (ICMEs) has simple flux rope-like magnetic fields, named magnetic clouds (MCs). The aim of this work is create a methodology to characterize the dynamics of MCs from signals received by satellites in the interplanetary medium. For that, a dataset from ACE spacecraft localized at L1 Lagrangian point about 1.5 million km from Earth are used. We have tested physical-mathematical tools to study 41 MCs identified by other authors, where the plasma sheath region also was identified. The recurrence plot is a visual tool for the investigation of temporal recurrence in phase space. The Spatio Temporal Entropy (STE) was implemented in Visual Recurrence Analysis (VRA) software to quantify the order in the recurrence plot. In physical terms, this quantity compares the distribution of distances between all pairs of vectors in the reconstructed state space with that of distances between different orbits evolving in time. Some test using time series with data file included in VRA software were performed to validate the method. On the other hand, we worked with IMF components Bx, By, Bz of 16 s. Time windows from March 1998 to December 2003 for some MCs were selected. We found higher STE values in the sheaths and zero STE values in some of the three components in most of the MCs (30 among 41 events). The trend is the principal cause of the lower STE values in the MCs. Also, MCs are most structuredness than sheath and "quiet" solar wind. We done a test considering the magnetic components of a cylindrically symmetric force-free constructed analytically, with result of zero STE value. It agrees with the physical assumption of finding zero STE values when studying experimental data in MC periods. The new feature just examined here adds to the usual features, as described in Burlaga et al., (1981), for the characterization of MCs. Thus, the STE calculation can be an auxiliary objective tool to identify flux-ropes associated with MCs, mainly during

events with no available plasma data but only with IMF.

Keywords: ICME, Magnetic Cloud, Entropy, Space Plasmas, IMF, Space Electrodynamics.

Current Stage - Manuscript submitted for publication in the Journal of Geophysical Research (2013-01-11)

3- The Entropy Index (EI): An Auxiliary Tool To Identify Flux Rope Associated With Interplanetary Magnetic Clouds

Ojeda, G. A., Mendes, O., Calzadilla, M. A., and Domingues, M. O.

Abstract

We propose the use of spatio-temporal entropy (STE) analysis as a mathematical tool to identify magnetic cloud (MC) candidates based only on the interplanetary magnetic field (IMF) data. Using recurrence plot analysis, the STE measures the level of organization/structuredness of process features in physical records. To build the methodology, we calculate the STE, as a function of time, for IMF components using magnetic records within a time windows corresponding approximately to 11.11 hours, physical parameter representative for MC events, displaced consecutively by a proper time step till the end of data series. The STE reaches values extremely close to zero at least for one of the IMF components during MC event, due to MC structure features. Not all the magnetic components in MCs have STE values equal zero at the same time. By that reason, we create a standardization index (called Interplanetary Entropy (IE) index). IE close to zero indicates the occurrence of a MC-candidate, and its probable time location. This tool found as results the known MCs compiled in earlier work, as well as new MC-candidates with appealing features deserving further investigations. Also, the use of IE index conjugated with MVA analysis becomes also possible, using only the IMF data, to delimit the MC boundaries. In a general sense, the proposed IE calculation could constitute the basis for an easy and automatic computational procedure for preliminary survey on MC occurrence for scientific goals, or even a convenient MC warning for space weather purposes.

Keywords: ICME, Magnetic Cloud, Entropy, Space Plasmas, IMF, Space Electrodynamics.

Current Stage - Manuscript submitted for publication in the Journal of Geophysical Research (2013-02-05)

4- Study of local regularities in the solar wind data and ground magne-

tograms.

Klausner V., Ojeda G. A., Domingues M. O., Mendes O., Papa A. R. R.

Abstract

Interplanetary coronal mass ejections (ICMEs) can reach the Earth's magnetosphere causing magnetic disturbances. It can be measured by satellite and ground-based magnetometers. Data from the ACE satellite and from the geomagnetic field was explored here via discrete wavelet decomposition (DWT). The increase of wavelet coefficient amplitudes of the solar wind parameters and geomagnetic field data analysis are well-correlated with the arrival of the shock and sheath region. As an auxiliary tool to verify the disturbed magnetic fields identified by the DWT, we developed a new approach called effectiveness wavelet coefficient (EWC) methodology. The first interpretation of the results suggests that DWT and EWC can be effectively used to characterize the fluctuations on the solar wind parameters and its contributions to the geomagnetic field. Further, these techniques could be implemented to real-time analysis for forecast space weather scenarios.

Keywords: Wavelet analysis, Solar wind-magnetosphere interaction, Magnetogram data, Geomagnetic storm.

Current Stage - Manuscript submitted for publication in the Journal of Atmospheric and Solar-Terrestrial Physics (2013-01-15)

PUBLICAÇÕES TÉCNICO-CIENTÍFICAS EDITADAS PELO INPE

Teses e Dissertações (TDI)

Teses e Dissertações apresentadas nos Cursos de Pós-Graduação do INPE.

Manuais Técnicos (MAN)

São publicações de caráter técnico que incluem normas, procedimentos, instruções e orientações.

Notas Técnico-Científicas (NTC)

Incluem resultados preliminares de pesquisa, descrição de equipamentos, descrição e ou documentação de programas de computador, descrição de sistemas e experimentos, apresentação de testes, dados, atlas, e documentação de projetos de engenharia.

Relatórios de Pesquisa (RPQ)

Reportam resultados ou progressos de pesquisas tanto de natureza técnica quanto científica, cujo nível seja compatível com o de uma publicação em periódico nacional ou internacional.

Propostas e Relatórios de Projetos (PRP)

São propostas de projetos técnico-científicos e relatórios de acompanhamento de projetos, atividades e convênios.

Publicações Didáticas (PUD)

Incluem apostilas, notas de aula e manuais didáticos.

Publicações Seriadas

São os seriados técnico-científicos: boletins, periódicos, anuários e anais de eventos (simpósios e congressos). Constam destas publicações o Internacional Standard Serial Number (ISSN), que é um código único e definitivo para identificação de títulos de seriados.

Programas de Computador (PDC)

São a seqüência de instruções ou códigos, expressos em uma linguagem de programação compilada ou interpretada, a ser executada por um computador para alcançar um determinado objetivo. Aceitam-se tanto programas fonte quanto os executáveis.

Pré-publicações (PRE)

Todos os artigos publicados em periódicos, anais e como capítulos de livros.